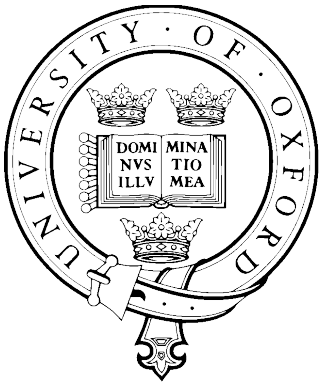
FADING PHENOMENA IN LI-RICH LAYERED OXIDE MATERIAL FOR LITHIUM-ION BATTERIES

Submitted by

Taehoon Kim

St Cross College



Department of Engineering Science
University of Oxford

A thesis submitted for the degree of

Doctor of Philosophy

Hilary Term 2015

Fading phenomena in Li-rich layered oxide material for Lithium-ion Batteries

Taehoon Kim, St Cross College, University of Oxford

Abstract

Lithium-rich layered transition metal oxide cathode, represented as the chemical formula of $x\mathrm{Li_2MnO_3} \cdot (1-x)\mathrm{LiMO_2}(\mathrm{M} = \mathrm{Mn, Ni, Co})$, retains immense interest as one of the most promising candidates for energy storage system ranging from mobile devices to electric vehicle applications (EV/HEV/PHEV). This battery type benefits from superior theoretical capacity (>250 $\mathrm{mAhg^{-1}}$), high chemical potential (>4.6 V vs $\mathrm{Li^0}$), good thermal stability, high discharge capacity and lower cost compared with conventional cathodes (e.g. $\mathrm{LiCoO_2}$, $\mathrm{Li(Ni_{1/3}Mn_{1/3}Co_{1/3})O_2}$ cathodes). However, there remain major barriers which still need to be improved in order to achieve a successful commercialization for large-scale devices or electric vehicle applications. The irreversible capacity loss of 40-100 $\mathrm{mAhg^{-1}}$ during the initial electrochemical cycle and the battery fading phenomena (capacity fading/voltage decay) on further cycles are the major problems which have emerged. The $\mathrm{Li^+}$ ion extraction accompanied by oxygen release from the active material in the form of oxide known as lithia ($\mathrm{Li_2O}$) along with the transition metal migration has been suggested as the dominant processes underlying the capacity fading mechanism. Those processes, in turn, cause a phase transition from a layered structure into a spinel within the electrode material. The interplay of the local atomic environments between $\mathrm{Li_2MnO_3}$ (monoclinic, C2/m) and $\mathrm{LiMO_2}$ (trigonal/hexagonal, $\mathrm{R\bar{3}m}$) holds the key to developing better cathodes with enhanced stability. In the present thesis, an *in operando* XAS study using a specially-designed cell of the graphene-coated $\mathrm{Li(Li_{0.2}Mn_{0.54}Ni_{0.13}Co_{0.13})O_2}$ cathode is employed to examine the chemical, electronic, and structural states of the transition metals (Mn, Co, and Ni) during electrochemical cycle(s). Precise oxidation states for the transition metals is evaluated by the combined analyses from the XANES and SQUID measurements. The K-edge XANES spectral shift is quantified to investigate the contribution to the charge compensation mechanism by the oxidation change. Absorption features in K-edge XANES are identified. These features describe the electronic state of the individual atoms in the cathode composite, as well as the local distortion from the octahedral structure of $\mathrm{MO_6}$. The Fourier transform of EXAFS offers a satisfactory description of the local structure changes with the connection to the cation arrangement. The description is generally involved with the peak amplitude, position, shape changes (trend), and coordination numbers in the real space. Hence, similarities or discrepancies in the local atomic environments could be compared at different state of charge. Major structural parameters are deduced from the EXAFS fitting process. These parameters can be used to distinguish different atomic environments upon voltage bias levels or investigate the appearance of the Jahn-Teller effect. A new approach to understand the atomic environment upon charge-discharge is demonstrated, namely, a Continuous Cauchy Wavelet Transform (CCWT) which enables the visualization of the EXAFS spectra in three dimensions by decomposing the *k*-space and R-space (uncorrected for phase shift) signals. The wavelet transform analysis provides possible evidence of the precursor that leads to the spinel phase transition in this battery system.

ACKNOWLEDGEMENTS

First of all, I would like to express my deepest gratitude to my supervisor, Professor Alexander M. Korsunsky. He instilled in me the belief that anything is possible as long as I am dedicated and persistent in pursuing my goal. He provided me the opportunity to participate in his wonderful research group and has given my work minute consideration during the doctoral course. I appreciate his continuous guidance that nurtures my knowledge and wisdom.

I wish record my appreciation to Professor Lu Li at National University of Singapore (NUS) in acknowledging the various kinds of help and support I have received. I would especially like to give my thanks to Dr. Bohang Song for providing me all the helps and sharing his knowledge of the Li-ion battery applications. His advice always motivated me in continuing my study in the battery research.

Additionally, I want to take this opportunity to thank all the people in the group: Dr. Xu Song, Dr. Jonathan Belnoue, Dr. Felix Hofmann, Dr. Brian Abbey, Dr. Mengyin Xie, Dr. Tan Sui, Alexander Lunt, Ricky Ying, Enrico Salvati, and Hongjia Zhang.

It is a particular pleasure to acknowledge my debt to Karen Shoobridge who is the laboratory coordinator at Diamond Light Source. I would like to record my gratitude to a number of individual who have provided me help in lab. experiments in the Research Complex at Harwell (Rutherford Appleton Laboratory). I would like to recognize the scientists and engineers who worked at the synchrotron facilities in Diamond Light Source (DLS, UK), European Synchrotron Radiation Facility (ESRF, France), and SOLEIL (France).

My gratitude goes to my parents In-Dal Kim and Young-Ri Lee for their persistent love and patience, providing inspirations. Thank you for your moral support and belief in me.

Finally, I would like to deeply thank to my lovely wife, Minjeong Song who is also in the doctoral course and my cute son Minwoo Kim. The period during which this thesis was being written will always remain associated with the birth of my son. Without their support and encouragement, I could not have completed my thesis.

TABLE OF CONTENTS

1 Chapter 1 Introduction 1

1.1 Background 1

1.2 Aims and scope of the present research 5

1.3 Thesis structure 7

2 Chapter 2 Literature Review 11

2.1 Electrochemistry basics 11

2.2 Working principle of Li-ion batteries 16

2.3 Considerations for battery components: cathode, anode, and electrolyte 17

2.4 Conventional lithium intercalation cathodes 20

2.4.1 Spinel type ($LiMn_2O_4$) 20

2.4.2 Olivine type ($LiFePO_4$) 21

2.4.3 Lithium layered oxide cathode ($LiXO_2$) 22

2.4.3.1 Single transition metal Oxide: $LiCoO_2$, $LiNiO_2$, $LiMnO_2$ cathodes 23

2.4.3.2 Mixed nickel-manganese oxide type: $Li(Ni_{1/2}Mn_{1/2})O_2$ Cathode 27

2.4.3.3 NMC type: $Li(Ni_{1/3}Mn_{1/3}Co_{1/3})O_2$ cathode 28

2.5 High-energy density lithium intercalation cathode 29

2.5.1 Lithium-rich layered transition metal oxide 29

2.5.2 Integrated composite and solid-solution concept ($Li_2MnO_3-LiMO_2$) 30

2.5.3 Origin of the high capacity and structural property 31

2.5.4 Electrochemistry of Li-rich layered oxide cathode 34

2.5.5 Reaction mechanism during 1st electrochemical cycle 36

2.5.5.1 Chemical reaction of irreversible oxygen loss 36

2.5.5.2 Charge compensation mechanism 36

2.5.6 Considerations in local atomic environment 38

2.5.6.1 Transition metal composition 38

2.5.6.2 Crystal Field Theory 40

2.5.6.3 Jahn-Teller distortion 43

2.6 Ageing mechanism in the lithium-ion battery 45

2.6.1 Overview of the ageing mechanism 45

2.6.2 Phase transition issue in Li-rich layered oxide cathode: layered into spinel structure 47

3 Chapter 3 X-ray Absorption Fine Structure (XAFS) Theory 48
3.1 Physics of X-ray Absorption Fine Structure (XAFS) 48
3.2 X-ray Absorption Near-edge Structure (XANES) 51
3.3 Extended X-ray Absorption Fine Structure (EXAFS) 54
3.3.1 EXAFS oscillation 54
3.3.2 Theoretical description of EXAFS equation 55
3.4 XAFS interpretation method 57
3.4.1 EXAFS data reduction and modelling 57
3.4.2 Statistics for EXAFS data analysis 61
4 Chapter 4 Experimental Methods 63
4.1 Active material synthesis 63
4.1.1 Spray-dryer assisted sol-gel synthesis 63
4.1.2 Graphene coating by Hummers method 63
4.1.3 Carbonate assisted co-precipitation method 64
4.2 Cell design and electrochemical characterization 64
4.2.1 Cell design for *in operando* XAS study and cell assembling 64
4.2.2 Galvanostatic measurement 66
4.2.3 Differential analysis (dQ/dV curve) 67
4.3 Synchrotron X-ray Absorption Spectroscopy (XAS) 68
4.4 X-ray Diffraction (XRD) and Rietveld refinement 69
4.5 RAMAN spectroscopy 71
4.6 SQUID magnetic measurement 74
4.7 ATR-FTIR Spectroscopy 75
4.8 Scanning Electron Microscopy (SEM) and Energy-dispersive X-ray spectroscopy (EDX) 76
4.9 Continuous Cauchy Wavelet Transform (CCWT) analysis 77
5 Chapter 5 The effect of doping and synthesis temperature on the structure and electrochemical performance of the Li-rich layered oxide cathode 78
5.1 Introduction 78
5.2 Experimental Section 80
5.2.1 Active material synthesis 80
5.2.2 Electrochemical characterization 82
5.2.3 Active material characterization 83
5.2.4 Synchrotron XAS experiment/interpretation 83
5.3 Results and Discussion 84

5.3.1 Electrochemical properties of P/G/C-type lithium-ion batteries 84
5.3.2 Investigation of electrochemical activity in Li_2MnO_3 component 89
5.3.3 Formation of the integrated components in the active materials 90
5.3.4 Evaluation of magnetic properties 97
5.3.5 Investigation of local atomic environment by XANES/EXAFS 100
5.3.6 Characterization of local surface environments upon different synthesis temperatures . 107
5.3.7 Magnetic measurements upon different synthesis temperatures 111
5.3.8 K-edge XANES investigation of Mn, Co, and Ni atomic states upon different synthesis temperatures 115
5.4 Conclusion 119
6 Chapter 6 Charge Compensation Mechanism in the Graphene-coated $Li_{1.2}Mn_{0.54}Ni_{0.13}Co_{0.13}O_2$ Cathode 121
6.1 Introduction 121
6.2 Experimental Section 123
6.2.1 Active material synthesis 123
6.2.2 Electrochemistry test on the normal coin cell 124
6.2.3 In operando XAS cell preparation 124
6.2.4 Synchrotron XAS experiment and data analysis 124
6.3 Results and Discussion 125
6.3.1 Evaluation of the electrochemical properties of the Graphene-coated $Li(Li_{0.2}Mn_{0.54}Ni_{0.13}Co_{0.13})O_2$ cathode 125
6.3.2 In operando XANES at Mn K-edge 127
6.3.3 In operando XANES at Co and Ni K-edge 130
6.3.4 In operando EXAFS at Mn, Co, and Ni K-edge 132
6.4 Conclusion 137
7 Chapter 7 In Operando XAS Study of Atomic Phase Reversibility in the Graphene Coated $Li(Li_{0.2}Mn_{0.54}Ni_{0.13}Co_{0.13})O_2$ Cathode 139
7.1 Introduction 139
7.2 Experimental Section 141
7.2.1 Active material synthesis 141
7.2.2 Magnetic measurement 142
7.2.3 Assembling of *in operando* coin cell 142
7.2.4 In operando XANES/EXAFS 142
7.2.5 XAS Data interpretation and CCWT analysis 143
7.3 Results and Discussion 144

7.3.1 Oxidation states evaluation and magnetic properties measurements 144
7.3.2 In operando XANES of Mn, Co, and Ni K-edge 147
7.3.3 In operando EXAFS of Mn, Co, and Ni with Wavelet Transform Analysis 150
7.4 Conclusion 161
8 Chapter 8 Charge Rate Dynamic in the Graphene Coated Li-rich Mn-based Cathode Studied by In Operando XAS 163
8.1 Introduction 163
8.2 Experimental Section 168
8.2.1 Active material synthesis 168
8.2.2 Assembling of *in operando* coin cell 168
8.2.3 Synchrotron X-ray Absorption Spectroscopy (XAS) 168
8.2.4 XAS data interpretation 169
8.3 Results and Discussion 170
8.3.1 In operando XANES at Mn K-edge 170
8.3.2 In operando XANES at Co K-edge 174
8.3.3 In operando XANES at Ni K-edge 176
8.3.4 In operando EXAFS at Mn K-edge 177
8.3.5 In operando EXAFS at Co K-edge 180
8.3.6 In operando EXAFS at Ni K-edge 181
8.3.7 Two-stage reaction and general implications 184
8.4 Conclusion 187
9 Chapter 9 Evidence of the Precursor that Triggers Spinel Phase Transition in the Li-rich layered Mn-based Oxide Cathode System 188
9.1 Introduction 188
9.2 Experimental Section 190
9.2.1 Active material synthesis 190
9.2.2 Electrochemical analysis and active material characterization 190
9.2.3 In operando XAS Study 191
9.2.4 Data interpretation for XAS and CCWT 191
9.3 Result and Discussion 192
9.3.1 Electrochemical characterization of the graphene-coated cathode 192
9.3.2 Active material characterization. 194
9.3.3 In operando XANES on Mn, Co and Ni K-edge. 197
9.3.4 In operando EXAFS on Mn, Co and Ni K-edge 200
9.3.5 In operando CCWT at Mn, Co and Ni K-edge 203

9.4 Conclusion 214

10 Chapter 10 Conclusions and Future Research 217

10.1 Conclusions 217

10.1.1 Integrated-composite system in the Li-rich layered transition metal oxide cathode 217

10.1.2 Charge compensation mechanism in the graphene-coated $Li(Li_{0.2}Mn_{0.54}Ni_{0.13}Co_{0.13})O_2$ lithium-ion battery 218

10.1.3 Charge rate dynamic in the Li-rich layered oxide cathode 219

10.1.4 Local atomic environment changes and phase transition into spinel 220

10.2 Recommendations for future research 221

List of Tables

Table 5.1 Rietveld refinement on the pristine $Li(Li_{0.2}Mn_{0.54}Ni_{0.13}Co_{0.13})O_2$ (P-type) active material (synthesized at 800 °C) using two-phase model of $Li(Ni_{1/3}Mn_{1/3}Co_{1/3})O_2$ (R3m) and Li_2MnO_3 (C2/m). 91

Table 5.2 Rietveld refinement on the graphene-coated $Li(Li_{0.2}Mn_{0.54}Ni_{0.13}Co_{0.13})O_2$ (G-type) active material (synthesized at 800 °C) using two-phase model of $Li(Ni_{1/3}Mn_{1/3}Co_{1/3})O_2$ (R3m) and Li_2MnO_3 (C2/m). 92

Table 5.3 EDX quantitative analysis of the active material. 95

Table 5.4 Experimental/calculated effective magnetic moment with Weiss constant and evaluated oxidation state of Mn in the pristine $Li(Li_{0.2}Mn_{0.54}Ni_{0.13}Co_{0.13})O_2$ (P-type) and graphene-coated $Li(Li_{0.2}Mn_{0.54}Ni_{0.13}Co_{0.13})O_2$ cathodes (G-type). 100

Table 5.5 Fitting results for the Fourier transformed data (k^3-weighted) of pristine $Li(Li_{0.2}Mn_{0.54}Ni_{0.13}Co_{0.13})O_2$ cathode (P-type) and graphene-coated $Li(Li_{0.2}Mn_{0.54}Ni_{0.13}Co_{0.13})O_2$ cathode (G-type) at Mn, Co, and Ni K-edge. (CN: Coordination number, σ: Mean-square relative displacement from EXAFS Debye-Waller factor, R-range:Fitting range, $S02$: Amplitude reduction factor and ΔE_0: Energy shift parameter). 106

Table 5.6 Experimental/calculated effective magnetic moment with Weiss constant and evaluated oxidation state of Mn of $Li(Li_{0.2}Mn_{0.54}Ni_{0.13}Co_{0.13})O_2$ active materials synthesized by sol-gel method at 600 °C (P-600), 700 °C (P-700), 800 °C (P-800), and 1000 °C (P-1000). 114

List of Figures

Figure 1.1 Ragone plot for diverse energy storage or conversion systems[6]. 2

Figure 1.2 BMW hybrid electric vehicle (HEV). 1) High efficient BMW V8 gasloline engine 2) Electric motor (15 kW/210Nm) 3) High voltage electronics, directly mounted to the transmiss 4) 8 gear automatic transmission, and 5) Lithium-ion battery (120 Volts). Image taken from reference[9] 3

Figure 2.1 Schematic illustration of intercalated lithium ions and vacancies in active material. Structure was generated with wireframe model of trigonal $LiMO_2$ (M: transition metal). 12

Figure 2.2 Principle of a lithium-ion battery on the lithium-layered oxide cathode (M=Transition Metals) 16

Figure 2.3 Illustration of open circuit energy diagram for a lithium-ion battery at $V_{oc.}$ 18

Figure 2.4 Representation of $LiMn_2O_4$ spinel structure. 20

Figure 2.5 Representation of olivine $LiFePO_4$ structure. 21

Figure 2.6 (a) Schematics of a layered $LiXO_2$ crystal structure. (b) Ball-stick model of α-NaFeO2-type structure (Trigonal, $R3m$) with unit cell in $LiXO_2$ (X= Co, Ni, Mn, Cr, V…). 22

Figure 2.7 Energy vs density of states (DOS) comparison between $LiCoO_2$ and $LiNiO_2$. E_f indicates the Fermi energy (highest filled state at O K). Image was redrawn from reference[32] ... 23

Figure 2.8 Open-circuit voltage (OCV) curve of $Li_{1-x}NiO_2$ cathode (at 30 ℃) in non-aqueous lithium-ion battery[51]. 26

Figure 2.9 HRTEM image of the $xLi2MnO3 \cdot 1 - xLiMn1/3Ni1/3Co1/3O2$ (x =0.5) composite , showing 4.7 Å lattice fringes[72]. 31

Figure 2.10 XRD patterns of the $xLi2MnO3 \cdot 1 - xLiMO2$ composite at different *x* concentration. The peaks from the cation ordering from Li2MnO3 can be observed at 2θ ~ 21-25°[73]. 32

Figure 2.11 Illustration of cation ordering of transition metals in xLi2MnO3 $\cdot 1 - x$LiMO2 composite. The yellow dash line represents the reduced $\sqrt{3}ahex \times \sqrt{3}ahex$ supercell and the blue dash line represents the unit cell. 33

Figure 2.12 Illustration of cation ordering of transition metals on the transition metal layer in Li2MnO3 component with reduced supercell. 33

Figure 2.13 (a) Galvanostatic profile of Li-rich layered oxide cathode; (b) capacity vs cycles; (c) dQ/dV plot of the initial cycle; and (d) dQ/dV plots of further cycles. Results obtained within the current study. 35

Figure 2.14 The five 3*d* orbitals with x,y,z coordinate axes. Orbitals were constructed in accordance with the quantum number of *n*=3, *l*=d, and *m*=2 or 0 (*n*: principle quantum number, *l*: azimuthal (orbital) quantum number, *m*: magnetic quantum number, and *s*: spin quantum number). 'd' indicates any *d* orbitals type. 41

Figure 2.15 Schematics of energy level of *d* orbitals in the octahedral complex with crystal field splitting. In a free transition metal ion (M^{n+}), it is degenerated with the same energy level of the five *d* orbitals. The spherical field around the transition metal ion leads to the rise of the energy level, but the orbitals remain degenerate. When negative charged ligand ions approach, the orbitals are split into two sets of energy level forming an octahedral complex. The $\Delta 0$ indicates the crystal field splitting energy. 43

Figure 2.16 Schematic illustration of a Jahn-Teller distortion (elongation along the red arrows) of MnO_6 with the energy splitting in octahedral complex. The energy level of splitting is $\Delta octahedra$ >> $\delta 1$>$\delta 2$. 44

Figure 2.17 Illustration of ageing mechanism in cathode materials[119]. 45

Figure 2.18 Some origins of battery ageing[120]. 46

Figure 3.1 An abrupt increase in absorption edge at L_3, L_2, L_1, and K[127] 48

Figure 3.2 Photoelectric effect by X-ray absorption. (a) Release of photoelectron. (b) Energy level diagram with core electron orbitals. Kinetic energy of the photoelectron is given by $E\text{-}E_0$ where m_e is the mass of electron, E_0 the binding (ionization) energy, and v the velocity of electron. 49

Figure 3.3 Presentation of atom scatterings. 49

Figure 3.4 Normalised XAS spectra at Mn K-edge on pristine material of $Li[Li_{0.2}Mn_{0.54}Ni_{0.13}Co_{0.13}]O_2$ active material with XANES and EXAFS regimes in the X-ray absorption spectroscopy. 51

Figure 3.5 Schematics of EXAFS oscillation from wave inteferences. 54

Figure 3.6 EXAFS fitting process with IFEFFIT (FEFF 6 algorithm). 58

Figure 3.7 The absorption spectra data of NMC cathode at Mn K-edge (a) Raw data (b) k-space conversion (c) R-space conversion, and (d) Inverse transformed k-space (q-space). 59

Figure 3.8 The envelope (blue) of the radial distribution function with real (red curve) and imaginary (green) parts of Mn K-edge in the NMC cathode. Fourier transformation is applied with k^3 weighting. 61

Figure 4.1 Schematics of the In Operando XAS cell design. 65

Figure 4.2 Active materials (left) and lithium-ion battery parts (right) 66

Figure 4.3 Galvanostatic charge-discharge with multi-channel wires. 67

Figure 4.4 In Operando XAS setup with the electrochemical cells at synchrotron beamlines: Diamond Light Source (UK) (a) I18 (b) B18 (c) I18 and (d) SOLEIL DIFFABS (France). Illustration of the XAS experiment (bottom). 69

Figure 4.5 Presentation of Bragg diffraction on constructive interference (left) and destructive interference (right)[143]. 70

Figure 4.6 Illustration of Raman scattering concept. 72

Figure 4.7 Raman ($\nu1, \nu2, \nu5$) and infrared (IR) activities of normal modes in the octahedral MO_6 molecules[145] 73

Figure 4.8 SQUID magnetometer (a) working principle and (b) sample installation. 74

Figure 4.9 Schematics of Attenuated total reflection (ATR) principle. 76

Figure 5.1 Electrochemical property of pristine $Li(Li_{0.2}Mn_{0.54}Ni_{0.13}Co_{0.13})O_2$ cathode (P-type). (a) Galvanostatic profile up to 30th cycle with current rate of 0.2 C. (b) Specific charge (black circle) and discharge capacity (white square) with Coulombic efficiency (%). (c) dQ/dV plot of initial cycle. (d) dQ/dV plots on furher cycles. 85

Figure 5.2 Electrochemical property of graphene-coated $Li(Li_{0.2}Mn_{0.54}Ni_{0.13}Co_{0.13})O_2$ cathode (G-type). (a) Galvanostatic profile up to 30th cycle with current rate of 0.2 C. (b) Specific charge (black circle) and discharge capacity (white triangle) with Coulombic efficiency (%). (c) dQ/dV plot of initial cycle. (d) dQ/dV plots on furher cycles. 86

Figure 5.3 Electrochemical property of $Li(Li_{0.2}Mn_{0.54}Ni_{0.13}Co_{0.03}Cr_{0.10})O_2$ cathode (C-type). (a) Galvanostatic profile up to 50th cycle with current rate of 0.2 C. (Formation cycles used 0.05 C-rate). (b) Specific charge (white triangle) and discharge capacity (black circle) with Coulombic efficiency (%). (c) dQ/dV plot of initial cycle. (d) dQ/dV plots on furher cycles.Red arrows indicate the spectra shifts upon charge-discharge. 88

Figure 5.4 Electrochemical property of Li_2MnO_3 cathode. (a) Galvanostatic profile during 50 cycles and (b) charge/discharge specific capacity with Coulombic efficiency (%). 89

Figure 5.5 X-ray diffraction patterns of (a) pristine $Li(Li_{0.2}Mn_{0.54}Ni_{0.13}Co_{0.13})O_2$ cathode (P-type), (b) graphene-coated $Li(Li_{0.2}Mn_{0.54}Ni_{0.13}Co_{0.13})O_2$ cathode (G-type), and (c) $Li(Li_{0.2}Mn_{0.54}Ni_{0.13}Co_{0.03}Cr_{0.10})O_2$ cathode (C-type). P-type and G-type cathodes were indexed with two phases of R3m (red) and C2/m (blue). 93

Figure 5.6 SEM image of the pristine $Li(Li_{0.2}Mn_{0.54}Ni_{0.13}Co_{0.13})O_2$ cathode (P-type), the graphene-coated $Li(Li_{0.2}Mn_{0.54}Ni_{0.13}Co_{0.13})O_2$ cathode (G-type), $Li(Li_{0.2}Mn_{0.54}Ni_{0.13}Co_{0.03}Cr_{0.10})O_2$ cathode (C-type), and Li_2MnO_3 cathode. Samples were synthesized at 800 °C. 94

Figure 5.7 EDX mapping of O, Mn, Co, and Ni in (a) Pristine and (b) Graphene coated $Li(Li_{0.2}Mn_{0.54}Ni_{0.13}Co_{0.13})O_2$. 95

Figure 5.8 (a) ATR-FTIR spectra and (b) Raman spectra of pristine $Li(Li_{0.2}Mn_{0.54}Ni_{0.13}Co_{0.13})O_2$ cathode (P-type), graphene-coated $Li(Li_{0.2}Mn_{0.54}Ni_{0.13}Co_{0.13})O_2$ cathode (G-type), $Li(Li_{0.2}Mn_{0.54}Ni_{0.13}Co_{0.03}Cr_{0.10})O_2$ cathode (C-type), $Li(Ni_{1/3}Mn_{1/3}Co_{1/3})O_2$ (NMC) cathode, and Li_2MnO_4 (Spinel) cathode. 97

Figure 5.9 Measurement of the magnetic properties (magnetization:left and magnetic susceptibility:right). (a) Pristine $Li(Li_{0.2}Mn_{0.54}Ni_{0.13}Co_{0.13})O_2$ cathode (P-type), (b) graphene-coated $Li(Li_{0.2}Mn_{0.54}Ni_{0.13}Co_{0.13})O_2$ cathode (G-type), and (c) $Li(Li_{0.2}Mn_{0.54}Ni_{0.13}Co_{0.03}Cr_{0.10})O_2$ cathode (C-type). 98

Figure 5.10 Normalised XANES spectra of pristine $Li(Li_{0.2}Mn_{0.54}Ni_{0.13}Co_{0.13})O_2$ cathode (P-type), graphene-coated $Li(Li_{0.2}Mn_{0.54}Ni_{0.13}Co_{0.13})O_2$ cathode (G-type), and $Li(Li_{0.2}Mn_{0.54}Ni_{0.13}Co_{0.03}Cr_{0.10})O_2$ cathode (C-type) at (a) Mn K-edge, (b) Co K-edge, and (c) Ni K-edge. 101

Figure 5.11 Fourier transform magnitudes (k^3-weighted) at (a) Mn K-edge, (b) Co K-edge, and (c) Ni K-edge of pristine $Li(Li_{0.2}Mn_{0.54}Ni_{0.13}Co_{0.13})O_2$ cathode (P-type), graphene-coated $Li(Li_{0.2}Mn_{0.54}Ni_{0.13}Co_{0.13})O_2$ cathode (G-type), and $Li(Li_{0.2}Mn_{0.54}Ni_{0.13}Co_{0.03}Cr_{0.10})O_2$ cathode (C-type). TM represents the transtion metals (Mn, Co, and Ni). 103

Figure 5.12 EXAFS fitting to the real part of Fourier transformed data for (a) P-type at Mn K-edge, (b) G-type at Mn K-edge, (c) P-type at Co K-edge, (d) G-type at Co K-edge, (e) P-type at Ni K-edge, and (f) G-type at Ni K-edge. 104

Figure 5.13 SEM images of $Li(Li_{0.2}Mn_{0.54}Ni_{0.13}Co_{0.13})O_2$ active materials synthesized by sol-gel method (a) at 600 °C (P-600) (b) at 700 °C (P-700) (c) at 800 °C (P-800), and (d) at 1000 °C (P-1000). 107

Figure 5.14 Raman spectra of $Li(Li_{0.2}Mn_{0.54}Ni_{0.13}Co_{0.13})O_2$ active materials synthesized by sol-gel method at 600 °C (P-600), 700 °C (P-700), 800 °C (P-800), 1000 °C (P-1000) and spectra of SPINEL (Li_2MnO_4), NMC ($LiNi_{1/3}Mn_{1/3}Co_{1/3}O_2$) for comparison. 109

Figure 5.15 Figure FTIR spectra of $Li(Li_{0.2}Mn_{0.54}Ni_{0.13}Co_{0.13})O_2$ active materials synthesized by sol-gel method at 600 °C (P-600), 700 °C (P-700), 800 °C (P-800), 1000 °C (P-1000) and spectra of SPINEL (Li_2MnO_4), NMC ($LiNi_{1/3}Mn_{1/3}Co_{1/3}O_2$) for comparison. 110

Figure 5.16 Magnetization plots of $Li(Li_{0.2}Mn_{0.54}Ni_{0.13}Co_{0.13})O_2$ active materials synthesized by sol-gel method at 600 °C (P-600), 700 °C (P-700), 800 °C (P-800), and 1000 °C (P-1000). 112

Figure 5.17 Magnetic susceptibility of $Li(Li_{0.2}Mn_{0.54}Ni_{0.13}Co_{0.13})O_2$ active materials synthesized by sol-gel method at 600 °C (P-600), 700 °C (P-700), 800 °C (P-800), and 1000 °C (P-1000). The black lines indicate the fit to the Curie-Weiss law. 113

Figure 5.18 Normalised XANES spectra of $Li(Li_{0.2}Mn_{0.54}Ni_{0.13}Co_{0.13})O_2$ (a) at Mn K edge (b) (b) at Mn K pre-edge. The active materials were synthesized by sol-gel method at 600 °C (P-600), 700 °C (P-700), 800 °C (P-800), and 1000 °C (P-1000). 115

Figure 5.19 Normalised XANES spectra of $Li(Li_{0.2}Mn_{0.54}Ni_{0.13}Co_{0.13})O_2$ (a) at Co K-edge (b) (b) at Ni K-edge. The active materials were synthesized by sol-gel method at 600 °C (P-600), 700 °C (P-700), 800 °C (P-800), and 1000 °C (P-1000). 117

Figure 6.1 Electrochemical property of graphene-coated $Li(Li_{0.2}Mn_{0.54}Ni_{0.13}Co_{0.13})O_2$ cathode (G-type). (a) Galvanostatic profile up to 50th cycle with current rate of 0.2 C (Formation cycles used 0.05 C-rate). (b) Specific charge (black circle) and discharge capacity (white triangle) with

Coulombic efficiency (%). (c) dQ/dV plot of initial cycle. (d) dQ/dV plots on furher cycles. Red arrow indicates the curve shift upon electrochemical cycles. 126

Figure 6.2 Galvanostatic profile on the in operando cells at a charge rate of 0.125 C. Points signify the collection of XAS spectra numbered 1, 2 …18, collected at charge points in the galvanostatic profile. REF indicates the measurement of coin cell without any current. 127

Figure 6.3 Normalised XANES spectra of $Li(Li_{0.2}Mn_{0.54}Ni_{0.13}Co_{0.13})O_2$ during the initial charge (a) at Mn K-edge and (b) Mn K pre-edge. Numbers indicate the collection point of XAS spectra, which corresponds to the charge points in the galvanostatic profile. REF represents the measurement point of the coin cell without any current. NMC is the $Li(Ni_{1/3}Mn_{1/3}Co_{1/3})O_2$ composite used for comparison. Red arrows indicate the trend of spectra shift upon charge. ... 129

Figure 6.4 Normalised XANES spectra of $Li(Li_{0.2}Mn_{0.54}Ni_{0.13}Co_{0.13})O_2$ during the initial charge (a) at Co K-edge and (b) Ni K-edge. Numbers indicate the collection point of XAS spectra, which corresponds to the charge points in the galvanostatic profile. REF represents the measurement point of the coin cell without any current. NMC represents the $Li(Ni_{1/3}Mn_{1/3}Co_{1/3})O_2$ composite used for comparison. Red arrows indicate the trend of spectra shift upon charge..... 131

Figure 6.5 (a) Fourier transform magnitudes (k^3-weighted) at Mn K-edge of the graphene-coated $Li(Li_{0.2}Mn_{0.54}Ni_{0.13}Co_{0.13})O_2$ and (b) evaluation of the atomic bond-lengths on the 1st coordination shell (Mn-O) during charge with the the mean-square disorder ($\sigma 2$) from the EXAFS Debye-Waller factor..... 133

Figure 6.6 (a) Fourier transform magnitudes (k^3-weighted) at Co K-edge of the graphene-coated $Li(Li_{0.2}Mn_{0.54}Ni_{0.13}Co_{0.13})O_2$ and (b) evaluation of the atomic bond-lengths on the 1st coordination shell (Co-O) during charge with the the mean-square disorder ($\sigma 2$) from the EXAFS Debye-Waller factor. 134

Figure 6.7 (a) Fourier transform magnitudes (k^3-weighted) at Ni K-edge of the graphene-coated $Li(Li_{0.2}Mn_{0.54}Ni_{0.13}Co_{0.13})O_2$ and (b) evaluation of the atomic bond-lengths on the 1st coordination shell (Ni-O) during charge with the the mean-square disorder ($\sigma 2$) from the EXAFS Debye-Waller factor. Black arrow indicates the spectral shift at R ~4.9 Å during charge. 136

Figure 7.1 Oxidation states and magnetic properties of graphene-coated $Li(Li_{0.2}Mn_{0.54}Ni_{0.13}Co_{0.13})O_2$. Normalised XANES spectra (a) at Mn K-edge in REF (no current applied) and last discharged point (2.182 V), (b) at Co K-edge in REF (no current applied) and last discharged point (2.182 V), and (c) at Ni K-edge in REF (no current applied) and last discharged point (2.182 V). (d) Reciprocal magnetic susceptibility. The straight red-line is the fit to the Curie-Weiss law in the range of 150 – 300 K. Applied magnetic field is 1000 Oe. (e) Magnetization curve at 5 K. 144

Figure 7.2 Normalised XANES spectra at K-edge of graphene-coated $Li(Li_{0.2}Mn_{0.54}Ni_{0.13}Co_{0.13})O_2$. Spectra shift of Mn K-edge (a) during 1st charge and (b) 1st discharge. Spectra shifts in Mn K pre-edge (c) during 1st charge and (d) 1st discharge. (e) Galvanostatic profile with XAS collection points.(0.5 C-rate). 148

Figure 7.3 Normalised XANES spectra at K-edge of graphene-coated $Li(Li_{0.2}Mn_{0.54}Ni_{0.13}Co_{0.13})O_2$. Spectra shift of Co K-edge (a) during 1st charge and (b) 1st discharge. Spectra shifts of Ni K-edge (c) during 1st charge and (d) 1st discharge. 149

Figure 7.4 In operando EXAFS measurement of Mn in graphene-coated $Li(Li_{0.2}Mn_{0.54}Ni_{0.13}Co_{0.13})O_2$.during the 1st cycle. (a) k^3-weighted EXAFS oscillations $\chi(k)$ above Mn K-edge during charge-discharge. (b) k^3-weighted Fourier transform magnitudes of Mn K-edge

during charge-discharge (TM = Mn, Co, and Ni). Red and blue arrows indicate charge and discharge, respectively. 150

Figure 7.5 In operando EXAFS measurement of Mn in graphene-coated $Li(Li_{0.2}Mn_{0.54}Ni_{0.13}Co_{0.13})O_2$ during the 1st cycle with continuous Cauchy wavelet transform (CCWT) analyses of EXAFS spectra for each voltage point. The color intensity is the magnitude of the CCWT modulus. Dark-red signifies higher intensity, while blue is the lower intensity.. 153

Figure 7.6 In operando EXAFS measurement of Co in graphene-coated $Li(Li_{0.2}Mn_{0.54}Ni_{0.13}Co_{0.13})O_2$.during the 1st cycle. (a) k^3-weighted EXAFS oscillations $\chi(k)$ above Co K-edge during charge-discharge. (b) k^3-weighted Fourier transform magnitudes of Co K-edge during charge-discharge (TM = Mn, Co, and Ni). Red and blue arrows indicate charge and discharge, respectively. 154

Figure 7.7 In operando EXAFS measurement of Co in graphene-coated $Li(Li_{0.2}Mn_{0.54}Ni_{0.13}Co_{0.13})O_2$ during the 1st cycle with continuous Cauchy wavelet transform (CCWT) analyses of EXAFS spectra for each voltage point. The color intensity is the magnitude of the CCWT modulus. Dark-red signifies higher intensity, while blue is the lower intensity.. 155

Figure 7.8 In operando EXAFS measurement of Ni in graphene-coated $Li(Li_{0.2}Mn_{0.54}Ni_{0.13}Co_{0.13})O_2$.during the 1st cycle. (a) k^3-weighted EXAFS oscillations $\chi(k)$ above Ni K-edge during charge-discharge. (b) k^3-weighted Fourier transform magnitudes of Ni K-edge during charge-discharge (TM = Mn, Co, and Ni). Red and blue arrows indicate charge and discharge, respectively. 'C' in the color denotes those spectra belong to charge group..... 156

Figure 7.9 In operando EXAFS measurement of Ni in graphene-coated $Li(Li_{0.2}Mn_{0.54}Ni_{0.13}Co_{0.13})O_2$ during the 1st cycle with continuous Cauchy wavelet transform (CCWT) analyses of EXAFS spectra for each voltage point. The color intensity is the magnitude of the CCWT modulus. Dark-red signifies higher intensity, while blue is the lower intensity.. 158

Figure 7.10 Evolution of the bond length and structural disorder ($\boldsymbol{\sigma}$) changes during charge-discharge for graphene-coated $Li(Li_{0.2}Mn_{0.54}Ni_{0.13}Co_{0.13})O_2$ battery. (a) Mn-O with 1st shell disorder. (b) Co-O with 1st shell disorder. (c) Ni-O with 1st shell disorder. Ni-O bond-length is separated because of the Ni^{3+} Jahn-Teller effect..... 160

Figure 8.1 Crystal structure of (a) $LiMO_2$ (trigonal, R3m) and (b) Li_2MnO_3 (monoclinic, C2/m). Due to the presence of the interlayer spacing (~4.7 Å), the crystal structure can be combined in an integrated composite. Black arrows indicates the extraction of the lithium-ions. In principle, Li+ must be deintercalated from lithium layer and TM-layer either continuously or simultaneously during charge..... 164

Figure 8.2 In operando synchrotron investigation of lithium-ion batteries. (a) In Operando XAS setup. (b) Illustration of the special modified cell design. (c) Scanning Electron Microscopy of $Li(Li_{0.2}Mn_{0.54}Ni_{0.13}Co_{0.13})O_2$ cathode. (d) Galvanostatic profile of the operando cells at fast charge (0.5 C) and (e) slow charge (0.125 C) rates. Points signify the collection of XAS spectra numbered 1, 2 …18, collected at charge points in the galvanostatic profile. Ref indicates the measurement of coin cell without any current. 166

Figure 8.3 Normalised XANES spectra at Mn K-edge of $Li(Li_{0.2}Mn_{0.54}Ni_{0.13}Co_{0.13})O_2$ during the initial charge (a) Distinctive absorptions and the trend of the spectra shift in the fast charge (0.5 C) cell (G1). (b) Distinctive absorptions and the trend of the spectra shift in the slow charge (0.125 C) cell (G2). POINT signifies the collection point of XAS spectra and it is numbered as 1, 2 …18,

which corresponds to the charge points in the galvanostatic profile. REF indicates the measurement point of the coin cell without any current. 171

Figure 8.4 Normalised XANES spectra at Mn K pre-edge of $Li(Li_{0.2}Mn_{0.54}Ni_{0.13}Co_{0.13})O_2$ during the initial charge at (a) fast charge (0.5 C) and (b) slow charge (0.125 C) cells. (c) Illustration of the crystal field splitting diagram of d-orbitals in Mn octahedral environment. Δ_o denotes crystal field splitting energy. 172

Figure 8.5 Normalised XANES spectra at Co K-edge of $Li(Li_{0.2}Mn_{0.54}Ni_{0.13}Co_{0.13})O_2$ during the initial charge of (a) fast charge (0.5 C) and (b) slow charge (0.125 C) cells. 174

Figure 8.6 Normalised XANES spectra at Co K pre-edge of $Li(Li_{0.2}Mn_{0.54}Ni_{0.13}Co_{0.13})O_2$ during the initial charge of (a) fast charge (0.5 C) and (b) slow charge (0.125 C) cells. 175

Figure 8.7 Normalised XANES spectra at Ni K-edge of $Li(Li_{0.2}Mn_{0.54}Ni_{0.13}Co_{0.13})O_2$ during the initial charge of (a) fast charge (0.5 C) and (b) slow charge (0.125 C) cells. 176

Figure 8.8 Fourier transform magnitudes (k^3-weighted) at Mn K-edge of the graphene-coated $Li(Li_{0.2}Mn_{0.54}Ni_{0.13}Co_{0.13})O_2$ during charge of (a) fast charged (0.5 C) G1 and (b) slow charged (0.125 C) G2 cells. Evaluation of the atomic bond-lengths of (c) G1 1st shell (Mn-O) and (d) G2 1st shell (Mn-O). (e) Comparison of Mn-O changes vs voltage during charge. POINT signifies the collection point of XAS spectra and it is numbered as 1, 2 …18, which corresponds to the charge points in the galvanostatic profile. REF (point 0) indicates the measurement point of the coin cell without any current. 178

Figure 8.9 Fourier transform magnitudes (k^3-weighted) at Co K-edge of the graphene-coated $Li(Li_{0.2}Mn_{0.54}Ni_{0.13}Co_{0.13})O_2$ during charge of (a) fast charged G1 (0.5 C) and (b) slow charged G2 (0.125 C) cells. Evaluation of the atomic bond-lengths of (c) G1 1st shell (Co-O) and (d) G2 1st shell (Co-O). (e) Comparison of Co-O changes vs voltage during charge. POINT signifies the collection point of XAS spectra and it is numbered as 1, 2 …18, which corresponds to the charge points in the galvanostatic profile. REF (point 0) indicates the measurement point of the coin cell without any current. 180

Figure 8.10 Fourier transform magnitudes (k^3-weighted) at Ni K-edge of the graphene-coated $Li(Li_{0.2}Mn_{0.54}Ni_{0.13}Co_{0.13})O_2$ during charge of (a) fast charged G1 and (b) slow charged G2 cells. Evaluation of the atomic bond-lengths of (c) G1 1st shell (Ni-O) and (d) G2 1st shell (Ni-O). (e) Comparison of Ni-O changes vs voltage during charge. POINT signifies the collection point of XAS spectra and it is numbered as 1, 2 …18, which corresponds to the charge points in the galvanostatic profile. REF (point 0) indicates the measurement point of the coin cell without any current. 182

Figure 9.1 Electrochemical properties of the graphene incorporated $Li(Li_{0.2}Mn_{0.54}Ni_{0.13}Co_{0.13})O_2$ lithium-ion battery. (a) Galvanostatic profile until 22nd cycle (cycled with 0.2 C-rate). (b) Charge and discharge capacity with columbic efficiency. The dQ/dV plots during (c) initial cycle and (d) further cycles. 193

Figure 9.2 Characterization of graphene incorporated $Li(Li_{0.2}Mn_{0.54}Ni_{0.13}Co_{0.13})O_2$ electrode. (a) XRD pattern with two-phase indexing. (b) Raman spectroscopy (Superlattice: superlattice ordering, NMC: $Li(Ni_{1/3}Mn_{1/3}Co_{1/3})O_2$ compound, and P-800: pristine material without graphene) (c) Plot of reciprocal magnetic susceptibility. Fitting according to Curie-Weiss law (yellow line). (d) Magnetization curve obtained at 5 K with 60k Oe applied. (e) SEM images on electrode particles. (f) Presentation of two-phase composite system. 195

Figure 9.3 In Operando XANES measurements. (a) Galvanostatic profiles (0.5 C-rate) on 1st and 2nd electrochemical cycles. Normalised XANES spectra at (b) Mn K-edge, (c) Mn K pre-edge, (d) Co K-edge, and (e) Ni K-edge of graphene-coated $Li(Li_{0.2}Mn_{0.54}Ni_{0.13}Co_{0.13})O_2$ battery during initial and second cycles. Red arrow indicates the direction of charge, whereas black arrow represents the discharge trend. 198

Figure 9.4 Fourier transform magnitudes (k^3-weighted) at (a) Mn, Co, and Ni K-edge of the graphene-coated $Li(Li_{0.2}Mn_{0.54}Ni_{0.13}Co_{0.13})O_2$ during two electrochemical cycles. (b) The corresponded k^3-weighted EXAFS oscillations $\chi(k)$ above Mn, Co, and Ni K-edge. REF is the reference point without any current applied. Red arrow indicates charge process, while black arrow represents discharge process. 201

Figure 9.5 Continuous Cauchy Wavelet Transform (CCWT) analyses on Mn K-edge EXAFS spectra at different voltage levels in graphene-coated $Li(Li_{0.2}Mn_{0.54}Ni_{0.13}Co_{0.13})O_2$. Cathode. (a) 1st cycle CCWT (b) Back-scattering contribution (maxima variations in the 1st and 2nd shells) (c) 2nd cycle CCWT. The 1st coordination shell (Mn-O) is presented from top..... 204

Figure 9.6 Continuous Cauchy Wavelet Transform (CCWT) analyses on Co K-edge EXAFS spectra at different voltage levels in graphene-coated $Li(Li_{0.2}Mn_{0.54}Ni_{0.13}Co_{0.13})O_2$. cathode. (a) 1st cycle CCWT (b) Back-scattering contribution (maxima variations in the 1st and 2nd shells) (c) 2nd cycle CCWT. The 1st coordination shell (Co-O) is presented from top..... 206

Figure 9.7 Continuous Cauchy Wavelet Transform (CCWT) analyses on Ni K-edge EXAFS spectra at different voltage levels in graphene-coated $Li(Li_{0.2}Mn_{0.54}Ni_{0.13}Co_{0.13})O_2$. cathode. (a) 1st cycle CCWT (b) Back-scattering contribution (maxima variations in the 1st and 2nd shells) (c) 2nd cycle CCWT. The 1st coordination shell (Ni-O) is presented from top. 209

Figure 9.8 Evolution of the bond length and structural disorder (σ) changes during electrochemical cycles (2 cycle) for graphene-coated $Li(Li_{0.2}Mn_{0.54}Ni_{0.13}Co_{0.13})O_2$ battery. (a) Mn-O bond length change with structural disorder (b) Co-O bond length change with structural disorder. CCWT images correspond to the structural disorders with high value. Red arrow indicates charge process, while the black arrow represents the discharge process. 'LMO' signifies a part of the Li_2MnO_3 phase..... 211

Figure 9.9 Evolution of the Ni-O bond length and structural disorder (σ) changes during electrochemical cycles (2 cycle) for graphene-coated $Li(Li_{0.2}Mn_{0.54}Ni_{0.13}Co_{0.13})O_2$ battery. (a) Ni-O bond length change with long (black) and short (red) Ni-O bonds. (b) Ni-O bond length change for those with major coordination number. The CCWT image corresponds to the structural disorders with a high value. Red arrow indicates charge process, while the black arrow represents the discharge process..... 213

"As a man who has devoted his whole life to the most clear headed science, to the study of matter, I can tell you as a result of my research about atoms this much: There is no matter as such. All matter originates and exists only by virtue of a force which brings the particle of an atom to vibration and holds this most minute solar system of the atom together. We must assume behind this force the existence of a conscious and intelligent mind. This mind is the matrix of all matter."

- Max Planck

Chapter 1 Introduction

1.1 Background

Worldwide energy shortage has become a central issue with the dramatic economic growth in 21st century. The past decade has seen the rapid development of alternative energy sources that can replace the finite fossil fuels, which are responsible for the global warming. Accordingly, there have been increasing demands for sustainable energy resources that are environmentally friendly, namely, green energy sources such as solar cells or tidal/wind powers have emerged as the alternative resources. However, a major drawback of these energy sources is the uncontrollable nature with intermittent availability, and thus it leads to the requirement of an efficient energy storage system, i.e., batteries and supercapacitors. Rechargeable batteries provide an electrochemical storage system which is highly efficient to store the green energy sources since the batteries are portable with a relatively high energy density and available on demand. Especially, the lithium-ion battery is considered to be the promising energy storage due to its high energy density, simple reaction mechanism, good safety, and compact design. A Ragon plot that describes the correlation between specific power and specific energy for electrochemical storage or conversion system is illustrated in Figure 1.1. Since the commercialization of the Li-ion battery in 1991 (C/$LiCoO_2$ cell), they have been widely utilized as a power source for portable electronic devices such as notebook computers, cameras, mobile phones and smart watches. Recently, with the development of high-capacity lithium-ion cathode, much attention has been paid to the use of the rechargeable batteries in the electric vehicle (EV) and hybrid electric vehicle (HEV) or plug-in hybrid electric vehicle (PHEV) applications (Figure 1.2). A particular interest is given to the Li-rich layered transition metal oxide battery represented as the chemical formula of $x\mathrm{Li_2MnO_3} \cdot (1-x)\mathrm{LiMO_2}(\mathrm{M} = \mathrm{Mn, Ni, Co})$, which is proposed by Thackeray et al.[1–5]. Whereas the

conventional Li-ion batteries show a single crystal structure, the Li-rich layered transition metal oxide system reveals the structural integration of the two distinct crystallographic phases between Li_2MnO_3 (monoclinic, C2/m) and $LiMO_2$ (trigonal/hexagonal, $R\bar{3}m$), where M represents the 3d-transition metals.

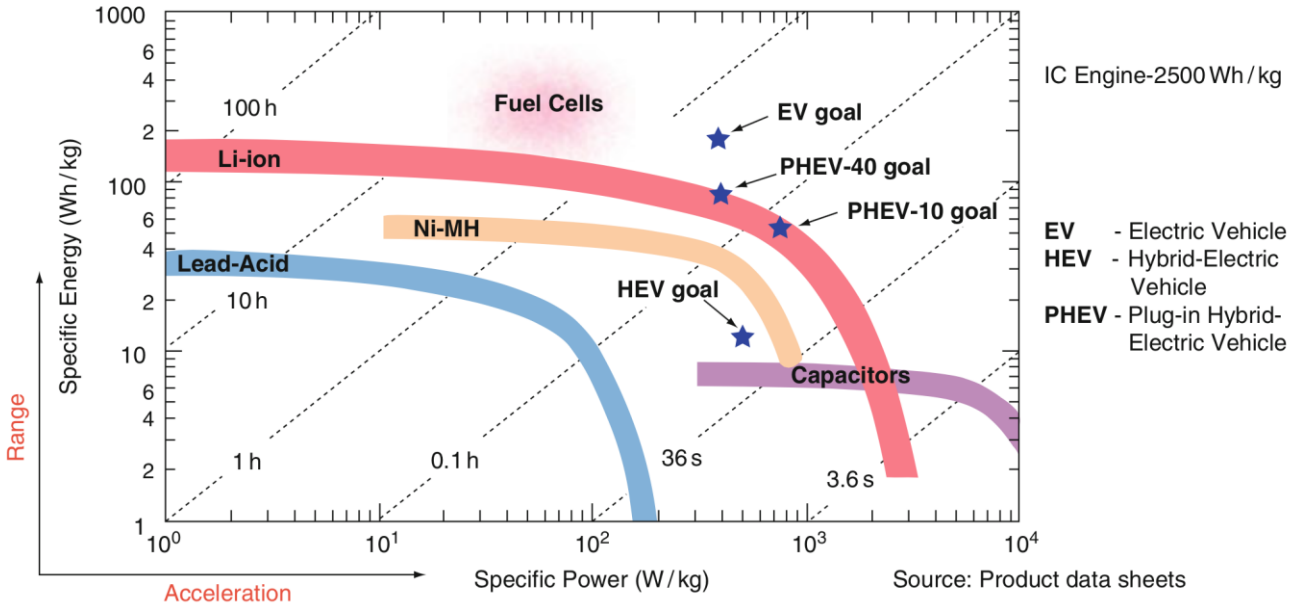


Figure 1.1 Ragone plot for diverse energy storage or conversion systems[6].

A key factor for delivering high charge capacity in this system is the intimate integration of the two crystallographic components attributed to the interleaving of close-packed layers from the two compounds, namely, the (001) planes from Li_2MnO_3 and the (003) planes from $LiMO_2$ with the interlayer spacing of ~4.7 Å. The Li-rich layered transition metal oxide cathode benefits from superior theoretical capacity (>250 $mAhg^{-1}$) with high chemical potential (>4.6 V vs Li^0), good thermal stability, high discharge capacity and lower cost compared with conventional cathodes (e.g. $LiCoO_2$, $LiFePO_4$, NMC)[2–4]. As such, the Li-rich layered cathode is regarded as an ideal candidate for the electric transportations. Despite its efficacy and economical advantage, this battery system suffers from two major drawbacks. In general, a large irreversible capacity loss of 40-100 $mAhg^{-1}$ can be observed during the initial electrochemical cycle. The Li^+ ion extraction

accompanied by oxygen release as a lithia form (Li_2O) is known to be the dominant process of the capacity deterioration[7,8]. Furthermore, a phase transition from the layered structure into the spinel occurs with capacity fading/voltage decay on further cycles. Eventually, these are the major barriers still need to be improved in order to achieve a successful commercialization for large-scale devices or electric vehicles applications. Enormous efforts have been made to improve the essential limitations of the Li-(rich) layered transition metal oxide battery system such as surface doping or coating with metal oxides, incorporating mixed transition metals (Mn, Co, Ni, Cr), and using special functional materials, i.e., graphene coating. Although those treatments are efficient to improve the capacity fading and voltage decay on charge-discharge, the irreversible capacity loss during the initial cycle and the phase transition from layered structure into the spinel remains unsolved.



Figure 1.2 BMW hybrid electric vehicle (HEV). 1) High efficient BMW V8 gasloline engine 2) Electric motor (15 kW/210Nm) 3) High voltage electronics, directly mounted to the transmiss 4) 8 gear automatic transmission, and 5) Lithium-ion battery (120 Volts). Image taken from reference[9].

The interplay between Li_2MnO_3 (monoclinic, C2/m) and $LiMO_2$ (trigonal/hexagonal, $R\bar{3}m$) components is the key to understand the electrochemical process involved with the structural

environments of the battery cathode. The main aspects can be treated under five headings: 1) The charge compensation mechanism of Mn, Co, and Ni in the layered $LiMO_2$ component; 2) Electrochemical activation of the Li_2MnO_3 component above ~4.5 V by the lithia (Li_2O) extraction; 3) Cation ordering of $LiMn_6$ in the Li_2MnO_3 component; 4) Transition metals migration into the lithium-layers; and 5) The Jahn-Teller effect from the Ni^{3+} (d^7) ions. The layered-to-spinel phase transition could be explained by two separate origins. It has been reported that the migration of the transition metals into the lithium-layer causes the transition to spinel phase of the $LiMO_2$ ($R\bar{3}m$) domain[10]. On the other hand, the phase transition into the spinel from Li_2MnO_3 (C2/m) domain is attributed to the lithia (Li_2O) removal which is responsible for the lattice strains in the electrode[10].

A large number of studies have been devoted to the *in situ* investigations on the crystal structure of the battery cathode during electrochemical cycles using synchrotron XRD. They report the crystal lattice changes and the appearance of the spinel phase upon further cycles. At the crystal structure level, the observation is correct. However, one of the problems dealing with the long-range structure investigated by XRD is that they cannot not examine the local atomic environment changes which are crucial to understand the phase transition mechanism that deteriorates the battery performance and stability. In addition, the synchrotron XRD measurements are not sufficiently sensitive to capture the inter-atomic reactions in the highly complicated cathode material (e.g. $Li_{1.2}Mn_{0.54}Ni_{0.13}Co_{0.13}O_2$) upon the electrochemical process. In fact, the trigger point that initiates the phase transition from the layered structure into the spinel appears to be present already in the initial charge, as evidenced by XAS investigations.

In order to establish an understanding of local environment changes during Li^+ (de)intercalation, synchrotron XAS is the suitable method for this purpose. The highly element-specific manner of synchrotron XAS allows to precisely examine the chemical, structural, and electronic states of the transition metals (Mn, Co, and Ni) during electrochemical cycle. The *in*

operando investigation on the oxidation state and electronic structure of the absorber atom by XANES provides the core information about the charge compensation mechanism in the lithium-ion battery. The Fourier transform of Extended X-Ray Absorption Fine Structure (EXAFS) provides a satisfactory description of the local structure changes with the connection to the cation arrangement for the integrated-composite system. The description is generally involved with the peak amplitude, position, shape changes (trend), and coordination numbers in the R-space. Structural parameters could be also quantified with the help of the Extended X-Ray Absorption Fine Structure (EXAFS). Bond length changes resulting from oxygen removal or loss of symmetry on charge-discharge and bond length separation attributed to the Jahn-Teller effect can be deduced from the EXAFS quantification.

EXAFS signals for the complex composite can be examined with a new approach, namely, a Continuous Cauchy Wavelet Transform (CCWT) enables the visualization of the EXAFS spectra in three dimensions by decomposing the *k*-space and *R*-space (uncorrected for phase shift) signals. As a result, the wavelet transform offers detailed information on the local atomic structure with the visualized signals which are difficult to be identified in a one-dimensional decomposition, such as Fourier Transform magnitudes on EXAFS.

1.2 Aims and scope of the present research

The present study aims to develop a better understanding of the impact of the Li^+ (de)intercalation on the local atomic environment of the high-capacity lithium-ion battery in order to improve the knowledge of the phase transition phenomena linked to the battery performance and stability issues. The *in operando* synchrotron X-ray Absorption Spectroscopy (XAS) method is considered as the optimum tool to characterize the electrochemical process of the battery that involves various chemical, electronic, and physical interactions at an atomic scale. Due to the highly element-

specific manner of synchrotron XAS, it is capable of investigating a particular atomic environment even in a complex material system during the battery operation. Thereby, XAS provides unique advantages over other *in situ* methods such as synchrotron XRD and neutron diffraction.

The present thesis also demonstrates a new approach that allows the examination of the atomic state of the transition metals in more detail with the help of the Continuous Cauchy Wavelet Transform (CCWT) analysis performed on the *in operando* XAS data for the Li-rich Mn-based oxide cathode. The wavelet transform analysis enables the visualization of the EXAFS spectra in three dimensions with the *k*-space (wave-vector), R-space (uncorrected for phase shift), and CCWT modulus. As a consequence, complex signals from different scattering contributions can be discerned in various *k*-values.

The principle objectives of the present thesis are: to obtain the full structural description of the cathode material of $Li_{1.2}Mn_{0.54}Ni_{0.13}Co_{0.13}O_2$ with the consideration of the integrated two components between Li_2MnO_3 (monoclinic, C2/m) and $LiMO_2$ (trigonal/hexagonal, $R\bar{3}m$); to investigate the improvement treatments (graphene coating and Cr-substitution) on the pristine material; to understand the charge compensation mechanism in the graphene-coated $Li_{1.2}Mn_{0.54}Ni_{0.13}Co_{0.13}O_2$ lithium-ion battery; to examine whether the local-atomic environment (atomic phase) is reversible on charge-discharge; to study the charge rate dynamic in the integrated-composite system; and to identify the signal of the phase transition into the spinel during electrochemical cycles. Also, a particular attention is paid to the cation arrangement/ordering in the Li_2MnO_3 (monoclinic, C2/m) and $LiMO_2$ (trigonal/hexagonal, $R\bar{3}m$) components with the consideration of the phase transition phenomena.

1.3 Thesis structure

The thesis is organised with ten chapters including the introduction.

Chapter 2 provides a literature review on the general aspects of the lithium-ion batteries. The electrochemistry of a lithium-ion battery is outlined first. In addition, diverse cathode materials (conventional Li-layered type, olivine type, spinel type, and Li-rich layered oxide type) are compared and reviewed. A particular attention is devoted to the Li-rich layered oxide cathode represented as the chemical formula of $x\mathrm{Li_2MnO_3} \cdot (1-x)\mathrm{LiMO_2}(\mathrm{M} = \mathrm{Mn, Ni, Co})$. Especially, review is focused on the reaction mechanism during the 1st electrochemical cycle including the charge compensation process and considerations in local atomic environment of this cathode system such as the composition of the transition metals, crystal field theory and Jahn-Teller effect. Another key issue addressed in this chapter is the phase transition from the layered structure into the spinel on charge-discharge.

Chapter 3 presents the X-ray Absorption Fine Structure (XAFS) Theory. The underlying physics for the synchrotron X-ray Absorption Spectroscopy (XAS) is given with the descriptions based on the quantum mechanical phenomenon. Two particular regimes, namely, X-ray absorption near edge structure (XANES) and extended X-ray absorption fine structure (EXAFS) are introduced. Explanations are focused on the distinctive information that can be obtained from XANES and EXAFS. XAFS interpretation method is also presented in detail. EXAFS data reduction, modelling, and fitting process by ATHENA/ARTEMIS applications with IFEFFIT code are described.

Chapter 4 treats the experimental methods including the active material synthesis process. Three chemical synthesis methods are presented: spray-dryer assisted sol-gel method for pristine cathode ($\mathrm{Li(Li_{0.2}Mn_{0.54}Ni_{0.13}Co_{0.13})O_2}$), Hummers method for graphene-coating, and carbonate assisted co-precipitation method for the Cr-substituted cathode

($Li(Li_{0.2}Mn_{0.54}Ni_{0.13}Co_{0.03}Cr_{0.10})O_2$). The cell design of the general electrochemical cells and *in operando* cells that contain the synthesized active materials are described with a brief assembling procedure. Then, electrochemical characterization methods are introduced, i.e. differential analysis (dQ/dV plot). Various complementary methods to synchrotron XAS experiment are briefly described, e.g. X-ray diffraction (XRD), Rietveld refinement, Raman spectroscopy, magnetic measurement by Superconducting Quantum Interference Device (SQUID), Attenuated total reflectance (ATR)-Fourier transform infrared (FTIR) spectroscopy, and Scanning electron microscope (SEM) with Energy-dispersive X-ray spectroscopy (EDX). Another core method is the Continuous Cauchy Wavelet Transform (CCWT) analysis on the EXAFS signals. A brief introduction of CCWT method is made.

Chapter 5 presents the experimental works focused on the characterization of the lithium-ion batteries with cathodes having different treatments. The first part of this chapter focuses on the comparison of the pristine $Li(Li_{0.2}Mn_{0.54}Ni_{0.13}Co_{0.13})O_2$ cathode, graphene-coated $Li(Li_{0.2}Mn_{0.54}Ni_{0.13}Co_{0.13})O_2$ cathode, and $Li(Li_{0.2}Mn_{0.54}Ni_{0.13}Co_{0.03}Cr_{0.10})O_2$ cathode. The effect of the graphene coating and Cr-substitution are discussed. Especially, the impact on the phase transition into the spinel by those treatments is pointed out. Also, the formation of the integrated composite between Li_2MnO_3 (monoclinic, C2/m) and $LiMO_2$ (trigonal, $R\bar{3}m$) components in the active materials is addressed. The full structural description (chemical, electric, and crystal structures) are discussed based on the combined interpretations from XRD/Rietveld refinement (GSAS), Raman spectroscopy, ATR-FTIR, SQUID analysis, and XANES. A precise investigation of the oxidation states of the transition metals is shown with the help of XANES and SQUID analyses. Local atomic environment of the active materials is described using XANES/EXAFS. The later part of this chapter focuses on the effect from different thermal treatments (calcination temperature of 600, 700, 800, and 1000 °C) during chemical synthesis. A particular interest is

devoted to the interplay between the Li_2MnO_3 and $LiMO_2$ components. The reason why the graphene-coated $Li(Li_{0.2}Mn_{0.54}Ni_{0.13}Co_{0.13})O_2$ cathode with the calcination temperature of 800 °C is considered to be optimum is explained in the last section.

Chapter 6 reports the charge compensation mechanism in the graphene-coated $Li(Li_{0.2}Mn_{0.54}Ni_{0.13}Co_{0.13})O_2$ cathode studied by *in operando* XAS using a specially-designed coin cell. The K-edge XANES spectral shifts for each transition metal (Mn, Co, and Ni) upon charge are discussed. The local atomic environment changes are presented in Fourier transform magnitudes (k^3-weighted) at Mn, Co, and Ni K-edge, and their pattern change upon charge is discussed. The quantifications of the local-atomic environment by EXAFS are also compared. The appearance of the bond splitting into the long Ni-O and short Ni-O is discussed.

Chapter 7 discusses the impact from Li^+ (de)intercalation on the local atomic environments of the graphene-coated $Li(Li_{0.2}Mn_{0.54}Ni_{0.13}Co_{0.13})O_2$ cathode with the consideration of the 'atomic phase reversibility' during charge and discharge. Chemical and electric structure changes upon charge-discharge are compared in Mn, Co, and Ni K-edge XANES. The oxidation state change for each transition metal is discussed. The pattern changes of the k^3-weighted EXAFS oscillations $\chi(k)$ above Mn, Co, and Ni K-edge and the corresponded k^3-weighted Fourier transform magnitudes on charge-discharge are reported. A particular interest is devoted to the trend of the spectral changes and their similarities in the shape. The analyses of the Continuous Cauchy Wavelet Transform (CCWT) on the *in operando* EXAFS signals of the lithium-ion battery electrode is presented for the first time. Interatomic bond length changes of Mn-O, Co-O, and Ni-O on initial cycle are presented. As such, the 'atomic phase reversibility' is discussed in three manners: oxidation state, interatomic bond length, and wavelet transforms for Mn, Co, and Ni.

Chapter 8 presents the *in operando* XAS study on the graphene-coated $Li(Li_{0.2}Mn_{0.54}Ni_{0.13}Co_{0.13})O_2$ cathode cells with different charge rates (0.125 C vs 0.5 C). The

concept of concurrent charge (first charge stage) and saturation charge (second charge stage) are briefly introduced. The hopping mechanism of the Li^+ are described. The distinguishing difference in the structural impact on the local environments of the transition metals upon different charge rates are discussed. The identification of two local-atomic environments separated at the voltage level of 4.224 V by EXAFS is presented and discussed.

Chapter 9 is devoted to the identification of the initial signal that is related to the phase transition from the layered structure into the spinel in the graphene-coated $Li(Li_{0.2}Mn_{0.54}Ni_{0.13}Co_{0.13})O_2$ cathode. The structural, chemical, and electronic state changes between the 1st cycle with the large voltage-plateau and 2nd cycle without the plateau are discussed based on the K-edge XANES results. *In operando* EXAFS data is presented with the implication of the cation ordering during two electrochemical cycles. A particular attention is paid to the interplay between the Li_2MnO_3 (monoclinic, C2/m) and $LiMO_2$ (trigonal, $R\bar{3}m$) components upon charge and discharge based on the k^3-weighted Fourier transform magnitudes results. Also, the CCWT analysis is performed on the *in operando* EXAFS data. In this chapter, semi-quantitative analyses are introduced on the back-scattering signals from the constituent elements in the wavelet transforms, so as to quantify the individual activation or contribution of the transition metals on electrochemical process.

Chapter 10 contains a crucial review of the results obtained in the present thesis. The recommendations for the future research are also discussed.

Chapter 2 Literature Review

2.1 Electrochemistry basics

Thermodynamics approaches provide solid basis for understanding equilibrium chemistry in the electrochemical system. An oxidation-reduction reaction is the key process involved in the energy conversion between the chemical and electrical energies in electrochemical cells. In a voltaic cell, the electrode at which reduction appears is called 'Cathode', whereas the electrode at which oxidation (or anodic reaction) takes place is called 'Anode' in the cell. Thus, the reaction can be represented as following equations (n: number of electrons, C_{OX}: cathode, and A_{Rd}: anode):

Cathode $$C_{OX} + ne^- \leftrightarrow C_{OX}^{n-} \quad (2.1)$$

Anode $$A_{Rd}^{n-} \leftrightarrow A_{Rd} + ne^- \quad (2.2)$$

Overall $$C_{OX} + A_{Rd}^{n-} \leftrightarrow C_{OX}^{n-} + A_{Rd} \quad (2.3)$$

If the overall reaction is not at a chemical equilibrium, there still remains driving force for the flow of the electrons due to the potential difference between the cathode and anode. This potential difference is called the electrochemical cell potential, which is the voltage of a cell.

Hence, the cell voltage (E_{cell}) is given by:

$$E_{cell} = E_{cathode} - E_{anode} \quad (2.4)$$

The potential (E^0) under standard conditions for the cell can be described in a thermodynamic case by the following expression:

$$E^0 = \frac{-\Delta G^0}{nF} \quad (2.5)$$

where ΔG^0 is the standard Gibbs free energy, n is the number of electrons, and F is the Faraday constant (≅96485 C).

On the other hand, cell potentials (E) under non-standard condition is determined by Nernst equation as following:

$$E = E^0 - \frac{RT}{nF}\ln\left(\frac{a_{A_{Rd}}\, a_{C_{OX}^{n-}}}{a_{C_{OX}}\, a_{A_{Rd}^{n-}}}\right) \tag{2.6}$$

where, E^0 = standard cell potential, R = gas constant, T = absolute temperature (K), and a_X = activity of component X. According to the thermodynamic law, a spontaneous reaction appears when the Gibbs free energy in the reaction is negative ($\Delta G < 0$, $E > 0$). This is the case when $E_{cell} = E_{cathode} - E_{anode} > 0$, and this type of cell is known as the 'voltaic cell'.

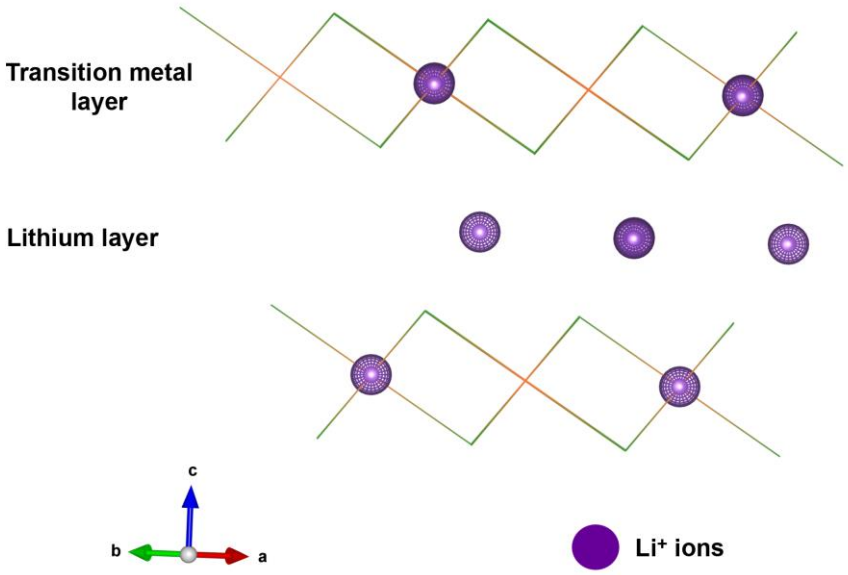


Figure 2.1 Schematic illustration of intercalated lithium ions and vacancies in active material. Structure was generated with wireframe model of trigonal $LiMO_2$ (M: transition metal).

The addition of lithium atoms to the cathode materials results in the formation of a new phase, or an increasing concentration of this phase in the mixture. A conceptual representation of the lithium-ion insertion electrode can be seen in Figure 2.1. If the entropic contribution is stronger than the enthalpy contribution to the free energy of Li intercalation into the active material, the process can be explained by a simple model of an ideal mixture between Li^+ and vacancies in the host structure. The chemical potential of lithium is likely to be considered as the partial Gibbs free

energy of Li in the host structure per mole. The free energy ($g(x)$) of mixing per site can be expressed as following:

$$\frac{g(x)}{k_{\mathrm{B}}T} = x\ln x + (1-x)\ln(1-x) \tag{2.7}$$

where k_{B} is the Boltzmann constant , x is the mole fraction of the lithium ions in the active material, and T is the absolute temperature (K). Hence, the chemical potential ($\mu(x)$) can be described as below:

$$\frac{\mu(x)}{k_{\mathrm{B}}T} = \frac{1}{k_{\mathrm{B}}T}\frac{\partial \mathrm{g}(x)}{\partial \mathrm{x}} = \ln\frac{x}{1-x} = \frac{1}{k_{\mathrm{B}}T}(\mu_{\mathrm{LiH}} - \mu_{\mathrm{H}}) \tag{2.8}$$

Equation 2.8 represents the chemical potential of an intercalated lithium ion with excluded vacancy. For the positive electrode material, therefore, open circuit voltage (V_o) can be written as:

$$V_O(x) = V^* - \frac{k_{\mathrm{B}}T}{\mathrm{e}}\ln\frac{x}{1-x} \tag{2.9}$$

where V^* corresponds to the voltage at state of charge (SOC) of 50 %.

Ceder et al.[11] studied the phase diagrams of lithium transition metal oxides based on the first principle modelling. It has been concluded that the phase transition in the lithium intercalation system is mainly attributed to the lithium vacancies in the host structure, as well as the electronic properties of the host material. One interesting feature in the lithium intercalation system is the two-phase transition, which is normally reflected in the galvanostatic profile as a voltage plateau. Especially, a very wide voltage plateau can be observed in a lithium iron phosphate cathode ($LiFePO_4$). In this cathode type, the voltage plateau is the indicative of a two-phase separation into Li-rich and Li-poor regions. On the other hand, the two-phase separation can be regarded as a 'Metal-insulator' transition in the lithium-layered oxide cathode material[11]. For example, in Li_xCoO_2 composite, a semiconducting property was observed in the range of $0.97 < x < 1$, while it showed metallic property when $x < 0.8$[12]. Thus, a two-phase region would exist between a lithium

concentration of 0.8 and 0.97. A thermodynamic understanding of the two-phase separation can be described with a non-ideal solution model. Homogenous free energy density for a non-ideal mixing can be written as following according to the regular solution model on the electrodes per site.

$$\mathrm{g}(x) = H_{mix}x(1-x) + k_{\mathrm{B}}T[x\ln x + (1-x)\ln(1-x)] \tag{2.10}$$

where k_{B} is the Boltzmann constant , x is the mole fraction of the lithium ions in the active material, and T is the absolute temperature (K). It should be noted that the added free energy term ($H_{mix}x(1-x)$) here is related to the particle-hole repulsion which causes the immiscibility of the lithium and the active host material. The chemical potential for the equilibrium path can be expressed as:

$$\mu(x) = \frac{\partial \mathrm{g}(x)}{\partial x} = H_{mix}(1-2x) + k_{\mathrm{B}}T\ln\frac{x}{1-x} \tag{2.11}$$

Therefore, open circuit voltage (V_{o}) become (V^*: voltage at state of charge (SOC) of 50 %):

$$V_{\mathrm{O}}(x) = V^* + \frac{H_{mix}}{\mathrm{e}}(2x-1) - \frac{k_{\mathrm{B}}T}{\mathrm{e}}\ln\frac{x}{1-x} \tag{2.12}$$

Though the regular solution model is a simplified thermodynamic model for the Li-ions intercalation system, it offers some insights into the relationship between chemical potential and phase transition during charge-discharge.

Capacity (Q: mAh or C)

During a discharge, electrons flow along the external circuit. They are released at the anode from the active material by oxidation and taken at the cathode with a reduction reaction. There exists a correlation between the current (I) and the mass (m) of the electrode material. This can be described by Faraday's first law as following:

$$m = \frac{M}{n\mathrm{F}}It \tag{2.13}$$

where m is the mass of electrode material, M the molar mass, n is the number of electrons exchanged, F is Faraday constant (=96,485 C mol^{-1}), and t the elapsed time. With the applied current (I), the battery capacity (Q) is given by the following relation:

$$\mathrm{Q} = \int_{\mathrm{t1}}^{\mathrm{t2}} I(t)\mathrm{dt} \tag{2.14}$$

Thus, equation (2.13) and (2.14) lead to the correlation as below:

$$\mathrm{Q} = \frac{mn\mathrm{F}}{M} \tag{2.15}$$

The capacity (Q) signifies the total amount of electric charge that can be stored in the battery, and it has a direct relationship to the mass of active material. A specific capacity (Q/m), precisely a specific charge, can be defined as the amount of electric charge per unit mass ($mAhg^{-1}$).

Battery Energy (Wh) and Power (W)

Energy is a product resulting from the cell chemical potential and specific charge, and it is proportional to the amount of active materials. Specific energy (Wh kg^{-1}) or energy density (Wh dm^{-3}) is generally used to compare the electrical energy that a battery can deliver. Power can be regarded as the rate of energy delivery, which is linked to the electrochemical reaction kinetics. The condition of active materials, i.e. particle morphology has a significant influence on the battery power.

Coulombic Efficiency (%)

Coulombic efficiency is the ratio of the number of electrons discharged by a number of electrons required to be charged to bring the battery back to its initial state. This can be expressed with the charge and discharge capacity as below:

$$Coulombic\ efficiency\ (\%) = \frac{Q_{discharge}}{Q_{charge}} \times 100 \tag{2.16}$$

C-rate (A)

The charge rate, denoted as C-rate, is a charge or discharge rate that corresponds to the total capacity in Ah (or mAh). For example, a 1500 mAh battery would provide 1500 mA for 1 hour when the battery is discharged at 1 C-rate. With C/2 rate (=750 mA), thus, it will take 2 hours to fully charge.

2.2 Working principle of Li-ion batteries

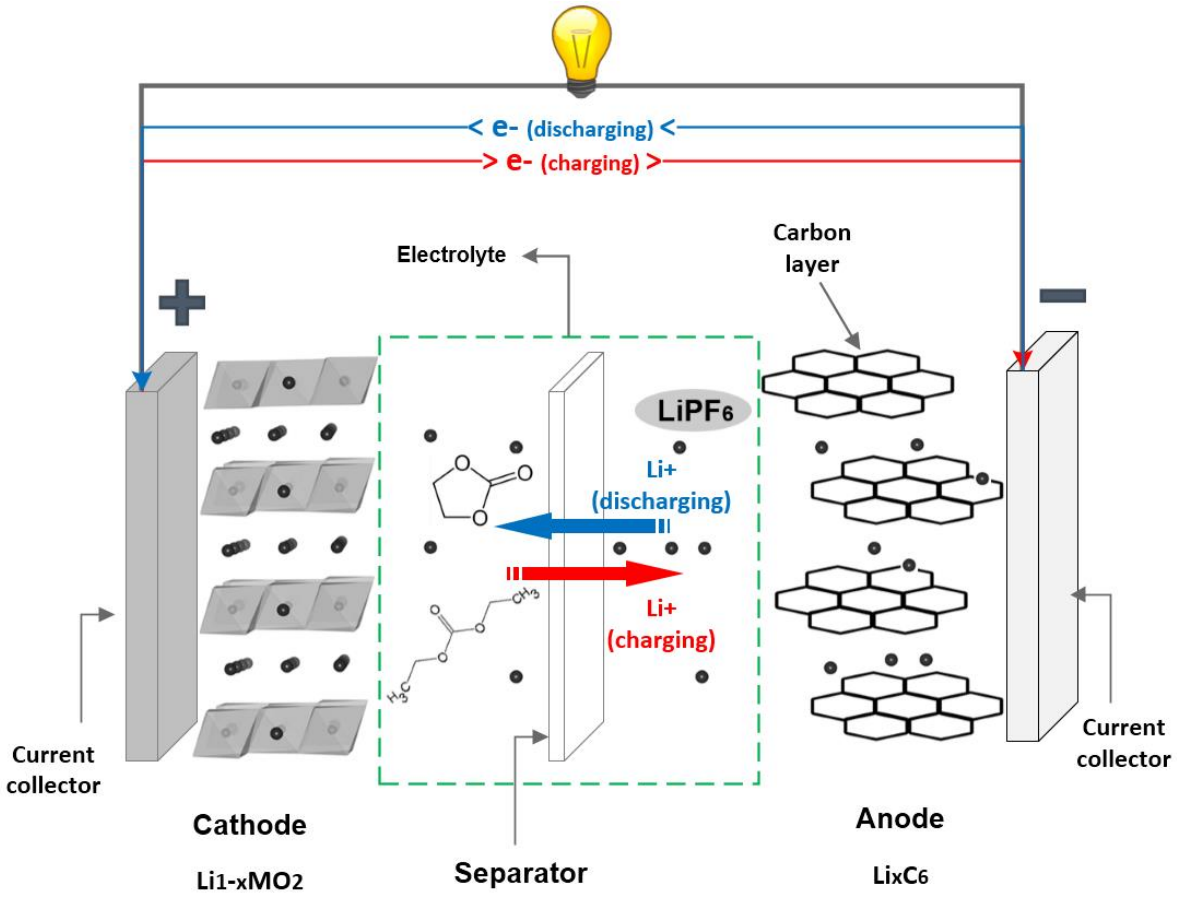


Figure 2.2 Principle of a lithium-ion battery on the lithium-layered oxide cathode (M=Transition Metals).

A typical lithium-ion battery consist of an anode and a working electrode (cathode), and they are separated by an electrolyte. The working principle of lithium-ion battery is illustrated in Figure 2.2. Lithium-ions are deintercalated from the cathode and move into the carbon layer passing through the electrolyte during the charge with the flow of electron through the external circuit.

This process is reversed during the discharge. In this respect, the lithium-ion battery is called "rocking-chair battery" as it describes the back-and-forth movement of the Li^+ between the anode and cathode. This is regarded to be an appropriate expression in solid-state intercalation chemistry in terms of the battery system[13]. Li-ion batteries use intercalation compound or solid as host material for electrodes where atoms may be inserted or removed without a major interruption on the structure[13,14]. The Li^+ (de)intercalation process in Figure 2.2 can be described as a redox reaction as following:

Cathode $$LiMO_2 \leftrightarrow Li_{1-x}MO_2 + xLi^+ + xe^- \quad (2.17)$$

Anode $$6C + xLi^+ + xe^- \leftrightarrow Li_xC_6 \quad (2.18)$$

Overall $$LiMO_2 + 6C \leftrightarrow Li_{1-x}MO_2 + Li_xC_6 \quad (2.19)$$

The definition of anode (oxidation occurs) and cathode (reduction occurs) in the lithium-ion battery is identical to the voltaic cell[15]. Note this definition is based on the discharge process.

2.3 Considerations for battery components: cathode, anode, and electrolyte

In the lithium-ion battery, the cathode is a positive electrode that accepts the electrons during discharge, whereas the anode is a negative electrode which provides the electrons on discharge. The change of the chemical potential during the Li^+ (de)intercalation defines the open-circuit voltage (OCV). It is typically determined by the chemical potential of the exchanged Li^+ into the cathode ($\mu_{Li}^{Cathode}$) and the anode (μ_{Li}^{Anode}). Thus, the OCV is given by:

$$V_{oc} = \frac{\mu_{Li}^{Anode} - \mu_{Li}^{Cathode}}{n\mathrm{F}} \quad (2.20)$$

where V_{oc} is the open-circuit voltage and F is Faraday's constant. n is the number of electrons participated in the electrochemical reaction. With the internal resistance (R), the cell voltage (V) is defined as (I = current):

$$V = V_{OC} - IR \tag{2.21}$$

Figure 2.3 exhibits an energy diagram of a lithium-ion battery at open circuit. μ_A and μ_C indicate the chemical potential of the anode and cathode, respectively. The potential window (E_g) of the electrolyte is defined as the energy band gap between the highest occupied molecular orbital (HOMO) and the lowest unoccupied molecular orbital (LUMO). The chemical potential between cathode and anode must lie within the potential window of the electrolyte in order to achieve the thermodynamic stability[16,17]. This consideration leads to the following expression:

$$V_{OC} = (\mu_A - \mu_C)/F \leq E_g \tag{2.22}$$

where F is Faraday constant (=96,485 C mol^{-1}). If the chemical potential of anode (μ_A) is above LUMO, it will cause the reduction of the electrolyte.

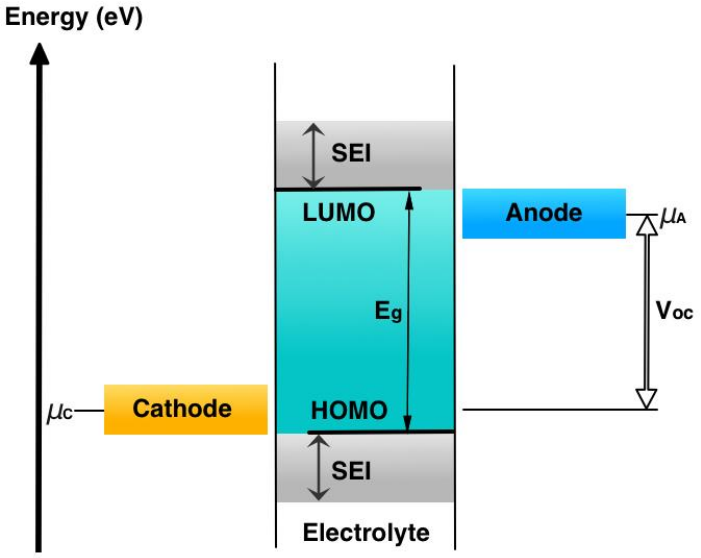


Figure 2.3 Illustration of open circuit energy diagram for a lithium-ion battery at $V_{oc.}$

Otherwise, a chemical potential of cathode (μ_C) lower than HOMO results in the oxidation of the electrolyte. This electrolyte decomposition would be prevented by the formation of an appropriate solid-electrolyte interface layer (SEI) as it can hinder the electron transfer from the electrolyte HOMO to the cathode or from the anode to the electrolyte LUMO[16,17]. One major type of the electrolyte for the lithium-ion battery is the $LiPF_6$ (1 M) in ethylene carbonate (EC) : dimethyl

carbonate (DC) = 1:1. The ethylene carbonate (EC) plays an important role in generating the optimized SEI layer, a passivating layer, for the thermodynamic stability on cycling[18,19].

The cathode (positive electrode) is one of the vital components of the lithium-ion battery. During discharge, Li^+ are extracted from the anode and move through the electrolytic solution, and intercalate to the cathode composite. At the same time, electrons move from the anode to cathode along the external circuit (Figure 2.2). A battery performance is determined by the energy stored per unit weight and volume in the electrodes. To achieve a battery performance with high capacity, it requires a cathode material with high chemical potential. Thus, a particular challenge that remains to address in the lithium-ion battery is to develop cathode materials with high specific capacities. Intercalation compounds are the ideal type of active material for lithium-ion battery cathodes due to their superior capability of insertion and extraction of Li^+ per compound unit[13]. Such material offers certain advantages by minimizing the Li^+-ion kinetic barriers resulting from incomplete diffusion, nucleation, and growth concerned with solid-state reactions on electrochemical cycles[13]. Key requirements for the intercalation material are[13,17,20,21]: (i) The intercalation compound for the cathode must have a low chemical potential of lithium, while the anode must have a high chemical potential of lithium to obtain high voltage. (ii) It should allow for intercalation of a large amount of Li^+ (iii) The compound must have a good lithium-ion conductivity and an electronic conductivity to lower polarization losses during cycles. (iv) It must react with lithium-ions with a high free energy, which is associated to the high capacity, high voltage, and thus high-energy storage. (v) The active material should have high lithium-ion diffusion coefficient to achieve high power density. (vi) The redox energy of the electrodes must be within the electrolyte band gap. (vii) The compound must be chemically and physically stable under the operation condition, i.e., minimum change of crystal lattice or degradation from electrolyte contact. (viii) The material must be environmentally friendly and inexpensive.

2.4 Conventional lithium intercalation cathodes

2.4.1 Spinel type ($LiMn_2O_4$)

Oxides with the formula of LiM_2O_4 (M=Ti, Mn) crystallize in the $A[B_2]O_4$ spinel-type structure (cubic, $Fd\bar{3}m$), where Li^+ occupy tetrahedral 8a sites and Mn cations occupy octahedral 16d sites of the cubic close-packed array of O^{2-} lattice as illustrated in Figure 2.4. The Li^+ at tetrahedral sites share common faces with four vacant octahedral sites at 16c in the transition metal layer. This forms a three-dimensional structure that provides pathways for the Li^+ diffusion along the interconnected interstitial sites[22].

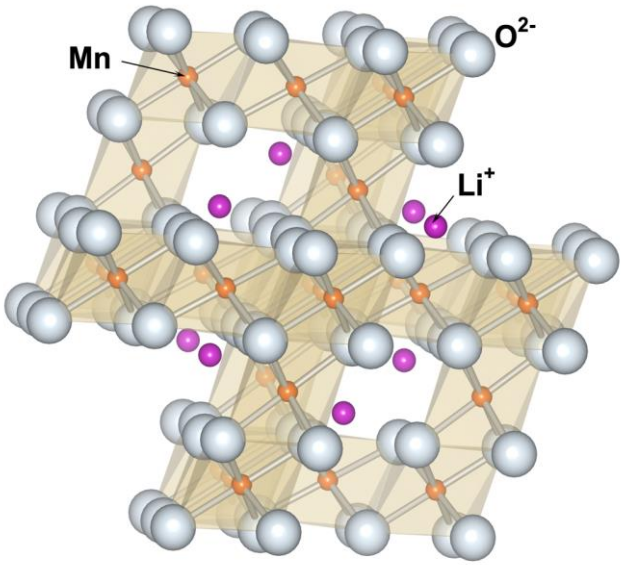


Figure 2.4 Representation of $LiMn_2O_4$ spinel structure.

On the other side, the edge-shared MO_6 octahedral structure offers good conductivity by hopping. This cathode composite was first proposed by Thackeray et al.[22] in 1983. Since then, it has been studied extensively as an active material for the lithium-ion battery cathode owing to the abundance resources of Mn in nature, low cost, and environmentally benign property. However, the spinel LiM_2O_4 suffers from large capacity fading during cycles, in particular at elevated temperatures. Several factors have been suggested as the sources for the capacity fading. These

are: (i) dissolution of Mn^{3+} into Mn^{2+} and Mn^{4+} in the electrolyte, (ii) oxidation of the organic electrolyte on the cathode surface, and (iii) structural instability attributed to the Jahn-Teller distortion resulting from a high spin Mn^{3+}:$3d^4$ ($t_{2g}^3 e_g^1$).

2.4.2 Olivine type ($LiFePO_4$)

The olivine $LiFePO_4$ is a polyanion material crystallized in the orthorhombic system (space group: Pnma), and it has the slightly distorted hexagonally close-packed (HCP) oxygen array where the Li^+ and Fe^{2+} occupy octahedral sites, while the P is located in tetrahedral sites. The structure of an olivine $LiFePO_4$ is presented in Figure 2.5. The FeO_6 octahedra share corners, whereas the LiO_6 octahedra share edges.

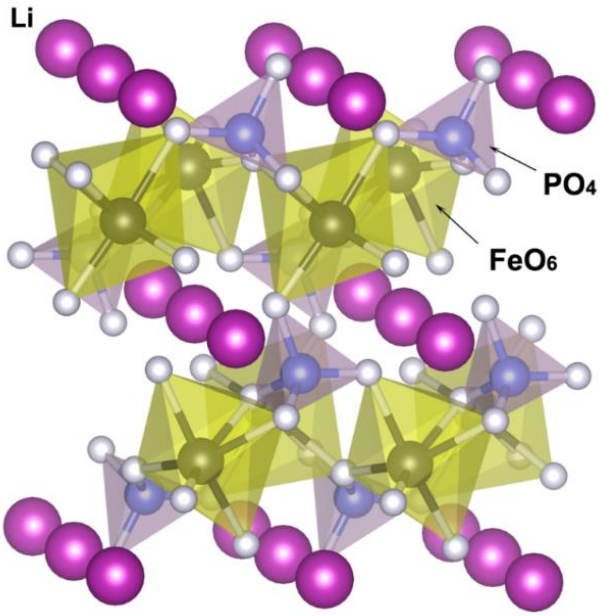


Figure 2.5 Representation of olivine $LiFePO_4$ structure.

The composite was introduced as a new type of positive electrode material known as phospho-olivines in 1997 by Goodenough[23]. This olivine type cathode benefits from electrochemical/thermal stability, low cost, and non-toxic property[24–26]. The covalent bond of P-O in the $(PO_4)^{3-}$ is the key factor for stabilizing the entire olivine unit, as well as bridging neighbouring FeO_6 octahedra[26]. The structural nature of $LiFePO_4$ results in the formation of one-

dimensional Li^+ diffusion channel. As such, Li^+ (de)intercalation can be blocked by defects or impurities. The rechargeable capacity of olivine $LiFePO_4$ was found to be approximately $170mAgh^{-1}$ at a voltage of 3.45 V vs Li^+/Li^0 [24,25]. The electrochemical property of the olivine cathode can be described by a flat plateau in the galvanostatic profile at approximately 3.45 V. The plateau indicates the two-phase region attributed to the reaction of "$LiFePO_4 \leftrightarrow xFePO_4 + (1-x)FePO_4 + xLi^+ + e^-$". A major limitation of the $LiFePO_4$ cathode is the low electronic conductivity ($\sim 10^{-9}$ S/cm) which leads to the poor rate capability[23,27].

2.4.3 Lithium layered oxide cathode ($LiXO_2$)

The chemical formula of $LiXO_2$ (X= Co, Ni, Mn, Cr, V…) represents the lithium-layered oxide cathode in general. They have been widely used as a lithium-ion battery cathode in portable electronic devices ranging from mobile phones to laptop computers.

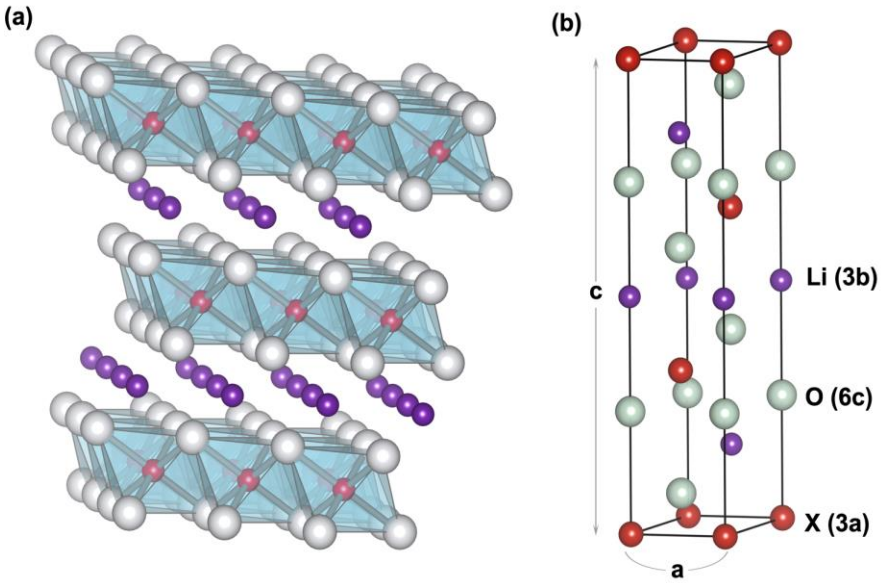


Figure 2.6 (a) Schematics of a layered $LiXO_2$ crystal structure. (b) Ball-stick model of α-NaFeO2-type structure (Trigonal, $R\bar{3}m$) with unit cell in $LiXO_2$ (X= Co, Ni, Mn, Cr, V…).

The cathode crystallizes in a layered structure (closed-packed oxygen layers) where the transition metal and Li^+ occupy the octahedral sites of alternate (111) planes with an ABCABC stacking sequence, forming a hexagonal symmetry (trigonal unit cell) in overall as shown in Figure 2.6[20,21].

The $LiXO_2$ is isostructural to a α-$NaFeO_2$ rock-salt structure. As such, it is designated as an O3-type structure, where O indicates the local atomic geometry of octahedral and '3' signifies the numbers of XO_2 sheet, according to the Delmas notation[28]. Those three XO_2 sheets per unit cell in the $LiXO_2$ allows the Li^+ (de)intercalation due to the edge-shared octahedral arrangement of the LiO_6. The lithium diffusion in the crystal structure is usually explained by the Li^+ hopping mechanism between octahedral sites via an intermediate tetrahedral site[29,30]. An edge-shared XO_6 octahedra in the layered structure maintains a direct X-X interaction, and this feature contributes to the improvement of electronic conductivity[31]. It is the structural nature of the α-$NaFeO_2$ rock-salt that facilitates the use of the lithium-layered transition metal oxides as a positive electrode.

2.4.3.1 Single transition metal Oxide: $LiCoO_2$, $LiNiO_2$, $LiMnO_2$ cathodes

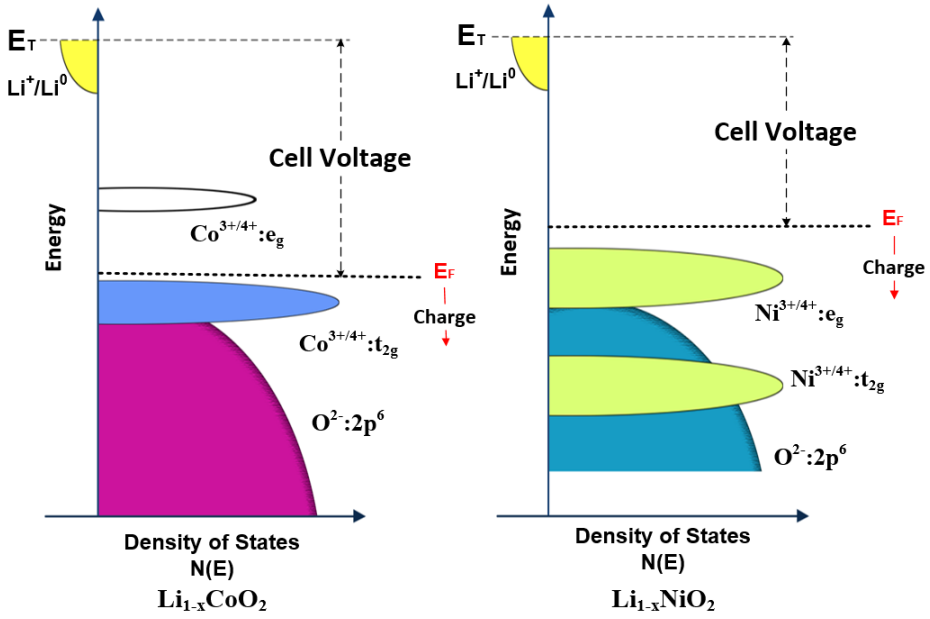


Figure 2.7 Energy vs density of states (DOS) comparison between $LiCoO_2$ and $LiNiO_2$. E_f indicates the Fermi energy (highest filled state at O K). Image was redrawn from reference[32].

$LiCoO_2$ was identified as an attractive electrode material for lithium-ion battery by John Goodenough[33]. This cathode material has been extensively used since the commercialization of the C/$LiCoO_2$ rocking chair-cell by Sony Corporation in 1991. The main advantages of using this battery type are the high operational voltage, fair electrical conductivity, high energy density, good

life span, and simple synthesis method. The conductivity (10^{-3} S/cm) is likely to be attributed to the octahedral arrangement of the edge-shared CoO_6 by the Co-Co direct interaction[31]. Its high energy density is due to the good mobility of the lithium-ion in the layered structure. For the host material, the trigonal structure ($R\bar{3}m$) is well suited for the intercalation of large amount of lithium-ions. The major structure can be described by the unit cell comprising three of CoO_2 layers with a stacking sequence of ABCABC, and thus provides a two-dimensional diffusion channel for the lithium-ions. The presence of the low-spin Co^{3+} and Co^{4+} at the octahedral site offer high operational voltage (~4 V), as well as some structural stability in the cathode. A theoretical specific capacity of $LiCoO_2$ is estimated to be 275 $mAhg^{-1}$ based on its molecular weight. In practice, however, only half of the theoretical capacity (~140 $mAhg^{-1}$) can be used because of the chemical instability from $Co^{3+/4+}$ at deep charge where it corresponds to $0.5 < x < 1$ in $Li_{1-x}CoO_2$[34,35]. In the energy diagram on the electronic structure, the chemical instability could be explained by the band overlapping between the $Co^{3+/4+}$:t_{2g} and the top of O^{2-}:2*p* bands (Figure 2.7). The continuous removal of the lithium-ions leads to the oxidation change from Co^{3+} into Co^{4+} with the removal of electrons from t_{2g} band, and further charge will remove electrons also from the O^{2-}:2*p* band. This reaction is believed to cause the phase transition between trigonal and monoclinic symmetry above ~4.2 V ($x > 0.5$)[36]. In addition, as a side reaction, the extraction of the Co from the host structure into the electrolyte produces a solid electrolyte interface (SEI) layer. The formation of the SEI layer can increase the impedance of the battery. Therefore, doping or surface modification by metal oxides such as Al_2O_3, MgO, TiO_2, and ZnO can effectively suppress the dissolution of the cathode into the electrolyte and thus improve the stability[37–41]. For instance, Al_2O_3-coated $LiCoO_2$ displays less polarization and specific capacity drops compared with the bare $LiCoO_2$ during the electrochemical cycles.

$LiNiO_2$ is an alternative layered compound that may replace the $LiCoO_2$. Ni is cheaper and less toxic than Co. $LiNiO_2$ offers a cell voltage of 3.8-4.0 V with a larger reversible capacity. The voltage of the $Ni^{3+/4+}$ is slightly lower than that of the $Co^{3+/4+}$ in the layered structure. The lower cell voltage can be understood by the density of states with the different energy levels involved in the redox reaction on charge-discharge. The redox reaction of Ni^{3+}:$t_{2g}^2 e_g^1$ is related to the high-energy bonding (e_g), while the reaction of Co^{3+}:$t_{2g}^2 e_g^0$ is associated with the low-energy bonding (t_{2g}) (Figure 2.7). Since the deintercalation of Li^+ in the $LiNiO_2$ only involves the e_g band, which lies well above the O:2*p* band, the impacts from oxygen loss is minimized during the deep charge as compared with the $LiCoO_2$[32,34,35] . A problem arises, however, when an attempt is made to synthesize this cathode material. It is challenging to produce a stoichiometric $LiNiO_2$ with a stable Ni^{3+} oxidation state because of the reduction of some Ni^{3+} into the Ni^{2+}, as well as the loss of Li^+ during the synthesis[42]. The reduction leads to the migration of the Ni^{2+} to the lithium 3a-site due to the similarities of the ion size between Li and Ni. This can increase the resistance of the lithium diffusion channel and thus result in a poor battery performance[42]. Whereas the pristine material of $LiNiO_2$ develops Ni^{2+} ions, the charged state ($Li_{1-x}NiO_2$) involves a migration of Ni^{3+} from the octahedral sites of the Ni layer into the octahedral sites of the lithium layer. Another major problem with this electrode material is the Jahn-Teller distortion originated from the low spin Ni^{3+}:$d^7(t_{2g}^6 e_g^1)$ which is linked to the phase transition of the cathode during the electrochemical cycles[13,43,44]. Further charge alters the oxidation state from Ni^{3+} to Ni^{4+} leading to a phase transition from layered structure into a spinel-like phase accompanied by oxygen loss[45]. This reaction, in turn, leads to a large irreversible capacity loss on cycle.

Ohzuku et al.[46] examined the transformation of the crystal structure during the electrochemical reaction on the $Li_{1-x}NiO_2$ cathode as shown in Figure 2.8. In region (I), where $0 < x < 0.25$, the crystal structure of the active material displays a rhombohedral lattice. Further charge

between x=0.25 and x=0.55, where it corresponds to region (II), leads to the transformation from the rhombohedral lattice to the monoclinic lattice. Continuous deintercalation of the Li^+ from x=0.55 to x=0.75, in region (III), results in the reappearance of the rhombohedral lattice owing to the removal of the Jahn-Teller distortion from NiO_6. In region (IV), a clear plateau can be observed with the implication of a rhombohedral two-phase reaction.

$LiMnO_2$ has attracted attention as an alternative electrode material for $LiCoO_2$ and $LiNiO_2$ due to its economical and environmental advantages, as well as its high theoretical capacity (=285 $mAhg^{-1}$) compared with $LiCoO_2$ and $LiNiO_2$ cathodes[47]. Apparently, the formation of the compound is based on the layered $LiXO_2$ type, but the structure of the $LiMnO_2$ has been examined as a modified rock-salt structure where the Li^+ and Mn ions occupy the octahedral interstitial sites as alternating zigzag layers[48–50].

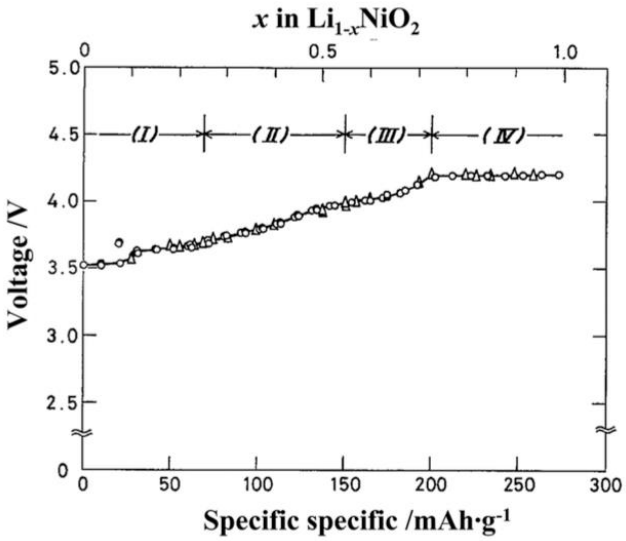


Figure 2.8 Open-circuit voltage (OCV) curve of $Li_{1-x}NiO_2$ cathode (at 30℃) in non-aqueous lithium-ion battery[51].

This structure is not identical to the layered O3-type because the energetically favoured phase crystallizes in an orthorhombic structure (space group: P*mmm*). In principal, an iso-structural compound of $LiMnO_2$ with the layered $LiXO_2$ can be prepared by ion-exchange synthesis from α-$NaMnO_2$[48,50]. However, a reduction in crystal symmetry appears from trigonal to monoclinic and

thus leads to the formation of the m-$LiMnO_2$ (monoclinic, C2/m) because of the Jahn-Teller distortion from high-spin Mn^{3+} ions. Although the $LiMnO_2$ cathode benefits from its high power density, its consecutive charge-discharge causes a phase transition into a spinel structure ($LiMn_2O_4$), irreversibly[47,52,53].

2.4.3.2 Mixed nickel-manganese oxide type: $Li(Ni_{1/2}Mn_{1/2})O_2$ Cathode

The $Li(Ni_{1/2}Mn_{1/2})O_2$ cathode is a binary transition metal oxide composite highlighted by Ohzuku et al.[54] as a possible alternative to the conventional layered oxide cathodes. This composite has drawn attention because of its better thermal stability, higher energy density and lower cost than $LiCoO_2$ or $LiNiO_2$[54,55]. The $Li(Ni_{1/2}Mn_{1/2})O_2$ is a one-to-one mixture of $LiNiO_2$ and $LiMnO_2$ in a solid state, and its crystal structure is the hexagonal structure with $R\bar{3}m$ symmetry with the 10% displacement of Ni and Li^+ in the lithium and transition metal layers[56]. The combination of two different kinds of transition metals (Mn, Ni) offers certain advantages from both elements. The high reversible capacity of about 200 mAh/g is attributed to the presence of the Ni metal. Practically, Ni is the only component that contributes to the specific capacity in $Li(Ni_{1/2}Mn_{1/2})O_2$ through the redox reaction by the oxidation changes between Ni^{2+} and Ni^{4+}. On the other side, since the Mn remains as a constant oxidation state of +4 through the electrochemical cycle, it plays an important role in a stabilizing framework for the host structure[57]. In this mixed cathode, the Li^+ tends to simultaneously deintercalate both from the Li-layer and transition metal layer of the $Li(Ni_{1/2}Mn_{1/2})O_2$ composite[58]. Further charge leads to the migration of the Li and Ni into the tetrahedral site in the transition metal layer. It is believed that the mobility and migration of the Ni-ions are the key feature which leads to the excellent reversibility of this cathode composite[58].

2.4.3.3 NMC type: $Li(Ni_{1/3}Mn_{1/3}Co_{1/3})O_2$ cathode

The $LiNi_xMn_xCo_{1-2x}O_2$, generally denoted as NMC, is much of interest for its high capacity and good cyclability, and it has been generally considered as a practical replacement for the commercial $LiCoO_2$ owing to its better thermal stability and reasonable cost[59,60]. The structure of this compound can be characterized with a hexagonal single phase (α-$NaFeO_2$ rock-salt). One well-known type from this series is the $LiNi_{1/3}Mn_{1/3}Co_{1/3}O_2$ composite (x=1/3). This composite is generally described as a one-to-one solid solution between $LiCoO_2$, $LiNiO_2$, and $LiMnO_2$, and it has been developed to take the full advantage of each transition metal to overcome the drawbacks emerge from a single transition metal cathode[54,60]. The NMC cathode shows a rechargeable capacity of 150 $mAhg^{-1}$ within the voltage of 3.5-4.2 V at 30 °C, and further charge up to 4.6 V reveals a rechargeable capacity of 200 mAh/g[61]. The high chemical stability of the NMC cathode retains the initial O3-type structure up to high state of charge (~80% SOC)[60]. One major drawback of this material is the cation mixing between Li and Ni because of the similarity in the ionic radius of Ni^{2+} (0.69 Å) and Li^+ (0.9 Å). The cation mixing on the 3b-sites of NMC lattice will deteriorate the battery performance[62,63]. Several attempts have been made to better understand the atomic environments and chemical states of the transition metals with the redox reaction in the NMC cathode during electrochemical cycles[64–66]. The information about the oxidation state and electronic structure of the transition metal provides the optimized voltage range for stable operation. Such information can be deduced by X-ray Absorption Spectroscopy (XAS) or *ab initio* computation such as 'First principle' calculation or their combined method[67].

In a study which set out to determine the first cycle characteristic of the NMC cathode by *ex situ* XAS/XRD, Kim et al.[65] found that the redox reaction of Ni^{2+}/Ni^{4+} is linked to the lower plateau around 3.75 V in the galvanostatic profile, whereas the Co^{3+}/Co^{4+} appears entire range. It has been also reported that the volume change of the crystal lattice in NMC cathode was small and thus

shows a good cyclability of the battery. Another study from Kim et al.[64] reveals that the Ni/(Mn + Co) ratio must be reduced to achieve a good electrochemical performance. Deb et al.[66] investigated the charge-compensation mechanism and structural changes of the NMC cathode by *in situ* XAS. The initial oxidation states of the transition metals in the cathode are found to be Ni^{2+}, Co^{3+}, and Mn^{4+}. During charge, the oxidation state of Mn remains as Mn^{4+}, while Ni^{2+} is oxidized to Ni^{4+} through an intermediate oxidation state of Ni^{3+}. Co^{3+} is also oxidized to Co^{4+} through the entire range of x in $Li_{1-x}Ni_{1/3}Mn_{1/3}Co_{1/3}O_2$ cathode.

2.5 High-energy density lithium intercalation cathode

2.5.1 Lithium-rich layered transition metal oxide

The past two decades have seen the enormous development of the lithium layered oxide cathode, $LiMO_2$ (M=Mn, Co, Ni or their combination), for the lithium-ion battery. Although they are successfully commercialized, there still remain major drawbacks such as insufficient energy density, structural instability during charge-discharge, limited operating voltage, and high cost. There have been intensive efforts to improve the limitations of the lithium layered oxide cathode by doping or coating the surface with metal oxides (e.g. Al_2O_3, MgO, and TiO_2) or incorporating mixed transition metals, i.e $Li(Ni_{1/2}Mn_{1/2})O_2$ and NMC cathode. However, some inherent limitations prevent them being used for high-energy density lithium ion batteries that are well suited to the portable energy storage for the electric vehicles (EV/HEV). Accordingly, a new class of lithium-layered cathode material has been proposed, namely, 'Lithium-rich layered transition metal oxide' cathode or 'Li-excess layered Mn-based oxide' has been studied by Thackeray et al.[1–5]. This cathode material, denoted as $x\mathrm{Li_2MnO_3} \cdot (1-x)\mathrm{LiMO_2}(\mathrm{M} = \mathrm{Mn, Ni, Co})$, shows superior specific capacity (> 200 $mAhg^{-1}$) with high chemical potential (> 4.6 V vs Li^0) while lowering cost compared to the conventional cathodes (e.g. $LiCoO_2$)[2–4], and thus emerges as a promising

candidate for the electronic vehicle applications (EV/HEV/PEV). However, a major problem with this type of composite is the irreversible capacity loss of 40-100 $mAhg^{-1}$ during the first electrochemical cycle[7]. The Li^+ ion extraction accompanied by oxygen release, known as lithia (Li_2O), from the active material has been suggested as the dominating process of the capacity deterioration[7,8].

2.5.2 Integrated composite and solid-solution concept ($Li_2MnO_3-LiMO_2$)

Some researches[68–70] considered the lithium-rich layered cathode as a solid solution between Li_2MnO_3 and $LiMO_2$ (M=Transition Metals) with the notation of $Li_{1+(x/(2+x))}M'1-_{(x/(2+x))}O_2$. Jarvis et al.[69] investigated the atomic structure of lithium-rich layered oxide cathode by scanning transmission electron microscopy (STEM) and provided the evidence of a solid-solution of this electrode material. A further study by Koga et al.[70] has supported the concept of the solid-solution. He characterized the $Li_{1.20}Mn_{0.54}Co_{0.13}Ni_{0.13}O_2$ structure by NMR, neutron diffraction, and Raman spectroscopy, and reported that the cathode material existed as a homogenous single phase rather than a separation of $LiNi_{1/3}Mn_{1/3}Co_{1/3}O_2$ and Li_2MnO_3 domains. On the other side, Thackeray et al.[1–5] proposed the integrated composite concept with the notation of as $xLi_2MnO_3 \cdot (1-x)LiMO_2 (M = Mn, Ni, Co)$. A recent study from Long et al.[71] with X-ray absorption fine structure (XAFS), magic-angle-spinning nuclear magnetic resonance (MAS-NMR), and high-resolution TEM (HR-TEM) identifies two significantly different local domains, supporting the idea of the two-composite concept. In addition, the EXAFS results from this study do not corroborate to the characteristic of the solid-solution phase. Long[71] claims that the solid-solution behavior cannot be examined by a long-range averaged technique (e.g. X-ray diffraction).

2.5.3 Origin of the high capacity and structural property

The intimate integration of the two crystallographic components is attributed to the interleaving of close-packed layers from the two compounds, namely, the (001) planes from Li_2MnO_3 and the (003) planes from $LiMO_2$ with the interlayer spacing of ~4.7 Å as shown in Figure 2.9. Lithium ions and transition metal ions occupy the 3b sites and 3a sites, respectively, in the layered $LiMO_2$ component without cation ordering.

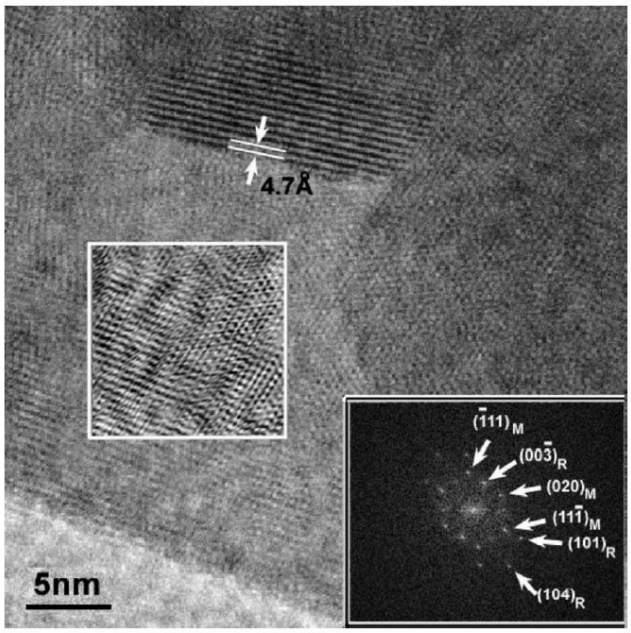


Figure 2.9 HRTEM image of the $xLi_2MnO_3 \cdot (1-x)LiMn_{1/3}Ni_{1/3}Co_{1/3}O_2$ (x=0.5) composite , showing 4.7 Å lattice fringes[72].

In layered Li_2MnO_3, both the transition metals and a fraction of the lithium-ions occupy the transition metal layers (3b-sites) where the cation ordering of $LiMn_6$ appears. The cation ordering is the major process that develops the structural characteristic of the lithium-rich layered oxide cathode. Unlike the conventional lithium-layered oxide, this active material shows excessive lithium ions in the transition metal layer (slab) as one third of the sites in the slab are replaced by lithium ions. In this regard, it is possible to denote this component as $Li[Li_{1/3}Mn_{2/3}]O_2$ instead of Li_2MnO_3. The cation ordering resulting from the LiO_6 octahedron surrounded by six MnO_6

contributes to the weak peaks at 2θ ~ 21-25° in the X-ray diffraction pattern of Li_2MnO_3 as shown in Figure 2.10[2,73]. Weill et al.[74] studied the cation ordering in $Li_{1+x}TM_{1-x}O_2$ (TM=Ni, Mn, and Co) cathode and revealed the in-plane $\sqrt{3}a_{hex} \times \sqrt{3}a_{hex}$ superstructure in the transition metal layers of Li_2MnO_3 by the help of X-ray diffraction and electron diffraction analyses. In thermodynamic aspect, the cation ordering is an energetically favoured process that minimizes the strains in the TM-layer and thus increases the stability of the active material[74,75].

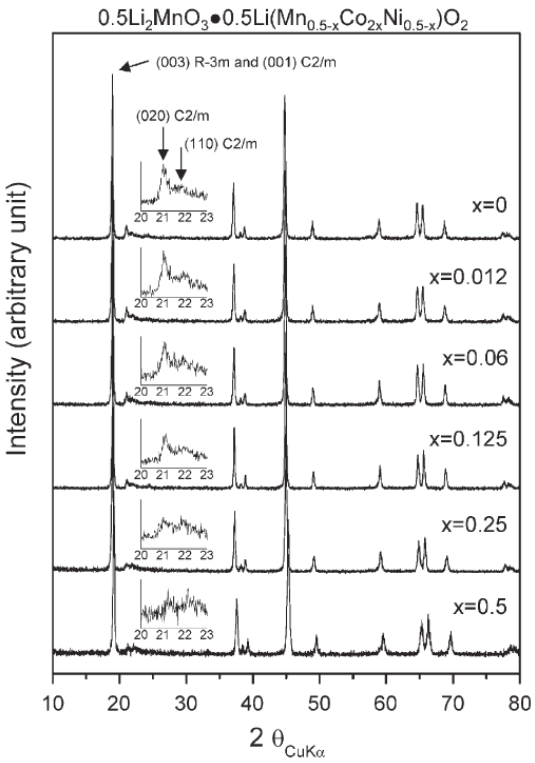


Figure 2.10 XRD patterns of the $xLi_2MnO_3 \cdot (1-x)LiMO_2$ composite at different *x* concentration. The peaks from the cation ordering from Li2MnO3 can be observed at 2θ ~ 21-25°[73].

The ordering process between transition metals leads to the formation of two significant sites in the in-plane superstructure, namely, α-site for the large Li^+ and Ni^{2+} ions and β-site for the small Mn^{4+}, Ni^{3+}, and Co^{3+} ions[58,74,75]. The Li-rich layered oxide composite (e.g. $Li(Li_{0.2}Mn_{0.54}Ni_{0.13}Co_{0.13})O_2$) can be characterized by the ratio of 1:2 between large cation and small cation groups (Figure 2.11). Within the Li_2MnO_3 component, a strong cation tendency between Li^+ and Mn^{4+} is observed with the ratio of 1:2[74] as presented in Figure 2.12. The cation

ordering of Li/Mn is likely to be the dominant factor which determines the local atomic environment in $x\mathrm{Li_2MnO_3} \cdot (1-x)\mathrm{LiMO_2}$, and thus it is linked to the stability of O3 layered structure and lithium diffusivity[58].

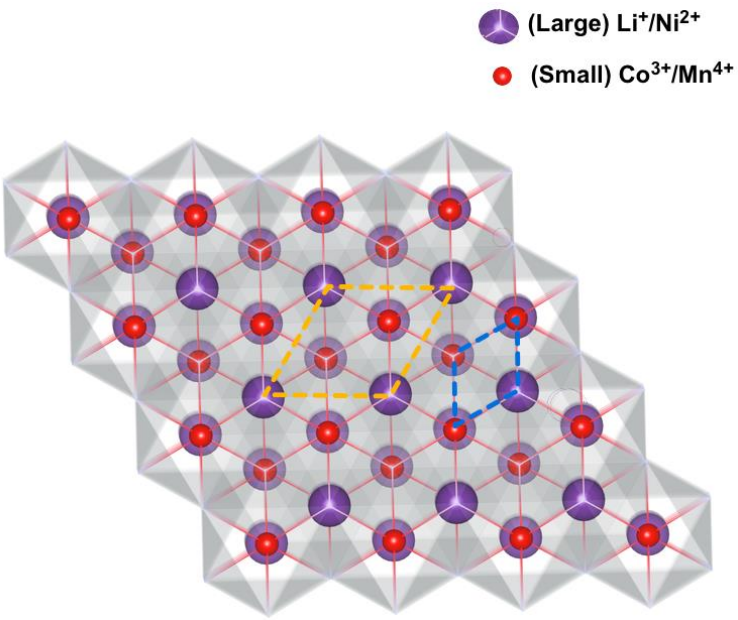


Figure 2.11 Illustration of cation ordering of transition metals in $x\mathrm{Li_2MnO_3} \cdot (1-x)\mathrm{LiMO_2}$ composite. The yellow dash line represents the reduced $\sqrt{3}a_{hex} \times \sqrt{3}a_{hex}$ supercell and the blue dash line represents the unit cell.

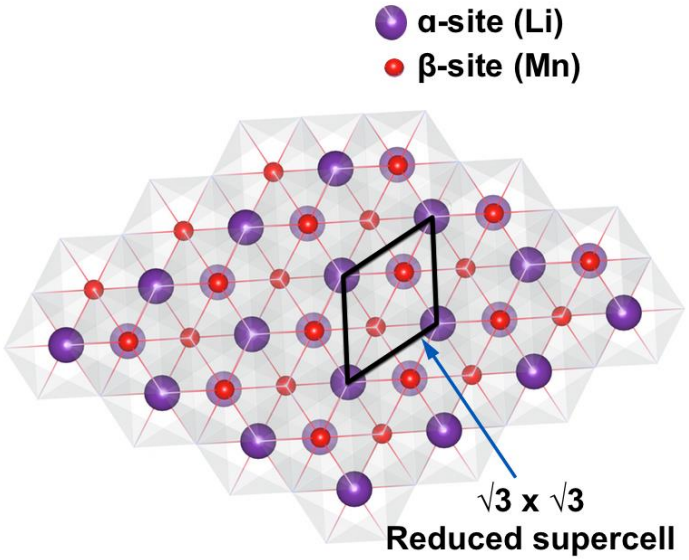


Figure 2.12 Illustration of cation ordering of transition metals on the transition metal layer in $\mathrm{Li_2MnO_3}$ component with reduced supercell.

The relationship between cation ordering and electrochemical cycle has been widely investigated[58,76,77]. Studies have revealed that the superstructure of $\sqrt{3}a_{hex} \times \sqrt{3}a_{hex}$ tends to be significantly weakened upon charge and disappeared after the 1st electrochemical cycle. Mohanty et al.[77] correlated the cation ordering with the voltage fade phenomena in a Li-Mn-rich transition metal oxide cathode by utilizing magnetic measurements and TEM. He conducted the charge-discharge experiment with two cut-off voltages such as 4.2 V and 4.8 V. In the pristine material of $Li_{1.2}Co_{0.1}Mn_{0.55}Ni_{0.15}O_2$, Mn^{4+}-Co^{3+}-Ni^{2+} cation ordering was observed. The cation ordering was preserved after the charge up to 4.2 V and discharge to 2.4V. However, the ordering disappeared in the case of the charge up to 4.8V and discharge to 2.4V. It is therefore likely that a reaction appears that alters the cation arrangement at the voltage-plateau in the galvanostatic profile.

2.5.4 Electrochemistry of Li-rich layered oxide cathode

The electrochemical property of the Li-rich layered oxide cathode is characterized by a two-stage reaction in the galvanostatic profile during the 1st charge-discharge of the battery (Figure 2.13a). In the first stage, a slope can be observed up to ~4.5 V vs. Li/Li^+ due to the redox reaction of Ni^{2+}/Ni^{4+} and Co^{3+}/Co^{4+} (Co is not fully oxidized to tetravalent). In the second stage, a plateau like region appears between 4.5 V and 4.8 V only during the 1st charge because of the Li^+ deintercalation from the Li_2MnO_3 component[2,7,8,78]. The lithia (Li_2O) extraction from the Li_2MnO_3 leads to an irreversible oxygen loss from the lattice[2,3,7,8,78]. As a result, a layered MnO_2 component will be produced on lithia removal ($Li_2MnO_3 \rightarrow Li_2O + MnO_2$). With the redox reaction of Ni^{2+}/Ni^{4+} and Co^{3+}/Co^{4+}, the Li^+ would intercalate back into the layered MnO_2 component on discharge. The high discharge capacity of this cathode type is mainly attributed to the MnO_2 component as it increases the available sites for the lithium ions during electrochemical cycle. Therefore, the coulombic efficiency (%) of the lithium-ion battery tends to increase with further cycles as presented in Figure 2.13b. To get a better insight into the redox reaction of the transition

metals, a dQ/dV plot that describes the voltage change as a function of 1st order differentiation of galvanostatic curve with respect to the voltage is generally used (Figure 2.13c). As to the integrated composite, two oxidation peaks (O_1 and O_2) would be observed in the dQ/dV plot during the initial charge and two reduction peaks (R_1 and R_2) during the discharge. The peak O_1 and R_1 would stem from the redox reaction of Ni^{2+}/Ni^{4+} and Co^{3+}/Co^{4+} in the layered $LiMO_2$ (M=Mn, Co, Ni)[2,79–81].

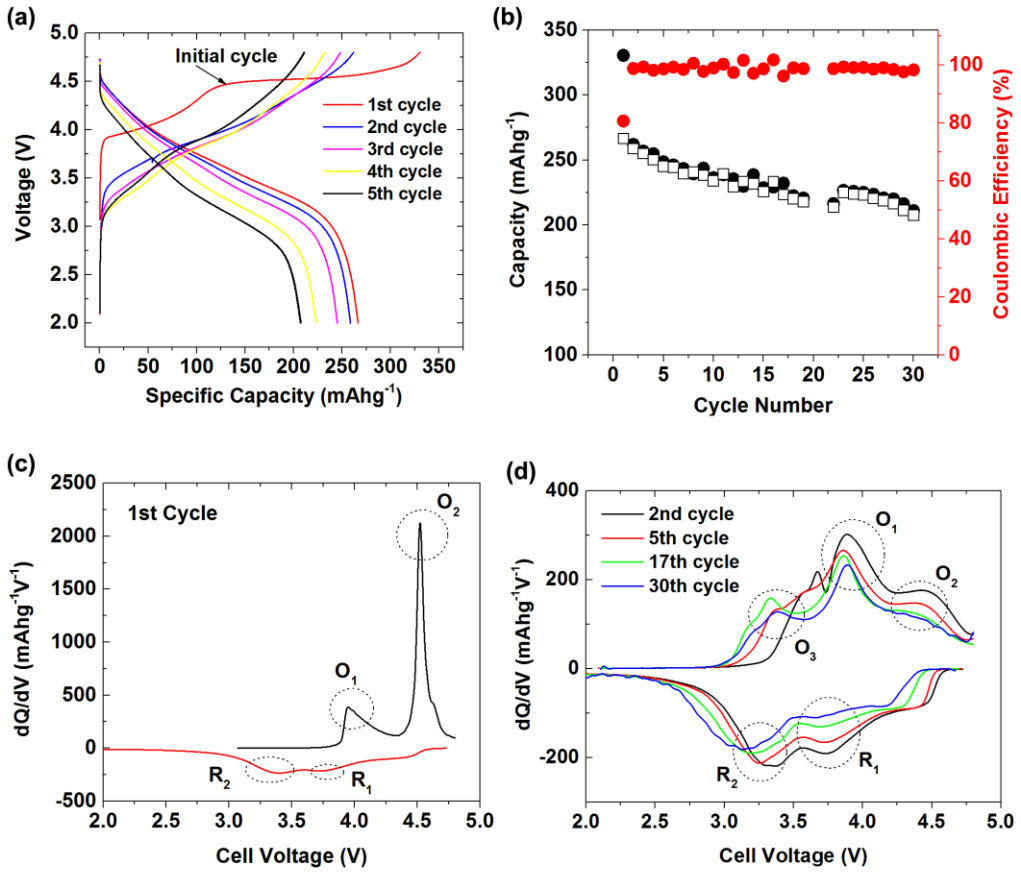


Figure 2.13 (a) Galvanostatic profile of Li-rich layered oxide cathode; (b) capacity vs cycles; (c) dQ/dV plot of the initial cycle; and (d) dQ/dV plots of further cycles. Results obtained within the current study.

The sharp peak (O_2) at ~4.5 V corresponds to the lithia (Li_2O) loss from the Li_2MnO_3 lattice[8,82,83]. The R_2 peak is possibly attributed to the redox reaction of $Mn^{4+}/Mn^{(4-x)+}$ in $LiMnO_2$ and MnO_2-rich domains[2,8,82]. On the other hand, the 'O_3' peak is related to the activation of the Li_2MnO_3 phase, which is responsible for the phase transition from the layered structure into the spinel[84].

2.5.5 Reaction mechanism during 1st electrochemical cycle

2.5.5.1 Chemical reaction of irreversible oxygen loss

It has been already pointed out that the Li_2MnO_3 involves not only in the structure stabilizing, but also providing extra capacity to the battery system by chemical decomposition during the further charge above ~4.5 V. With this consideration, the irreversible reaction that leads to the formation of MnO_2 by the simultaneous extraction of Li+ and oxygen (O^{2-}) ions can be represented by the reactions below [85]:

$$xLi_2MnO_3 \cdot (1-x)LiMO_2 \xrightarrow{charge} xLi_2MnO_3 \cdot (1-x)MO_2 + (1-x) \cdot Li \quad (2.23)$$

$$xLi_2MnO_3 \cdot (1-x)MO_2 \xrightarrow{charge} xMnO_2 \cdot (1-x)MO_2 + x \cdot Li_2O \quad (2.24)$$

$$xMnO_2 \cdot (1-x)MO_2 + Li \xrightarrow{discharge} xLiMnO_2 \cdot (1-x)LiMO_2 \quad (2.25)$$

As can be seen from the reactions (2.23 and 2.24), 2*x*·Li and (1-*x*)·Li are deintercalated from the Li_2MnO_3 and $LiMO_2$ components, respectively. Hence, the total amount of the Li^+ deintercalated from the host structure becomes (1+*x*)·Li during initial charge. Because of the irreversible oxygen loss after ~4.5 V charge, only a single lithium ion is able to intercalate back into the host structure during discharge. This reaction results in the formation of $LiMnO_2$ and $LiMO_2$ by inserting *x*Li and (1-*x*)·Li into the MnO_2 and MO_2 components, respectively.

2.5.5.2 Charge compensation mechanism

The charge compensation mechanism during the initial charge and further electrochemical cycles is not yet clearly understood. The underlying principle of the mechanism is the redox reaction of the transition metals with the ability to reach their maximum oxidation state (+4) during the initial charge. A number of studies[64,66,83,86–92] have been carried out to investigate the charge compensation from the transition metals by using XAS. The oxidation state for each transition metal (Mn, Co, and Ni) would be evaluated with a finger-print method by comparing the spectra

pattern between the cathode material and reference composites at K-edge XANES. The XANES spectra suggest the full oxidation of the Ni^{2+} and Co^{3+} into Ni^{4+} and Co^{4+} during the charge up to ~4.5 V in the lithium-rich layered oxide cathode[83,88,90,92]. In particular, the redox reaction of nickel is believed to be consisted of a two-stage reaction such as Ni^{2+}/Ni^{3+} and $Ni^{3+/}Ni^{4+}$. The two-stage redox reaction of nickel contributes to the relatively large energy shift (approximately 3.0 ~ 4.0 eV) in K-edge XANES as compared with that of the Co and Mn[66,88,90,92]. On the other hand, there is little or minimum change in the Mn K-edge XANES indicating no charge compensation since the Mn is tetravalent (+4) in the pristine material. However, debate continues about the actual oxidation state of the Mn in the pristine material of the lithium-rich layered oxide cathode. Huang et al.[93] predicted the presence of the low-spin Mn^{3+} ion in the lithium-layered composite. A combined study between First-principle calculation and XAS by Prasad et al.[94] also revealed the low-spin configuration of the Mn ions (Mn^{3+}) in the lithium-layered oxide material. Recently, Simonin et al.[91] has found that the pristine material of the lithium-rich layered oxide contains an amount of Mn^{3+} in low spin configuration, showing the Mn oxidation state as +3.75 on average with the help of *in situ* XAS and magnetic measurement by superconducting quantum interference device (SQUID). The slight spectral shift in Mn K-edge XANES during charge may indicate the small change of the oxidation state such as from +3.75 to +4. Regardless of the pristine state, all the transition metals are expected to be fully oxidized up to tetravalent (+4) during the full-charge. However, the battery capacity attributed to the oxidation of the transition metals cannot cover the entire reversible capacity. For instance, the reversible capacity of $Li_{1.2}Ni_{0.17}Co_{0.07}Mn_{0.56}O_2$ is estimated to be 199 $mAhg^{-1}$ from the oxidation changes of the Ni, Co, and Mn, but this value is much lower than the empirical capacity (~266 mAhg-1)[88]. It is therefore likely that there might exist another charge compensation process after the oxidation change of the transition metals, which can compensate the insufficient capacity. Armstrong et al.[95] reported the oxygen loss and

associated structural change during Li^+ deintercalation in the lithium-rich layered oxide material at ~4.5 V voltage plateau. With the Li^+ extraction, electrons tends to be removed from the coordinated O^{2-} in the crystal lattice providing extra capacity. However, the amount of the O^{2-} in the bulk active material is still not enough to cover the entire extra charge. Thus, the participation of the O^{2-} from the surface of the electrode has been also considered as a vital part of the charge compensation mechanism[76,95,83]. Both the oxygen ions from the surface and bulk are oxidized leading to the oxygen evolution from the surface. This is followed by the Li^+ migration from the transition metal layers into the lithium layers forming vacancies in the transition metal layers. Eventually, lithia (Li_2O) is removed from the electrode component (Li_2MnO_3) above 4.4 V on charge producing MnO_2 composite which is electrochemically active. This process corroborates to equation 2.24. Simultaneously, transition metal ions migrate into the lithium layers through the vacancies formed. The migration of the transition metals from the surface into the vacated lithium sites was suggested by Tran et al.[76] with a densification model. Irreversible cation rearrangement was observed in the transition metal layer at the voltage plateau because of the lattice densification attributed to the cation migration.

2.5.6 Considerations in local atomic environment

2.5.6.1 Transition metal composition

The electrode type (e.g. α-$NaFeO_2$-type) and chemical composition in the electrode material are the major contributing factors for the electrochemical property and stability of the battery cathode. One approach that can be considered for the improvement of the battery performance is tailoring the unit components that constitute the electrode composite. For instance, diverse two-phase system such as ‘layered-layered’, ‘layered-spinel’, and ‘layered-rocksalt’ has been developed by a novel synthesis method to fabricate a high-capacity composite cathode[96]. Another approach would be the cation substitution or chemical treatment on the electrode such as coating/doping and

surface modification. For example, chromium (Cr) substitution has been proposed to improve the stability on oxide ion framework of the lithium-rich layered oxide cathode, owing to its ability to suppress the oxygen loss during charge[97]. It is thus very important to understand the role of the transition metals that compose the basic framework of the lithium-rich layered oxide system in order to successfully improve battery properties. As described in previous sections, the incorporation of Mn in the lithium-layered oxide cathode not only increases the battery capacity, but also it stabilizes the composite structure. Moreover, the replacement of Co in the lithium-layered oxide by Mn offers advantages in terms of ecological and economical aspects. Mixed transition metals provides more synergetic benefits over a single transition metal. The presence of mixed transition metals with various oxidation states such as Ni^{2+}, Co^{3+}, and Cr^{3+} is generally useful for the charge compensation mechanism. Furthermore, the electronegative transition elements (e.g. Co, Ni, and Cr) play an important role in maintaining the average oxidation state of Mn above +3. The presence Co^{3+} ions tend to suppress the structural distortion resulting from the Ni^{3+} Jahn-Teller effect[98,99] by partially disrupting the Ni^{2+}/Mn^{4+} cation ordering[74].

The correlation between the ratio of cathode elements (Mn, Co, Ni and Li) and electrochemical property has been widely addressed[64,81,83,100–104]. Kim et al.[64] found that the Ni/(Mn+Co) ratio in the $Li[Ni_{1/3}Co_{1/3}Mn_{1/3}]O_2$, $Li[Li_{1/10}Ni_{3/10}Co_{3/10}Mn_{3/10}]O_2$, and $Li[Li_{1/10}Ni_{2/10}Co_{3/10}Mn_{4/10}]O_2$ directly affects the electrochemical property of the battery, and he suggested the lowest Ni/(Mn+Co) ratio as the best for the capacity retention. The optimized transition metal ratio (Mn:Co:Ni=4:1:1) in a lithium-rich layered oxide cathode ($(Li(Li_{0.2}Mn_{1.6/3}Ni_{0.4/3}Co_{0.4/3})O_2 \approx Li(Li_{0.2}Mn_{0.54}Ni_{0.13}Co_{0.13})O_2$) has been revealed by Jiang et al. [100] and Yabuuchi et al.[83]. The type of the transition metals are associated with the Li^+ ion mobility which has emerged as a central issue that needs to be elucidated in order to understand the rate capability of the lithium-ion battery. The cathode composite consisted of alternating layers

provides an optimized two-dimensional conduction pathway for the lithium-ions in the lithium-layered oxide cathode. It has been suggested as the mechanism of lithium ions transportation in the crystal structure that the Li^+ are hopping between octahedral sites *via* an intermediate tetrahedral site by an *ab initio* modelling study[29,30]. The Li^+ mobility in the layered oxide structure (O3 structure) is determined by the slab spacing and the electrostatic repulsion between Li^+ and transition metals (Mn, Co, and Ni)[29,30]. The activation barrier for the Li^+ diffusion decreases with the increase of Li slab spacing due to the reduced compressive stress on lithium-ions. The mobility of the lithium-ions is highly sensitive to the distance between the oxygen layers, such as the change of spacing as low as ~0.02 Å can give rise to the activation barrier by 20~30 meV[30]. The electrostatic repulsion between Li^+ and the transition metal ions at the tetrahedral sites is also a vital factor related to the mobility. It is not only the type of transition metals, but also their oxidation states that affects the Li^+ mobility. For example, the activation barrier of Co^{3+} is lower than Co^{4+} as the lower oxidation states have weaker electrostatic interaction with the diffusing Li^+ ion. The electrostatic interaction appears to be screened by the increased electron density of oxygen or by the transition metals with diverse oxidations states[105]. A reduced screening results in a higher activation barrier because of the increased interaction between the Li^+.

2.5.6.2 Crystal Field Theory

The transition metals (Mn, Co, Ni, Cr, Fe) in the lithium-layered oxide system are surrounded by six oxygen ions, which are the ligand atoms, forming MO_6 octahedral complex. The electronic structure resulting from the interaction between the 3*d* orbitals of the transition element and the *p* orbitals of the oxygen ions holds the key to the fundamental understanding of the nature and process involved in the battery application. The interaction between the orbitals can be systematically investigated by a special atomic model, namely, 'Crystal Field Theory' describes the effect of neighbouring atoms on the energies in accordance with their valence orbitals. A single

transition metal ion in a free space remains degenerate with the same energy level of the five 3*d* orbitals (Figure 2.14). When a negatively charged ion, i.e. O^{2-} ions, approaches the transition metal, the energy state of the *d* orbitals change due to the Coulomb repulsion between the negative charges and the electrons in *d* orbitals.

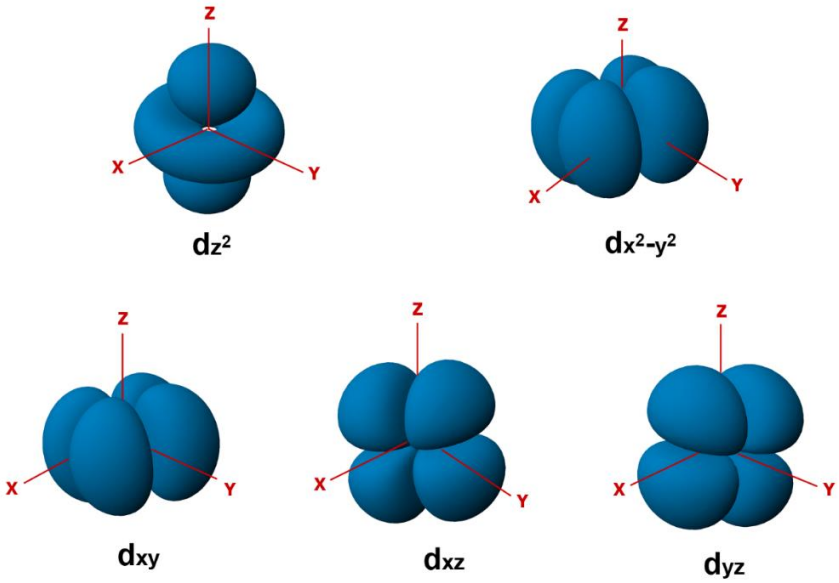


Figure 2.14 The five 3*d* orbitals with x,y,z coordinate axes. Orbitals were constructed in accordance with the quantum number of *n*=3, *l*=d, and *m*=2 or 0 (*n*: principle quantum number, *l*: azimuthal (orbital) quantum number, *m*: magnetic quantum number, and *s*: spin quantum number). 'd' indicates any *d* orbitals type.

If the transition element is encircled by a spherically symmetrical field of negative charges then the energy of the *d* orbitals will increase, but still the five *d* orbitals remain degenerate. However, if the distribution of the negative charge is not uniform around the transition element the degeneracy of the *d* orbitals is removed and this results in energy splitting of the two groups of *d* orbitals, named as e_g and t_{2g} (Figure 2.15). The lower energy orbital (t_{2g}) corresponds to d_{xy}, d_{xz}, d_{yz} orbitals, whereas the higher energy orbital (e_g) corresponds to d_z^2 and d_x^2-$_y^2$. As such, t_{2g} is named as a triply degenerate orbital set and e_g as a doubly degenerate orbital set. The energy difference between the two sets of *d* orbitals is the crystal field splitting energy (Δ_o). If the splitting energy (Δ_o) is larger than the spin pairing energy, it results in a low-spin configuration with minimum number of unpaired electrons. But, if the splitting energy (Δ_o) is smaller than the spin

pairing energy the configuration would result in high-spin state with the maximum number of unpaired electrons. In the high-spin state, the electrons tend to spread over the available empty *d* orbitals. The crystal field theory provides a theoretical basis to understand the different degree of XANES spectral shift upon transition metal types and states, as well as the presence of the double peaks at K pre-edge in the transition metals. The formation of the bonding between the transition metal (TM) and oxygen ions (ligand) is due to the presence of d_z^2 and $d_{x^2-y^2}$ orbitals as only they can orient to overlap with the ligand orbitals to make a pair between bonding (O-2p:σ_d) and antibonding (e_g:σ_d^*)[93,106,107]. On the other hand, the d_{xy}, d_{xz}, and d_{yz} orbitals (t_{2g} set) are the non-bonding character as they don't overlap with the ligand. Thus, the impact on the atomic environment is higher when there appears an atomic configuration change in the e_g set relative to t_{2g} set. This explains the different energy shift of the XANES spectra in the transition metal ions. For instance, the outer most electron configuration of Co^{3+} and Co^{4+} can be written as $t_{2g}^6 e_g^0$ and $t_{2g}^5 e_g^0$, respectively, and the configuration for Ni^{2+}/Ni^{3+}/Ni^{4+} are $t_{2g}^6 e_g^2/t_{2g}^6 e_g^1/t_{2g}^6 e_g^0$. In the Co electron configuration, there is no electron that occupies the e_g orbital. By contrast, in the Ni configuration, there are a maximum of two electrons that are able to occupy the e_g orbital. Hence, the Ni redox reaction normally causes larger impact on the local structure of the transition metals, and this is reflected as a larger spectral shift in XANES than that of the Co redox reaction.

In the Mn K pre-edge, there are two discernible peaks which could be found between 6538 and 6543 eV at the near-edge spectra. These peaks are assigned to 1*s*-3d_{t2g} (lower energy) and 1*s*-3d_{eg} (higher energy) transitions. The transition from a core 1s electron to an unoccupied 3*d* orbital, i.e. Mn^{4+} ($t_{2g}^3 e_g^0$), is formally dipole-electric forbidden in a centrosymmetric system, but these peaks appear from a weak quadrupole transition[108] or/and 3*d*-4*p* orbital hybridization by the loss of the centrosymmetric environment of the octahedral 3a-site in the $R\bar{3}m$ space group. The

presence of those weak peaks in the pre-edge signifies the symmetry of the octahedral environment around the absorber atom, as opposed to the tetrahedral environment of which the peak intensity is very strong[109]. As such, the intensity of the double peaks increase upon the distortion of the MO_6 octahedral environment[110]. In general, the double peaks in Mn K pre-edge grow during the deintercalation of the lithium ions from the host lattice.

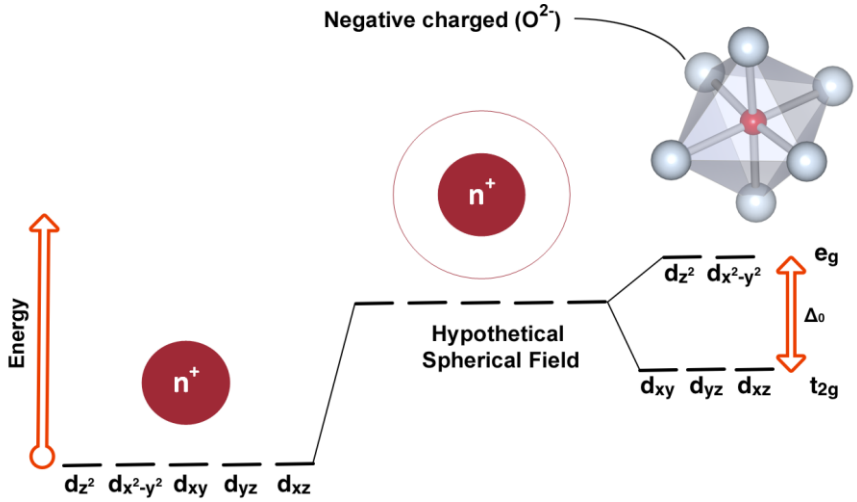


Figure 2.15 Schematics of energy level of *d* orbitals in the octahedral complex with crystal field splitting. In a free transition metal ion (M^{n+}), it is degenerated with the same energy level of the five *d* orbitals. The spherical field around the transition metal ion leads to the rise of the energy level, but the orbitals remain degenerate. When negative charged ligand ions approach, the orbitals are split into two sets of energy level forming an octahedral complex. The Δ_0 indicates the crystal field splitting energy.

It is thus probable that the local atomic environment of octahedral MnO_6 undergoes distortion during charge. In addition, it has been also reported that the splitting energy (Δ_o) decreases upon the lithium ion deintercalation because of the symmetry effects[89].

2.5.6.3 Jahn-Teller distortion

Oxidation state changes of the transition metals are essential for the charge compensation mechanism in order to produce the battery capacity. However, particular oxidation states of transition metals undergo a special distortion perturbing the complex symmetry, namely, Jahn-Teller distortion occurs when any non-linear molecular system is not stable. This distortion will remove the degeneracy of the atomic orbitals and thus lower the energy of the system. In the

lithium-ion intercalation system, the high-spin Mn^{3+} and low-spin Ni^{3+} are considered as the typical Jahn-Teller ions[111,112]. The high spin configuration of $3d^4$ orbital in the Mn^{3+} ($t_{2g}^3 e_g^1$) ion leads to the distortion (elongation) on the octahedral MO_6 structure by reducing the crystal symmetry from rhombohedral to monoclinic (SG:C2/m)[48,113] as illustrated in Figure 2.16. As a result, this distortion from Mn^{3+} is reflected on the pre-edge region of the Mn K-edge XANES showing a single peak, as opposed to the double peaks in the Mn^{4+}.

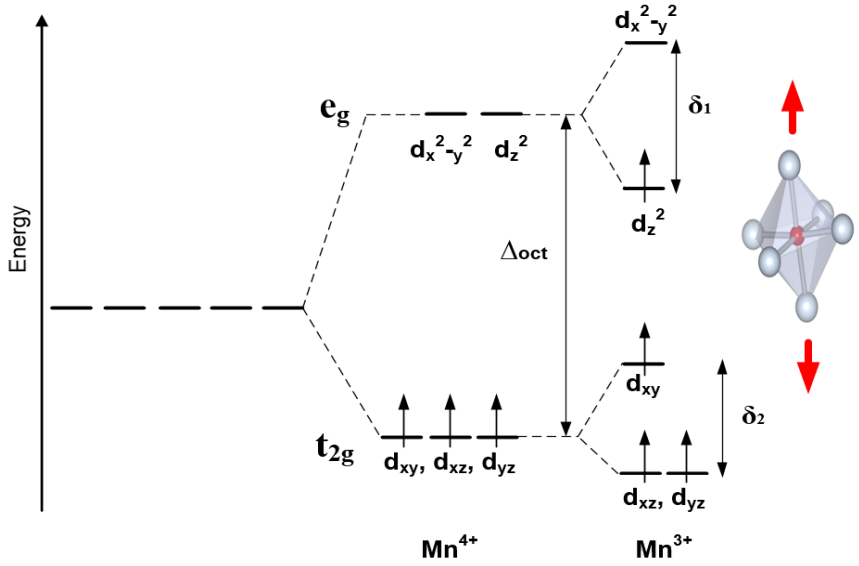


Figure 2.16 Schematic illustration of a Jahn-Teller distortion (elongation along the red arrows) of MnO_6 with the energy splitting in octahedral complex. The energy level of splitting is $\Delta_{octahedra} >> \delta_1 > \delta_2$.

As to the spinel cathode ($LiMn_2O_4$), the Jahn-Teller Mn^{3+} causes the phase transformation from cubic to tetragonal structure[114]. On the other hand, it has been reported that the layered $LiMnO_2$ undergoes a phase transformation from a layered structure into a spinel structure during the electrochemical cycle due to the Mn^{3+} ions[101,113].

Studies have identified that the Ni^{2+} is oxidized to Ni^{4+} through an intermediate state of Ni^{3+} during the charge compensation mechanism[66,86,115,116] in the lithium-layered oxide material. Thus, by the Jahn-Teller effect, this system is expected to undergo the distortion from the low-spin Ni^{3+}:d^7($t_{2g}^6 e_g^1$) on the octahedral environment of the NiO_6 complex. The presence of the Ni^{3+} can

be generally identified by the Ni-O bond splitting during EXAFS fitting. For instance, if NiO_6 forms an ideal octahedral symmetry, the bond length of six Ni-O coordination must be identical, i.e. ~2.04 Å. However, in the case of Jahn-Teller distortion, there appears four short bonds of Ni-O (e.g. ~1.90 Å) and two long bonds of Ni-O (e.g. ~2.08 Å). In the Fourier transformed R-space, the impact from the Jahn-Teller distortion of Ni^{3+} results in the decrease of the first coordination amplitude (Ni-O peak) with peak broadening whereas the disappearance of the distortion results in an increased amplitude of Ni-O peak[89,92,117,118]. This can be also examined by the appearance of the multiple coordination numbers during the EXAFS fitting process.

2.6 Ageing mechanism in the lithium-ion battery

2.6.1 Overview of the ageing mechanism

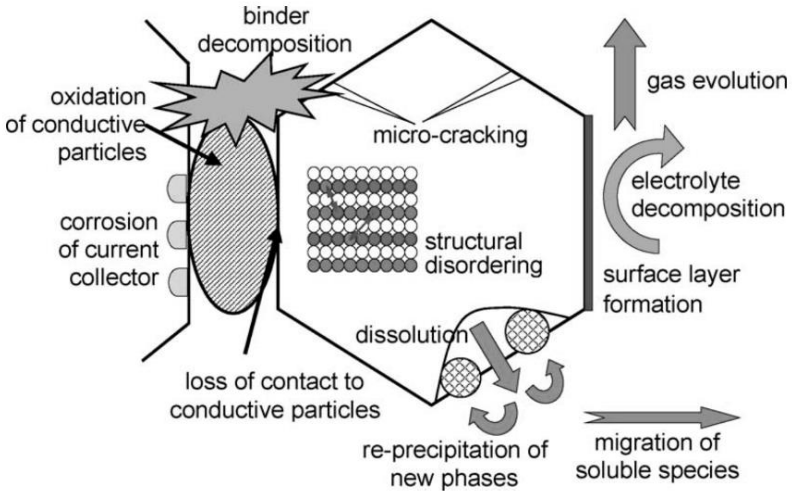


Figure 2.17 Illustration of ageing mechanism in cathode materials[119].

Ageing phenomenon is a complex effect that involves various electro-chemical and mechanical processes that occur at different scales and cannot be understood independently[119] as shown in Figure 2.17. The ageing process is likely to be associated with the structural modification of the electrodes during lithium (de)intercalation, particularly the cathode that constitutes the core component that determines the performance of the batteries in the lithium-layered oxide system.

The broad use of the term ‘ageing’ is sometimes equated with the ‘capacity fading’. To be precise, the capacity fading during further cycles is considered as one type of ageing mechanisms[119,120].

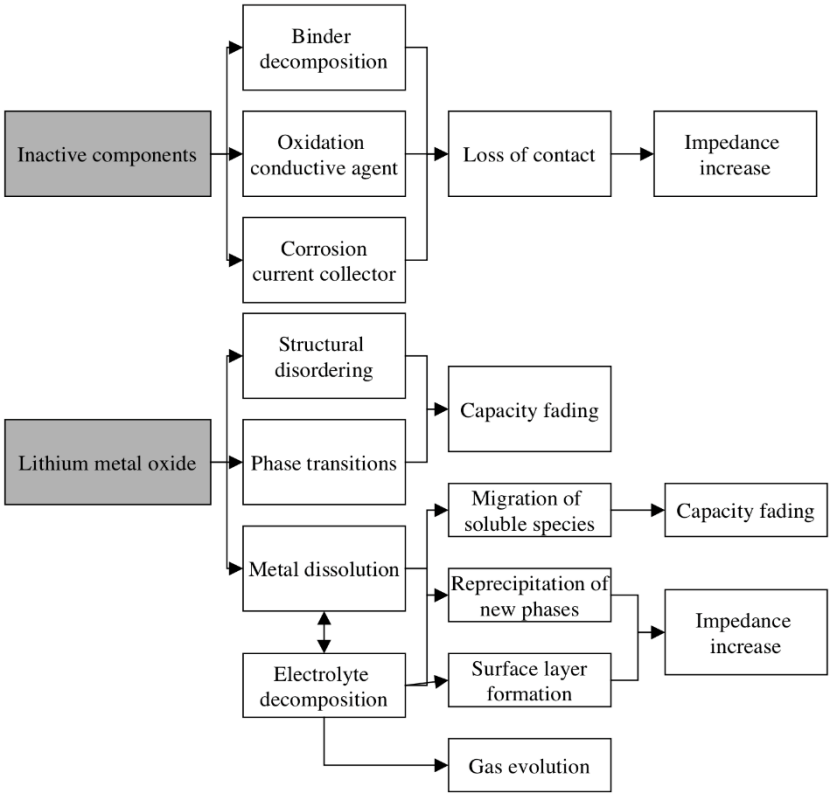


Figure 2.18 Some origins of battery ageing[120].

The general aspect of capacity fading at cathode materials can be divided into three main categories: (1) Structural modifications during electrochemical cycle, (2) Chemical decomposition reaction, and (3) Surface modification[120]. Figure 2.18 presents the possible causes of the capacity fading and impedance increase which leads to the power fading. Structural disordering and phase transitions in the lithium-metal oxide directly results in capacity fading of the battery. The condition of the cathode material is the crucial part that is linked to the lifespan of the battery. There are number of factors that can alter the native property of the cathode, these are: decomposition of the active material itself; degradation of electrode components (e.g. binder, conducting agents, and current collector); SEI formation; electrolyte oxidation; and by-products from chemical reactions at the anode.

2.6.2 Phase transition issue in Li-rich layered oxide cathode: layered into spinel structure

Layered-to-spinel phase transition during Li^+ (de)intercalation in the lithium-layered oxide cathode has been studied by Reed et al.[121]. The *ab initio* calculation in this study suggests a two-stage process which leads to the phase transition. The core of the transition is likely to be originated from the presence of Mn ions in the layered structure (trigonal, $R\bar{3}m$). The driving force that initiates the phase transition is the Jahn-Teller distortion from Mn reducing the layered symmetry into the monoclinic structure. Firstly, a number of Mn ions move to the adjacent tetrahedral sites into the inter slab which corresponds to the 16d position of the spinel. Secondly, a number of lithium ions move to the tetrahedral sites on the opposite part where the octahedral vacancies formed, and this would be correspond to the 8a positions of the spinel structure. A formation of the spinel structure will be completed by the coordinated rearrangement between the Mn ions in tetrahedral site and the remaining Li^+ in the octahedral site. Also, several studies[10,122–124] have revealed the empirical evidences of the layered-to-spinel phase transition in the lithium-rich layered oxide materials. Meng et al.[10] reported that the migration of the transition metals into the lithium-layer causes the transition to spinel phase of the $LiMO_2$ ($R\bar{3}m$) domain. On the other side, the origin of the phase transition to spinel on Li_2MnO_3 (C2/m) domain is attributed to the lithia (Li_2O) removal process which is associated with the generation of lattice strains in the host structure. Mohanty et al.[123] investigated the phase transition process in a $Li_{1.2}Co_{0.1}Mn_{0.55}Ni_{0.15}O_2$ cathode material by applying a constant voltage of 4.5 V during charge. The phase transition from the layered structure to spinel occurred even at a constant voltage. A recent study from Nayak et al.[124] confirms the layered-to-spinel phase transition on the $Li_2MnO_3{\cdot}LiNi_{1/3}Mn_{1/3}Co_{1/3}O_2$ cathode material with capacity fading and voltage decay during electrochemical cycle.

Chapter 3 X-ray Absorption Fine Structure (XAFS) Theory

3.1 Physics of X-ray Absorption Fine Structure (XAFS)

Since the discovery of X-ray by Röntgen in 1895, the first observation on the absorption edge was reported in 1913 by Maurice De Broglie. The first theory of X-ray absorption fine structure was suggested in 1931 by Kronig et al. describing electron scattering in the crystal lattice[125]. However, until the late 1960's, there was no more further progress in terms of establishing a correct theory for the XAFS. The theoretical questions about the XAFS could be solved due to the collaboration between Stern, Sayers, and Lytle in 1971[126]. They demonstrated also the practical use of the XAFS method in determining structural information. Owing to the development of the synchrotron radiation facility around 1970, the XAFS theory has evolved remarkably since 1970's.

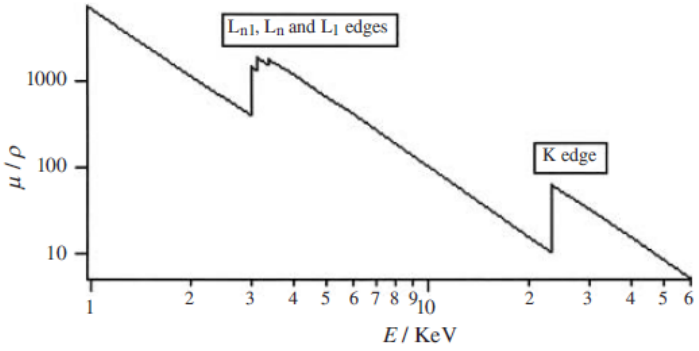


Figure 3.1 An abrupt increase in absorption edge at L_3, L_2, L_1, and K[127].

XAFS is a quantum mechanical phenomenon on the modulation of X-ray absorption probability in an atom by the photoelectric effect[110,128,129]. X-ray radiations are the electromagnetic waves with the energies between 100 eV and 300 keV. When a beam of light with a frequency higher than threshold (binding energy) is allowed to irradiate on an atom, electrons will be ejected from a low-lying orbitals (1*s*, 2*s* and $2p_{1/2}$) and the ejected photo-electron is produced with the kinetic energy that corresponds to the excess energy of the X-ray photon over the critical value

required for ionisation (Figure 3.2). As a consequence, an abrupt increase in absorption occurs when the incident X-ray has enough energy to promote a core-level electron into the continuum (or LUMO level).

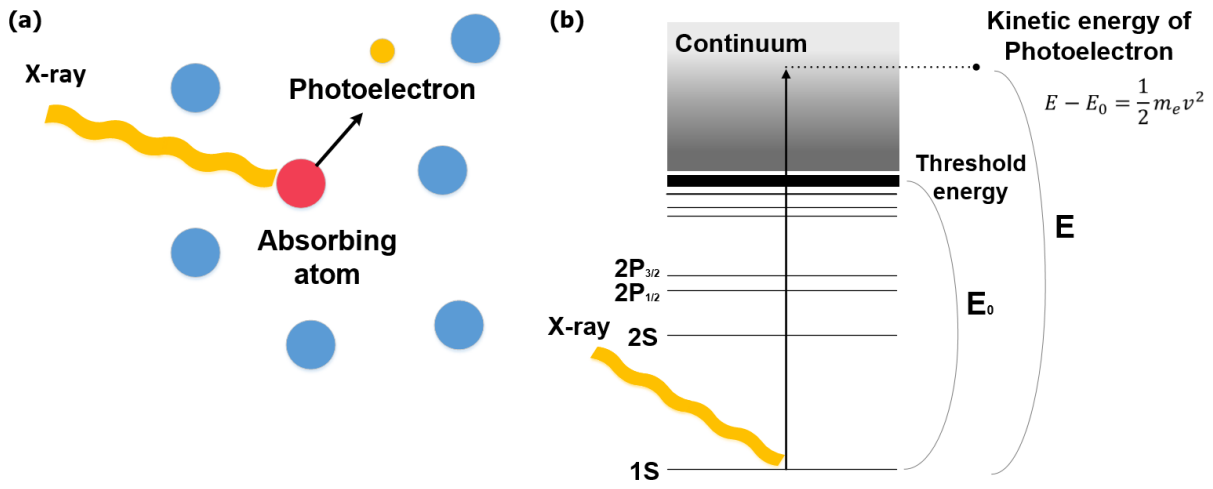


Figure 3.2 Photoelectric effect by X-ray absorption. (a) Release of photoelectron. (b) Energy level diagram with core electron orbitals. Kinetic energy of the photoelectron is given by $E\text{-}E_0$ where m_e is the mass of electron, E_0 the binding (ionization) energy, and v the velocity of electron.

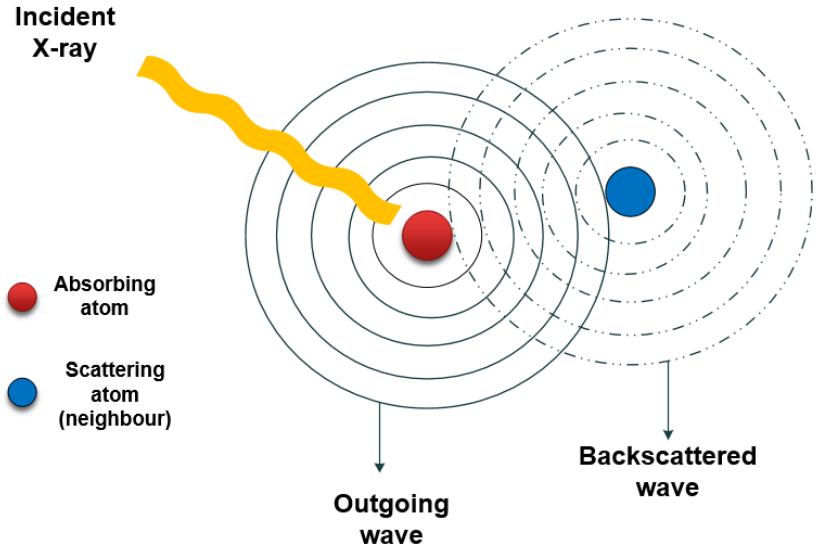


Figure 3.3 Presentation of atom scatterings.

This process is known as the photoelectric effect, which describes the absorption of a photon by an electron in a specific quantum level. For instance, the absorption edge attributed to the 1*s* to 3*d*

or 1*s* to 4*p* transitions corresponds to the K-edge, while the transitions from 2*s* or 2*p* to 3*d* corresponds to the L-edge (Figure 3.1). The wave nature of the photoelectrons is the key aspect of the XAFS theory. When the X-ray strikes an atom, wave scatters from the atom creating backscattering from the neighboring atom as illustrated in Figure 3.3. The interference between the wave scattering of absorbing atom and backscattering of neighboring atom leads to an energy dependent variation with the absorption coefficient (μ) on the quantum mechanical probability in the X-ray absorption. This absorption coefficient (μ) defines the fraction of the X-ray beam intensity that is lost when it passes through a material. Namely, the Beer-Lambert law describes the reduction of intensity from that of the incident beam (I_0) to that of the transmitted beam (I) upon passage through a sample of thickness x by the monochromatic X-ray according to the following equation:

$$\ln(\frac{I_o}{I}) = \mu x \qquad (3.1)$$

The linear absorption coefficient (μ) depends on the sample density (ρ), atomic number (Z), atomic mass (A), and the X-ray energy (E). The relationship can be approximately expressed by:

$$\mu \approx \frac{\rho Z^4}{AE^3} \qquad (3.2)$$

Since absorption is directly related to the re-emission of characteristic photons, the absorption coefficient (μ) can be measured not only in the transmission mode, but also by fluorescence.

The key principle of XAFS analysis is the collection of data on the absorption coefficient at specific X-ray photon energies, and subsequent interpretation of the data in terms of the energy level structure of an atom. The obtained data from the initial stage is the x-ray absorption spectrum with the energy involved. Generally, the XAFS spectrum is divided into X-ray absorption near edge structure (XANES) and extended X-ray absorption fine structure (EXAFS) regions. The physical origin of their spectra are fundamentally same, but the information they provide differs

with different theoretical approaches. Moreover, when we refer the XAFS as a utilization of experimental tool, it is preferred to use the term 'X-ray Absorption Spectroscopy (XAS)' in this thesis.

3.2 X-ray Absorption Near-edge Structure (XANES)

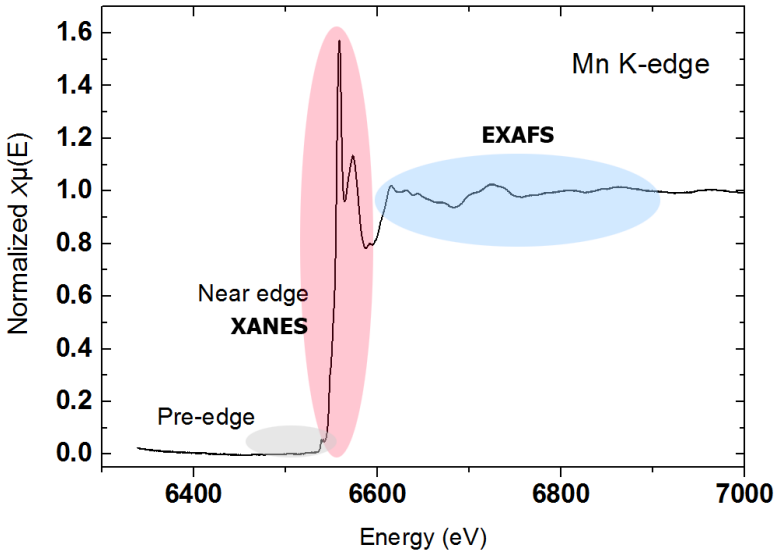


Figure 3.4 Normalised XAS spectra at Mn K-edge on pristine material of $Li[Li_{0.2}Mn_{0.54}Ni_{0.13}Co_{0.13}]O_2$ active material with XANES and EXAFS regimes in the X-ray absorption spectroscopy.

The X-ray absorption near-edge structure (XANES) is the region of XAS spectrum that lies 30~50 eV beyond the absorption edge[110,130], as presented in Figure 3.4. Information about the oxidation state, coordination chemistry, and molecular orbitals can be obtained from the XANES region[110,130]. The principle of XANES analysis is the consideration of multiple-scattering resonances of the photoelectrons which are ejected at low kinetic energies[110,128,130,131].

XANES is a reflection of the selective angular momentum in the unoccupied state, and it is generally described by the photo-absorption coefficient (μ_p) with a wavefunction of ψ_i at a given core state, according to the Fermi's Golden rule:

$$\mu_p \propto \sum_f \left|\langle\psi_f|e^{i\vec{k}\cdot\vec{r}}\cdot\hat{\boldsymbol{e}}\cdot\boldsymbol{U}|\psi_i\rangle\right|^2 \delta(\hbar\omega - E_f + E_i) \qquad (3.3)$$

where ψ_f indicates the wavefunction at the final state, $\hbar\omega$ is X-ray energy, E_i is the core level energy, E_f is the final state energy, k represents wavenumber vector and $\hat{\boldsymbol{e}}$ denotes the unit vector of the X-rays polarization direction. The sum of the linear momentum operators of each electron is denoted as $\boldsymbol{U}$. In case of XAS, the Fermi's Golden rule can be approximated by the standard quasi-particle theory as $\overrightarrow{k} \cdot \vec{r} << 1$ and $e^{i\overrightarrow{k}\cdot\vec{r}} \approx 1$ using one electron wavefunction as following[128]:

$$\mu_p \propto \sum_f \left|\langle \emptyset_f | \hat{\boldsymbol{e}} \cdot \boldsymbol{r} | \emptyset_i \rangle\right|^2 \delta(\hbar\omega - E_f + E_i) \tag{3.4}$$

$\boldsymbol{r}$ indicates the location where the excited electron exits. When we also consider the electric quadrupole term, equation (3.4) can be written as:

$$\mu_p \propto \sum_f \left|\langle \emptyset_f | \hat{\boldsymbol{e}} \cdot \boldsymbol{r} + \boldsymbol{i}(\hat{\boldsymbol{e}} \cdot \boldsymbol{r})(\vec{\boldsymbol{k}} \cdot \boldsymbol{r}) | \emptyset_i \rangle\right|^2 \delta(\hbar\omega - E_f + E_i) \tag{3.5}$$

The one-electron approximation provides the vital link to the electric dipole transition. The FEFF code for the XAFS interpretation is based on this approximation.

The primary contribution to the K-edge spectrum is attributed to the 1*s* → *np* transition, in which *np* signifies the lowest unoccupied *p* orbital. The 2*s* → *p* transition produces the L_1-edge, while the transition from *p* to *d* orbital results in L_2 and L_3 edges, respectively. This transition exhibits strong peaks due to the empty *d*-states. Therefore, XANES can be utilised simply as a fingerprint of oxidation state and phases by comparing with XANES spectra of reference samples. Small intensity peaks are often observed in the pre-edge region of XANES. The weak pre-edge peaks can be described using the bound state transition principle. In K-edge metals, theses peaks appear because of the 1*s* → 3*d* transition. Higher energy states must obey the 'dipole selection rule'. Electric dipole approximation in K-edge allows $\Delta l = \pm 1$. Those weak peaks associated with the 1*s* → 3*d* transition arise due to this transition being electric-dipole forbidden. The presence of those peaks is explained by the 3*d*-4*p* orbital mixing originating from non-centrosymmetric environment and quadrupolar coupling ($\Delta l = 0, \pm 2$). Intensity of the peak provides the information

about the atomic geometry and the associated degree of 3*d*-4*p* orbital mixing. Higher intensity implies more distorted condition compared to centrosymmetric environment. For instance, octahedral structure shows weaker pre-edge peaks, while tetrahedral exhibits higher pre-edge peaks. Multi-electron transition could be also observed in the XANES. This type of transition is called 'shake-up transition' as the term 'shaking' is used to signify the excessive energy that the X-ray can provide and thus excite an extra electron into the higher energy state of orbital. By contrast, there can occur also a 'shake-down transition' in the XANES due to the ligand-to-metal charge transfer (LMCT). It results in a lower energy than the direct transition. Since XANES is highly sensitive to the oxidation (valence) state and the symmetry of the absorber atom[110,130], it provides information about coordination chemistry, electronic structure, and multiple scattering even in a dilute and complicated system due to its intense signal[110,130,132]. The energy of the absorption edge shifts towards higher energy with higher oxidation state[110,133,134]. This shift can be readily distinguished and linked to positive charge changes in the atom[128,130]. In all atoms except hydrogen there is more than one electron orbiting the nucleus. Hence, the attraction between the positive charge of the nucleus and the photo-electron is not only the interaction that needs to be considered. Other electrons located at different shell orbitals within the atom exert repulsive forces on the outer electrons. This effect is called 'shielding effect'[134]. Since the higher oxidation state of the metal implies more positive overall charge of the atom, more energy is required in order to eject the target electron from its orbital. Owing to atomic shielding, the position of the absorption edge shifts when the oxidation state is changed.

3.3 Extended X-ray Absorption Fine Structure (EXAFS)

3.3.1 EXAFS oscillation

As illustrated in Figure 3.5, the oscillations observed above the edge are generally referred to as extended X-ray absorption fine structure (EXAFS). The oscillation is a direct consequence of the wave nature from the photoelectron. The photoelectron is produced by the absorption of energy from the X-ray photon. If the photon energy (E) is higher than the ionization energy (E_0), a photoelectron can be released from the absorbing atom.

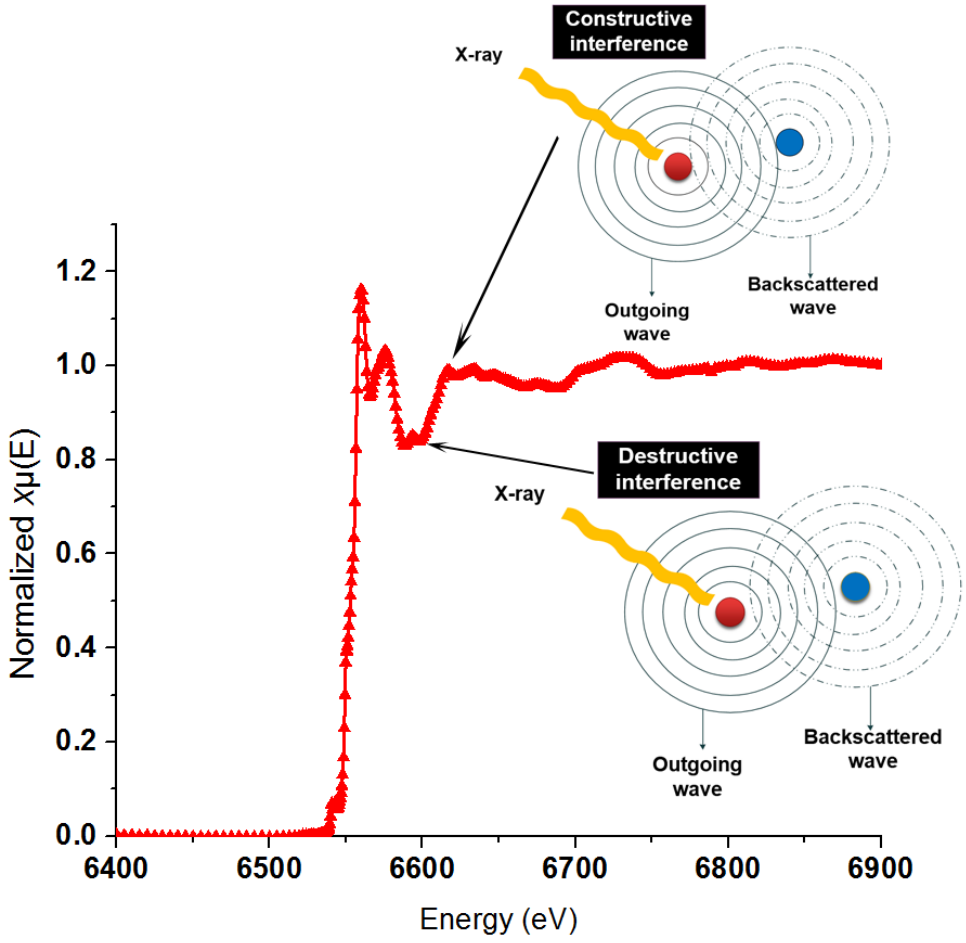


Figure 3.5 Schematics of EXAFS oscillation from wave inteferences.

The conservation of energy requires that the kinetic energy of the photoelectron be given as following (m_e: electron mass and v: velocity of the photoelectron):

$$(E - E_0) = \frac{1}{2}\mathrm{m_e}v^2 \qquad (3.6)$$

The EXAFS is better understood if the expression for the photoelectron wave vector (k) is used, as given by the de Broglie relation. The released photoelectron can be thought of as a spherical wave with wavelength λ in quantum mechanics as following:

$$\lambda = \frac{2\pi}{k} \qquad (3.7)$$

From the photoelectron kinetic energy expression (3.6) and the de Broglie relation ($\lambda = h/m_e v$), the expression for the wave vector can be written as (h: Planck constant):

$$k = \frac{2\pi}{h}\sqrt{2m_e(E - E_0)} \qquad (3.8)$$

A general expression for the EXAFS oscillation is defined by the fractional modulation in the absorption coefficient, which normalises the difference between the measured absorption coefficient ($\mu(k)$) and the free-atom absorption coefficient ($\mu_0(k)$) by the free-atom absorption coefficient, as given below:

$$x(k) = \frac{\mu(k) - \mu_0(k)}{\mu_0(k)} \qquad (3.9)$$

Equation (3.9) can be arranged as below:

$$\mu(k) = \mu_0(k)[1 + x(k)] \qquad (3.10)$$

3.3.2 Theoretical description of EXAFS equation

A formal description of EXAFS equation is suggested based on the 'Fermi's Golden Rule' which is identical to that used in XANES. The absorption coefficient (μ) is proportional to the transition between two quantum states, namely, the initial and final states of the electrons affected by the wave scattering interference (transition matrix element).

Scattering for a single atom can be defined as following:

$$x(k) = \frac{f(k)}{kR^2}\sin[2kR + \delta(k)] \qquad (3.11)$$

In practice, static disorders can be considered (attributed to the radial distribution of neighbours), as well as dynamic disorders from thermal vibration of the atoms. Therefore, the relationship is given by:

$$x(k) = \frac{Ne^{-2k^2\sigma^2} f(k)}{kR^2} \sin[2kR + \delta(k)] \tag{3.12}$$

where N is the coordination number and σ^2 is the mean-square displacement in the distance (R) of atomic bond. In a real system, there is usually more than one type of neighbouring atom around the absorbing atom. Hence, the quantitative EXAFS modulation $x(k)$ can be written as follows:

$$x(k) = \sum_j \frac{N_j f_j(k) e^{-2k^2\sigma_j^2}}{kR_j^2} \sin[2kR_j + \delta_j(k)] \tag{3.13}$$

where N_j indicates the number of equivalent backscattering (=coordination number) for the individual atoms(j) at a distance R_j from the absorbing atom. Here, the $e^{-2k^2\sigma_j^2}$ is known as the EXAFS Debye-Waller factor, which is directly associated with the mean-square displacement (σ^2). The displacement is likely to be attributed to the structural disorder of the atom or thermal vibrations. However, equation (3.13) doesn't consider the inelastic scattering effect from other objects such as conduction band electrons and phonons. Due to the inelastic scattering of the photoelectron, the back scattering towards the absorbing atom may not be accomplished. In order to take the impact from the inelastic scattering into consideration, a damped spherical wave function is adopted:

$$\psi(k, r) = \frac{e^{ikr} e^{-2r/\lambda(k)}}{kr} \tag{3.14}$$

Hence, equation (3.13) becomes (λ(k) is mean free path of the photoelectrons):

$$x(k) = \sum_j \frac{N_j f_j(k) e^{-2R_j/\lambda(k)} e^{-2k^2\sigma_j^2}}{kR_j^2} \sin[2kR_j + \delta_j(k)] \tag{3.15}$$

The last term that should be considered is the 'amplitude reduction factor (S_0^2)'. This term must be introduced due to the shake-up/shake-off process[128]. This process is caused by the excitation and relaxation of all the other electrons in the absorbing atom. Although EXAFS deals with a one-electron model, it is necessary to consider the secondary emission from the relaxation of one of the (*N-1*) remaining electrons when a core hole is created[128]. Finally, we obtain **the formal EXAFS equation** as following:

$$x(k) = \sum_j \frac{N_j S_0^2 f_j(k) e^{-2R_j/\lambda(k)} e^{-2k^2\sigma_j^2}}{kR_j^2} \sin[2kR_j + \delta_j(k)] \qquad (3.16)$$

A few physical conclusions arise from the formal EXAFS equation. Scattering properties ($f(k)$, $\delta_j(k)$) of the neighbouring atom together with the mean free path allow us to determine the coordination number (N) of the atom, distance to the neighbouring atom (R), and the mean-square disorder parameter (σ^2) of neighbouring distance. It should be also mentioned that the scattering amplitude ($f(k)$) and phase-shift ($\delta_j(k)$) factor are highly affected by the atomic number of the neighbouring atom, as well as that of the absorber.

3.4 XAFS interpretation method

3.4.1 EXAFS data reduction and modelling

The EXAFS interpretation process is presented in Figure 3.6. Simply, there are two main stages involved in the analysis of EXAFS data. The first stage is the reduction of the measured absorption spectra to EXAFS data format $x(k)$, independently of whether XAS was performed in transmission or fluorescence mode. The formal EXAFS equation can be applied after data reduction. Data reduction involves the normalization of the absorption spectra, and *k*-space conversion. The second stage is EXAFS data modelling (fitting), that ultimately allows to compute the structural parameters (e.g. N, R, and σ^2). This process involves the curve fitting that starts with

the known structural parameters generally obtained from powder diffraction. The collected XAS spectra must be converted to the absorption coefficient μ(E). Then, the pre-edge base profile should be subtracted to remove the background signals from the instrument or absorption from other edges (Figure 3.7a). This is followed by the XAS normalization process, which is a significant procedure that regularizes the obtained data that may vary between different experimental environments.

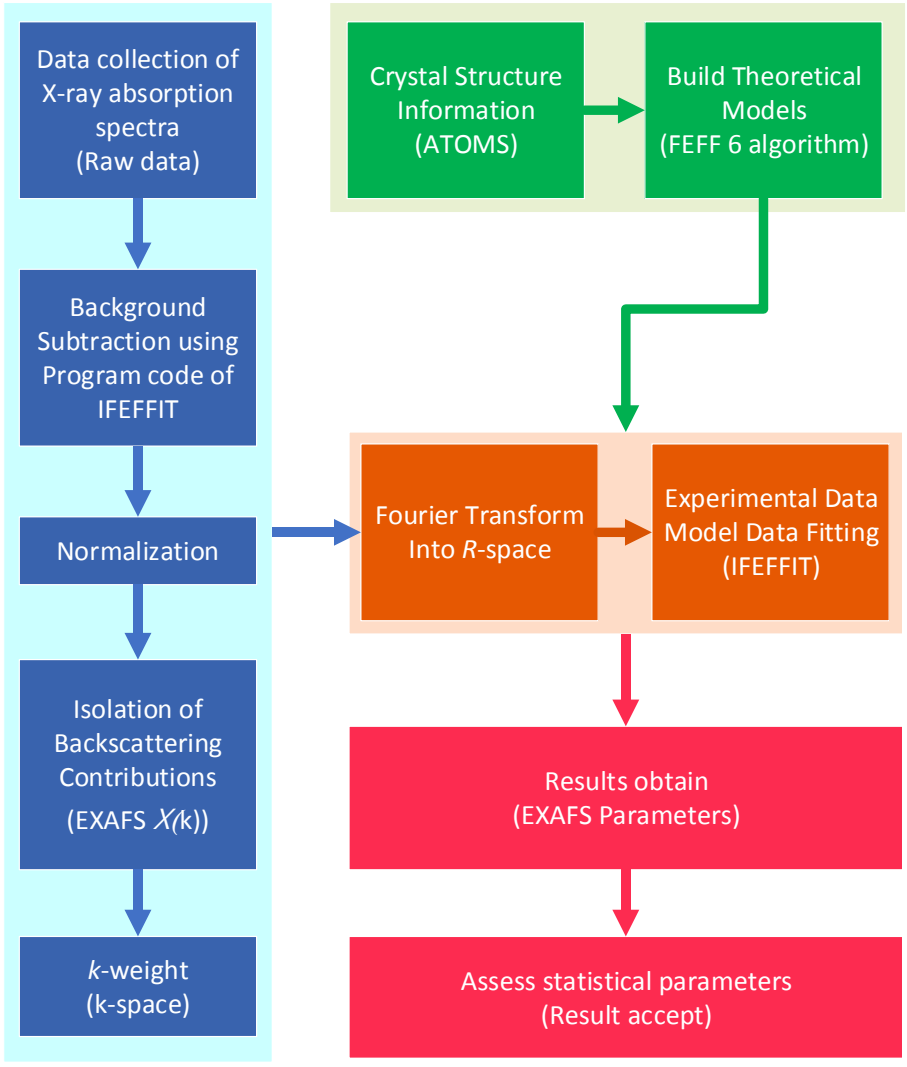


Figure 3.6 EXAFS fitting process with IFEFFIT (FEFF 6 algorithm).

To represent the unit absorption (1.0) of the X-ray, edge step normalization is generally utilised. An equation for the normalization can be given as following:

$$x(E) = \frac{\mu(E) - \mu_0(E)}{\Delta\mu_0(E)} \tag{3.17}$$

where $\mu(E)$ is the measure absorption coefficient, $\mu_0(E)$ is the background function, and $\Delta\mu_0(E)$ is the edge step. In order to approximate the $\mu_0(E)$, post-edge background function should be removed. The post-edge background is represented by a spline function that mostly corresponds to the low frequency of the absorption coefficient. The background function used in the application (ATHENA) is based on the AUTOBK algorithm. The normalization procedure is followed by the calculation of the edge energy (threshold energy: E_0) in order to convert the data from energy space to *k*-space. The relationship between energy space and *k*-space is presented in equation (3.5). The edge energy is generally measured by the inflection point of the energy curve. Therefore, the maximum peak in the first derivative of the absorption edge is defined as the edge energy. Figure 3.7b represents the converted EXAFS spectrum in the *k*-space.

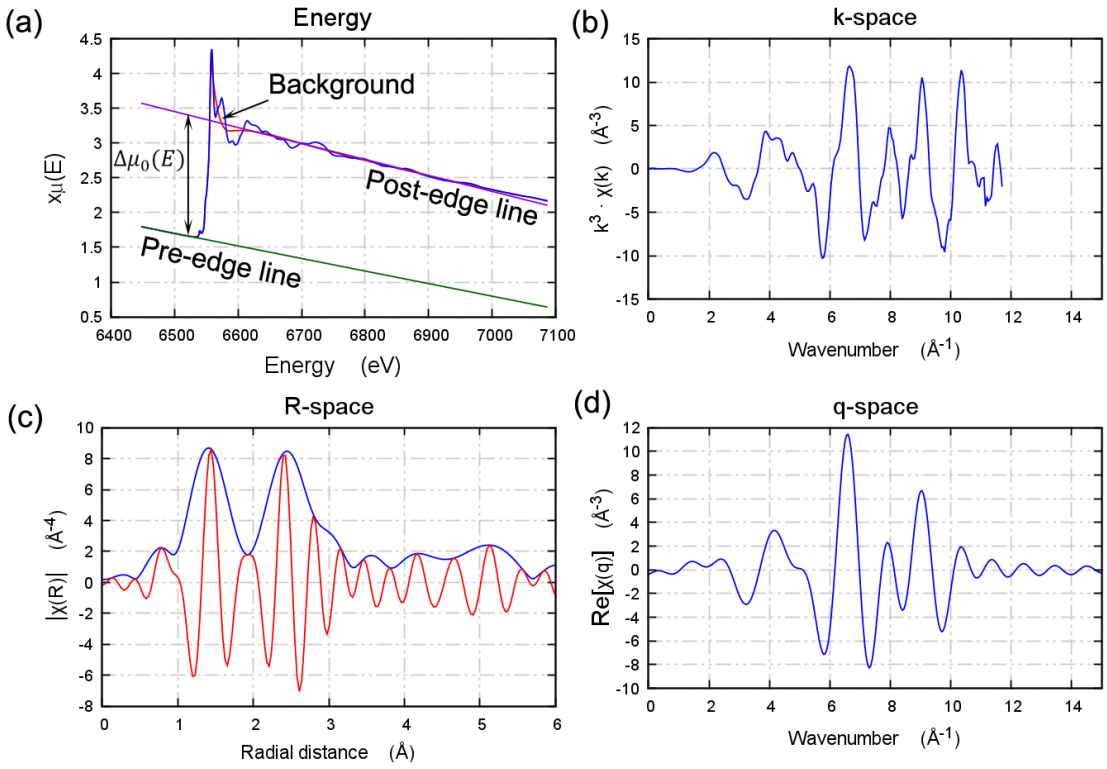


Figure 3.7 The absorption spectra data of NMC cathode at Mn K-edge (a) Raw data (b) k-space conversion (c) R-space conversion, and (d) Inverse transformed k-space (q-space).

The *k*-space representation is usually weighted by k^2 or k^3, in order to avoid decay of the oscillations and thus leading to better interpretation. Especially, this is useful to identify between high and low atomic number scatterers as the element with low atomic number will dominate the scattering at lower k-space values, while the element with high atomic number will mainly scatter at higher k-space values. The EXAFS oscillations can be completely described by the formal EXAFS equation. However, visualising this equation with the purpose of extracting structural information is not straightforward. For this reason, a frequency conversion algorithm is applied. Fourier transform gives structural parameters by decomposing the *k*-space signal into frequencies from different constituents. The decomposition allows distinguishing the frequency components of the signal. Sayers et al.[126] demonstrated that the Fourier transform of the EXAFS function *x(k)* gives a radial distribution function *x(R)* that represents the probability of finding other atoms at certain distances from the absorber atom. It should be mentioned that the amplitude obtained from the Fourier transform is ***not*** the actual radial distribution function, as it is difficult to establish a direct relationship with the electron density around the absorber atom due to the energy dependent phase-shift factor and scattering factor in the EXAFS equation. The Fourier transformation used here can be represented by the following equation:

$$FT(R) = \frac{1}{\sqrt{2\pi}} \int_{k_{\min}}^{k_{\max}} k^n x(k) e^{i2kR} dk \qquad (3.18)$$

Hence, the distance computed in Fourier transformation is around 0.2-0.5 Å shorter than the real distance[131]. The R-space plot obtained from the Fourier transformation of the EXAFS data in the *k*-space is a complex function including both imaginary and real components.

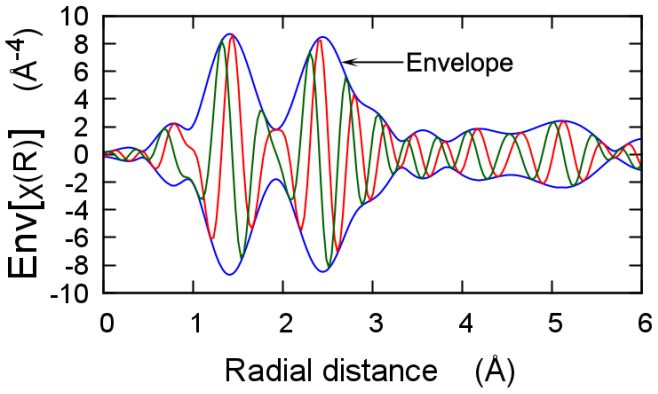


Figure 3.8 The envelope (blue) of the radial distribution function with real (red curve) and imaginary (green) parts of Mn K-edge in the NMC cathode. Fourier transformation is applied with k^3 weighting.

Figure 3.8 presents the envelope of the Fourier transformation of the Mn K-edge spectra. The envelope can be described by the following relationship:

$$Abs = \sqrt{\mathrm{Im}^2 + \mathrm{Re}^2} \tag{3.19}$$

where Re signifies the real part, whereas Im signifies the imaginary part of the signal.

It is mainly the number of neighbouring atoms and the disorder in their positions that determine the magnitude part in the R-space[131]. The imaginary part in the envelope can be used to determine the distance between the absorber and scattering element. The EXAFS modelling in this thesis is based on FEFF calculation that is generated by FEFF 6 algorithm with given crystal structures obtained from synchrotron X-ray diffractions

3.4.2 Statistics for EXAFS data analysis

EXAFS data analysis is a curve fitting process (refinement) to determine the structural parameters, such as the coordination number (N) of the neighbouring atom, distance to the neighbouring atom (R), and the mean-square disorder (σ^2) of the distance to neighbouring atoms. Fourier transformation allows choosing the most appropriate range of $x(k)$ based on the visual judgment for the refinement. The number of free (independent) parameters allowed in the refinement must be also considered[135]. For this purpose, the Nyquist Criterion is used as following:

$$Number\ of\ independent\ parameteres\ (N) = \frac{2\Delta k \Delta R}{\pi} + 2 \qquad (3.20)$$

where Δk is the range of k used for Fourier transform, and ΔR is the range of the evaluated fit in R-space. The Nyquist theorem is not a precise estimation since it mostly represents an upper bound of the actual information of the EXAFS data[131]. IFEFFIT is one of the popular application-engines that can be used in data the reduction and analysis process[136]. IFEFFIT uses a Levenberg-Marquardt non-linear least-squares algorithm, which interpolates between the Gauss-Newton algorithm and the method of gradient descent. IFEFFIT deals with a standard chi-squared (x^2) function which is an indicative of a good fitness[127], as follows:

$$\chi^2 = \frac{N_{idp}}{\epsilon N_{data}} \sum_{i=min}^{max} \{[Re(\chi_d(R_i) - \chi_t(R_i))]^2 + [Im(\chi_d(R_i) - \chi_t(R_i))]^2\} \qquad (3.21)$$

where ϵ is the measurement uncertainty, N_{data} the number of data points in the fitting range, and N_{idp} the number of independent points in the computation.('t' and 'd' denote experimental and model data, respectively). The provided model for the EXAFS fitting can be assessed by a reduced chi-square parameter (x_v^2) with the number of variables (N_{var}) used in the IFEFFIT application as below:

$$\chi_v^2 = \frac{\chi^2}{v} \qquad (3.22)$$

where $v\ (number\ of\ degree\ of\ freedom) = N_{idp} - N_{var}$.

EXAFS *R*-factor

In practice, the statistical criteria for validating the goodness of fit is the *R*-factor. It describes the misfit between the model and experimental data for the real (Re) and imaginary (Im) parts of the Fourier transform, and the acceptable value is approximately R-factor < 0.02 for a good fit.

$$R - factor = \sum_{i=1}^{N} \frac{\{[Re(\chi_d(R_i) - \chi_t(R_i))]^2 + [Im(\chi_d(R_i) - \chi_t(R_i))]^2\}}{\{[Re(\chi_d(R_i))]^2 + [Im(\chi_d(R_i)]^2\}} \qquad (3.23)$$

Chapter 4 Experimental Methods

4.1 Active material synthesis

4.1.1 Spray-dryer assisted sol-gel synthesis

The synthesis of the active material of $Li(Li_{0.2}Mn_{0.54}Ni_{0.13}Co_{0.13})O_2$ was conducted according to the spray-dryer assisted sol-gel method. Stoichiometric amounts of metal acetates of Mn, Ni, and Co (molar ratio Mn: Ni: Co = 0.54:0.13:0.13) were dissolved in a 200 mL aqueous solution of 0.32 M. The dissolved solution was slowly added into a solution (300 mL) of 3% excess amount of lithium acetate and citric acid (chelating agent) with the identical stoichiometry as the metal ions, with continuous stirring. A spray-dryer (YC-015, Shanghai Politech Instrument & Equipment Co. Ltd) was used to dry the obtained solution. Further drying was performed on the as-sprayed precursor at 80 °C overnight. This process was followed by the calcination at 800 °C for 15 h at a heating rate of 5 °C min^{-1} for the standard active material, while it was calcined at lower temperature (600 or 700 °C) to produce smaller particles sizes. The powders were cooled down in air after the calcination process.

4.1.2 Graphene coating by Hummers method

For the G-type samples, the graphene coating was carried out by a previous reported method[137]. Graphene oxide was prepared by a modified Hummers method[138] with the starting material of powdered flake graphite. The coating began by taking the 0.3g of pristine material into 30 mL polyallylamine hydrochloride (PAH) with continuous stirring for 1 hr. Then, the pristine powders were mixed in the 15 ml graphene oxide aqueous solution (2g/L) with continuous stirring for another 5 hr. This process was followed by the centrifugation, and the precipitated particles were rinsed three times with distill water. The rinsed particles were added into L-ascorbic acid (LAA) aqueous solution at 95 °C for 30 min with continuous stirring. Then, the synthesized powder was

dried at 80 °C overnight. In the final stage, the coated powder was heat treated at 250 °C or 350 °C for 2h.

4.1.3 Carbonate assisted co-precipitation method

The Cr substituted $Li(Li_{0.2}Mn_{0.54}Ni_{0.13}Co_{0.03}Cr_{0.10})O_2$ active material was prepared by the carbonate assisted co-precipitation method[139,140]. At first, a 0.2 M solution of $MnSO_4 \cdot H_2O$ (≥99%, Sigma-Aldrich), $NiSO_4 \cdot 7H_2O$ (99%, Sigma-Aldrich), $CoSO_4 \cdot 7H_2O$ (≥99%, Sigma-Aldrich) and $Cr(NO_3)_3 \cdot 9H_2O$ (99%, Sigma-Aldrich) (Mn : Ni : Co : Cr = 0.54 : 0.13 : 0.03 : 0.10) was made. Separately, a solution of 2.0 M NH_4HCO_3 (≥99.5%, Sigma-Aldrich) was also prepared. At second, the 0.2 M solution of metal-ions was slowly added, drop by drop, into the 2.0 M NH_4HCO_3 solution with continuous stirring (at 60°C with pH=8.0), so as to produce $(Mn_{0.54}Ni_{0.13}Co_{0.03}Cr_{0.10})(CO_3)_{0.13}$ precursor. After then, the carbonate precursor was precipitated using a centrifuge. This was followed by a rinsing process with distilled water. The rinsed precursor was dried overnight at 80°C. The dried powder was homogenously mixed with Li_2CO_3 (≥ 99%, Sigma-Aldrich) with 3% excess (molar ratio) in order to compensate the loss of lithium during the calcination process. This was followed by heat treating processes. Pre-heating was conducted at 600°C for 15 h with the heating rate of 5°C/min in order to decompose the carbonate. After then, a calcination was performed at 800°C for 15 h with the heating rate of 5°C/min to produce the final product $Li(Li_{0.2}Mn_{0.54}Ni_{0.13}Co_{0.03}Cr_{0.10})O_2$ cathode.

4.2 Cell design and electrochemical characterization

4.2.1 Cell design for *in operando* XAS study and cell assembling

A special design of *in operando* XAS cell was developed in order to examine the precise atomic environment during the electrochemical cycle, as illustrated in Figure 4.1. The novelty of this operando cell lies in the ability of correctly mimicking the environment on the commercially

available battery applications. A number of previous studies have employed reconstructed cell designs for the *in situ* investigations. However, those *in situ* cells are not only bulky, but also complicated and expensive to manufacture. Moreover, although they are well reconstructed for X-ray beam experiment, the internal environment is likely to be different from a commercial standard because of its manipulation.

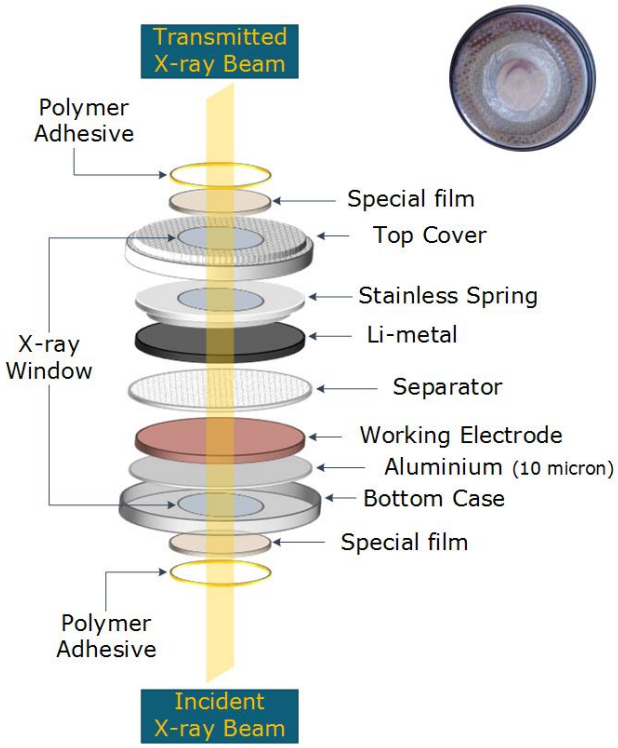


Figure 4.1 Schematics of the In Operando XAS cell design.

This may lead to a misunderstanding about the electrochemical reaction mechanism in actual battery operations. Owing to the XAS operando cells, some precise information about the atomic phase transition during charge-discharge could be examined. The specially-designed cells with X-ray windows were manufactured to perform the *in operando* test. The electrode slurry was prepared by mixing a pristine material or a graphene-coated $Li(Li_{0.2}Mn_{0.54}Ni_{0.13}Co_{0.13})O_2$, carbon black and polyvinylidene fluoride (PVDF) with the weight ratio of 80 : 10 : 10, respectively, in the n-methyl-2-pyrrolidone (NMP) solution. This was followed by constant stirring for overnight

to obtain homogenous dispersion. The prepared slurry was added onto an aluminium foil which was dried at 120°C for overnight, prior to the cutting into many pieces of working electrodes with ~12 mm diameter. The operando cells were assembled with the Li-foil (anode), working electrodes (cathode), and two pieces of separator (Celgard 2500). On both cases, a special Al-film was attached in order to increase the electrical conductivity. 1 M $LiPF_6$ in ethylene carbonate (EC): dimethyl carbonate (DEC) = 1:1 organic solution was used for the electrolyte. The dimension of the operando cells employed for the *in operando* XAS were 20 mm in diameter and 2.5 mm in thickness. The normal coin cells, as half cells, were produced with the same procedure (doctor-blade method) that of the operando cells, but without the x-ray window and special parts.



Figure 4.2 Active materials (left) and lithium-ion battery parts (right)

4.2.2 Galvanostatic measurement

The prepared cells were charged and discharged using a galvanostatic battery charger (NEWARE Battery Test Station) by recording the voltage as function of time (Figure 4.3). A constant-current mode was chosen to cycle the batteries. The galvanostatic experiment was conducted between 2.0-

4.8 V vs. Li^0/Li^+ at room temperature for the $Li(Li_{0.2}Mn_{0.54}Ni_{0.13}Co_{0.13})O_2$ based cells and 2.5-4.4 V vs. Li^0/Li^+ for the NMC cells. For the $Li(Li_{0.2}Mn_{0.54}Ni_{0.13}Co_{0.13})O_2$ active materials, 1C signifies 250 mA/g current density. A formation-cycle was applied with the rate of 0.05 C in prior to the main charge-discharge process for some samples in order to deeply activate the Li^+ (de)intercalation process. Diverse C-rates were used with the consideration of the experiment purpose. The rate was evaluated based on the weight of active materials. For example, as to the charge dynamic experiment, slow charge is defined as 0.125 C, while fast charge used the charge rate of 0.5 C. For a long-period cycles, a charge rate of 0.2 C was normally applied.

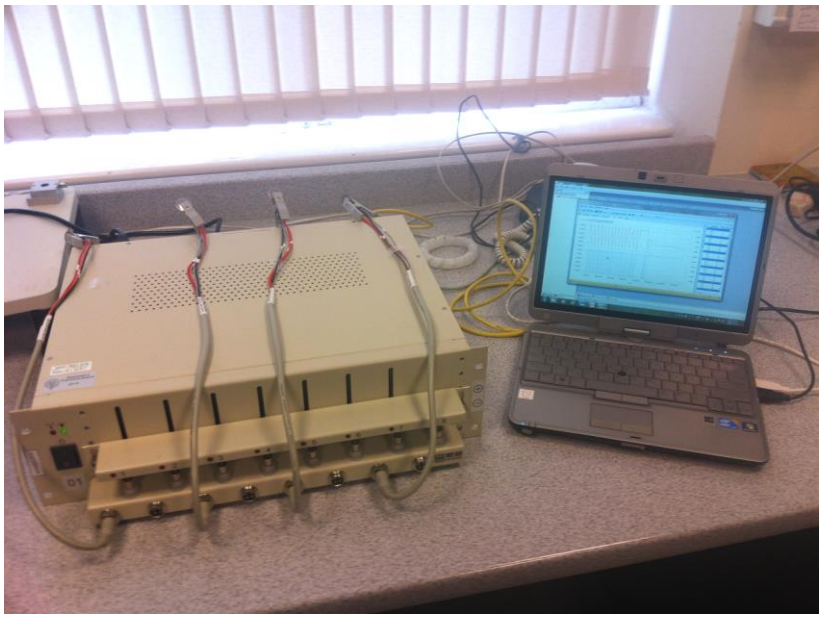


Figure 4.3 Galvanostatic charge-discharge with multi-channel wires.

4.2.3 Differential analysis (dQ/dV curve)

The voltage data from half-cell on electrodes provides useful information to identify phase transition during electrochemical cycles. Bloom et al.[141,142] has demonstrated the differential voltage method on lithium-ion batteries. In the half-cell electrodes, one can write the voltage of a cell as following:

$$V_{CELL} = V_{Cathode} - V_{Anode} \tag{4.1}$$

Hence, the dV/dQ can be expressed as:

$$\left(\frac{\mathrm{dV}}{dQ}\right)_{CELL} = \left(\frac{\mathrm{dV}}{dQ}\right)_{Cathode} - \left(\frac{\mathrm{dV}}{dQ}\right)_{Anode} \tag{4.2}$$

Equation (4.2) is the form of differential voltage. This is an expression that combined the individual contributions from cathode and anode, linearly. On the other hand, the reciprocal of the differential voltage can be written as:

$$\left(\frac{\mathrm{dQ}}{dV}\right)_{CELL} = \frac{1}{\left(\frac{\mathrm{dV}}{dQ}\right)_{Cathode} - \left(\frac{\mathrm{dV}}{dQ}\right)_{Anode}} \tag{4.3}$$

The dQ/dV (differential capacity) offers the information about the phase equilibria with the indication of redox reaction at the sharp peak[141]. In current study, the differential-capacity (dQ/dV) method was carried out on the galvanostatic data in order to identify the phase transitions of the cathode during electrochemical cycles. The sharp peaks in the differential-capacity curves indicate the redox reaction of the transition metals (Mn, Co, and Ni) at the electrodes.

4.3 Synchrotron X-ray Absorption Spectroscopy (XAS)

The synchrotron XAS/XRD experiments presented in this thesis were performed in SOLEIL (France) at DIFFABS beam-line (bending magnet, Si(111) double crystal monochromator (DCM), 3-23 keV), Diamond Light Source (UK) at B18 Core XAFS beam-line (bending magnet, Si(111) DCM, 2-20 keV), and Diamond Light Source (UK) at I18 beam-line (undulator, Si(111) double crystal monochromator (DCM), 2.05-20.5 keV). The specially designed coin cells with the X-ray transmission window were directly clamped to the galvanostatic charger with wires in order to perform the *in operando* XAS investigation. The electrochemical cell design is shown in Figure 4.1 (refer to section 4.2.1). The full description of the synchrotron method and X-ray Absorption Spectroscopy can be found in 'Chapter 3 X-ray Absorption Fine Structure (XAFS) Theory'.

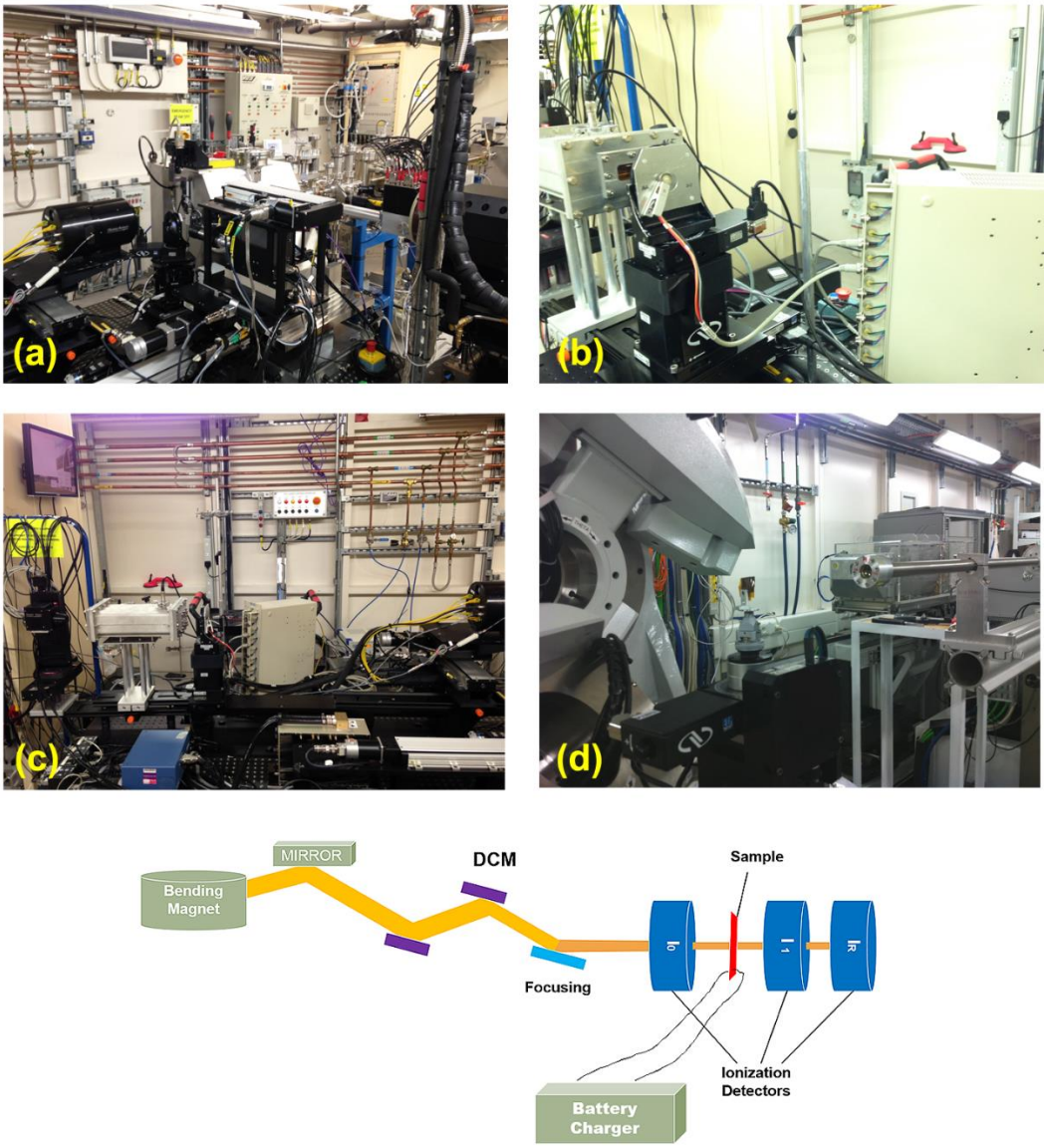


Figure 4.4 In Operando XAS setup with the electrochemical cells at synchrotron beamlines: Diamond Light Source (UK) (a) I18 (b) B18 (c) I18 and (d) SOLEIL DIFFABS (France). Illustration of the XAS experiment (bottom).

4.4 X-ray Diffraction (XRD) and Rietveld refinement

X-ray diffraction (XRD) is a precise and non-destructive method, allowing the detailed study of the crystal structure on the active material. A diffraction pattern can be obtained as a function of angle when the X-ray beam hit a crystalline sample of set of lattice planes. The diffraction condition must satisfy Bragg's law with known wavelength (or energy applied) as following:

$$n\lambda = 2d_{hkl}\sin\theta \quad (4.4)$$

where, λ is the wavelength of incident X-rays; d_{hkl} is the interplanar distance between lattice planes described by Miller indices, θ is the angle of incidence with the lattice planes (2θ:diffraction angle), and *n* is an integer which is the order of diffraction.

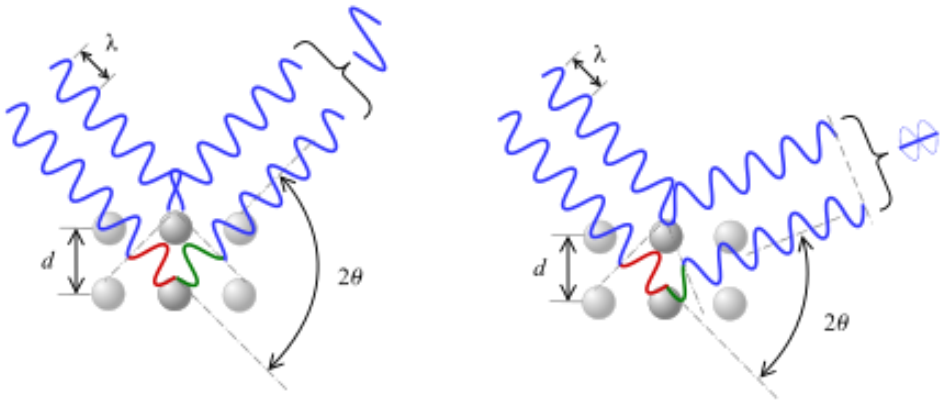


Figure 4.5 Presentation of Bragg diffraction on constructive interference (left) and destructive interference (right)[143].

The geometric relationships is illustrated in Figure 4.5. A direct correlation between the diffraction angle (2θ), lattice planes of (h k l), and crystal system can be established with plane-space equations. For instance, in a cubic system, the plane-space equation is given by:

$$\frac{1}{d^2} = \frac{(h^2 + k^2 + l^2)}{a^2} \quad (4.5)$$

By combining equation (3.24) and (3.22) with given wavelength of λ, it leads to the expression as following:

$$sin^2\theta = \frac{\lambda^2}{4a^2}(h^2 + k^2 + l^2) \quad (4.6)$$

Hence, the size and type of a unit cell can be determined from the diffraction patterns. The X-ray diffraction data on the lithium-ion battery cathodes were obtained from synchrotron (srXRD) experiments and thus sharp intensity peaks could be produced.

Rietveld Refinement

The Rietveld refinement[144] is a useful method for quantifying the structural information of the crystal lattice by considering the parameters associated with diffraction intensity. The underlying principle of the Rietveld refinement is the non-linear least squares minimization as following:

$$\phi = \sum_{i=1}^{n} w_i \, |I_i^E - I_i^C|^2 \tag{4.7}$$

where w_i is the weight parameter corresponds to the i^{th} step of the 2θ scale, I_i^E is the experimental intensity, and I_i^C is the calculated intensity which is given by:

$$I_i^C = \sum_{m=1}^{P} (s_m \sum_{s=1}^{K} L_s \left|F_{s,m}\right|^2 G_F(2\theta_i - 2\theta_{s,m}) O_{s,m} A_m) + Y_i^{bkg} \tag{4.8}$$

where s_m indicates a scale factor, L_s is the Lorentz-polarization coefficient, $F_{s,m}$ is the structure factor, $G_F(2\theta_i - 2\theta_{s,m})$ is the profile shape function, $O_{s,m}$ is the preferred orientations, A_m represents absorption correction, and Y_i^{bkg} accounts for the background intensity. 'P' and 'K' denotes number of phases and number of peaks, respectively. The Rietveld refinement was performed using the GSAS application to evaluate the crystal lattice parameters of the cathode materials. This information serves as a basis for the EXAFS fitting. The quality of the refinement is assessed by the weighted profile (R_{wp}):

$$R_{wp} = \sqrt{\frac{\sum w_i (y_i^{obs} - y_i^{cal})^2}{\sum w_i (y_i^{obs})^2}} \tag{4.9}$$

Similarly, the R value of Bragg-intensity (R_B) should be also considered with the R_{wp} evaluation, and the estimated R-values in the experiments were less than 4%.

4.5 RAMAN spectroscopy

When a light beam is passed through a medium (gas or liquid), it can be scattered either with the same frequency as the incident beam or with an altered frequency from the incident beam. The

scattering which appears with the altered frequency is called 'Raman effect', as an inelastic scattering, this effect is attributed to the energy exchange between the incident beam (photon) and the scattering molecule.

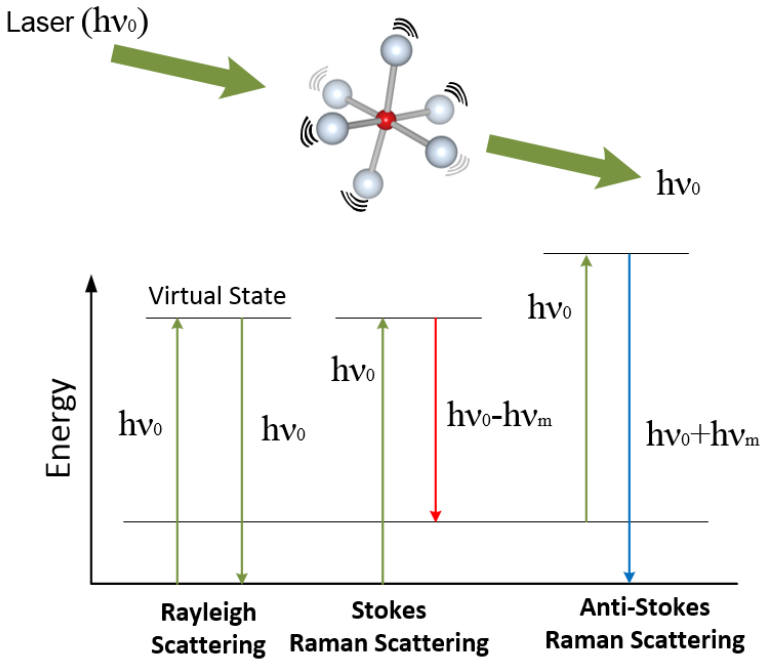


Figure 4.6 Illustration of Raman scattering concept.

An energy transfer from the photon to molecule results in the reduced energy in the scattered photon, while the energy transfer from the molecule to photon increase the energy of the scattered photon as shown in Figure 4.6. The former process is called 'Stokes Raman scattering', whereas the latter is called 'anti-Stokes Raman scattering'. The Raman spectroscopy is a type of vibrational spectroscopy which utilizes a laser source (normally a green type laser) to interact with molecules or excite photons, so as to investigate structural variation as well as the chemical fingerprints of the target material. The underlying principle of the Raman spectroscopy can be described by the classical electromagnetic field with the dipole moment ($\vec{\mu}$) induced by an electric field ($\vec{E}$). This is given by:

$$\vec{\mu} = \alpha \vec{E} \tag{4.10}$$

where constant α is the polarizability of the molecule. This constant represents how easily the electron cloud around the molecule would be distorted or electrons can be moved under the external electric field. It is the molecular vibration that change the polarizability and thus leads to the Raman scattering. Hence, to be a Raman active, anisotropic polarizability is required. This leads to the expression as following (Q_V is the normal vibrational coordinate):

$$\frac{d\alpha}{dQ_V} \neq 0 \tag{4.11}$$

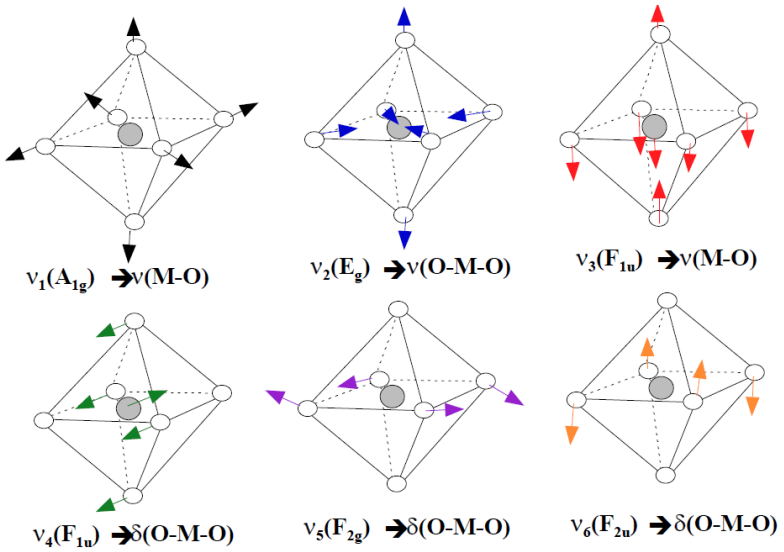


Figure 4.7 Raman (ν_1, ν_2, ν_5) and infrared (IR) activities of normal modes in the octahedral MO_6 molecules[145].

The Raman spectroscopy has been considered as a useful tool for characterizing Mn oxide-based compounds since it is highly sensitive to the state of metal oxides, i.e. diverse vibrational modes in the MnO_6 group[114,146]. It is therefore the Raman method is well-suited for the identification of the lattice vibrations in the electrode materials for lithium-ion batteries. Activity of the normal modes in the octahedral symmetry can be seen in Figure 4.7. For the active materials, in current study, Raman spectra were collected using a HORIBA LabRAM HR 800 Dual Microscope with a wavelength of 532 nm green laser as excitation source. Generally, a 50x lens was utilized with 4-5 times measurements for the samples.

4.6 SQUID magnetic measurement

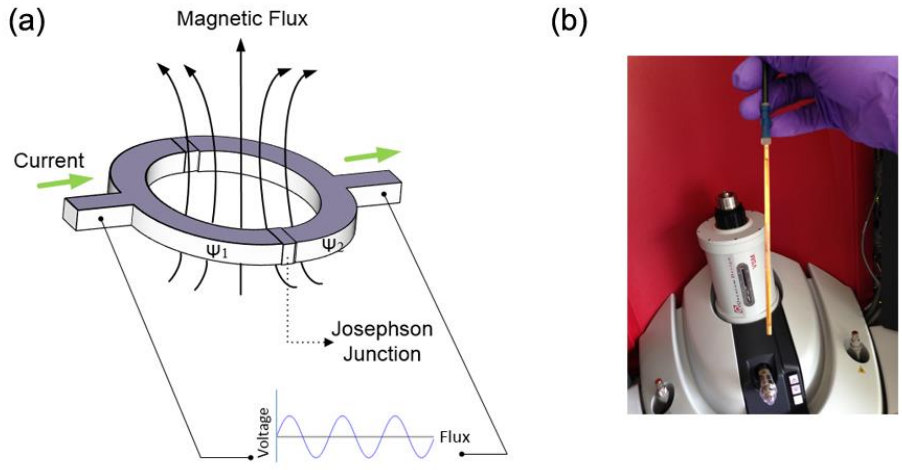


Figure 4.8 SQUID magnetometer (a) working principle and (b) sample installation.

The magnetic behaviour of the cathodes was investigated by a superconducting quantum interference device (SQUID). Quantization of magnetic flux is the core principle of the SQUID equipment. The device consist a pair of Josephson junctions separated by an insulating layer in a superconducting ring where currents flow depending on the magnetic flux (Figure 4.8). The practical quantization is based on the voltage measurement, not by the current, as the evaluation of voltage oscillations allows to measure the flux change. A working principle of the magnetometer can be described by the Josephson Effect using quantum mechanical wave functions. Eventually, the SQUID quantify the change of the voltages that correspond to the magnetic flux variations. The magnetic measurement not only gives the information about the magnetic behaviour, but also it provides insights into the electronic state in the pristine material. This serves as a supplementary analysis to the XANES investigations. In addition, a precise oxidation state could be evaluated due to the measurement of the reciprocal molar magnetic susceptibility (H/M). For the SQUID operation, a sample must be precisely weighted by a digital balance first. Then, it should be inserted in a capillary tube as a powder. This capillary was taken into a brass holder to preliminary adjust the location of the middle point where the powders are loaded. Finally, the brass holder

was inserted into the SQUID device (Figure 4.8b). Magnetic measurements of susceptibility and magnetization were performed with a SQUID-VSM Magnetometer (Quantum Design). Measurement of magnetization was performed under a magnetic field of 1000 Oe in the temperature range of 5 – 300 K. Magnetic field of 60k Oe was applied to the samples for the measurement of magnetic susceptibility at 5 K.

4.7 ATR-FTIR Spectroscopy

Similar to Raman spectroscopy, Fourier transform infrared (FTIR) spectroscopy is a suitable method to study the lattice dynamics of the transition metal oxides[146]. The difference between the FTIR and Raman spectroscopy is the nature of the molecular transitions. For Raman analysis, there should be a transition in the polarizability of the molecule while vibrating. However, for FTIR, a dipole moment transition in the molecule is the key for it to be infrared active. Thus, Raman spectroscopy and FTIR spectroscopy are complementary methods because of their different selection rule between quantum states. Attenuated total reflection (ATR)-FTIR is an infrared spectroscopy which utilized the Attenuated total reflection (ATR) sampling method. This method is able to investigate single or multiple layers of deposited/adsorbed chemical components both at solid and liquid. The ATR-FTIR benefits from the thin sampling path length and depth of penetration of the infrared beam. The IR beam in the ATR system is reflected internally through a crystal system creating an evanescent wave, whereas the general FTIR use the transmission beam (Figure 4.9). In the experiments, FTIR spectra for the electrode materials were collected using a ThermoScientific Nicolet Is10 FT-IR spectrometer equipped with an attenuated total reflectance (ATR) unit. The recording frequency range was 550 – 4000 cm^{-1} with a gain value of 2.0.

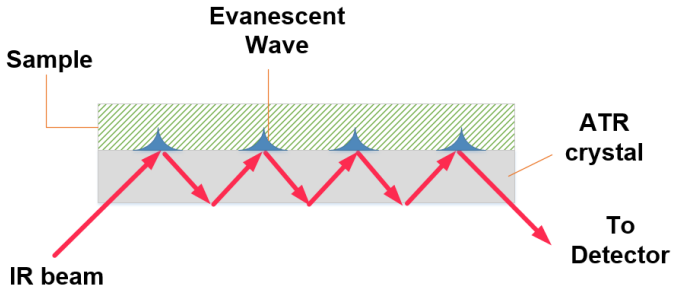


Figure 4.9 Schematics of Attenuated total reflection (ATR) principle.

4.8 Scanning Electron Microscopy (SEM) and Energy-dispersive X-ray spectroscopy (EDX)

The principle of the scanning electron microscope (SEM) can be described by a high-energy beam of electrons generated from a tungsten filament or similar sources. Electromagnetic lenses inside the SEM produce a thin beam of the electrons, so as to apply it for the surface scanning on the sample. The incident electrons will interact with the atoms of the specimen and thus leads to the emission of diverse electrons such as elastically scattered secondary electrons (SE), backscattered electrons (BSE), and photons. The SE and BSE signals are commonly used to visualize the electron images. Energy-dispersive X-ray spectroscopy (EDX) is a complementary analytical to SEM, and it is equipped with a sensitive X-ray detector (crystal type) which is placed to intercept X-ray emissions from the specimen. The crystal of the detector absorbs the energy from the X-ray ionization, producing free electrons. The absorption signal is converted into the electrical voltages, which correspond to the characteristic X-ray of the specimen. Hence, it allows to analyse the type of the element with quantification of elemental composition. The sampling depth is approximately 1-2 microns. In the current study, the morphology of the electrode materials were observed using JEOL JSM-6610LV SEM with Oxford Instruments EDX system. The active materials were coated with Platinum (Pt) using a Quorum Q150T ES sputter coater, in previous of the SEM analysis. EDX was also conducted in order to investigate the stoichiometry of the composites.

4.9 Continuous Cauchy Wavelet Transform (CCWT) analysis

The continuous Cauchy wavelet transform (CCWT)[147,148] is a computation method for visualizing the XAFS (EXAFS) signals in three-dimension with the wave-vector (k), the interatomic distance (uncorrected phase shift) in R-space, and the CCWT modulus which corresponds to the continuous decomposition of the amplitude term in the formal EXAFS equation. The visual inspection from this method provides some novel information about the local atomic phase in terms of the scattering contributions from the neighbouring atoms even in a complicated composite. The theoretical description of the CCWT can be deduced from a continuous wavelet transform with a XAFS oscillations of $\chi(k)$ as following:

$$W_{\psi}[\chi](b,a) = \langle \chi(k),\, \psi_{(b,a)}(k) \rangle = \frac{1}{a}\int_{-\infty}^{+\infty} \chi(k)\overline{\psi}(\frac{k-b}{a})\mathrm{dk} \qquad (4.12)$$

where $\langle \chi(k),\, \psi_{(b,a)}(k) \rangle$ indicates the scalar-product from EXAFS $\chi(k)$ and $\psi_{(b,a)}(k)$ function. The $\psi_{(b,a)}(k)$ represents the mother wavelet, and the parameter *a* corresponds to n/2R^*(R^* in R-space) and *b* indicates a k-vector value. The numerical computation is further processed with a fast Fourier transform algorithm and a series of mathematical calculation method[147]. The core expression of this wavelet transform can be described by the CCWT modulus as below:

$$\left|W_{\psi_n}[\chi]\right|(b, a = a_l(b)) \approx \frac{1}{2}\hat{\psi}_n(n)A_l(b) \qquad (4.13)$$

where each l^{th} ridge $a_l(b)$ is defined as $n/\phi'_l(b)$. Here, $\phi'_l(b)$ is the phase shift term in the formal EXAFS equation. In this present study, CCWT analyses were performed on the EXAFS spectrum which were k^3 or k^2-weighted using a Matlab code. A Hanning window (dk=1) function was chosen for the multiplication of the spectra data. The applied range in R-space was from 0.2 to 6.0, and the interval was set to 400, which is the scale parameter (a). Cauchy wavelet order (n) of 500, 150, and 250 were used for Mn, Co, and Ni K-edge EXAFS.

Chapter 5 The effect of doping and synthesis temperature on the structure and electrochemical performance of the Li-rich layered oxide cathode

In this chapter, a particular attention is devoted to the characterization of the active materials with different treatments applied for the battery improvement. The graphene-coating on the pristine $Li(Li_{0.2}Mn_{0.54}Ni_{0.13}Co_{0.13})O_2$ cathode is expected to improve the battery performance by increasing the electronic conductivity, while the Cr-substitution is considered to improve the battery stability by suppressing the voltage decay on charge-discharge. The effect of those treatments on the phase transition into the spinel is also explored. Another major purpose is the investigation on the formation of the integrated composite between Li_2MnO_3 (monoclinic, C2/m) and $LiMO_2$ (trigonal, $R\bar{3}m$) components. Those components are the key factors that determine the battery stability and performance in the Li-rich Mn-based oxide cathode system. The later part of this chapter deals with the impact on the structural formation upon different calcination temperatures during chemical synthesis.

5.1 Introduction

Li-rich layered transition metal oxides have shown notable performance over the conventional lithium-layered cathodes ($LiCoO_2$, $LiNiO_2$, NMC) owing to its structural nature, namely, the integrated-composite system of $x\mathrm{Li_2MnO_3} \cdot (1-x)\mathrm{LiMO_2}(\mathrm{M} = \mathrm{Mn, Ni, Co})$ allows to achieve superior specific capacity (> 200 $mAhg^{-1}$) with high chemical potential (> 4.6 V vs Li^0)[2–4]. As such, they are considered as a promising electrode to fulfill the demands for the portable energy sources in electric vehicles. However, this type of battery system suffers from the irreversible capacity loss of 40-100 $mAhg^{-1}$ during the first electrochemical cycle, as well as the voltage decay/capacity fading on further cycles[7,122,124,149]. There have been intensive efforts to improve the limitations of

the cathode by doping or coating the electrode surface or incorporating mixed transition metals in the active material. For example, recently, the graphene coating on the Li-layered oxide cathode has emerged as an attractive treatment owing to its high electronic conductivity, large surface-to-volume ratio, and good chemical stability of graphene and thus leads to enhanced battery capacity during consecutive cycles[150–155]. Graphene is a single carbon layer material in which the atoms hybridized in the sp^2 state forming hexagonal patterns. This structural property enables the effective conducting network for Li^+ diffusion (as high as 4.4 x 10^{-6} cm^2s^{-1})[156] and electron transport in the electrode[150]. Another example of the improvement method is the chromium (Cr) substitution in the mixed transition metal component. Cr-substitution has been proposed to improve the stability of the oxide ion framework of the lithium-rich layered oxide cathode owing to its ability to suppress the oxygen loss during charge[97]. In addition, the diverse oxidation state of Cr^{3+}/Cr^{6+} contributes not only to the charge compensation mechanism, but also to the stabilization of the host structure at a particular oxidation state[157,158]. The formation of the integrated components between xLi_2MnO_3 and $(1-x)\cdot LiMO_2$ is likely to be affected by material synthesis condition. Long et al.[71] investigated the effect of cooling rates on phase separation in the Li-rich layered oxide cathode. In his study, the cooling rate seems to be not the major factor that affects the composite, but two-phase separation was identified regardless of the cooling rate. On the other hand, calcination temperature is a vital factor that determines the size of the electrode particles and thus has a direct relationship to the electrochemical performance[102].

In the present section, investigations were conducted on the Li-rich Mn-based oxide active material of pristine $Li(Li_{0.2}Mn_{0.54}Ni_{0.13}Co_{0.13})O_2$, graphene-coated $Li(Li_{0.2}Mn_{0.54}Ni_{0.13}Co_{0.13})O_2$, and Cr-substituted $Li(Li_{0.2}Mn_{0.54}Ni_{0.13}Co_{0.03}Cr_{0.10})O_2$ cathodes. The purpose of this study is to gain insight into the nature of the integrated-composite system of $xLi_2MnO_3 \cdot (1-x)LiMO_2 (M = Mn, Ni, Co)$. Also, it will be our purpose here to consider the electrochemical property of the

lithium-ion battery that contains the prepared active materials. In addition, the electrochemical activity of the Li_2MnO_3 component was examined. A differential capacity analysis (dQ/dV plot) method on the galvanostatic profile was chosen in order to investigate the redox reaction linked to the phase transition during electrochemical cycles. The formation of the integrated components between Li_2MnO_3 (monoclinic, C2/m) and $LiMO_2$ (trigonal, $R\bar{3}m$) was investigated by the X-ray diffraction (XRD), Rietveld refinement, Raman spectroscopy, Attenuated total reflection-Fourier transform infrared (ATR-FTIR) spectroscopy and SEM with EDX. The magnetic properties were also measured using Superconducting Quantum Interference Device (SQUID) in order to evaluate the precise oxidation states of the transition metals in the composite, as well as to confirm the presence of the Ni^+ ions in the Li-layers (interslab). To assess the local atomic environment of Mn, Co, and Ni in the composite, a synchrotron XAS was conducted on the cathode materials. Structural environment was quantified with the help of the Extended X-ray Absorption Fine Structure (EXAFS). Similarity in the local environment and oxidation state of the transition metals were estimated by X-ray absorption near-edge structure (XANES). In the last part, we demonstrate a systematic investigation in the impact of the synthesis (calcination) temperatures (600, 700, 800, and 1000 °C) on the formation of the integrated composite.

5.2 Experimental Section

5.2.1 Active material synthesis

The synthesis of the active material of $Li(Li_{0.2}Mn_{0.54}Ni_{0.13}Co_{0.13})O_2$ was performed by the spray-dryer assisted sol-gel method. Stoichiometric amounts of metal acetates of Mn, Ni, and Co (molar ratio Mn: Ni: Co = 0.54:0.13:0.13) were added in a 200 mL aqueous solution of 0.32 M. With continuous stirring, the dissolved solution was slowly mixed into a solution (300 mL) of 3% excess amount of lithium acetate and citric acid (chelating agent) with the identical stoichiometry as the

metal ions. A spray-dryer (YC-015, Shanghai Politech Instrument & Equipment Co. Ltd) was used in order to dry the obtained solution. Further drying was conducted on the as-sprayed precursor at 80 °C overnight. The spray-drying was followed by the calcination at 600, 700, 800, and 1000 °C for P-600, P-700, P-800 (P-type), and P-1000 samples, respectively, for 15 h at a heating rate of 5 °C min^{-1}.

The graphene-coating on the pristine material was carried out by a previous reported method[153]. Graphene oxide was produced from a modified Hummers method with the starting material of powdered flake graphite[138]. The coating was performed by adding the 0.3g of pristine material into 30 mL polyallylamine hydrochloride (PAH) with continuous stirring for 1 hr. This was followed by the addition of the pristine powders in the 15 ml graphene oxide aqueous solution (2g/L) with continuous stirring for another 5 hr. After then, the solution was centrifuged, and the precipitated particles were cleaned three times with distill water. The cleaned particles were mixed into L-ascorbic acid (LAA) aqueous solution at 95 °C for 30 min with continuous stirring. It followed by the overnight drying (80 °C) on the synthesized powder. Finally, the coated powder was heat treated at 250 °C or 350 °C for 2h. The graphene-coated $Li(Li_{0.2}Mn_{0.54}Ni_{0.13}Co_{0.13})O_2$ composite is denoted as 'G-type' sample.

The Cr substituted $Li(Li_{0.2}Mn_{0.54}Ni_{0.13}Co_{0.03}Cr_{0.10})O_2$ active material was prepared by the carbonate assisted co-precipitation method [139,140]. At first, a 0.2 M solution of $MnSO_4 \cdot H_2O$ (≥99%, Sigma-Aldrich), $NiSO_4 \cdot 7H_2O$ (99%, Sigma-Aldrich), $CoSO_4 \cdot 7H_2O$ (≥99%, Sigma-Aldrich) and $Cr(NO_3)_3 \cdot 9H_2O$ (99%, Sigma-Aldrich) (Mn : Ni : Co : Cr = 0.54 : 0.13 : 0.03 : 0.10) was made. Separately, a solution of 2.0 M NH_4HCO_3 (≥99.5%, Sigma-Aldrich) was also prepared. At second, the solution with metal-ions was slowly added, drop by drop, into the 2.0 M NH_4HCO_3 solution with continuous stirring (at 60°C with pH=8.0), so as to produce $(Mn_{0.54}Ni_{0.13}Co_{0.03}Cr_{0.10})(CO_3)_{0.13}$ precursor. After then, the carbonate precursor was precipitated using a centrifuge. This was

followed by rinsing process with distilled water. The rinsed precursor was dried overnight at 80°C. The dried powder was homogenously mixed with Li_2CO_3 (≥99%, Sigma-Aldrich) with 3% excess (molar ratio) in order to compensate the loss of lithium during the calcination process. This was followed by heat treating processes. Pre-heating was conducted at 600◦C for 15 h with the heating rate of 5°C/min in order to decompose the carbonate. After then, a calcination was performed at 800°C for 15 h with the heating rate of 5°C/min to produce the final product of $Li(Li_{0.2}Mn_{0.54}Ni_{0.13}Co_{0.03}Cr_{0.10})O_2$ cathode (denoted as 'C-type').

5.2.2 Electrochemical characterization

The electrode slurry was prepared by mixing the graphene-coated $Li(Li_{0.2}Mn_{0.54}Ni_{0.13}Co_{0.13})O_2$ into the carbon black and polyvinylidene fluoride (PVDF) with the weight ratio of 80 : 10 : 10, respectively, in the n-methyl-2-pyrrolidone (NMP) solution. The electrode slurry was constantly stirred for overnight to obtain homogenous dispersion. This was followed by the pasting onto an aluminium foil. The pasted foil was dried at 120°C for overnight. Thereafter, they were cut into many pieces of working electrodes with 12 mm diameter. The coin cell was assembled with the working electrodes (cathode), Li-foil (anode), two pieces of separator (Celgard 2500) and special conduction films on the X-ray window in a glove box filled with argon. An organic solution of 1 M $LiPF_6$ dissolved in the ethylene carbonate (EC) and diethyl carbonate (DEC) (volume ratio of EC:DEC = 1:1) was used as the electrolyte. The diameter and thickness of the coin cells were measured to be 20 mm and 2.5 mm, respectively. Coin cells were electrochemically cycled in the voltage range between 2.0 V and 4.8 V vs. Li^0/Li^+ using a galvanostatic charger. G-type (active material: 12.01 mg) and P-type (active material: 10.03 mg) coin cells were electrochemically cycled up to 30 cycles with the current rate of 0.2 C. The C-type (active material: 10.90 mg) and Li_2MnO_3 (active material: 5.13 mg) coin cells were firstly cycled with the current rate of 0.05 C (formation cycle) up to 2 cycles, and then they were cycled with the current rate of 0.2 C until the

50th cycle. The differential capacity analysis (dQ/dV plot) was performed on the galvanostatic profile for each coin cell to monitor the redox reactions on charge-discharge.

5.2.3 Active material characterization

SEM image on the active material was collected using JEOL JSM-6610 LV SEM. By using a HORIBA LabRAM HR 800 Dual Microscope, Raman spectra on the active material were collected with a wavelength of 532 nm green laser as excitation source. A 50x lens was used to identify the measurement points (4-5 points) on the composite. FTIR spectra were collected using a ThermoScientific Nicolet Is10 FT-IR spectrometer equipped with an attenuated total reflectance (ATR) unit. The recording frequency range was 550 – 4000 cm^{-1} with a gain value of 2.0. X-ray powder diffraction was carried out on the active materials with the X-ray photon energy of 11.0 keV (λ=1.127 Å) for P/G-type cathode and λ=0.825985 Å for C-type. Magnetic property investigation was carried out using a SQUID-VSM Magnetometer (Quantum Design). Magnetic field of 60k Oe (at 5 K) was applied in order to evaluate the magnetic susceptibility (H/M). Measurement of magnetization (M) was conducted with a magnetic field of 1000 Oe in the temperature range of 5 – 300 K.

5.2.4 Synchrotron XAS experiment/interpretation

The synchrotron XAS experiment was carried out on B18 Core EXAFS beamline at Diamond Light Source (DLS, UK). XAS spectra were collected in transmission mode at the Mn (6.537 keV), Co (7.712 keV), and Ni (8.339 keV) K-edges with a Si (111) double crystal monochromator at room temperature. The size of the beam-spot on the X-ray window was recorded to be ~140 x 140 microns. For Mn, Co, and Ni K-edge analysis, the photon energy was tuned to 7.1 keV, 8.225 keV, and 9.3 keV, respectively. Data interpretation was performed with a IFEFFIT computation code using the ATHENA[159] PC application package. The obtained XAS spectra were normalized, and

then the EXAFS spectra were converted from energy into frequency in *k*-space, with k^3-weighting to emphasize the oscillations in the high k-value ($k^3\chi(k)$). To evaluate the radial distance to the neighbouring atoms, the EXAFS oscillations (k-space) were Fourier transformed into the R-space. Major parameters such as the distance between the neighbouring shells (R), amplitude reduction factor (S_0^2), EXAFS Debye–Waller factor ($\exp(-2\sigma^2k^2)$), energy shift (ΔE_0), and the EXAFS *R*-factor (statistical purpose) were evaluated by fitting within the ARTEMIS application. The EXAFS fitting was processed according to the FEFF 6 algorithm with atomic coordination number (CN) of 6 for Mn and Co transition metals. After a preliminary refinement, the amplitude reduction factor (S_0^2) was scaled to 0.65, 0.67, and 0.88 for Mn, Co, and Ni, respectively. The EXAFS least square fits were performed based on two-phase composite system. The fitting range of the R-space was 1-3.65 Å for Mn, Co, and Ni.

5.3 Results and Discussion

5.3.1 Electrochemical properties of P/G/C-type lithium-ion batteries

Figure 5.1 compares the electrochemical property of the pristine $Li(Li_{0.2}Mn_{0.54}Ni_{0.13}Co_{0.13})O_2$ cathode (P-type) up to 30th cycle. During the initial charge, a large voltage plateau could be observed from ~4.5 V (Figure 5.1a). The generated capacity between 3.0 V and 4.5 V is likely to be attributed to the $LiMO_2$ component, whereas the capacity from 4.5 V and 4.8 V is associated with the Li_2MnO_3 component. However, the voltage plateau didn't appear on further cycles, and this leads to the large irreversible capacity loss showing low Coulombic efficiency (%) at initial cycle (Figure 5.1b). Figure 5.1c,d exhibits the dQ/dV plots on the battery cathode. The dQ/dV analysis is a useful method to investigate the redox reaction during electrochemical cycles and thus provides some information about phase transition in the cathode material. A large peak (O_c) was shown at ~4.5 V during the initial charge (Figure 5.1c). This peak can be explained by the Li^+

deintercalation as a lithia (Li_2O) formation from the Li_2MnO_3 component, which results in an irreversible oxygen loss from the lattice[2,3,7,8,78].

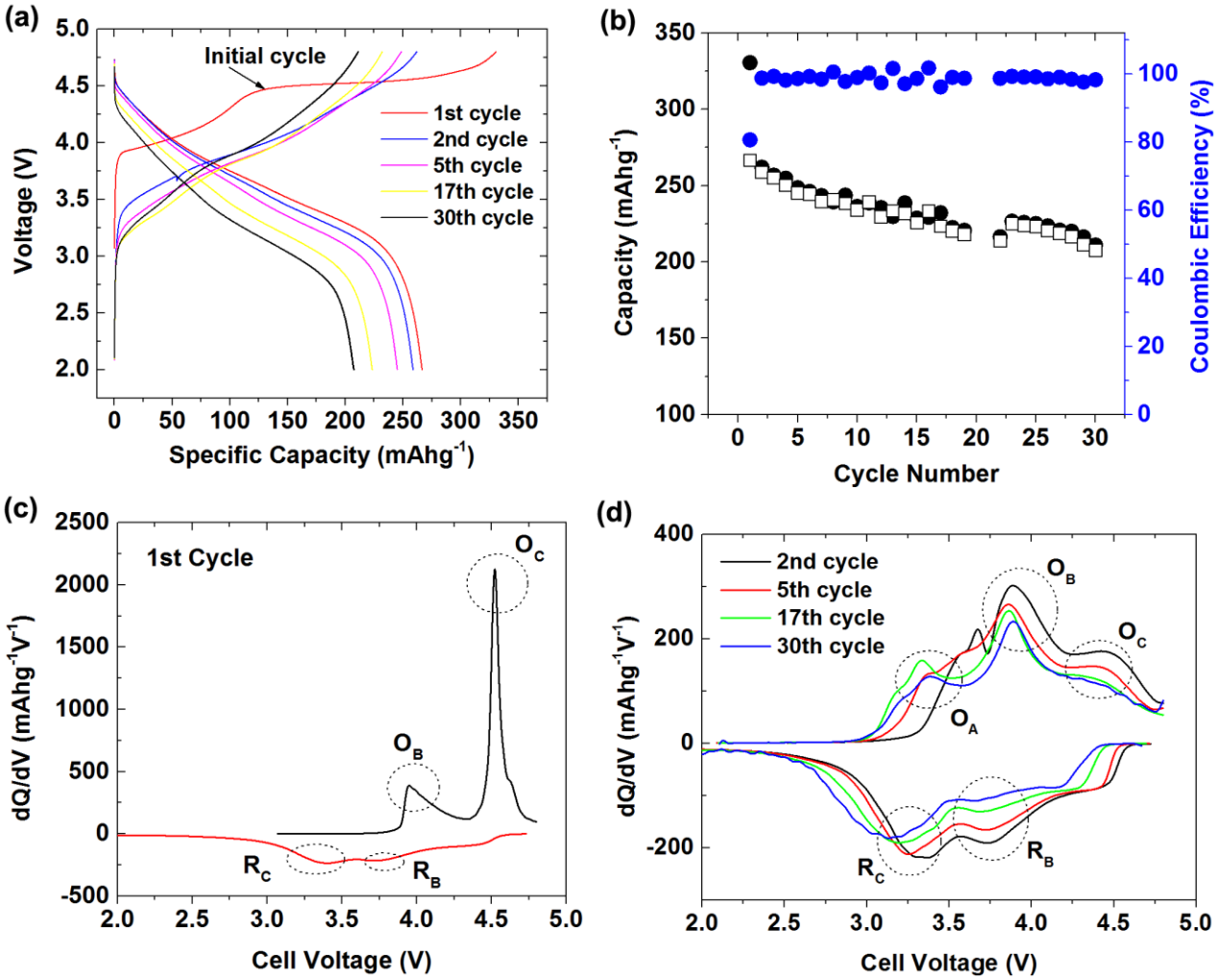


Figure 5.1 Electrochemical property of pristine $Li(Li_{0.2}Mn_{0.54}Ni_{0.13}Co_{0.13})O_2$ cathode (P-type). (a) Galvanostatic profile up to 30th cycle with current rate of 0.2 C. (b) Specific charge (black circle) and discharge capacity (white square) with Coulombic efficiency (%). (c) dQ/dV plot of initial cycle. (d) dQ/dV plots on furher cycles.

As a consequence, a layered MnO_2 component would be produced with the removal of the lithia ($Li_2MnO_3 \rightarrow Li_2O + MnO_2$). On the other hand, those peaks denoted as O_B and R_B are attributed to the the redox reaction of Ni^{2+}/ Ni^{3+}/Ni^{4+} and Co^{3+}/Co^{4+} in the layered $LiMO_2$ (M=Mn, Co, and Ni)[2,79–81]. The peak at R_C is probably due to the redox reaction of Mn^{4+}/$Mn^{(4-x)+}$ in $LiMnO_2$ and MnO_2-rich domains[2,8,82]. O_A is another significant peak which is responsible for the formation of

cubic spinel-like phase in the composite[84]. As shown in the dQ/dV plot, the variation in the dQ/dV curves became stable from 17th cycle.

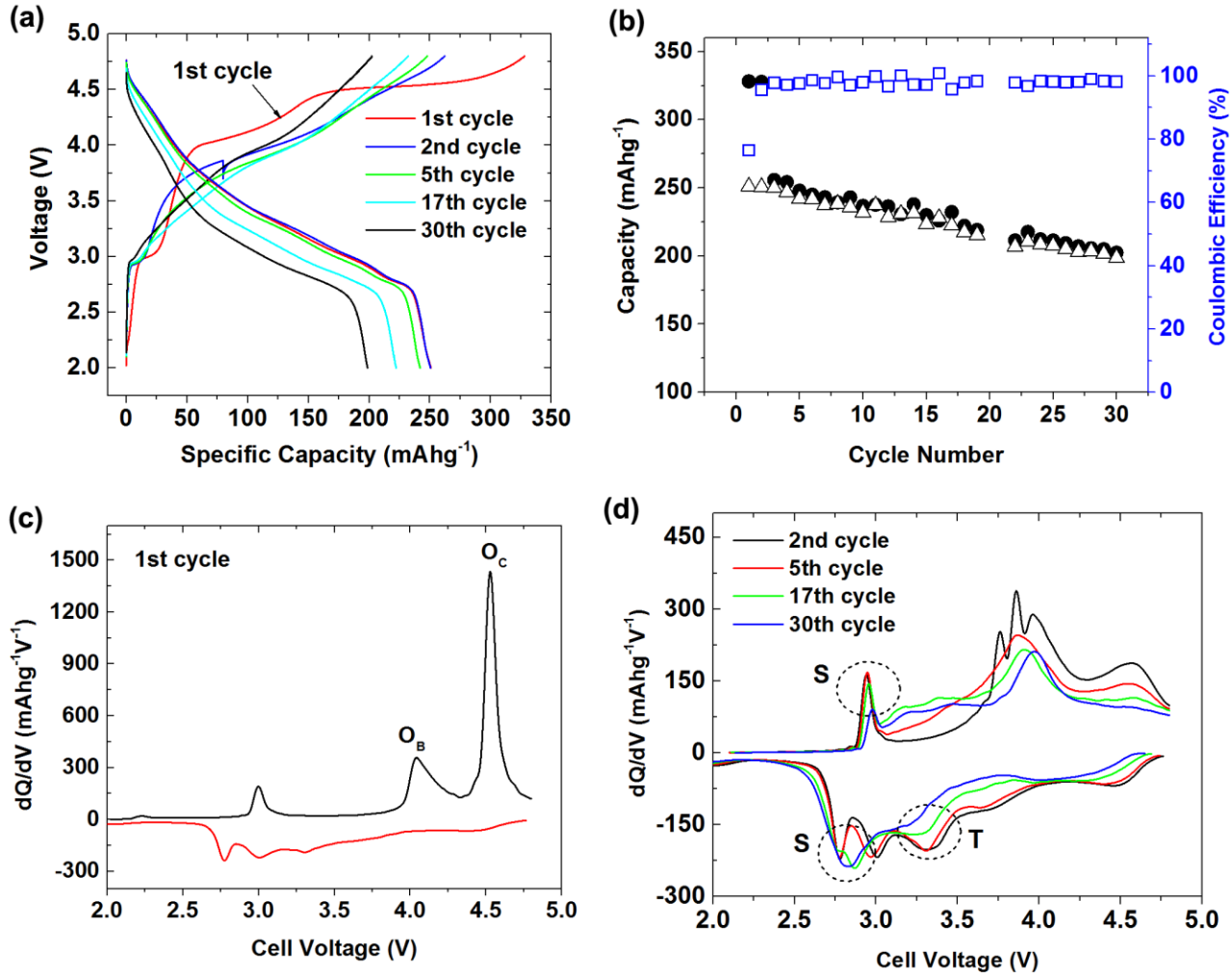


Figure 5.2 Electrochemical property of graphene-coated $Li(Li_{0.2}Mn_{0.54}Ni_{0.13}Co_{0.13})O_2$ cathode (G-type). (a) Galvanostatic profile up to 30th cycle with current rate of 0.2 C. (b) Specific charge (black circle) and discharge capacity (white triangle) with Coulombic efficiency (%). (c) dQ/dV plot of initial cycle. (d) dQ/dV plots on furher cycles.

The electrochemical property of the graphene-coated $Li(Li_{0.2}Mn_{0.54}Ni_{0.13}Co_{0.13})O_2$ cathode, denoted as G-type, is presented in Figure 5.2. The charge-discharge pattern was similar to that of the pristine cathode. Also, the chart on charge/discharge capacity and Columbic efficiency (%) reveals a similar trend to that of the P-type battery during electrochemical cycles as shown in Figure 5.2b. By contrast, there was a discrepancy in the dQ/dV plot between the P-type and G-

type batteries. A notable peak, denoted as S, appears at ~2.8-3.0 V in the graphene-coated cathode as displayed in Figure 5.2c,d. This peak is considered as an indicative of the phase transition from layered structure into the spinel (or cubic spinel-like) phase[84,160]. The peak T at ~3.3 V is attributed to redox reaction from Mn^{4+} into $Mn^{(4-x)+}$, where $0 < x < 1$, in the layered $Li_{1-x}MnO_2$ composite[84,160]. On further cycles, the peak T decreases with the increment of peak S. This is likely to be linked to the phase transition into the spinel phase during electrochemical cycles[84,121]. The peaks at O_B and O_C have the identical origin to those found in the pristine cathode (P-type). O_C explains the electrochemical activation of Li_2MnO_3 component, whereas O_B is attributed to the redox reaction of the transition metals (Ni^{2+}/ Ni^{3+}/Ni^{4+} and Co^{3+}/Co^{4+}).

Figure 5.3 shows the electrochemical property of Chromium-doped $Li(Li_{0.2}Mn_{0.54}Ni_{0.13}Co_{0.03}Cr_{0.10})O_2$ cathode (C-type). The initial and second charge-discharge process were cycled with a charge rate of 0.05 C. This process is known as a 'formation cycle' to fully activate the lithium-ion battery. The formation cycle was followed by the further cycles with a current rate of 0.2 C until 50th cycles. The results obtained from the electrochemical measurements are comparable to that of the P-type and G-type batteries. The Cr-doped cathode is essentially based on the integrated components of $xLi_2MnO_3{\cdot}(1-x)LiMO_2$ system. Thus, the electrochemical property is similar to that of the P-type and G-type batteries. However, the incorporation of Cr transition metal reveals a slightly different pattern of the redox peaks during electrochemical cycles. The major reason of Cr doping on 3a-site in the lithium-rich layered oxide cathode is because of its diverse oxidation state from Cr^{3+} to Cr^{6+} which contributes to the charge compensation mechanism, as well as to stabilizing the host structure at a particular oxidation state[157,158]. Four distinctive redox peaks (O_A, O_B, R_C, and R_D) were identified after the initial cycle as can be seen from Figure 5.3d. The O_A peak explains the redox reaction of Ni^{2+}/Ni^{3+}/Ni^{4+} and Co^{3+}/Co^{4+} in the $LiMO_2$ component. The redox reaction from Cr^{3+}/Cr^{6+} is related to the peak O_B.

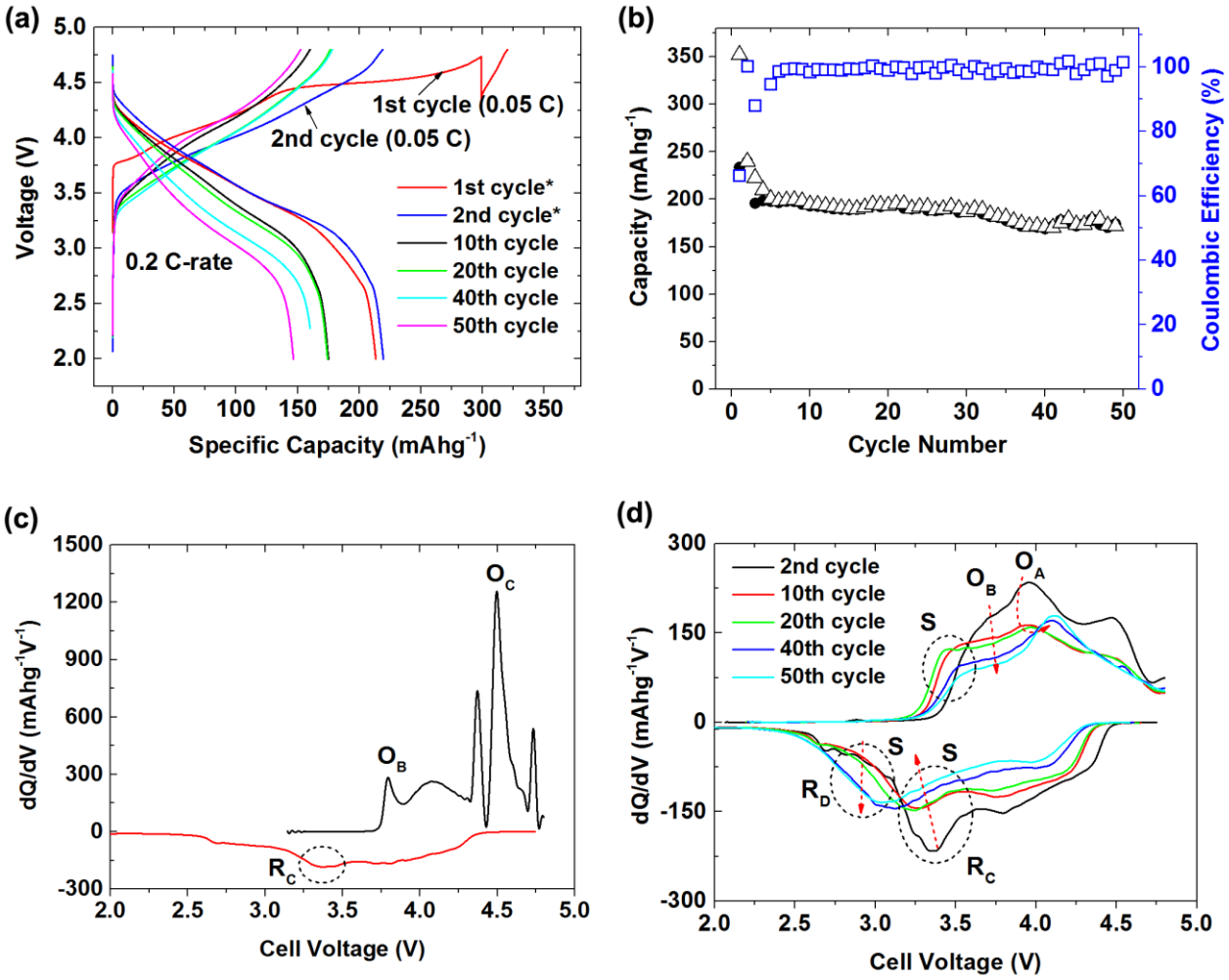


Figure 5.3 Electrochemical property of $Li(Li_{0.2}Mn_{0.54}Ni_{0.13}Co_{0.03}Cr_{0.10})O_2$ cathode (C-type). (a) Galvanostatic profile up to 50th cycle with current rate of 0.2 C. (Formation cycles used 0.05 C-rate). (b) Specific charge (white triangle) and discharge capacity (black circle) with Coulombic efficiency (%). (c) dQ/dV plot of initial cycle. (d) dQ/dV plots on furher cycles. Red arrows indicate the spectra shifts upon charge-discharge.

On charge-discharge, those peaks tend to move to lower dQ/dV value as shown in Figure 5.3d (red arrows). On the other side, the reduction peak at R_C is related to the Mn^{4+} /$Mn^{(4-x)+}$ redox reaction in the layered $Li_{1-x}MnO_2$ composite, where $0 < x < 1$. The peak at R_D is the indicative of the phase transition into the spinel, and this peak can be correlated to the R_C peak as it decreases while R_C increases during charge-discharge of C-type battery. Those peaks relevant to the spinel phase transition are denoted as 'S' in Figure 5.3d.

5.3.2 Investigation of electrochemical activity in Li_2MnO_3 component

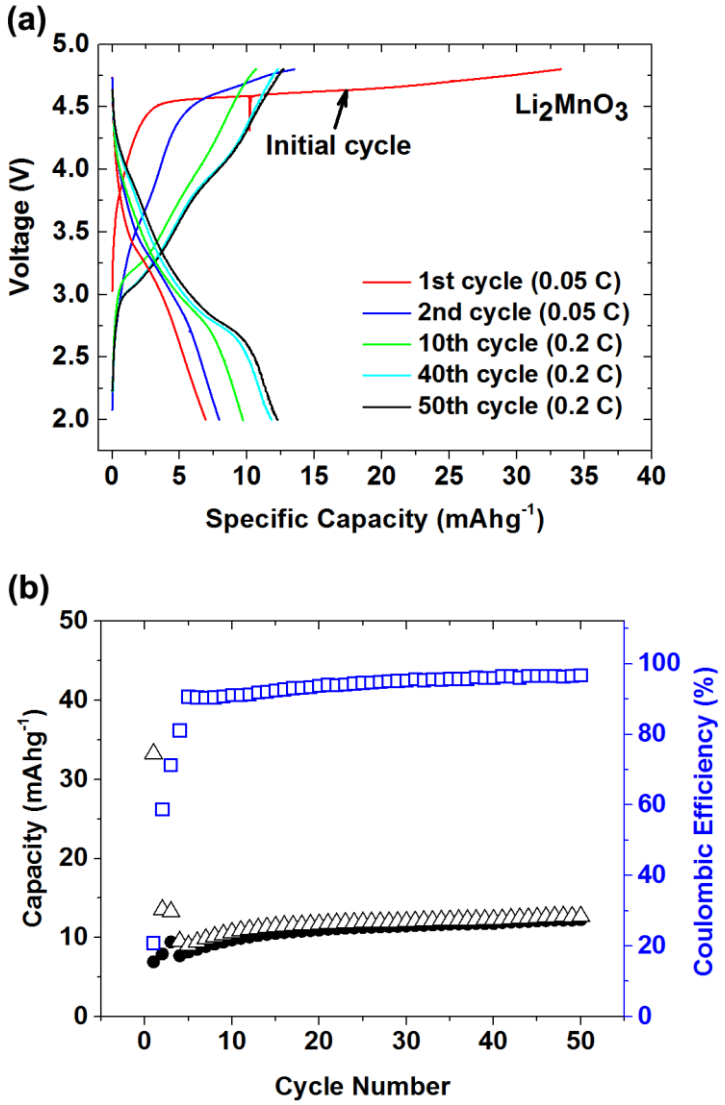


Figure 5.4 Electrochemical property of Li_2MnO_3 cathode. (a) Galvanostatic profile during 50 cycles and (b) charge/discharge specific capacity with Coulombic efficiency (%).

The key factor for delivering high charge capacity in the Li-rich layered oxide cathode system is the intimate structural integration between Li_2MnO_3 (monoclinic, C2/m) and $LiMO_2$ (trigonal/hexagonal, $R\bar{3}m$), where M indicates transition metals[2,4]. It is believed that the Li_2MnO_3 component can be electrochemically activated at higher voltages (> 4.5 V)[2,4,161,162], and this component is responsible for the extra charge capacity in this battery system. As such, an electrochemical investigation was conducted on the Li_2MnO_3 cathode to confirm its practical

charge capacity. The result obtained from the galvanostatic profile is shown in Figure 5.4a. Similarly to the C-type battery, the initial and second cycles are the formation cycle with the constant current of 0.05 C-rate in order to fully activate the battery. The electrochemical activation was confirmed. It appears that the initial charge deliver relatively larger capacity compared with other charge and discharge stages. The Columbic efficiency (%) shows stable trend after the initial charge as presented in Figure 5.4b

5.3.3 Formation of the integrated components in the active materials

The X-ray diffraction patterns (XRD) of P-type, G-type and C-type cathodes are displayed in Figure 5.5. Major peaks could be indexed by the trigonal structure of the $LiMO_2$ component. On the other hand, the weak peaks at ~ 2θ = 15-18° would be indexed to the monoclinic (C2/m) crystal lattice. The incorporation of the graphene in the cathode material seems to be hardly detectable. It was also possible to observe those major peaks resulting from $LiMO_2$ and Li_2MnO_3 component in the C-type battery, although the Li_2MnO_3 phase was relatively more notable in the C-type composite. The appearance of those peaks can be explained by the cation ordering of Li^+-ions in the transition metal layers of Li_2MnO_3 component[74,79]. Hence, the XRD pattern is one of the evidences that support the integrated composite concept in this material. The diffraction pattern between P-type and G-type battery is nearly identical. Rietveld refinement was conducted on the P-type and G-type active materials in order to get some insights into the precise crystal structure (Table 5.1 / Table 5.2) using a two-phase model of $Li(Ni_{1/3}Mn_{1/3}Co_{1/3})O_2$ ($R\bar{3}m$) and Li_2MnO_3 (C2/m). The XRD information also serves as a basis for the modelling process in the EXAFS fitting. The refinement provides reasonably a good fitting as can be seen from the R_{wp} and R_B factors. The result shows that ~2.1 % Ni ions are present in the P-type cathode lithium layer (inter-slab) and Ni/Li exchange between the lithium-layer and transition metal layer. Similarly, ~3 % Ni

ions are present in the G-type cathode lithium layer (inter-slab), and the exchange between both layers appears for Ni and Li. The G-type active material exhibits relatively higher value of lattice parameters on both phases. This may be attributed to the graphene coating on the electrode particles.

Table 5.1 Rietveld refinement on the pristine $Li(Li_{0.2}Mn_{0.54}Ni_{0.13}Co_{0.13})O_2$ (P-type) active material (synthesized at 800 °C) using two-phase model of $Li(Ni_{1/3}Mn_{1/3}Co_{1/3})O_2$ ($R\bar{3}m$) and Li_2MnO_3 (C2/m).

Pristine $Li(Li_{0.2}Mn_{0.54}Ni_{0.13}Co_{0.13})O_2$ (P-type) - Phase I (space group: $R\bar{3}m$)					
***a* = b = 2.855701 Å, c = 14.256641 Å α = β = 90° γ = 120° (R_{wp} = 8.22 % R_B = 5.09 %)**					
Atom	Site		Wyckoff Positions		Occupancy
Li	3a	0	0	0	0.2027
Ni	3a	0	0	0	0.1274
Co	3a	0	0	0	0.1469
Mn	3a	0	0	0	0.5203
Li	3b	0	0	0.5	0.9979
Ni	3b	0	0	0.5	0.0021
O	6c	0	0	0.264806	1.0000

Pristine $Li(Li_{0.2}Mn_{0.54}Ni_{0.13}Co_{0.13})O_2$ (P-type) - Phase II (space group: C2/m)					
***a* = 4.945596 Å, b = 8.567243 Å, c = 5.026222 Å α = β = 90° γ = 109.0074° (R_{wp} = 7.78 % R_B = 4.62 %)**					
Atom	Site		Wyckoff Positions		Occupancy
Li	2b	0	0.5	0	0.1943
Ni	2b	0	0.5	0	0.3520
Mn	2b	0	0.5	0	0.4537
Li	2c	0	0	0	0.9833
Ni	2c	0	0	0.5	0.0167
Li	4g	0	0.170000	0	0.2190
Mn	4g	0	0.171994	0	0.5810
Co	4g	0	0.325771	0	0.2000
Li	4h	0	0.613537	0.5	0.9867
Ni	4h	0	0.634460	0.5	0.0133
O	4i	0.2210	0	0.2270	1.0000
O	8j	0.2530	0.3310	0.2220	1.0000

Table 5.2 Rietveld refinement on the graphene-coated $Li(Li_{0.2}Mn_{0.54}Ni_{0.13}Co_{0.13})O_2$ (G-type) active material (synthesized at 800 °C) using two-phase model of $Li(Ni_{1/3}Mn_{1/3}Co_{1/3})O_2$ ($R\bar{3}m$) and Li_2MnO_3 (C2/m).

Graphene-coated $Li(Li_{0.2}Mn_{0.54}Ni_{0.13}Co_{0.13})O_2$ (G-type) - Phase I (space group: $R\bar{3}m$) **a = b = 2.857261 Å, c = 14.255763 Å α = β = 90° γ = 120° (R_{wp} = 6.99 % R_B = 4.45 %)**					
Atom	Site		Wyckoff Positions		Occupancy
Li	3a	0	0	0	0.2030
Ni	3a	0	0	0	0.1270
Co	3a	0	0	0	0.1473
Mn	3a	0	0	0	0.5200
Li	3b	0	0	0.5	0.9970
Ni	3b	0	0	0.5	0.0030
O	6c	0	0	0.270626	1.0000

Graphene-coated $Li(Li_{0.2}Mn_{0.54}Ni_{0.13}Co_{0.13})O_2$ (G-type) - Phase II (space group: C2/m) **a = 4.947698 Å, b = 8.567435 Å, c = 5.024964 Å α = β = 90° γ = 108.9721°** **(R_{wp} = 8.35 % R_B = 4.83 %)**					
Atom	Site		Wyckoff Positions		Occupancy
Li	2b	0	0.5	0	0.1930
Ni	2b	0	0.5	0	0.3531
Mn	2b	0	0.5	0	0.4539
Li	2c	0	0	0	0.9829
Ni	2c	0	0	0.5	0.0171
Li	4g	0	0.1706	0	0.2190
Mn	4g	0	0.170408	0	0.5780
Co	4g	0	0.325771	0	0.2040
Li	4h	0	0.679701	0.5	0.9860
Ni	4h	0	0.658700	0.5	0.0140
O	4i	0.249685	0	0.219314	1.0000
O	8j	0.266596	0.358733	0.195277	1.0000

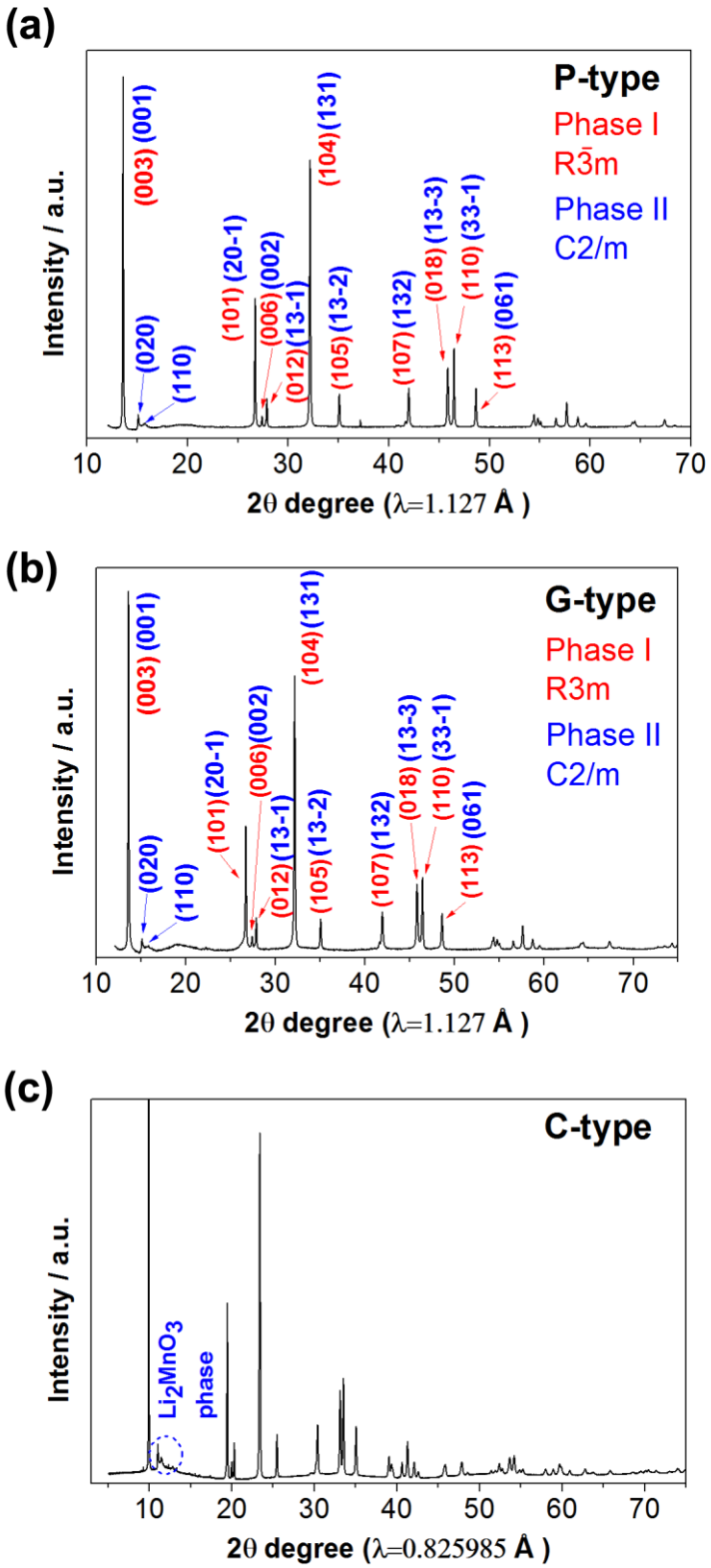


Figure 5.5 X-ray diffraction patterns of (a) pristine $Li(Li_{0.2}Mn_{0.54}Ni_{0.13}Co_{0.13})O_2$ cathode (P-type), (b) graphene-coated $Li(Li_{0.2}Mn_{0.54}Ni_{0.13}Co_{0.13})O_2$ cathode (G-type), and (c) $Li(Li_{0.2}Mn_{0.54}Ni_{0.13}Co_{0.03}Cr_{0.10})O_2$ cathode (C-type). P-type and G-type cathodes were indexed with two phases of $R\bar{3}m$ (red) and C2/m (blue).

The SEM images of the pristine $Li(Li_{0.2}Mn_{0.54}Ni_{0.13}Co_{0.13})O_2$ cathode (P-type), the graphene-coated $Li(Li_{0.2}Mn_{0.54}Ni_{0.13}Co_{0.13})O_2$ cathode (G-type), $Li(Li_{0.2}Mn_{0.54}Ni_{0.13}Co_{0.03}Cr_{0.10})O_2$ cathode (C-type), and Li_2MnO_3 cathode are compared in Figure 5.6. The calcination temperature was 800 °C for P-type, G-type, and C-type cathode materials. G-type particles displays relatively smaller dimension with homogeneous distribution, whereas C-type particles tend to agglomerate with larger particles.

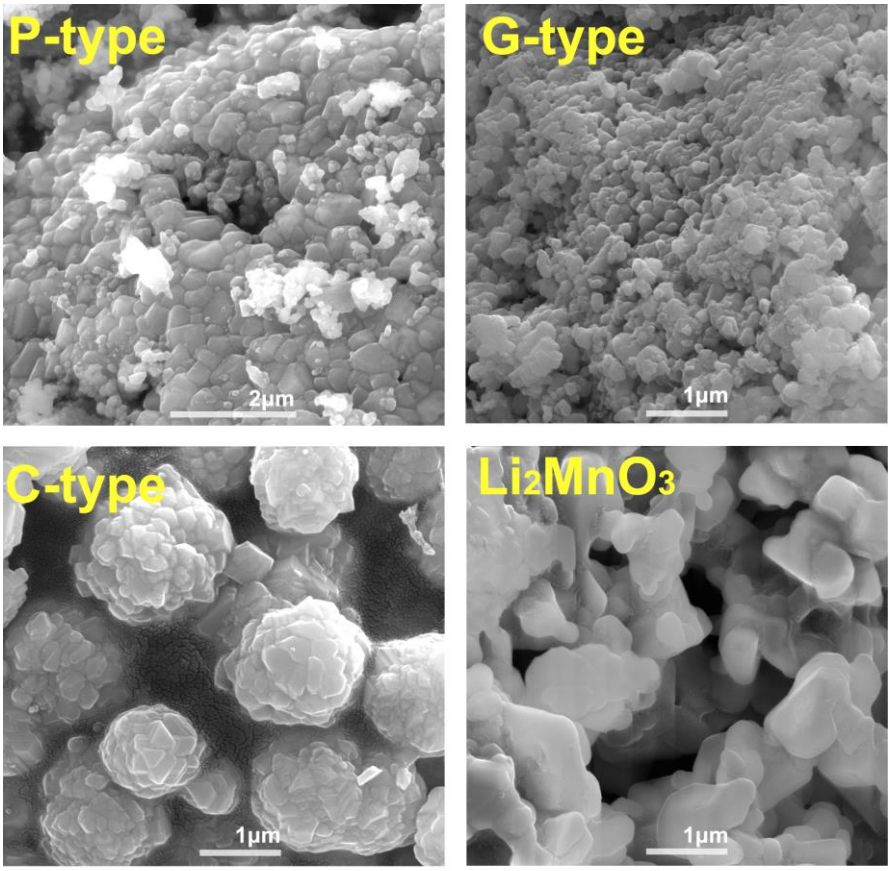


Figure 5.6 SEM image of the pristine $Li(Li_{0.2}Mn_{0.54}Ni_{0.13}Co_{0.13})O_2$ cathode (P-type), the graphene-coated $Li(Li_{0.2}Mn_{0.54}Ni_{0.13}Co_{0.13})O_2$ cathode (G-type), $Li(Li_{0.2}Mn_{0.54}Ni_{0.13}Co_{0.03}Cr_{0.10})O_2$ cathode (C-type), and Li_2MnO_3 cathode. Samples were synthesized at 800 °C.

The results obtained from the EDX mapping can be seen in Figure 5.7. Both the pristine and graphene coated samples reveal a largely homogeneous distribution of the oxygen and transition metal elements, indicating good quality of the chemical synthesis. Table 5.3 presents the results of the energy-dispersive X-ray (EDX) quantitative analysis of the cathode powders.

Table 5.3 EDX quantitative analysis of the active material.

Element	Atomic %	Relative Stoichiometry
Pristine $Li(Li_{0.2}Mn_{0.54}Ni_{0.13}Co_{0.13})O_2$		
O K	69.25	1.772
Mn K	21.1	0.54*
Co K	4.91	0.1256
Ni K	4.74	0.1213
Graphene-coated $Li(Li_{0.2}Mn_{0.54}Ni_{0.13}Co_{0.13})O_2$		
O K	73.65	2.241
Mn K	17.74	0.54*
Co K	4.29	0.1305
Ni K	4.32	0.1314

* Mn was fixed to be 0.54 in the relative stoichiometry.

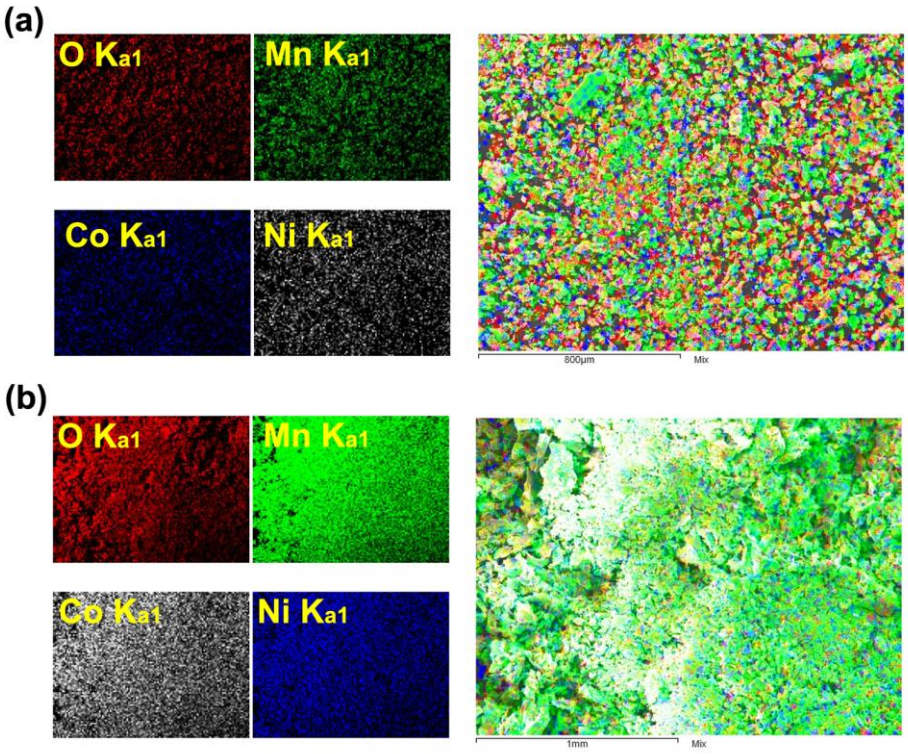


Figure 5.7 EDX mapping of O, Mn, Co, and Ni in (a) Pristine and (b) Graphene coated $Li(Li_{0.2}Mn_{0.54}Ni_{0.13}Co_{0.13})O_2$.

The graphene-coated cathode material reveals slightly different stoichiometry compared to the pristine sample. The post-synthesis treatment of the pristine particles could be the one of the

reasons for the slight difference in stoichiometry, as well as the presence of graphene/graphene oxide in G-type powders. On average, the quantitative analysis shows a reasonable stoichiometry of composites. There was no trace of impurities which may result from the chemical synthesis process.

Figure 5.8 compares the results obtained from ATR-FTIR and Raman spectroscopy measurements on the pristine $Li(Li_{0.2}Mn_{0.54}Ni_{0.13}Co_{0.13})O_2$ cathode (P-type), graphene-coated $Li(Li_{0.2}Mn_{0.54}Ni_{0.13}Co_{0.13})O_2$ cathode (G-type), $Li(Li_{0.2}Mn_{0.54}Ni_{0.13}Co_{0.03}Cr_{0.10})O_2$ cathode (C-type), $Li(Ni_{1/3}Mn_{1/3}Co_{1/3})O_2$ (NMC) cathode, and Li_2MnO_4 (Spinel) cathode. The Raman spectroscopy was chosen as it is a useful tool to investigate the local phase information on the particle surface due to its high sensitivity to local environment. The result from the Raman spectroscopy is presented in Figure 5.8b. Four significant peaks were observed at 81, 438, 491, and 601 cm^{-1} in the P/G/C cathode composites. The low frequency peak is generally related to Li-O bonding, while the Raman active modes between 400 and 650 cm^{-1} are ascribed to the octahedral MnO_6 [114,146,163,164]. Those peaks at 491 and 600 cm^{-1} can be assigned to the Raman active mode of E_g (O-M-O bending) and A_{1g} (M-O stretching), respectively[146,164]. The Raman activity of $A_{1g} + E_g$ scattering is ascribed to the hexagonal rock-salt structure of $R\bar{3}m$ space group. The peak at around 439 cm^{-1} explains the vibrational spectra associated to the super-lattice formation. The appearance of this peak is consistent to the weak peaks at ~ 2θ = 15-18° in the XRD analysis describing the cation ordering in the transition metal layers of Li_2MnO_3 component. There is a similarity in the Raman spectra between NMC composite and P/G/C/ cathodes as can be seen from Figure 5.8b. On the other hand, the spinel composite shows a different scattering pattern. Taken together, it can thus be suggested that the cathode composites of P/G/C-type are present in an integrated composite system between layered $Li(Ni_{1/3}Mn_{1/3}Co_{1/3})O_2$ and monoclinic Li_2MnO_3 (C2/m) at the initial stage. Figure 5.8a displays the FTIR spectra of the cathode composites. ATR-FTIR can be used as a

complement tool for the Raman investigation as it is particular useful in characterizing the surface chemistry. The FTIR spectra was collected from ~550 to 4000 cm^{-1} wavelength. Some peaks were recorded between 550 and 800 cm^{-1} of the cathode composites. These peaks would be ascribed to the stretching modes in an octahedral environment of MO_6 group[146,164]. Not much impurities were observed in P/G/C cathode composites. On the surface of the electrode particles, both P-type and G-type cathodes reveal a good layered structure than C-type cathode.

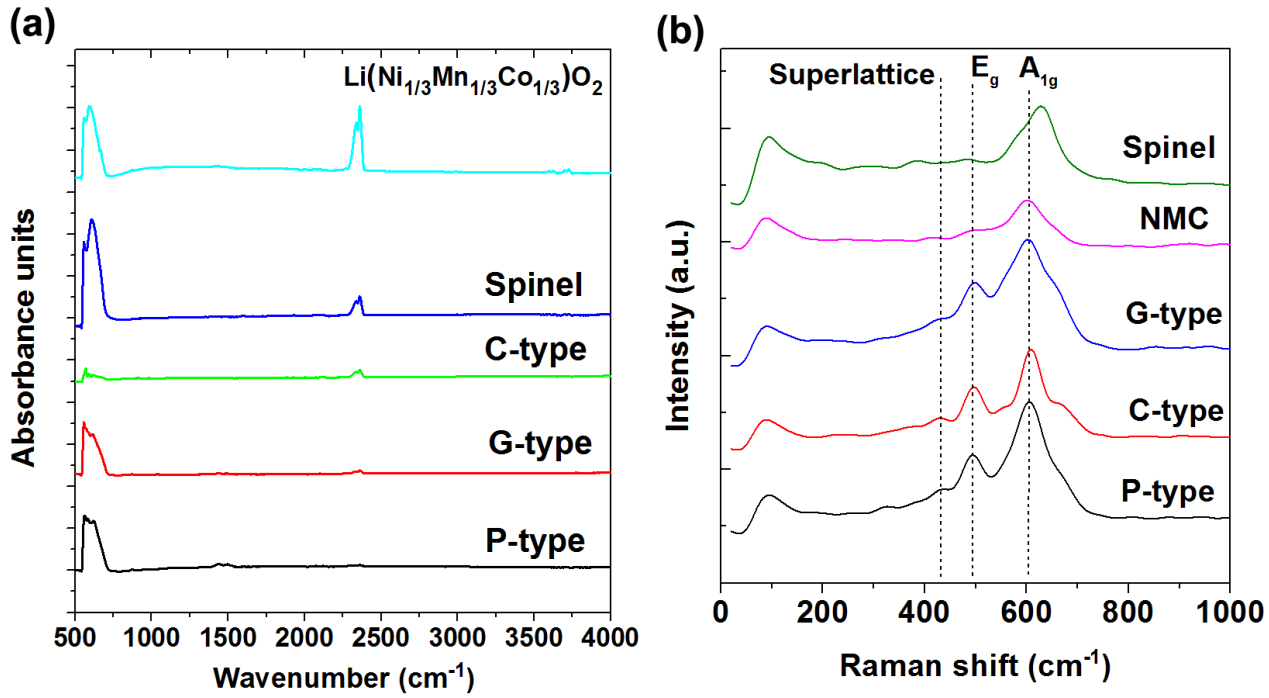


Figure 5.8 (a) ATR-FTIR spectra and (b) Raman spectra of pristine $Li(Li_{0.2}Mn_{0.54}Ni_{0.13}Co_{0.13})O_2$ cathode (P-type), graphene-coated $Li(Li_{0.2}Mn_{0.54}Ni_{0.13}Co_{0.13})O_2$ cathode (G-type), $Li(Li_{0.2}Mn_{0.54}Ni_{0.13}Co_{0.03}Cr_{0.10})O_2$ cathode (C-type), $Li(Ni_{1/3}Mn_{1/3}Co_{1/3})O_2$ (NMC) cathode, and Li_2MnO_4 (Spinel) cathode.

5.3.4 Evaluation of magnetic properties

Figure 5.9 shows the magnetic properties of the P/G/C-type cathode composites. The magnetization (M) vs applied magnetic field (H) at 5 K were compared for the active materials. A slight hysteresis loop could be observed for P-type and G-type cathode, whereas the plot in C-type cathode displayed almost a linear pattern. The observed remanent magnetizations were Mr ~12.30

emu · mol^{-1}, 23.27 emu · mol^{-1}, and 3.3 emu · mol^{-1} for P-type, G-type, and C-type cathodes, respectively.

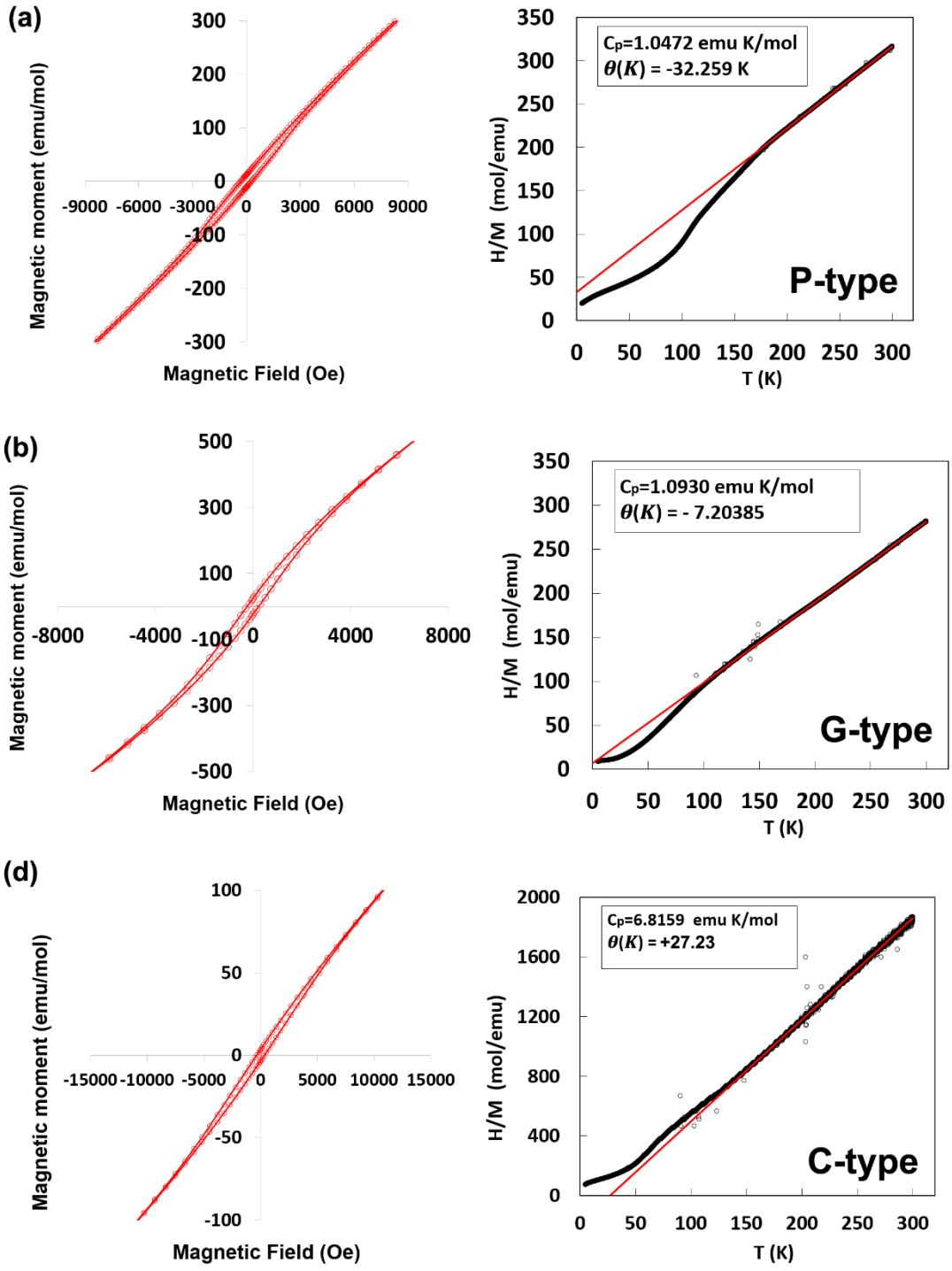


Figure 5.9 Measurement of the magnetic properties (magnetization:left and magnetic susceptibility:right). (a) Pristine $Li(Li_{0.2}Mn_{0.54}Ni_{0.13}Co_{0.13})O_2$ cathode (P-type), (b) graphene-coated $Li(Li_{0.2}Mn_{0.54}Ni_{0.13}Co_{0.13})O_2$ cathode (G-type), and (c) $Li(Li_{0.2}Mn_{0.54}Ni_{0.13}Co_{0.03}Cr_{0.10})O_2$ cathode (C-type).

For all samples, no saturation was recorded in the magnetization plot indicating an antiferromagnetic exchange. G-type cathode exhibits partially higher ferromagnetic behaviour compared with P-type and C-type cathodes as it presents the highest remanent magnetization. C-type can be considered as a non-ferromagnetic interaction. The reciprocal molar magnetic susceptibility (H/M) was also investigated for each cathode composite. It appears that the active materials obey the Curie-Weiss law at a temperature above 150 K showing the paramagnetic property in this range. The fitting with the Curie-Weiss law of $X_m = \mathrm{C}/(T - \theta)$, where θ is the Weiss constant and C is the Curie constant (C=$N\frac{\mu}{3k_B}$, *N:* Avogadro number and k_B: Boltzmann constant), allows to evaluate the effective magnetic moment and Curie-Weiss temperature for each cathode composite. The evaluated magnetic properties are listed in Table 5.4. The Curie constant of P-type cathode was 1.0472. The experimental value of the effective magnetic moment (μ_{exp}) on the P-type cathode was 2.8858 μ_B, which is lower than the theoretical magnetic moment ($\mu_{\mathrm{thero}} = 3.02829\ \mu_B,$). The μ_{thero} was calculated based on the assumption that the pristine active material is composed of Mn^{4+} (spin S=3/2, $\mu_S = 3.87\mu_B$), low-spin (LS) Co^{3+} (spin S=0, $\mu_S = 0\mu_B$), and Ni^{2+} (spin S=1, $\mu_S = 2.83\mu_B$) transition metals. As this assumption leads to a large discrepancy between μ_{exp} (μ_B) and μ_{thero} (μ_B), an alternative model would be considered. The incorporation of the low-spin (LS) Mn^{3+} results in the theoretical magnetic moment of $\mu_{\mathrm{thero}} = 2.8889\ \mu_B,$, which is close to the experimental magnetic moment. The presence of the LS Mn^{3+} has been reported in previous studies[93,94,107]. Similarly, the theoretical magnetic moment (μ_{thero}) of G-type cathode was calculated to be 2.9576 μ_B. This value is close to the experimental magnetic moment ($\mu_{exp} = 2.9482\ \mu_B$) of the G-type cathode.

Table 5.4 Experimental/calculated effective magnetic moment with Weiss constant and evaluated oxidation state of Mn in the pristine $Li(Li_{0.2}Mn_{0.54}Ni_{0.13}Co_{0.13})O_2$ (P-type) and graphene-coated $Li(Li_{0.2}Mn_{0.54}Ni_{0.13}Co_{0.13})O_2$ cathodes (G-type).

Active Materials	C_p (emu K/mol)	Weiss constant $\boldsymbol{\theta}$(K)	μ_{exp} (μ_B)	μ_{thero} (μ_B)	Evaluated oxidation state of Mn
P-type	1.04723	-32.259	2.8858	2.8889	+3.783
G-type	1.09302	-7.203	2.9482	2.9576	+3.888

The magnetic measurements allow to evaluate the correct oxidation state of the P-type and G-type composites in the initial stage. They were measured to be +3.783 for P-type and +3.888 for G-type composites. The Weiss constant (θ) were -32.259 K, -7.203 K, and +27.23 K for P-type, G-type, and C-type composites, respectively. For P-type and G-type samples, the Weiss constant shows negative values, which are the indicative of antiferromagnetic interactions. The condition of the cation arrangement in the cathode composite can be deduced from the magnetic measurement. The ferromagnetic cluster in the active material is an indicative of the increased Ni content in the Li-layer of the $Li(Li_{0.2}Mn_{0.54}Ni_{0.13}Co_{0.13})O_2$ composite in terms of the presence of the ferromagnetic interaction between Ni^{2+} ions with Mn^{4+} ions in the transition metal layer. The ferromagnetic property became relatively higher in the G-type cathode. A small amount of Ni^{2+} ions are likely to present in the Li-layer of the pristine and graphene-coated $Li(Li_{0.2}Mn_{0.54}Ni_{0.13}Co_{0.13})O_2$ cathode after the synthesis of active material. By contrast, the little remanent magnetizations with the dominant antiferromagnetic property implies the negligible amount of the Ni^{2+} ions in the Li-layer of the $Li(Li_{0.2}Mn_{0.54}Ni_{0.13}Co_{0.03}Cr_{0.10})O_2$ cathode (C-type).

5.3.5 Investigation of local atomic environment by XANES/EXAFS

The normalised XANES spectra at transition metal K-edge of pristine $Li(Li_{0.2}Mn_{0.54}Ni_{0.13}Co_{0.13})O_2$ (P-type), graphene-coated $Li(Li_{0.2}Mn_{0.54}Ni_{0.13}Co_{0.13})O_2$ (G-type), and $Li(Li_{0.2}Mn_{0.54}Ni_{0.13}Co_{0.03}Cr_{0.10})O_2$ (C-type) cathodes are presented in Figure 5.10. The local atomic environment at Mn K-edge of P-type and C-type cathodes are similar to that of the Li_2MnO_3

composite, whereas the G-type cathode seems to be close to the layered $Li(Ni_{1/3}Mn_{1/3}Co_{1/3})O_2$ (NMC) composite (Figure 5.10a).

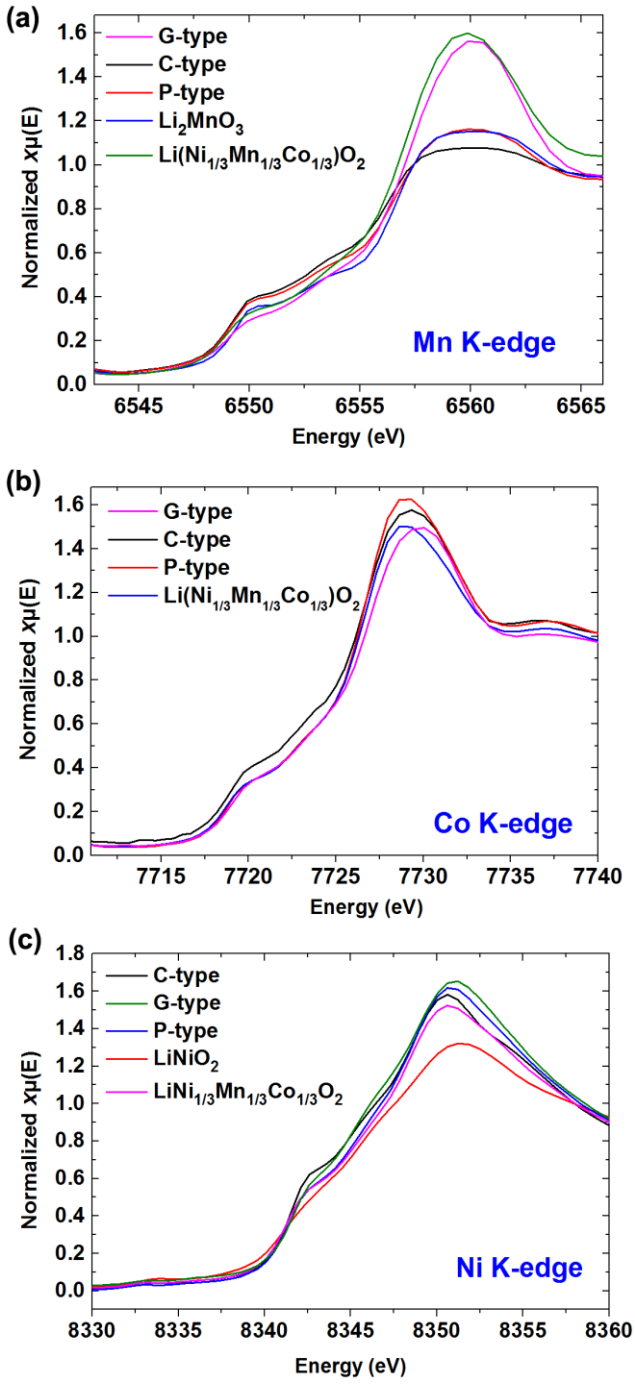


Figure 5.10 Normalised XANES spectra of pristine $Li(Li_{0.2}Mn_{0.54}Ni_{0.13}Co_{0.13})O_2$ cathode (P-type), graphene-coated $Li(Li_{0.2}Mn_{0.54}Ni_{0.13}Co_{0.13})O_2$ cathode (G-type), and $Li(Li_{0.2}Mn_{0.54}Ni_{0.13}Co_{0.03}Cr_{0.10})O_2$ cathode (C-type) at (a) Mn K-edge, (b) Co K-edge, and (c) Ni K-edge.

As the XANES is oxidation sensitive, the oxidation state of the transition metals could be estimated by the spectra comparison between the cathode samples and the corresponding reference compounds. The main edge of the G-type cathode was close at the reference compounds of $Li(Ni_{1/3}Mn_{1/3}Co_{1/3})O_2$ (NMC) and Li_2MnO_3 (Mn:+IV) composite. This implies that the Mn in G-type composite exists nearly as the oxidation state of +4. The Mn K-edge spectra of P-type and C-type composites were located slightly lower than that of G-type cathode, indicating slightly lower value than the oxidation state of +4. This result can be confirmed by the magnetic measurements as the oxidation state of Mn was evaluated to be +3.783 for P-type and +3.888 for G-type (Table 5.4). On the other hand, the local atomic environment around Co was similar between P-type, G-type, and C-type cathodes as shown in Figure 5.10b. The XANES spectra on P-type and G-type nearly correspond to that of the NMC cathode. This suggests that the oxidation state of the Co in these composites was nearly +3. The main edge of the C-type Co K-edge could be found at slightly lower energy level than the P/G-type cathodes. The Co is likely to be present in a lower oxidation state than +3. Similarly in Ni K-edge XANES, the local atomic environment between those cathodes appears to be similar as can be seen from Figure 5.10c. Among the composites, the XANES edge of P-type cathode at Ni K-edge appears to be close to the reference spectrum of NMC (Ni:+II), but the location was lower than the $LiNiO_2$ spectrum (Ni:+III). It can thus be suggested that the Ni ions are in the +2 oxidation state in the pristine material.

The Fourier transformed EXAFS data of Mn, Co, and Ni k-edge in R-space (real space) are compared in Figure 5.11. At the Mn K-edge, it is apparent that the 1st coordination shell (Mn-O) shows higher amplitude than the Mn-TM shell for all samples. This is because of the well-coordinated oxygen ions around the Mn absorber compared with the coordination from the transition metals (Mn, Co, and Ni). Simply, this can be understood by the ratio of Mn-O/Mn-TM atoms; the higher the ratio, the stronger the Mn-O peak.

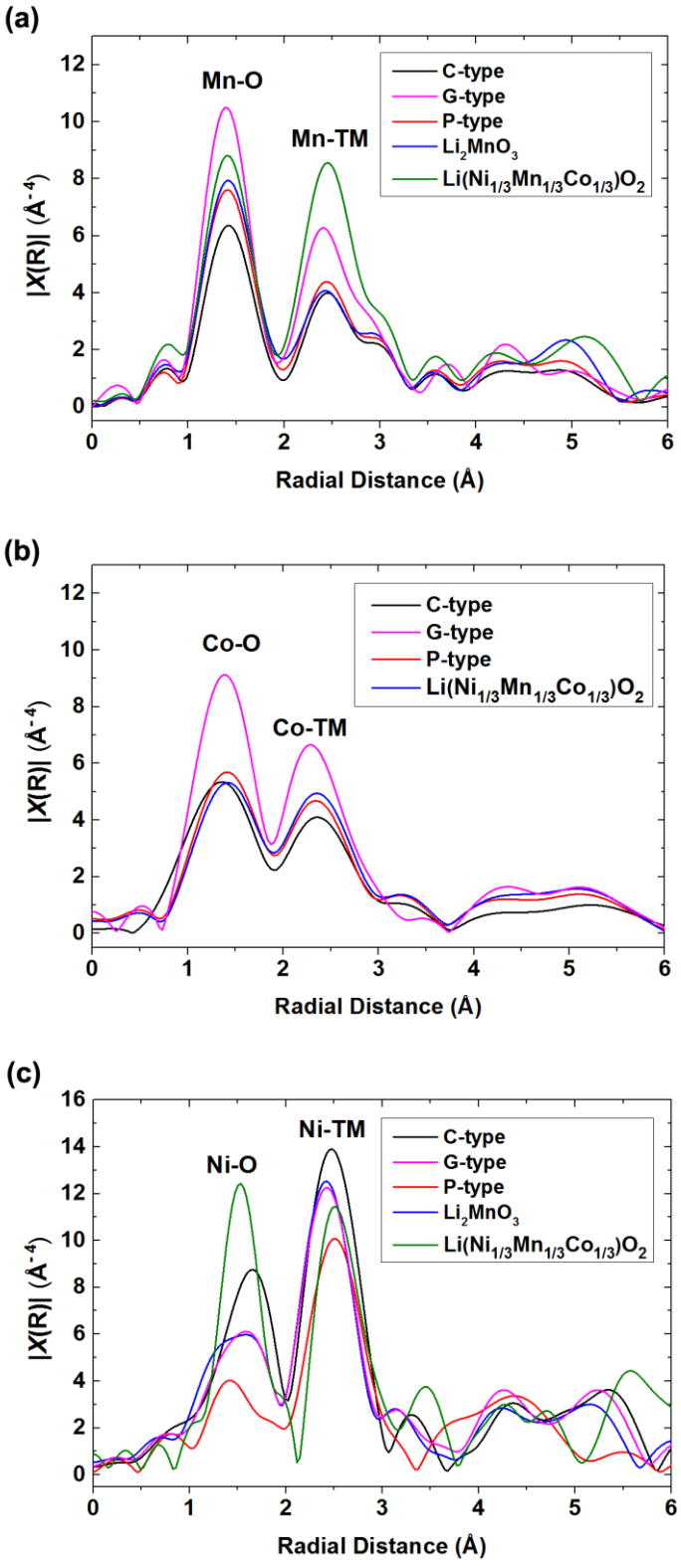


Figure 5.11 Fourier transform magnitudes (k^3-weighted) at (a) Mn K-edge, (b) Co K-edge, and (c) Ni K-edge of pristine $Li(Li_{0.2}Mn_{0.54}Ni_{0.13}Co_{0.13})O_2$ cathode (P-type), graphene-coated $Li(Li_{0.2}Mn_{0.54}Ni_{0.13}Co_{0.13})O_2$ cathode (G-type), and $Li(Li_{0.2}Mn_{0.54}Ni_{0.13}Co_{0.03}Cr_{0.10})O_2$ cathode (C-type). TM represents the transtion metals (Mn, Co, and Ni).

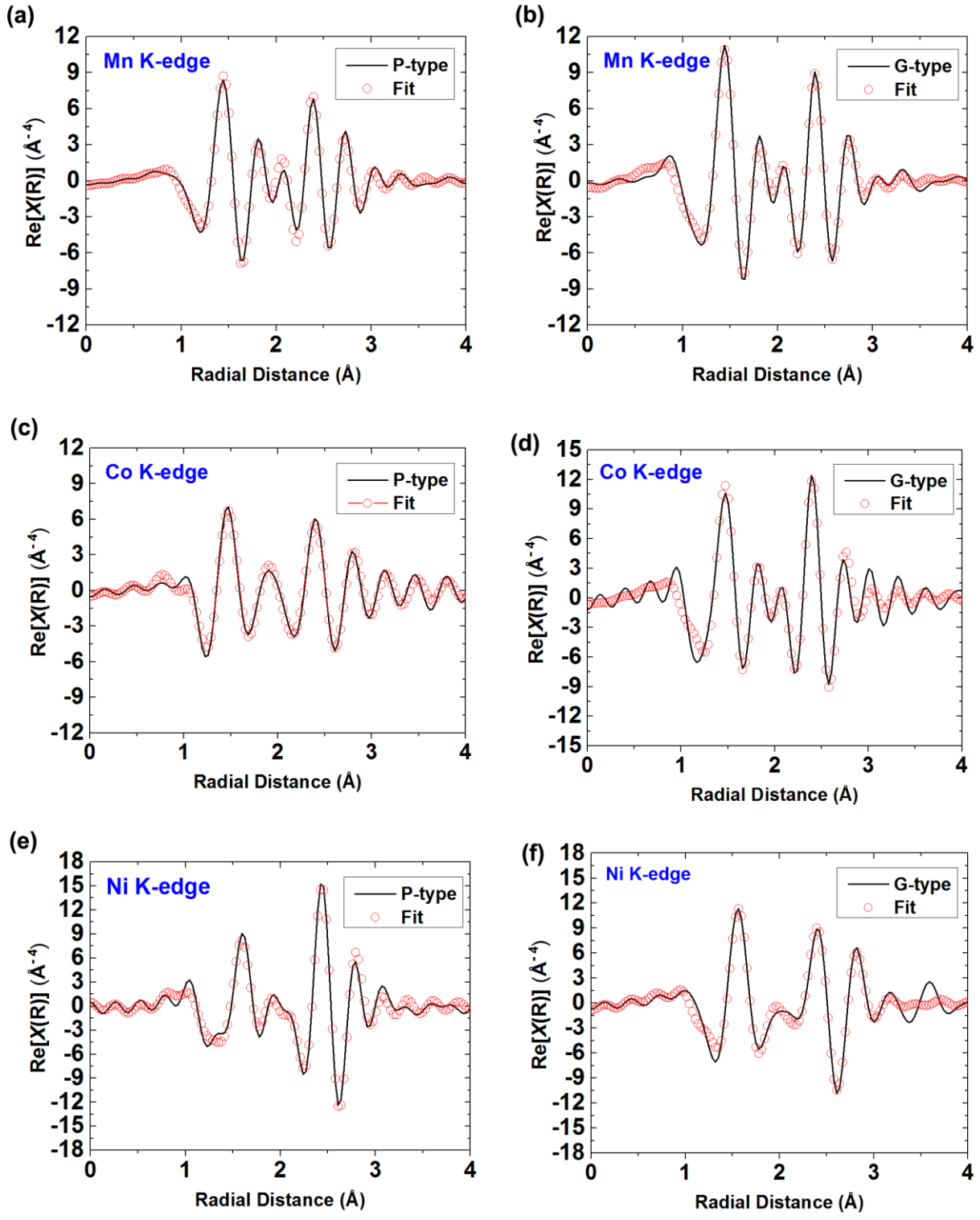


Figure 5.12 EXAFS fitting to the real part of Fourier transformed data for (a) P-type at Mn K-edge, (b) G-type at Mn K-edge, (c) P-type at Co K-edge, (d) G-type at Co K-edge, (e) P-type at Ni K-edge, and (f) G-type at Ni K-edge.

G-type cathode exhibits relatively higher peak intensity compared with P-type and C-type cathodes. This implies better symmetry in the octahedral MnO_6 structure. The shape of the Fourier transformed EXAFS spectrum is close to that of the NMC composite, indicating a well ordered Li-layered structure in the G-type cathode. On the other side, the local environment of the Co in G-type cathode was found to be different to that of the P-type, C-type and NMC composite as can be seen in Figure 5.11b. The Co K-edge EXAFS of G-type cathode accords well with that of the Mn, whereas the P/C-types display different patterns. With the graphene-coating, the Co tends to retain a good octahedral symmetry. Figure 5.11c presents the Fourier transformed EXAFS on Ni K-edge, and it shows much variations upon the type of the composites as compared with Mn and Co.The Ni-M peak presents relatively larger amplitude for P/G/C-type composites. It is therefore likely that there are a larger number of near-neighbouring heavy scatterers (e.g. metal atoms) around the Ni absorber. In contrast to the Mn and Co K-edge EXAFS, the C-type cathode revealed higher Ni-O/Ni-TM peak intensity, implying good symmetry in the octahedral NiO_6 environment.

Figure 5.12 compares the EXAFS fitting to the real part of Fourier transformed data of P-type and G-type cathodes. The EXAFS data was fitted by the integrated-composite system using the data obtained from the X-ray diffraction (Table 5.1 and Table 5.2). The EXAFS fitting parameters are summarized in Table 5.5. Fourier filtering was applied between 1 Å < R < 3.5 Å in R-space. From the chart we can see that the fitting is well performed both on the P-type and G-type cathodes. Also, the R-factors support the good quality of the fitting results since they are less than 0.020 for all cases. This signifies that there exists at least 98 % correspondence between the modelling data and the experimental data. Moreover, energy shift parameters (ΔE_0) displayed values within 10 eV, which is a very reasonable range. In the following chapters of this thesis, we will present only the R-factors and energy shift parameters (ΔE_0) as the statistical indicator for the fitting quality, but the best fitting parameters were chosen also with the consideration of visual

inspection such as the EXAFS fitting to the real part of Fourier transformed data. The major parameters that can be deduced from the EXAFS fitting are: the coordination number (*N*) of the atom, distance to the neighbouring atom (*R*), the mean-square disorder parameter (σ^2) of neighbouring distance, amplitude reduction factor (S_0^2), R-factor and energy shift parameter (ΔE_0). The coordination number (*N*) is usually set to a particular value (e.g. 6 for octahedral structure) if the structure of the composite is certain.

Table 5.5 Fitting results for the Fourier transformed data (k^3-weighted) of pristine $Li(Li_{0.2}Mn_{0.54}Ni_{0.13}Co_{0.13})O_2$ cathode (P-type) and graphene-coated $Li(Li_{0.2}Mn_{0.54}Ni_{0.13}Co_{0.13})O_2$ cathode (G-type) at Mn, Co, and Ni K-edge. (CN: Coordination number, σ: Mean-square relative displacement from EXAFS Debye-Waller factor, R-range:Fitting range, S_0^2: Amplitude reduction factor and ΔE_0: Energy shift parameter).

R-range (Å)	S_0^2	CN	ΔE_0 (eV)	R-factor	Shell type	Interatomic bond length (Å)	σ^2 (10^{-4} Å^2)
Pristine $Li(Li_{0.2}Mn_{0.54}Ni_{0.13}Co_{0.13})O_2$ cathode (P-type); calcination temperature 800 °C							
1-3.4	0.65	6	2.2	0.0136	Mn-O	1.9210	36.7
					Mn-TM	2.8008	45.1
1-3.39	0.67	6	-5.69	0.0138	Co-O	1.9471	30.3
					Co-TM	2.8456	99.0
1.1-3.4	0.92	6	-4.69	0.0183	Ni-O	2.0348	82.6
					Ni-TM	2.8813	48.8
Graphene-coated $Li(Li_{0.2}Mn_{0.54}Ni_{0.13}Co_{0.13})O_2$ cathode (G-type); calcination temperature 800 °C							
1-3.25	0.65	6	-5.2	0.015	Mn-O	1.908	33.4
					Mn-TM	2.787	86.6
1-3.5	0.67	6	-5.5	0.018	Co-O	1.943	44.2
					Co-TM	2.842	30.8
1.1-3.35	0.92	6	3.4	0.019	Ni-O	2.047	76.9
					Ni-TM	2.894	70.0

The amplitude reduction factor (S_0^2) is initially determined by the fitting on the reference samples. Then, it can be transferable between the compounds with same absorbing atom. The S_0^2 were 0.65, 0.67, and 0.92 for Mn, Co, and Ni, respectively. Another important factor is the mean-square

disorder parameter (σ^2) of neighbouring distance from the EXAFS Debye–Waller factor ($\exp(-2\sigma^2 k^2)$). Here the EXAFS Debye-Waller factor can represent either thermal vibrations or structural disorder on the central absorbing atoms (Mn, Ni, and Co)[126,128]. The σ^2 factor reveals higher values in the 1st coordination shell (TM-O) of NiO_6 compared with Mn and Co as shown in Table 5.5. The bond length of Mn-O/Mn-TM was notable higher in the P-type cathode, whereas the length of Co-O/Co-TM and Ni-O/Ni-TM reveals a small discrepancy between P-type and G-type cathodes. The graphene incorporation may affect the local atomic environment of Mn in the composite, distinctively.

5.3.6 Characterization of local surface environments upon different synthesis temperatures

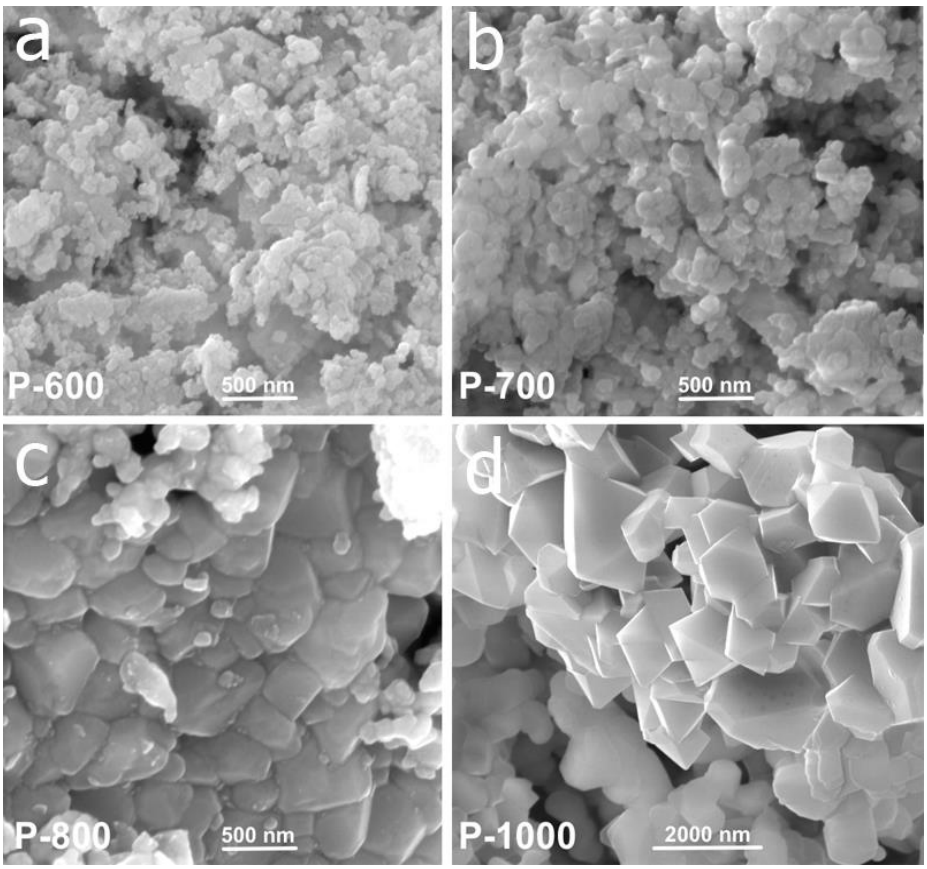


Figure 5.13 SEM images of $Li(Li_{0.2}Mn_{0.54}Ni_{0.13}Co_{0.13})O_2$ active materials synthesized by sol-gel method (a) at 600 °C (P-600) (b) at 700 °C (P-700) (c) at 800 °C (P-800), and (d) at 1000 °C (P-1000).

Figure 5.13 shows the SEM images of $Li(Li_{0.2}Mn_{0.54}Ni_{0.13}Co_{0.13})O_2$ active materials synthesized at different temperatures (600 °C, 700 °C, 800 °C and 1000 °C) by a sol-gel method. It can be seen from the microscope images that all samples form a polyhedral morphology with crystallization. Especially, the octahedron shape can be well observed in P-1000 sample. The minimum size of the particle was measured to be approximately 50 nm (Figure 5.13a), while the maximum size was approximately 2000 nm (Figure 5.13d). The particle size increases with the rise of the synthesis temperature and the size difference of the particles was remarkable.

The spectra obtained from the Raman scattering are presented in Figure 5.14. The Raman spectroscopy was chosen as it is a useful tool to investigate the local phase information on the particle surface due to its high sensitivity to local environment. Four distinctive peaks were observed at 81, 438, 491, and 601 cm^{-1} in the $Li(Li_{0.2}Mn_{0.54}Ni_{0.13}Co_{0.13})O_2$ cathode material. The low frequency peak is likely to be associated with Li-O bonding, while the Raman active modes between 400 and 650 cm^{-1} are generally related to the octahedral MO_6[114,146,163,164]. The peaks observed at 491 and 600 cm^{-1} is the Raman active mode of E_g (O-M-O bending) and A_{1g} (M-O stretching), respectively, in the $Li(Li_{0.2}Mn_{0.54}Ni_{0.13}Co_{0.13})O_2$ cathode material[146,164]. As the cathode contains Mn, Co, and Ni, there should be three of A_{1g} peaks and E_g peaks, total six of those modes, in the Raman scattering profile. However, it is very difficult to discern the peaks for each transition metal because of the similarity in atomic number which results in similar Raman scattering position. The Raman activity of $A_{1g} + E_g$ scattering characterizes the layered hexagonal rock-salt structure of $R\bar{3}m$ space group. The peak at around 439 cm^{-1} is the vibrational spectra that is connected to the super-lattice formation by the cation ordering from the Li_2MnO_3 component. The Raman profiles shows that there has been a very slight spectra shift of A_{1g} and E_g towards higher frequency with the increase of synthesis temperature. The position of A_{1g} Raman activity at lower synthesis temperature (P-600 and P-700) was almost identical with that of the $LiNi_{1/3}Mn_{1/3}Co_{1/3}O_2$

(NMC) component as presented in Figure 5.14. It should be noted that the $LiNi_{1/3}Mn_{1/3}Co_{1/3}O_2$ (NMC) composite is one of the components from the $Li(Li_{0.2}Mn_{0.54}Ni_{0.13}Co_{0.13})O_2$ (≈ $Li_2MnO_3{\cdot}LiNi_{1/3}Mn_{1/3}Co_{1/3}O_2$) active material. The peaks at A_{1g} is relatively well resolved in P-600, P-700, and P-800 samples.

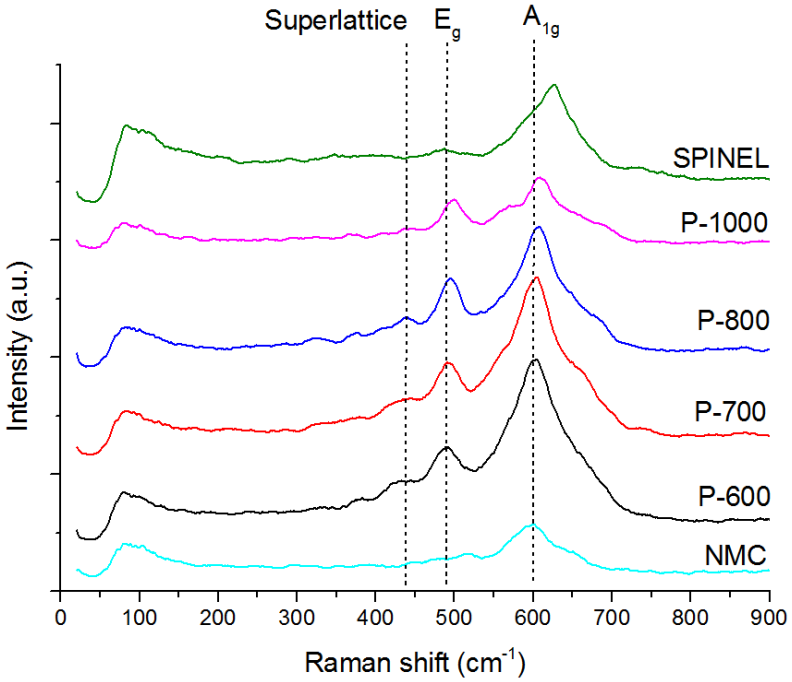


Figure 5.14 Raman spectra of $Li(Li_{0.2}Mn_{0.54}Ni_{0.13}Co_{0.13})O_2$ active materials synthesized by sol-gel method at 600 °C (P-600), 700 °C (P-700), 800 °C (P-800), 1000 °C (P-1000) and spectra of SPINEL (Li_2MnO_4), NMC ($LiNi_{1/3}Mn_{1/3}Co_{1/3}O_2$) for comparison.

This indicates well-ordered structure in the Li-layered oxide component. The A_{1g} activity mode in P-800 slightly increased towards higher frequency, but still it retains a sharp peak. On the other hand, P-800 exhibits a small peak approximately at 439 cm^{-1} indicating a formation of the superlattice by cation ordering in Li_2MnO_3. However, among the cathode samples, P-1000 reveals relatively poor-resolved peaks at A_{1g} activity, as well as less crystallization in the Li-layered oxide component. Moreover, it contains a part of a spinel-like phase since the Raman activity modes were shifted towards higher frequency (Figure 5.14). In general, a Li_2MnO_4 (Spinel) composite exhibits a dominant band between 630-650 cm^{-1} [146,164]. The shift can be possibly regarded as a phase transition from layered oxide to a spinel-like phase with the increment of the synthesis

temperature. Taken together, the Raman analysis suggests that the P-800, which is synthesized at 800 °C with a sol-gel method, is the most optimized product that contains both the characteristic of Li_2MnO_3 and $LiNi_{1/3}Mn_{1/3}Co_{1/3}O_2$ composites.

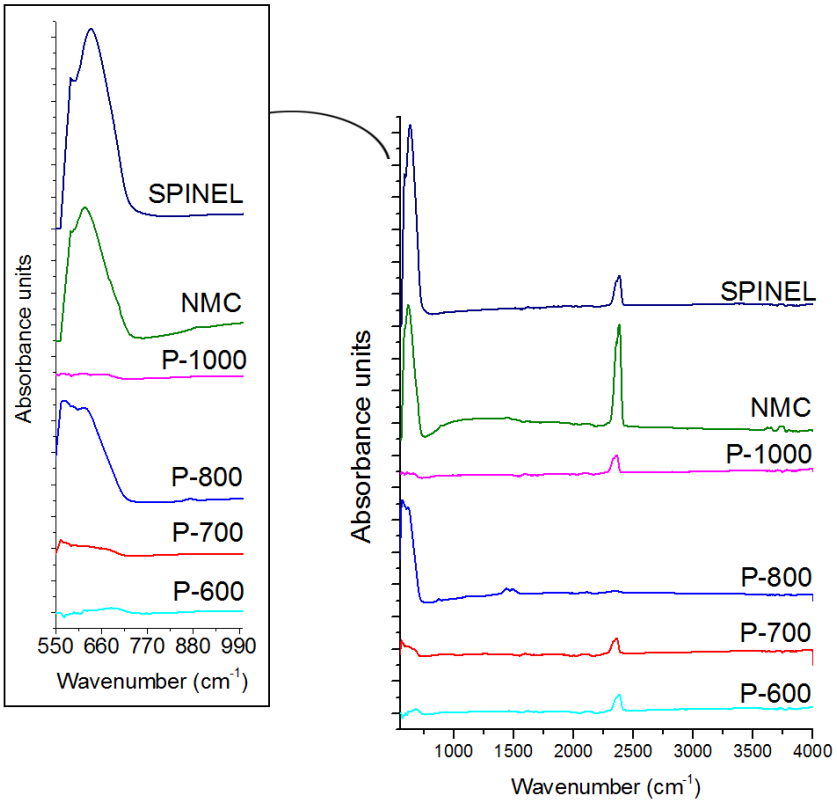


Figure 5.15 Figure FTIR spectra of $Li(Li_{0.2}Mn_{0.54}Ni_{0.13}Co_{0.13})O_2$ active materials synthesized by sol-gel method at 600 °C (P-600), 700 °C (P-700), 800 °C (P-800), 1000 °C (P-1000) and spectra of SPINEL (Li_2MnO_4), NMC ($LiNi_{1/3}Mn_{1/3}Co_{1/3}O_2$) for comparison.

Figure 5.15 compares the FTIR spectra of the active materials synthesized from different temperatures. For the phase comparison purpose, a spinel (Li_2MnO_4) and a NMC ($LiNi_{1/3}Mn_{1/3}Co_{1/3}O_2$) cathode were also investigated. ATR-FTIR was performed to complement the Raman analysis in terms of the surface chemistry, i.e. impurity formation. In the current investigation, the O-M-O asymmetric mode between 300-500 cm^{-1} was not measured as the FTIR spectra were collected from ~550 cm^{-1} wavelength. The peaks between 550 and 700 cm^{-1} are the infrared fingerprints which explain the stretching modes in an octahedral environment of MO_6 group [146,164]. P-800 reveals the best octahedral ordering among the active materials of

$Li(Li_{0.2}Mn_{0.54}Ni_{0.13}Co_{0.13})O_2$ cathode suggesting a well-ordered layered structure. There was also a significant peak between 2360 and 2380 cm^{-1} as shown in Figure 5.15. Interestingly, this peak didn't appear in the active material that was synthesized at 800°C (P-800). The infrared fingerprint around 2360~2380 cm^{-1} is generally ascribed to the carbon dioxide (CO_2). A CO_2 trapped in the transition metal composite can be explained by the following route: 1) The decomposition of the citric acid in the sol-gel method produces carbon dioxide (CO_2) or carbon monoxide (CO). 2) The resulting CO_2 is likely to react with the Li^+ or Li^+ with carbon black in the active material, followed by a reduction into a carbon monoxide (CO). 3) CO molecules can be adsorbed to the transition metal cations due to the well-coordinated electrostatic field[165]. This is followed by the evolution of CO into C and CO_2 which is bound to the cation by ion-induced dipole. Therefore, the peak around 2360~2380 cm^{-1} is possibly originated from the stretching vibration of physisorbed CO_2 in the active material[165,166]. It can be seen from the FTIR spectra that the NMC ($LiNi_{1/3}Mn_{1/3}Co_{1/3}O_2$) cathode revealed significantly much impurity than the other active materials. On the other hand, P-800 exhibits less impurity resulting from the chemical decomposition of the citric acid during the synthesis process. Hence, the FTIR measurements obtained from low and high frequencies suggest that the optimized temperature tends to be 800°C (P-800) for our composite type since it shows a good local ordering as evidenced from the peak at ~550 -700 cm^{-1}, with minimum impurities. P-700 sample shows slightly better ordering of the octahedral environment than that of the P-600 and P-1000, but the peak is much weaker than that of the P-800.

5.3.7 Magnetic measurements upon different synthesis temperatures

The magnetization (M) vs applied magnetic field (H) at 5 K were compared for the active materials of $Li(Li_{0.2}Mn_{0.54}Ni_{0.13}Co_{0.13})O_2$ as can be seen in Figure 5.16. There was a hysteresis loop in the P-1000, while the curves in P-600 and P-700 revealed almost a linear pattern indicating minimal hysteresis.

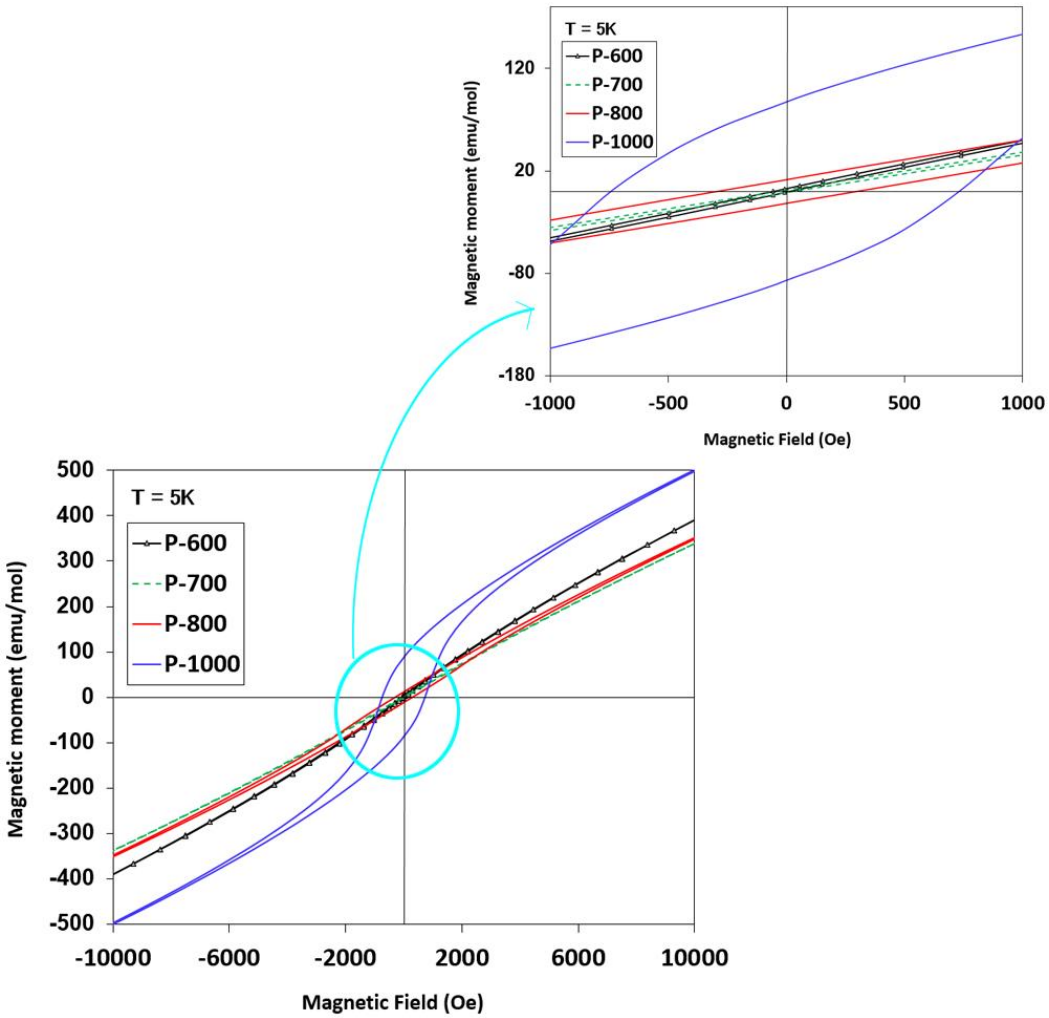


Figure 5.16 Magnetization plots of $Li(Li_{0.2}Mn_{0.54}Ni_{0.13}Co_{0.13})O_2$ active materials synthesized by sol-gel method at 600 °C (P-600), 700 °C (P-700), 800 °C (P-800), and 1000 °C (P-1000).

On the other side, although the curve is close to linear, P-800 exhibits a slight opening in the magnetization curve. The observed remanent magnetizations were Mr ~ 86 emu · mol^{-1} and Mr ~ 12 emu · mol^{-1} for P-1000 and P-800, respectively. There was no sign of the saturation of magnetization for all active materials. Therefore, the magnetic interaction for all active materials can be considered as an antiferromagnetic type. Within this magnetic interaction, it seems that the ferromagnetic behaviour increases in the active material with the rise of the synthesis temperature as evidenced from the hysteresis loop.

The reciprocal molar magnetic susceptibility (H/M) for the active materials was plotted in Figure 5.17. At a temperature above 150 K, it can be seen that the active materials obey the Curie-Weiss law indicating the system is paramagnetic.

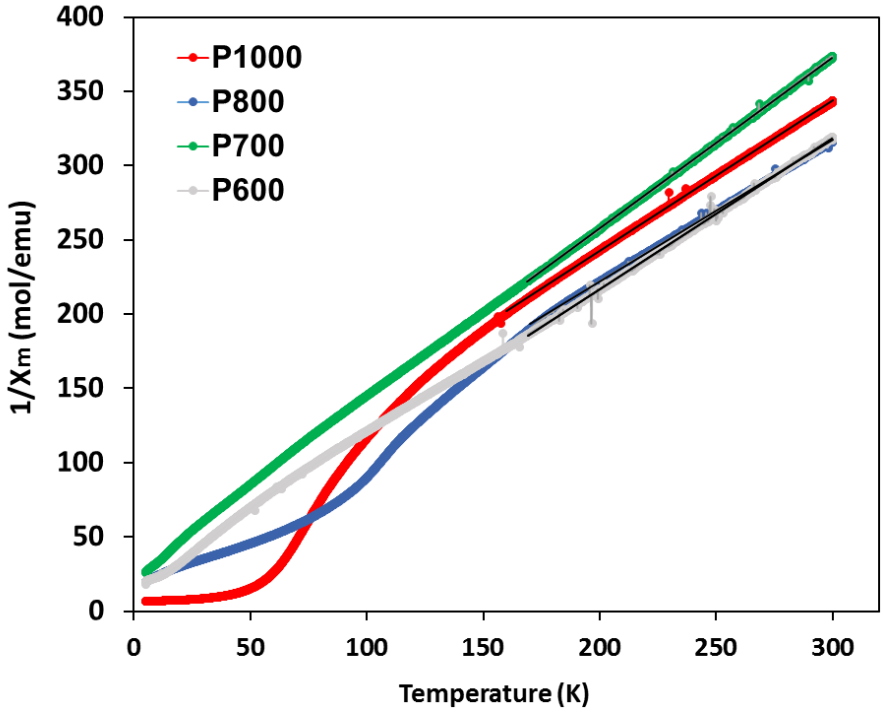


Figure 5.17 Magnetic susceptibility of $Li(Li_{0.2}Mn_{0.54}Ni_{0.13}Co_{0.13})O_2$ active materials synthesized by sol-gel method at 600 °C (P-600), 700 °C (P-700), 800 °C (P-800), and 1000 °C (P-1000). The black lines indicate the fit to the Curie-Weiss law.

Major magnetic parameters such as effective magnetic moment and Curie-Weiss temperature were obtained from the fit to the Curie-Weiss law, $X_m = C/(T - \theta)$ where θ is the Weiss constant and C is the Curie constant ($C=N\frac{\mu}{3k_B}$, N: Avogadro number and k_B: boltzmann constant). The experimental and calculated magnetic parameters for each active material are summarized in Table 5.6. The Curie constant of P-600 was measured to be $C_p = 0.982$ and it leads to the experimental value of the effective magnetic moment (μ_{exp}) of 2.79 μ_B. The lowest value of μ_{exp} (= 2.62 μ_B) was reported in the P-700 sample, whereas the highest value (= 2.88 μ_B) could be found in P-800 sample. However, almost all samples revealed lower μ_{exp} as compared with the μ_{cal} (theoretical magnetic moment). In principle, the active material is consisted of Mn^{4+} (spin S=3/2, $\mu_S =$

3.87μ_B), low-spin (LS) Co^{3+} (spin S=0, $\mu_S = 0\ \mu_B$), and Ni^{2+} (spin *S*=1, $\mu_S = 2.83\ \mu_B$) transition metal, but these theoretical values lead to a large discrepancy between μ_{exp} (BM) and μ_{cal} (BM). It should be thus assumed that the Mn would exist as a mixed state between Mn^{4+} and low-spin (LS) Mn^{3+}. The presence of the LS Mn^{3+} has been reported in previous studies[93,94,107]. The oxidation state for the P-800 was found to be the highest (+3.78) and closest to Mn^{4+}. The lowest oxidation state (+3.50) was observed in the P-700 sample. The negative values of the Weiss constant (θ) for each active material supports the antiferromagnetic interactions, which is likely to be proportional to the synthesis temperature.Taken together, the findings obtained from the magnetic measurement provides the vital information about the cation arrangement upon the synthesis temperature. Formation of the ferromagnetic cluster implies the increased Ni content in the Li-layer of the $Li(Li_{0.2}Mn_{0.54}Ni_{0.13}Co_{0.13})O_2$ composite since the Ni^{2+} can make a ferromagnetic interaction with Mn^{4+} in the transition metal layer. As presented in Figure 5.17 and Table 5.6, the tendency of the ferromagnetic interaction increases upon the synthesis temperature. This suggests that the active material synthesized at 1000°C (P-1000) locates relatively large number of Ni^{2+} on the lithium layer site.

Table 5.6 Experimental/calculated effective magnetic moment with Weiss constant and evaluated oxidation state of Mn of $Li(Li_{0.2}Mn_{0.54}Ni_{0.13}Co_{0.13})O_2$ active materials synthesized by sol-gel method at 600 °C (P-600), 700 °C (P-700), 800 °C (P-800), and 1000 °C (P-1000).

Active Materials	C_p (emu K/mol)	Weiss constant **θ**(K)	μ_{exp} (BM)	μ_{cal} (BM)	Evaluated oxidation state of Mn
P-600	0.982	-12.79	2.79	2.79	+3.65
P-700	0.867	-23.57	2.62	2.69	+3.50
P-800	1.047	-32.25	2.88	2.89	+3.78
P-1000	0.987	-39.48	2.80	2.84	+3.70

The Ni^{2+} and Li^+ are known to be preferentially occupy the crystallography α-site in the transition metal layer (slab) leading to the cation ordering that minimizes the strain in that layer. As such,

the reduced number of Ni^{2+} ions in the slab of P-1000 cathode may increase the disorder of the host structure.

5.3.8 K-edge XANES investigation of Mn, Co, and Ni atomic states upon different synthesis temperatures

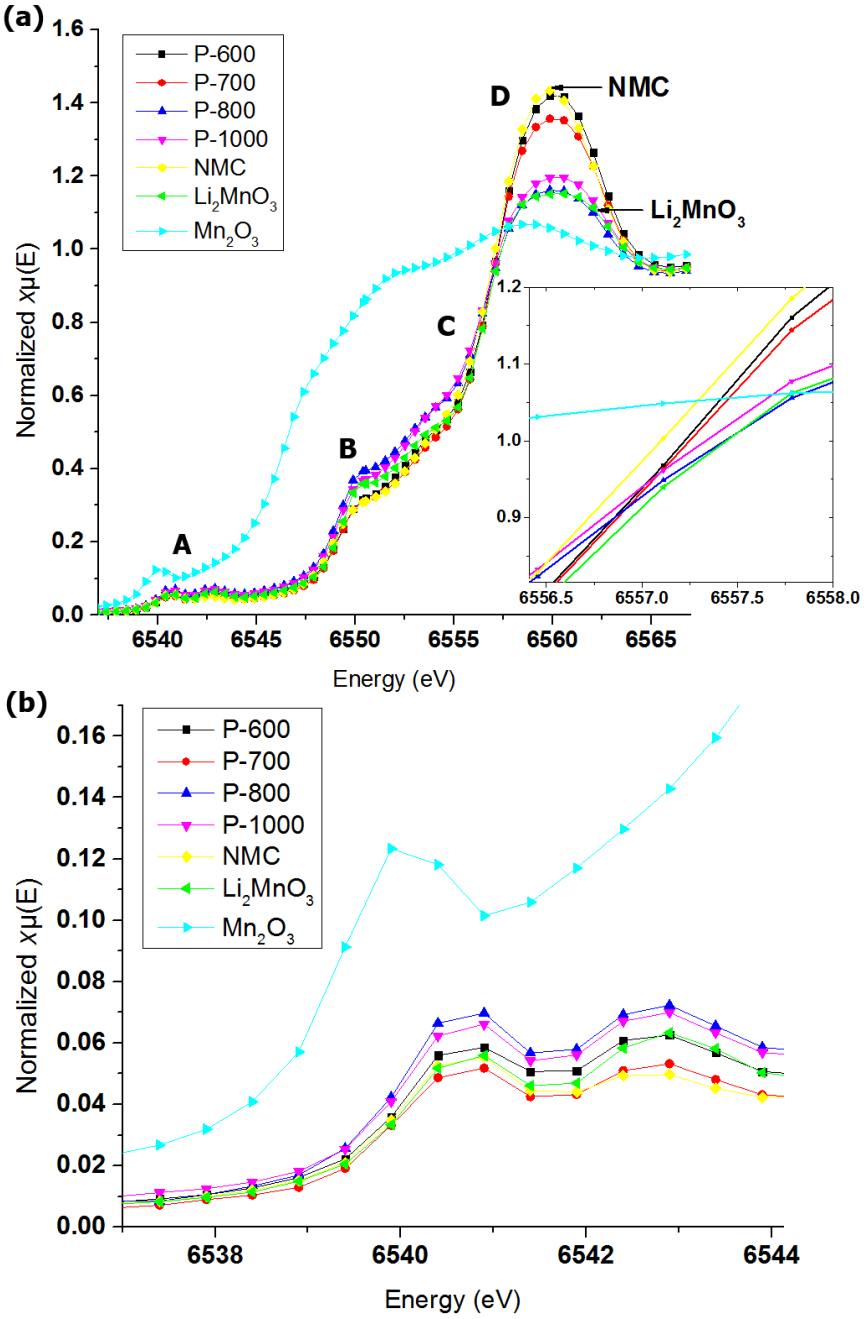


Figure 5.18 Normalised XANES spectra of $Li(Li_{0.2}Mn_{0.54}Ni_{0.13}Co_{0.13})O_2$ (a) at Mn K edge (b) (b) at Mn K pre-edge. The active materials were synthesized by sol-gel method at 600 °C (P-600), 700 °C (P-700), 800 °C (P-800), and 1000 °C (P-1000).

Synchrotron XAS was chosen as it is the spectroscopic method that provides combined and simultaneous information on the electronic, chemical and structural properties with an element specific probing, even in complicated composites. In particular, the X-ray absorption near-edge structure (XANES) region from XAS is connected to the coordination environment and oxidation state of the transition metal atoms. Normalized XANES spectra obtained from the Mn K-edge for each active material are presented in Figure 5.18. In order to compare phase similarities and oxidation states, a $Li(N_{1/3}Mn_{1/3}Co_{1/3})O_2$ (NMC) and a Li_2MnO_3 composites were used as they are the integrated components for the $Li(Li_{0.2}Mn_{0.54}Ni_{0.13}Co_{0.13})O_2$ cathode material. The Mn_2O_3 is the reference composite that shows the energy position of Mn^{3+}. The location of the edge energy offers information about the oxidation state by a finger-print comparison[110,167]. The XANES result verifies that the closest spectra to the Li_2MnO_3 (Mn:4+) composite was P-800, indicating similar Mn oxidation states between them. The correlation is clearly supported by the magnetic measurement using effective magnetic moments as the estimated oxidation state of Mn was +3.78 in the P-800. By contrast, the lowest oxidation value was evaluated to be +3.50 in P-700 active material. Four distinctive absorptions (A, B, C, and D) were observed in the Mn K-edge of the active (Figure 5.18a). Absorption 'C' can be defined as the main edge, while the absorption 'A' indicates the double pre-edge peaks, which are located between 6540 and 6544 eV (Figure 5.18b) at Mn K-edge. These peaks correspond to 1*s*-3d_{t2g} (lower energy) and 1*s*-3d_{eg} (higher energy) transitions. They are formally dipole-electric forbidden in a centrosymmetric system in octahedral geometry[168]. The appearance of those transitions is allowed due to a weak quadrupole transition or/and 3*d*-4*p* orbital hybridization from the loss of centrosymmetric environment attributed to the distortion of the octahedral 3a site in the $R\bar{3}m$ space group. From the Figure 5.18a, we can see that the $Li(Li_{0.2}Mn_{0.54}Ni_{0.13}Co_{0.13})O_2$ cathode materials synthesized at various temperatures can be all

considered as an integrated composite between a $Li(N_{1/3}Mn_{1/3}Co_{1/3})O_2$ (NMC) and a Li_2MnO_3 component.

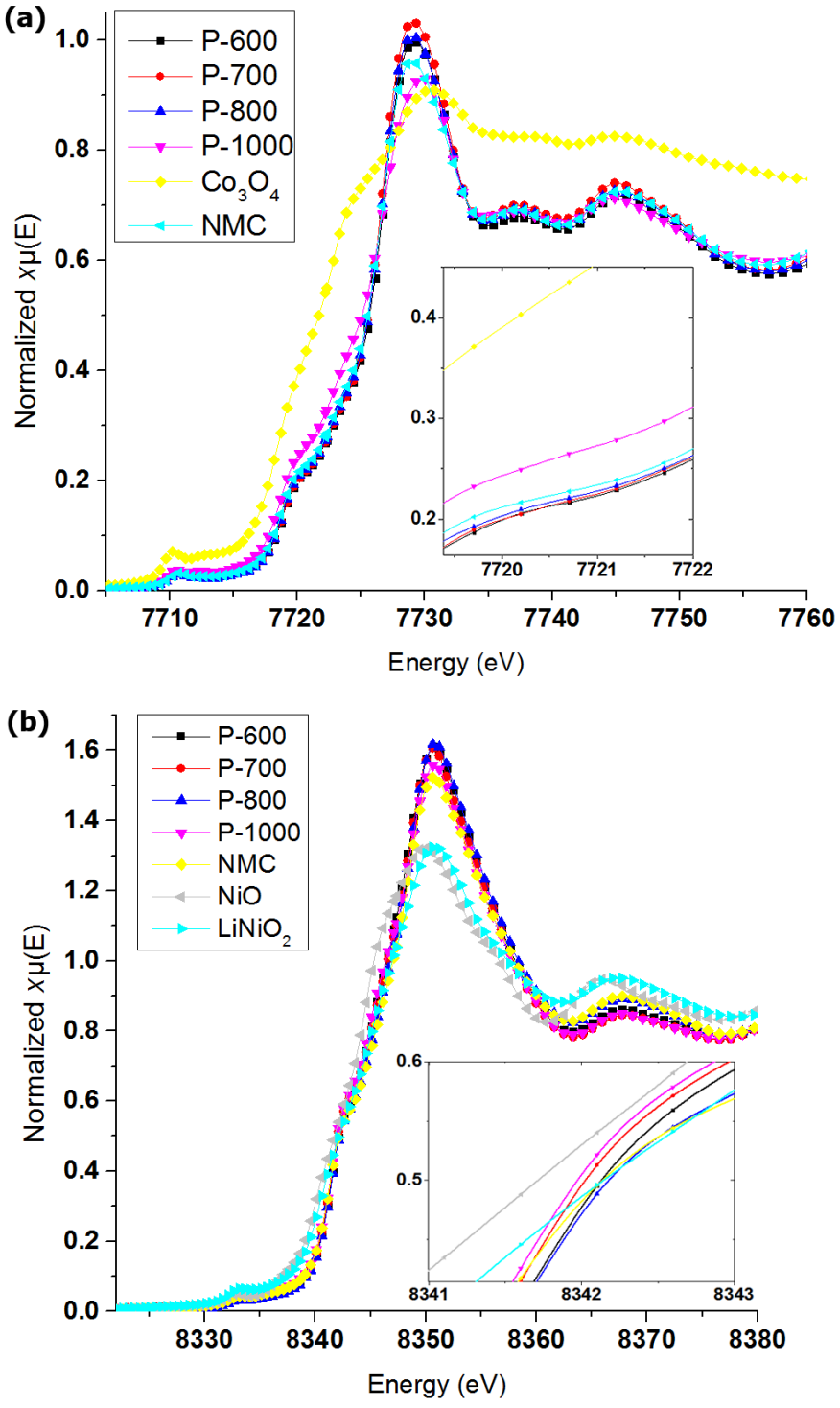


Figure 5.19 Normalised XANES spectra of $Li(Li_{0.2}Mn_{0.54}Ni_{0.13}Co_{0.13})O_2$ (a) at Co K-edge (b) (b) at Ni K-edge. The active materials were synthesized by sol-gel method at 600 °C (P-600), 700 °C (P-700), 800 °C (P-800), and 1000 °C (P-1000).

The active materials synthesized at 600 and 700 °C reveals similar local atomic environment which is close to the NMC cathode. Therefore, it is probable that the $NiMn_6$[99] would be the major unit for the cation ordering in the transition metal layer of those cathode materials. The atomic environment of the active material synthesized at 800 °C is similar to that of the material synthesized at 1000 °C, and they are both close to the Li_2MnO_3 spectra pattern. As such, the $LiMn_6$ units[2,71,99,169] can be considered as the major cation ordering in the transition metal layer for P-800 and P-1000. The correlation of the atomic phase separation upon synthesis temperature is also clearly supported by our Raman spectroscopy results (Figure 5.14).

Figure 5.19 presents the XANES spectra acquired from Co and Ni K-edge for the $Li(Li_{0.2}Mn_{0.54}Ni_{0.13}Co_{0.13})O_2$ cathode materials that are synthesized at different temperatures. P-1000 may exhibit slightly lower oxidation state than Co^{3+}, but no significant differences were found between the active materials at Co K-edge XANES as presented in Figure 5.19a. Co_3O_4 is a reference sample where the Co exists as the oxidation state of ~+2.67. All the main edges from the active materials nearly corresponds to the NMC spectra (Co^{3+}). The intensity of the dipole-allowed main transition ($1s \rightarrow 4p$) in Co K-edge was relatively low in P-1000 active material. This absorption feature is the most sensitive part, which is affected by the chemical condition, in the atomic structure as it is associated with the outer orbital. The decrease of the peak intensity signifies a reduction in the metal-ligand (Co-O) bond length. The global pattern of the Co K-edge XANES was similar to that of the Mn, suggesting similar atomic environment. The oxidation state of the Ni in the active materials was evaluated to be +2 according to the Ni K-edge XANES as shown in Figure 5.19b. Not a distinctive difference was observed in Ni K-edge XANES between the active materials.

5.4 Conclusion

This chapter presented both the electrochemical and structural understandings of the Li-rich Mn-based layered oxide cathodes. Cationic incorporation or coating with conducting agents are the general methods to overcome the limitations of the Li-rich layered cathode system. As such, we coated the graphene on the pristine electrode material (G-type) to increase the electronic conductivity and thus achieve higher rate-capability during electrochemical cycles. On the other side, chromium (Cr) has been incorporated into the pristine electrode (C-type) to improve the stability. It is believed that the Cr incorporation can suppress the voltage decay at a certain level during charge and discharge[158]. For all cathode types, a large voltage plateau could be observed at above ~4.5 V in the galvanostatic profile. This is also well reflected on the initial dQ/dV plots showing a sharp and large oxidation peak (O_c). Some dissimilarities could be also identified in the electrochemical measurements between the pristine $Li(Li_{0.2}Mn_{0.54}Ni_{0.13}Co_{0.13})O_2$ (P-type), (b) graphene-coated $Li(Li_{0.2}Mn_{0.54}Ni_{0.13}Co_{0.13})O_2$ (G-type), and (c) $Li(Li_{0.2}Mn_{0.54}Ni_{0.13}Co_{0.03}Cr_{0.10})O_2$ cathodes (C-type). Pristine material reveals an apparent voltage decay on charge-discharge, whereas the G-type and C-type cathodes tend to retain the initial voltage. However, C-type shows larger capacity fading during electrochemical cycles. The graphene-coated cathode appears to exhibit better performance with lower voltage decay on charge-discharge. The dQ/dV plots between P-type and C-type were slightly different, while the plot in the G-type cathode revealed a notable dissimilar pattern. In all cases, some peaks related to the phase transition from the layered structure into the spinel were identified. Regardless of the improved treatments in the cathode composite, the phase transition appears to be unavoidable during the Li^+ (de)intercalation. The electrochemical activation of Li_2MnO_3 component was also confirmed. The local structure of the integrated-composite system between Li_2MnO_3 (monoclinic, C2/m) and $LiMO_2$ (trigonal, $R\bar{3}m$) was successfully examined by the XRD, Raman spectroscopy, ATR-FTIR, SQUID, and

XANES/EXAFS. A precise estimation on the oxidation states of the P-type (+3.783) and G-type (+3.888) cathodes can be deduced from the SQUID magnetic measurement and XANES fingerprint analysis. Both cathodes revealed an oxidation state of Mn lower than +4, which is attributed to the presence of the low-spin (LS) Mn^{3+} in the composite. Therefore, a slight contribution to the charge compensation mechanism or XANES spectra shift would be anticipated also from the Mn during Li^{+} (de)intercalation. For all samples, the magnetic measurements confirm the presence of some Ni^{2+} ions in the lithium-layers of the cathode composites.

The atomic phase formation of the transition metals in the $Li(Li_{0.2}Mn_{0.54}Ni_{0.13}Co_{0.13})O_2$ cathode from different synthesis (calcination) temperature (600, 700, 800, and 1000 °C) has been also studied. The spectroscopic investigations suggest that the cathode has both the characteristic of Li_2MnO_3 and $LiMO_2$ (M=Mn, Co, and Ni) components. However, the leading character within the composite is likely to change upon the synthesis temperature. In the bulk, the composite synthesized at 600 and 700 °C reveals more $LiMO_2$ character, whereas the active material produced from 800/1000 °C shows more Li_2MnO_3 character. Our XAS findings suggest that the major source for the cation ordering also varies, depending on the calcination temperature. The condition of the cation arrangement in the pristine material is one of the key factors that governs the performance and stability of the lithium-ion battery during operation. Overall, the calcination temperature of 800 °C results in a balanced condition which is suitable for the pristine active material in the battery cathode.

Based on the experimental results, the graphene-coated active material calcined at 800 °C is intentionally chosen as the optimum cathode. However, the phase transition into the spinel during cycling couldn't be suppressed either by the Cr incorporation or graphene-coating. The issue of the phase transition is an intriguing topic which could be usefully explored in further chapters (Chapter7 and Chapter 9).

Chapter 6 Charge Compensation Mechanism in the Graphene-coated $Li_{1.2}Mn_{0.54}Ni_{0.13}Co_{0.13}O_2$ Cathode

In the previous chapter, the graphene-coated $Li_{1.2}Mn_{0.54}Ni_{0.13}Co_{0.13}O_2$ active material calcined at 800 °C was found to be the suitable cathode for the high-capacity lithium ion battery. In this chapter, an *in operando* XAS (XANES/EXAFS) investigation was conducted using a specially-designed coin cell with the active material included. The main purpose of this chapter is to examine the charge compensation mechanism that holds the key to the elucidation of the battery capacity in the integrated-composite cathode.

6.1 Introduction

Debate continues about the correct understanding of the charge compensation mechanism in the Li-rich layered oxide cathode. One major principle in this mechanism is the redox reaction of the transition metals (Mn, Co, Ni, Cr) with the ability to reach their maximum oxidation state on charge. It is well known that the intimate structural integration between Li_2MnO_3 (monoclinic, C2/m) and $LiMO_2$ (trigonal/hexagonal, $R\bar{3}m$), where M indicates transition metals, provides the high charge capacity showing a large voltage plateau above ~4.5 V during the initial charge in this battery system. Numerous studies[64,66,83,86–92] have examined the involvement of the transition metals on the charge compensation mechanism by using *in situ* X-ray absorption spectroscopy (XAS) method. It is generally accepted that the transition metals are likely to be fully oxidized into Mn^{4+}, Co^{4+}, and Ni^{4+} during the charge up to ~4.5 V[83,88,90,92]. To be specific, the oxidation of the Co changes from Co^{3+} into Co^{4+}, whereas the redox reaction of nickel consists of a two-stage reaction such as from Ni^{2+}/Ni^{3+} into Ni^{3+}/Ni^{4+} on charge. As a consequence, a larger energy shift (approximately 3.0 ~ 4.0 eV) would be identified in the Ni K-edge XANES compared with Co due

to the two-stage redox reaction of nickel[66,88,90,92]. On the other hand, the correct oxidation state of Mn in the pristine material remains unclear. It is beleived that the Mn oxidation state stays at +4 in the pristine material showing little participation in the charge compensation mechanism by the oxidation change. However, Huang et al.[93] reported the presence of the low-spin Mn^{3+} ion in the lithium-layered composite. Another study, conducted by Prasad et al.[94], also provides supportive evidence for the low-spin configuration of the Mn ions (Mn^{3+}) in the lithium-layered oxide cathode. In a more recent study, Simonin et al.[91] has found the presence of the low-spin Mn^{3+} ions in the cathode composite. The average oxidation state of Mn in the lithium-rich layered oxide was evaluated to be +3.75 by the combined analysis from the *in situ* XAS and magnetic measurement. Hence, a part of the spectral shift of the Mn K-edge XANES could be considered as an actual oxidation change from the oxidation state lower than tetravalent into the tetravalent. This may contribute to the charge compensation mechanism. However, the total oxidations from the transition metals are not sufficient to compensate the entire battery capacity[88–90,92]. It has been thus assumed that there exists another charge compensation mechanism. Armstrong et al.[95] reported the oxygen loss with structural modifications at ~4.5 V where the voltage plateau occurs. The Li^+ extraction from the host material leads to the removal of the electrons from the coordinated O^{2-} in the crystal lattice, and this process provides extra capacity. However, the amount of the O^{2-} in the bulk of the cathode is still not enough to cover the rest of the extra charge in the integrated-composite system. Detailed examination showed that the participation of the O^{2-} from the surface of the electrode also contributes to the large extra charge[76,95,83]. Eventually, the participation of the O^{2-} both from the surface and the bulk is likely to cause the oxygen evolution from the surface ($O^{2-} \rightarrow 1/2O_2 + 2e^-$). This reaction is followed by the migration of Li^+ from the transition metal layers into the lithium layers. Consequently, the migration produces the vacancies in the transition metal layers. A net loss of lithia (Li_2O) from the electrode component (Li_2MnO_3) above ~4.5 V can give

rise to the formation of the MnO_2 composite that is electrochemically activated (refer to equation 2.24 in section 2.5.5.1). Concomitantly, transition metal ions migrate into the lithium layers through the vacancies formed. The lithia (Li_2O) extraction followed by the migration of the transition metals from the surface into the vacated lithium sites was proposed by Tran et al.[76], namely, the lattice densification model suggest an irreversible cation rearrangement at the voltage plateau.

The aim of the present study is to investigate the 'charge compensation mechanism' in the graphene-coated $Li(Li_{0.2}Mn_{0.54}Ni_{0.13}Co_{0.13})O_2$ cathode for the lithium-ion battery. The highly element-specific manner of synchrotron XAS allows to precisely examine the chemical, structural, and electronic states of the transition metals (Mn, Co, and Ni) during the initial charge. A specially designed *in operando* cell enables to investigate the local atomic environment even in the highly complicated cathode material. The oxidation state change for Mn, Co, and Ni was evaluated by the XANES fingerprint method. Also, the spectral shift of K-edge XANES was measured to examine the contributions of the transition metals to the charge compensation mechanism. Fourier transform magnitudes (k^3-weighted) for Mn, Co, and Ni were presented in R-space upon charge. Structural changes were quantified by EXAFS fitting on the 1st coordination shells (Mn-O, Co-O, and Ni-O).

6.2 Experimental Section

6.2.1 Active material synthesis

The active material of $Li(Li_{0.2}Mn_{0.54}Ni_{0.13}Co_{0.13})O_2$ was prepared by the spray-dryer assisted sol-gel method. The detailed synthesis process is fully described in section 4.1.1 and 4.1.2. The graphene-coated $Li(Li_{0.2}Mn_{0.54}Ni_{0.13}Co_{0.13})O_2$ composite in this section is denoted as 'GR-type' composite.

6.2.2 Electrochemistry test on the normal coin cell

The normal coin cell without the X-ray window was electrochemically cycled in the voltage range between 2.0 V and 4.8 V vs. Li^0/Li^+ using a galvanostatic charger. At first, the coin cell (active material: 3.86 mg) was charged and discharged with the current rate of 0.05 C (0.0386 mA) for the initial two cycles. This slow charge process is known as 'formation cycle' to fully active the potential of the lithium-ion battery. At second, the coin cell was cycled with a current rate of 0.2 C (0.1544 mA) for 50 cycles. The dQ/dV analysis method was chosen to understand the redox reaction of graphene-coated $Li(Li_{0.2}Mn_{0.54}Ni_{0.13}Co_{0.13})O_2$ coin cell on charge-discharge. The analysis of dQ/dV plot was based on the galvanostatic profile up to 50th cycle.

6.2.3 In operando XAS cell preparation

A novel design coin cells (CR-2025Q) with X-ray windows were used to perform the *in operando* test. The cell assembling procedure is described in section 4.2.1 in detail. The diameter and thickness of the coin cells were measured to be 20 mm and 2.5 mm, respectively.

6.2.4 Synchrotron XAS experiment and data analysis

The *in operando* investigation was conducted with the synchrotron XAS. The beam experiment was carried out on B18 Core EXAFS beamline at Diamond Light Source (DLS, UK). The size of the beam spot on the cells was approximately 140 x 140 microns. XAS spectra were collected in transmission mode at the Mn (6.537 keV), Co (7.712 keV), and Ni (8.339 keV) K-edges using a Si (111) double crystal monochromator at room temperature. The beam energy was initially calibrated using Mn, Ni, and Co foils. The energy was tuned to 7.1 keV, 8.225 keV, and 9.3 keV, for Mn, Co, and Ni analysis respectively. The GR cell (active material: 6.587 mg) was charged at a rate of 0.125C (0.164 mA) in the voltage window of 4.8-2.0 V vs. Li^0/Li^+ in which the 1C

signifies 250 mA/g current density. The prepared coin cells were directly clamped to the galvanostatic charger with wires in order to perform the *in operando* XAS investigation.

Data interpretation was performed with ATHENA/ARTEMIS software package [159] using IFEFFIT code, by extracting the spectra data from EXAFS and XANES. The XAS data were normalized with a spline function, and the normalized EXAFS spectra were converted from energy (eV) to k-space and weighted by k^3. This was followed by the Fourier transformation into R-space (uncorrected phase shift). Structural parameters such as the distance between the neighbouring shells, EXAFS Debye–Waller factor ($\exp(-2\sigma^2 k^2)$), and the EXAFS R-factor were obtained by fitting within the ARTEMIS application with the FEFF 6 algorithm with atomic coordination number (CN) of 6 for Mn and Co. Multiple numbers of atomic coordination (e.g. CN=6, CN=4/2, CN=2/4) was chosen for the Ni EXAFS fitting during the first charge. The shift from the edge energy (ΔE_0) was also refined within the application. EXAFS fitting was carried out with two-phase system and the fitting ranges of the R-space were 1-3.35 Å, 1-3.8 Å, and 1-3.65 Å for Mn, Co, and Ni respectively.

6.3 Results and Discussion

6.3.1 Evaluation of the electrochemical properties of the Graphene-coated $Li(Li_{0.2}Mn_{0.54}Ni_{0.13}Co_{0.13})O_2$ cathode

Figure 6.1 exhibits the electrochemical property of the graphene-coated $Li(Li_{0.2}Mn_{0.54}Ni_{0.13}Co_{0.13})O_2$ coin cell (active material: 3.86 mg) without the X-ray window. First and second cycles were charged and discharged with a current rate of 0.05 C (0.0386 mA) in order to fully activate the electrochemical cell. This process is known as a formation cycle. Further cycles were charged and discharged with a current rate of 0.2 C (0.1544 mA). A capacity fading phenomena (red arrow in Figure 6.1a) could be observed on charge-discharge. The columbic

efficiency on the initial cycle reveals 76.5 %, but it remains high as ~98-99 % from the second cycle to the 50th cycle.

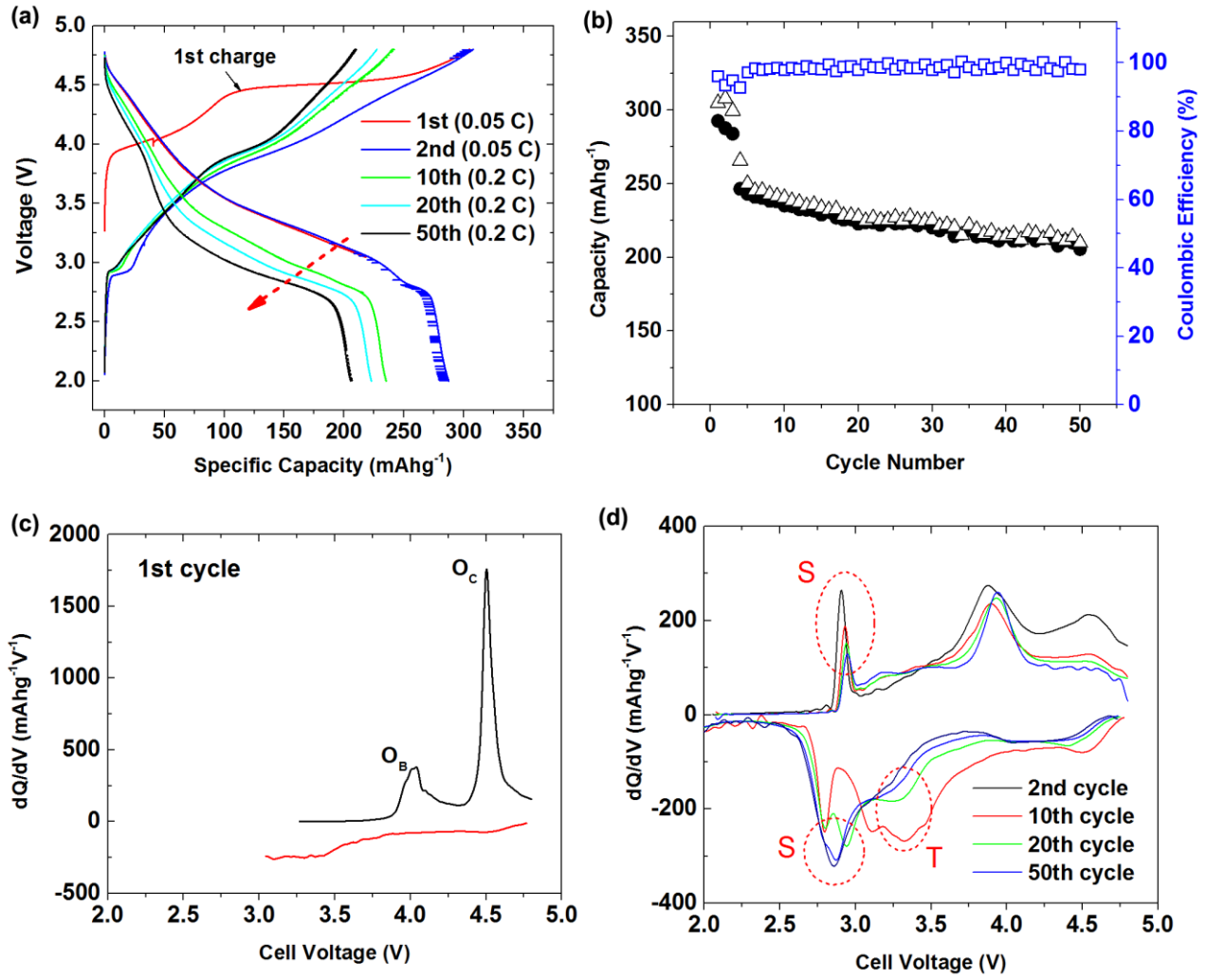


Figure 6.1 Electrochemical property of graphene-coated $Li(Li_{0.2}Mn_{0.54}Ni_{0.13}Co_{0.13})O_2$ cathode (G-type). (a) Galvanostatic profile up to 50th cycle with current rate of 0.2 C (Formation cycles used 0.05 C-rate). (b) Specific charge (black circle) and discharge capacity (white triangle) with Coulombic efficiency (%). (c) dQ/dV plot of initial cycle. (d) dQ/dV plots on furher cycles. Red arrow indicates the curve shift upon electrochemical cycles.

The high electrochemical performance is due to the integrated-composite system between Li_2MnO_3 (monoclinic, C2/m) and $LiMO_2$ (trigonal, $R\bar{3}m$) components. The dQ/dV plot on the initial cycle is presented in Figure 6.1c. Two distinctive peaks were recorded. Peak O_B is associated with the redox reaction of the transition metals (Ni^{2+}/ Ni^{3+}/Ni^{4+} and Co^{3+}/Co^{4+}), while peak O_C is attributed to the electrochemical activation of Li_2MnO_3 component. The dQ/dV plots on further

cycles are shown in Figure 6.1d. There were three notable peaks during the redox reaction. Those peaks at ~2.8-3.0 V (denoted as S) is related to the phase transition from layered structure into the spinel (or cubic spinel-like) phase[84,160]. The peak T at ~3.3 V explains the redox reaction from Mn^{4+} into $Mn^{(4-x)+}$, where 0<x<1, in the layered $Li_{1-x}MnO_2$ composite[84,160]. On further charge-discharge, the peak T decreases with the rise of peak S. This observation appears to be associated with the phase transition into the spinel phase on consecutive charge-discharge[84,121].

6.3.2 In operando XANES at Mn K-edge

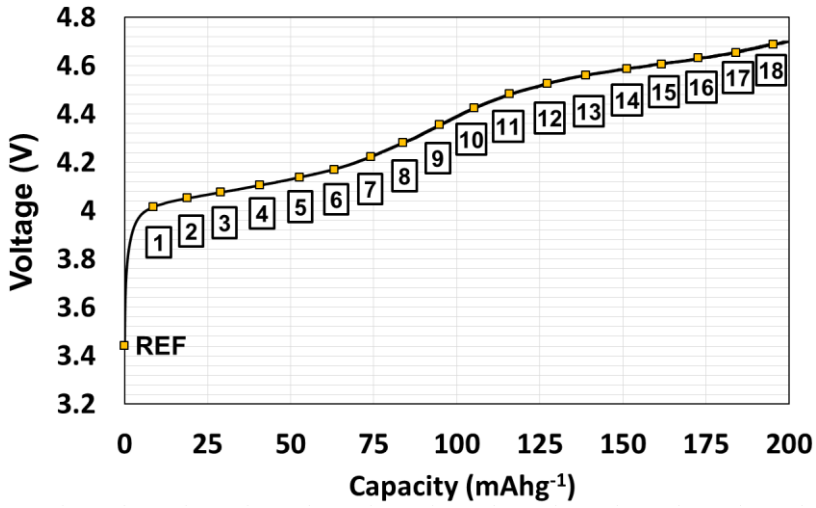


Figure 6.2 Galvanostatic profile on the in operando cells at a charge rate of 0.125 C. Points signify the collection of XAS spectra numbered 1, 2 …18, collected at charge points in the galvanostatic profile. REF indicates the measurement of coin cell without any current.

The galvanostatic profile on the *in operando* XAS measurement is presented in Figure 6.2. A total of 19 data points were collected. The XAS measurement began at the 'REF' point at which no current was applied. Figure 6.3 reveals the XANES investigation at the Mn K-edge and Mn K pre-edge of the graphene-coated $Li(Li_{0.2}Mn_{0.54}Ni_{0.13}Co_{0.13})O_2$ *in operando* cell. Three of significant absorptions (N1, N2, and N3) were identified with pre-edge peaks (P) at Mn K-edge XANES, as can be seen from Figure 6.3a. The red arrows indicate the the direction of spectral shifts on charge. Absorption **N1** would be assigned to the electric dipole transition from 1s to 4p with a shakedown process resulting from the ligand-to-metal charge transfer (LMCT), while absorption **N3**

corresponds to the electric dipole transition from 1s to 4p without the shakedown process. The final states of absorption **N1** and **N3** correspond to $1s^1c3d^{n+1}$ $L4p^1$ and $1s^1c3d^n4p^1$, respectively, where c is a 1s core hole and L is an oxygen 2p ligand (Mn^{4+}: n=3). The absorption N2 reveals spectra shifts in the opposite direction showing isosbestic points at ~6549 eV and ~6554 eV. The appearance of those isosbestic points may signify the change of the electronic structure with a constant oxidation state[90] or a single reaction[89,170]. The oxidation state at the REF point can be deduced from the fingerprint comparison with the NMC composite. The main edge position of the REF spectra was slightly lower than that of the $Li(Ni_{1/3}Mn_{1/3}Co_{1/3})O_2$ (NMC: $Mn^{4+}/Ni^{2+}/Co^{3+}$) spectra as shown in Figure 6.3a, indicating slightly lower oxidation state than +4. Indeed, it has been found that the Mn in the pristine state presents in a mixed oxidation state between low-spin Mn^{3+} and Mn^{4+} as evidenced by the results obtained from the SQUID measurements in section 5.1.3.4 and 5.2.3.2. During charge, the Mn K-edge XANES spectra moved towards higher energy. It is the third collection point (marked as 2) of XAS spectra (~4.05 V) that closely corresponds to the $Li(Ni_{1/3}Mn_{1/3}Co_{1/3})O_2$ (NMC) spectra. The entire spectral shift was found to be approximately 1.37 eV on charge.

It is interesting to note that a large amount of spectral shift (1.16 eV) was recorded before ~4.5 V as shown in Figure 6.3a, and this part probably involves with the charge compensation mechanism resulting from the oxidation state change. On the other hand, the spectral shift above ~4.5 V displays only 0.21 eV energy change which is very small portion to produce charge capacity from the oxidation change. However, the Li_2MnO_3 is believed to be electrochemically activated above ~4.5 V and thus provides large amount of extra capacity to the lithium-ion battery. It is probable that there might exist different reactions for the charge compensation mechanism above ~4.5 V in the Li-rich layered oxide cathode. One possible source is the Li^+ deintercalation from the coordinated O^{2-} in the crystal lattice providing extra capacity[95]. Another possible source which

could have contributed to the large capacity is the participation of the O^{2-} from the surface of the electrode[76,95,83].

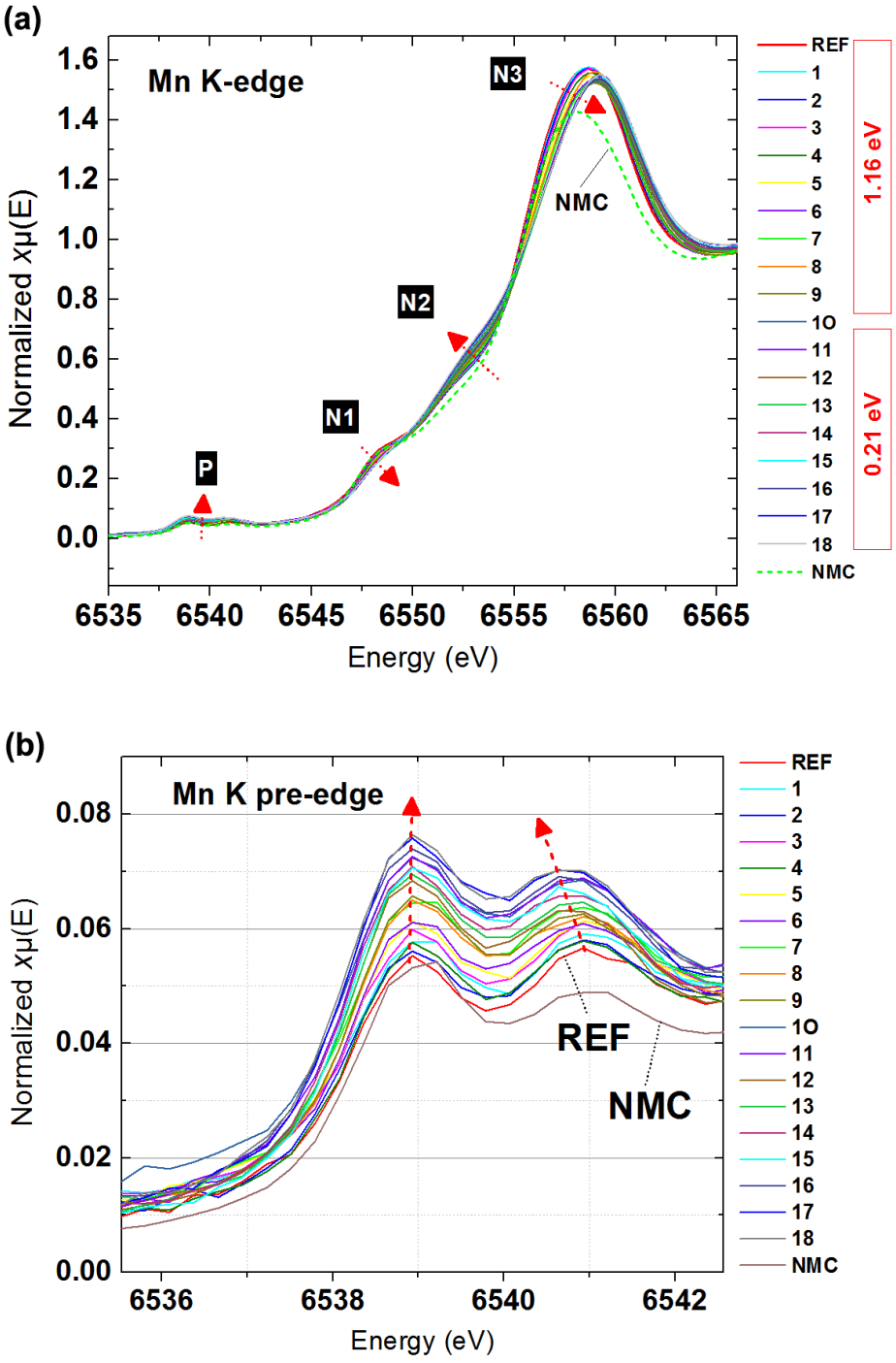


Figure 6.3 Normalised XANES spectra of $Li(Li_{0.2}Mn_{0.54}Ni_{0.13}Co_{0.13})O_2$ during the initial charge (a) at Mn K-edge and (b) Mn K pre-edge. Numbers indicate the collection point of XAS spectra, which corresponds to the charge points in the galvanostatic profile. REF represents the measurement point of the coin cell without any current. NMC is the $Li(Ni_{1/3}Mn_{1/3}Co_{1/3})O_2$ composite used for comparison. Red arrows indicate the trend of spectra shift upon charge.

The oxygen ions both in the surface and bulk involve with the evolution of the oxygen from the surface. The oxygen evolution is followed by the Li^+ migration from the transition metal layers into the lithium layers (interslab) forming vacancies in the transition metal layers. As a consequence, lithia (Li_2O) is extracted from the electrode component (Li_2MnO_3) above 4.5 V during charge and thus results in the formation of the MnO_2 component that is electrochemically active. Double pre-edge peaks were found between 6538 and 6542 eV at the Mn K-edge (Figure 6.3b). These peaks are assigned to 1s-$3d_{t2g}$ (~6538.9 eV) and 1s-$3d_{eg}$ (~6540.93 eV) transitions, which is formally dipole-electric forbidden in a centrosymmetric system. They are allowed here through a weak quadrupole transition or/and 3d-4p orbital hybridization from the loss of centrosymmetric environment by the distortion of the octahedral 3a site in the $R\bar{3}m$.

The intensity of those peaks can be used as an indicative of the distortion from the octahedral geometry. Higher intensity indicates larger distortion from the centrosymmetric environment of the octahedral structure. The intensity of the pre-edge peaks increases, implying a local atomic distortion in the octahedral MnO_6 during Li^+ deintercalation.

6.3.3 In operando XANES at Co and Ni K-edge

XANES spectra collected at the Co K-edge and Ni K-edge during the initial charge are presented in Figure 6.4. The Co K-edge XANES shifted towards higher energy on charge. The energy shift was measured to be ~2.11 eV. The main edge of the Co REF spectra was positioned higher than the Co_3O_4 (Co: +2.67) spectra, but the edge appears to be close to the NMC spectra (Co: +3). Hence, the spectral shifts toward higher energy indicate the redox reaction between Co^{3+} and Co^{4+}. There was a similarity in the oxidation state trend between Co and Mn upon charge. This similarity would be explained by the similar local environment. Ni XANES spectra shift towards higher energy upon charge as shown in Figure 6.4b. Unlike the Mn XANES spectra, no pre-edge peaks

were noted in the Ni K-edge XANES. Thus, it is probable that the atomic environment of Ni in the cathode material is highly symmetrical.

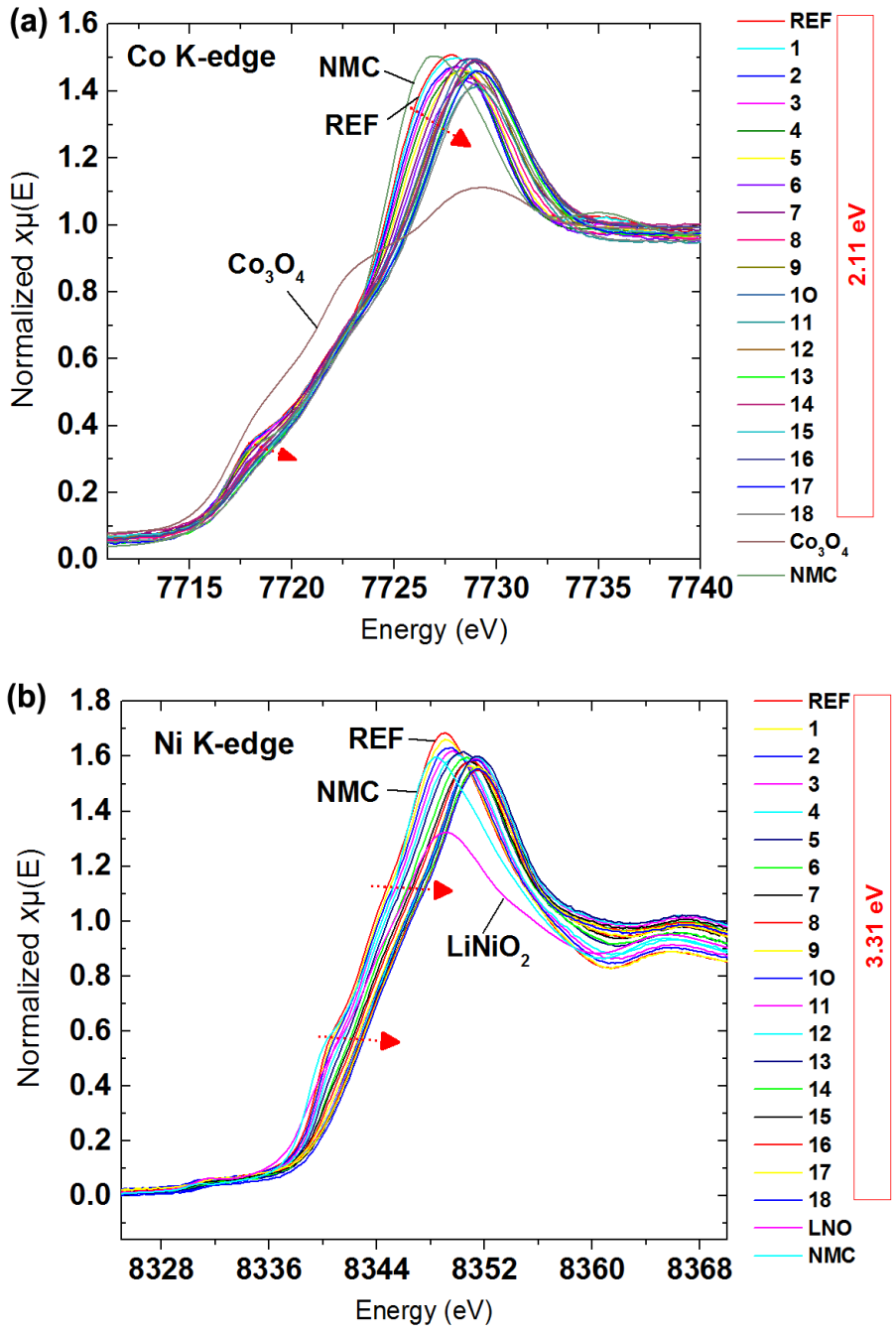


Figure 6.4 Normalised XANES spectra of $Li(Li_{0.2}Mn_{0.54}Ni_{0.13}Co_{0.13})O_2$ during the initial charge (a) at Co K-edge and (b) Ni K-edge. Numbers indicate the collection point of XAS spectra, which corresponds to the charge points in the galvanostatic profile. REF represents the measurement point of the coin cell without any current. NMC represents the $Li(Ni_{1/3}Mn_{1/3}Co_{1/3})O_2$ composite used for comparison. Red arrows indicate the trend of spectra shift upon charge.

Another prominent feature is the parallel energy shift of the XANES spectra, which implies a different local atomic environment compared with that of Mn and Co. The energy shift was calculated to be ~3.31 eV on charge. The Ni K-edge XANES spectra at 'REF' point nearly corresponded to that of the NMC composite (Ni: +2). Therefore, the oxidation state in the REF point can be estimated as +2. The XANES spectrum collected at point 6 (~4.17 V) nearly corresponded to the $LiNiO_2$ composite. This is the location where the oxidation state of Ni can be approximated to +3. The energy shift on Ni K-edge XANES is attributed to the two stage oxidation changes from Ni^{2+}/Ni^{3+} to Ni^{3+}/Ni^{4+}. As a consequence, a large energy shift could be observed in the Ni K-edge XANES as compared with that of the Co and Mn[66,88,90,92].

6.3.4 In operando EXAFS at Mn, Co, and Ni K-edge

The k^3-weighted Fourier transform magnitudes at Mn K-edge of the graphene-coated $Li(Li_{0.2}Mn_{0.54}Ni_{0.13}Co_{0.13})O_2$ cathode are presented in Figure 6.5. There has been a decrease in the level of the intensity from the first peak (Mn-O) on charge as can be seen from Figure 6.5a. This can be explained by the oxygen loss due to the charge compensation mechanism and/or structural distortion in the octahedral MnO_6 environment. The 1st coordination shell (Mn-O) showed relatively higher peak amplitude compared to the 2nd coordination shell of Mn-TM. It appears that the Mn absorber is well-coordinated with the oxygen ions, whereas there present more light scatterers (Li ions or vacancies) in the coordination of the transition metals (Mn, Co, and Ni). Bond length changes of Mn-O were evaluated during the initial charge. The coordination number was constrained to be 6 for the Mn fitting, while major EXAFS parameters such as radial distance to neighbouring atom (R), mean square disorder (σ^2) from the EXAFS Debye-Waller factor ($e^{-2\sigma k^2}$), energy shift (ΔE_0) and R-factors were refined by the calculation. The amplitude reduction factor (S_0^2) was initially refined by the reference compound, and it was scaled to a fixed value of 0.65.

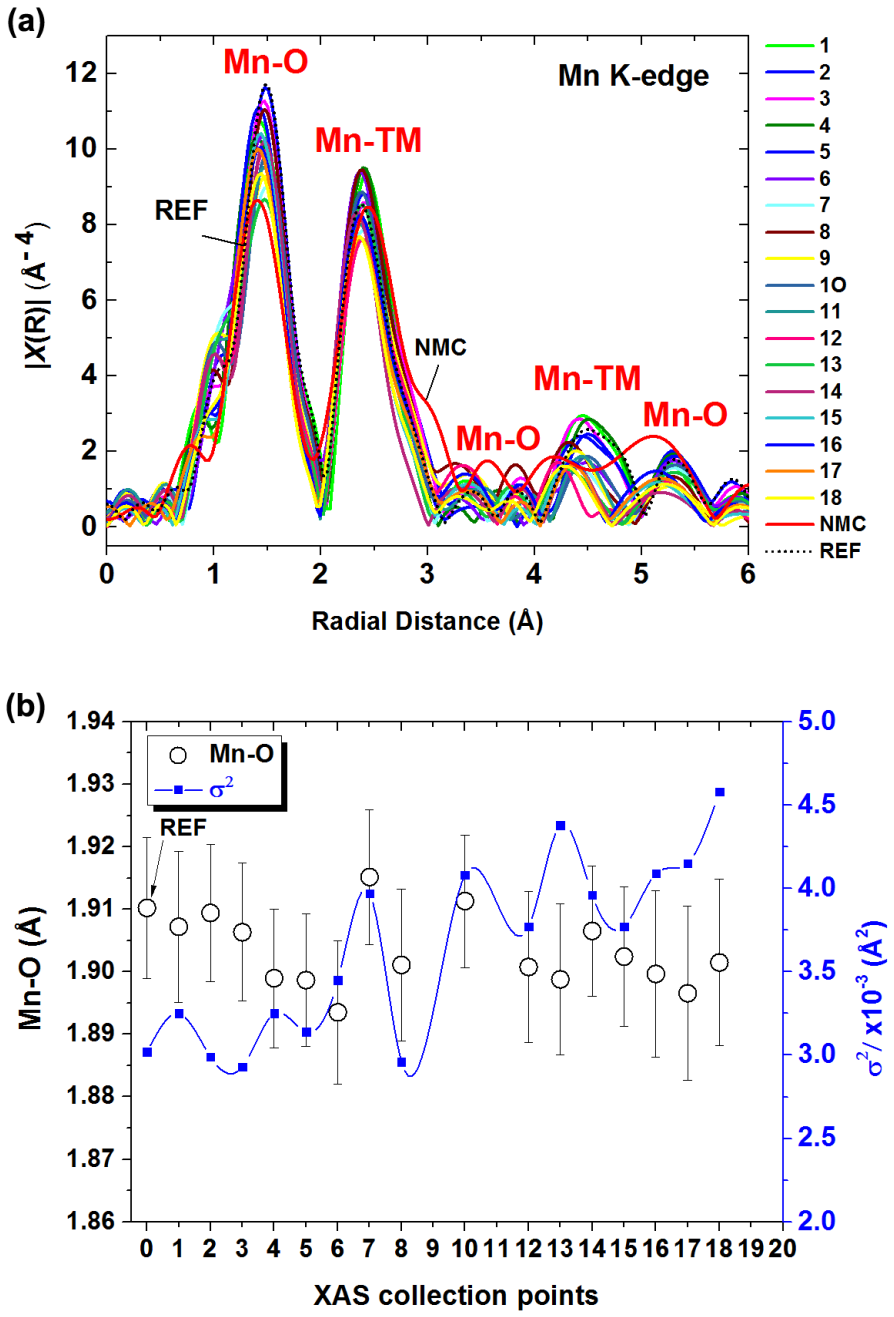


Figure 6.5 (a) Fourier transform magnitudes (k^3-weighted) at Mn K-edge of the graphene-coated $Li(Li_{0.2}Mn_{0.54}Ni_{0.13}Co_{0.13})O_2$ and (b) evaluation of the atomic bond-lengths on the 1st coordination shell (Mn-O) during charge with the the mean-square disorder (σ^2) from the EXAFS Debye-Waller factor.

The atomic bond-lengths of the Mn-O decreases until the XAS collection point 6, and it suddenly increased at point 7 where it corresponds to the voltage level of 4.2 V. Another trend of Mn-O drops could be observed on further charge. This may imply a separation into two different atomic environments in the Mn K-edge. Figure 6.6 compares the k^3-weighted Fourier transform

magnitudes at Co K-edge of the graphene-coated cathode. As in the case of Mn, the 1st coordination shell (Co-O) showed relatively higher peak amplitude compared to the 2nd coordination shell (Co-TM). It is likely that the Co retain a good octahedral symmetry in the CoO_6.

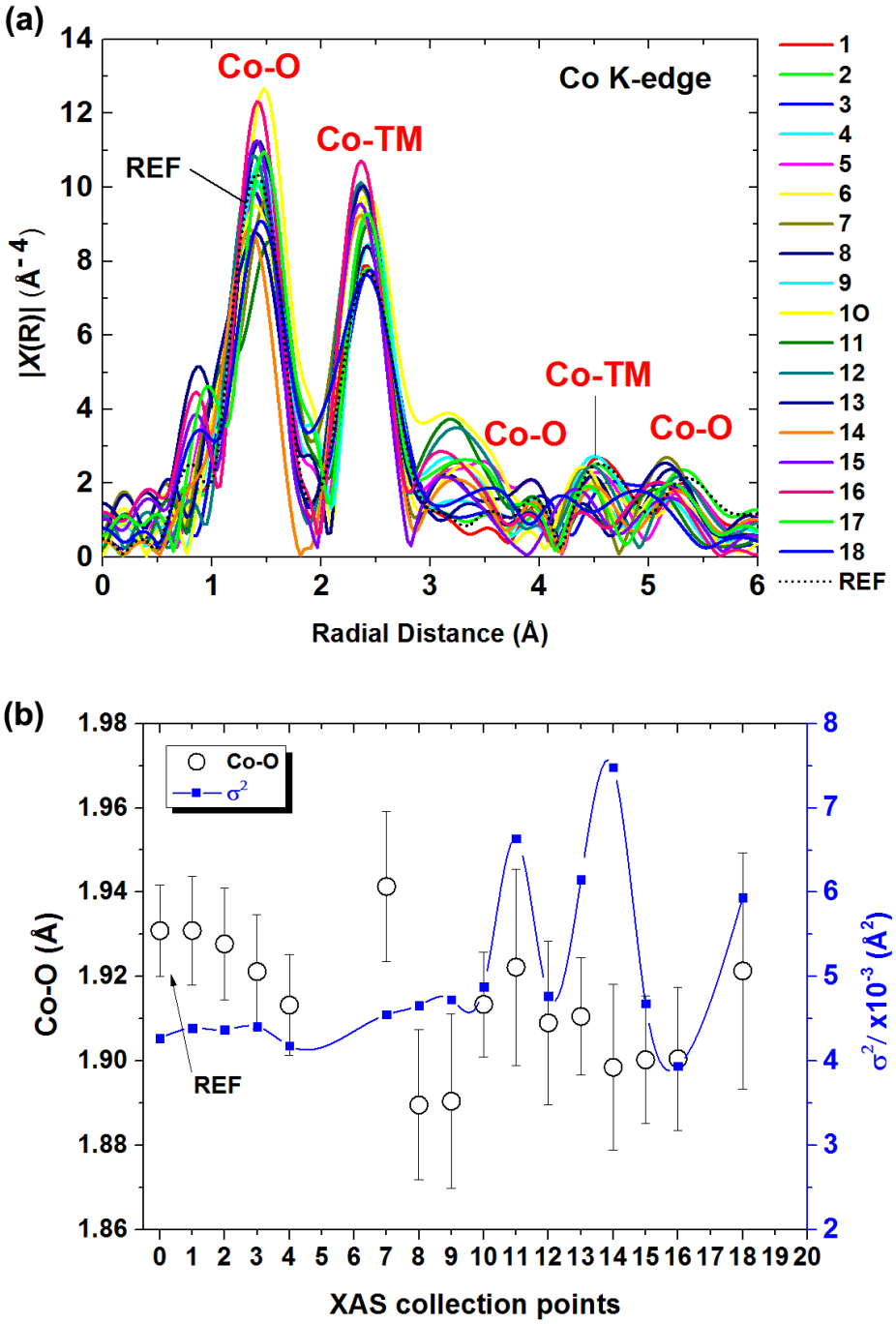


Figure 6.6 (a) Fourier transform magnitudes (k^3-weighted) at Co K-edge of the graphene-coated $Li(Li_{0.2}Mn_{0.54}Ni_{0.13}Co_{0.13})O_2$ and (b) evaluation of the atomic bond-lengths on the 1st coordination shell (Co-O) during charge with the the mean-square disorder (σ^2) from the EXAFS Debye-Waller factor.

Bond length changes of Co-O were evaluated during the initial charge with the identical EXAFS fitting procedure to that of the Mn. The amplitude reduction factor (S_0^2) was initially determined by the fitting, and it was scaled to a fixed value of 0.74. There has been a decrease in the Co-O lengths during charge, and a sudden increment could be identified at XAS collection point 7 (~4.2 V). This followed by the Co-O bond-lengths drop on the further charge as can be seen from Figure 6.6b. This is an indicative of a separation into two different atomic environments in the Co K-edge.

Figure 6.7 exhibits the k^3-weighted Fourier transform magnitudes at Ni K-edge of the graphene-coated cathode. The oscillations in the Ni K-edge EXAFS display dynamic variations upon charge (Figure 6.7a). It was not only the peak amplitudes that vary, but also the peak location that reveals a distinctive change during the initial charge. This may be explained by the appearance of two different lengths of Ni-O bonds attributed to the Jahn-Teller effect from Ni^{3+} (d^7) having an electronic configuration of $t_{2g}^6 e_g^1$. The notable amplitude decreases in the Ni-O on charge is related to the two-stage oxidation ($Ni^{2+} \rightarrow Ni^{3+} \rightarrow Ni^{4+}$) change of Ni. Thus, the octahedral NiO_6 distorts upon the Li^+ deintercalation. The relatively higher amplitude in the Ni-TM imply the presence of a larger number of transition metal atoms around the Ni absorber. It is of importance to note the appearance of the Ni-O-Ni peaks at R ~3.5 Å (Figure 6.7a). During charge, the peak amplitude dynamically deviates from the REF intensity. This peak is associated with those Ni ions that occupy the lithium layers of the cathode. The peak could be initially identified in the REF point, implying the Li/Ni exchange resulting from the chemical synthesis process. The Li/Ni exchange is also confirmed by the Rietveld refinement (refer to section 5.3.3 - Table 5.2) and SQUID analysis (section 5.3.4). A systematic spectral shift at R ~4.9 Å was also identified upon charge with a black-dash arrow. This peak is linked to the Ni-TM-TM scattering. Taken together, those variations at R ~3.5 Å and the systematic spectral shift at R ~4.9 Å may imply the migration of the transition metal ions during Li^+ deintercalation.

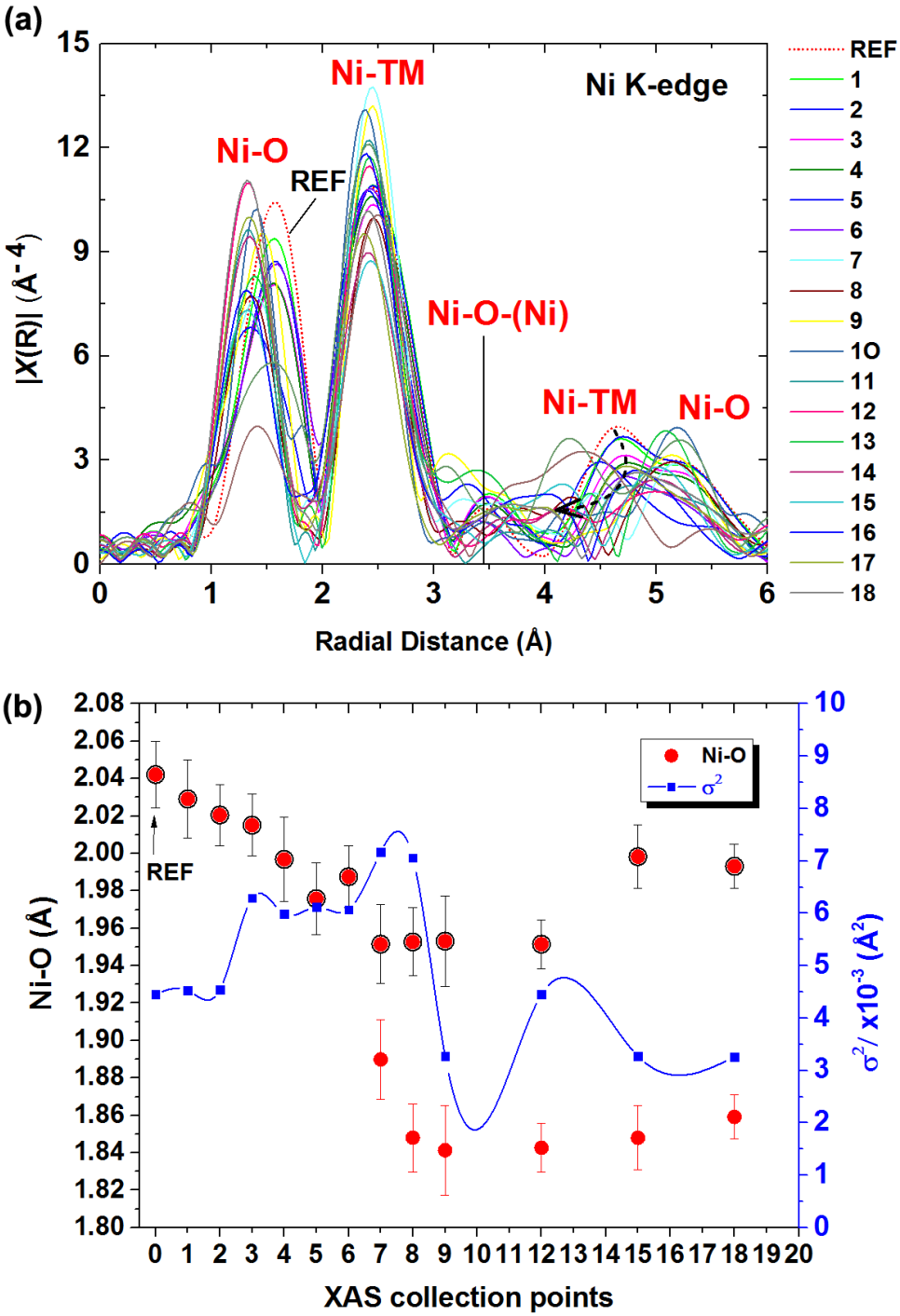


Figure 6.7 (a) Fourier transform magnitudes (k^3-weighted) at Ni K-edge of the graphene-coated $Li(Li_{0.2}Mn_{0.54}Ni_{0.13}Co_{0.13})O_2$ and (b) evaluation of the atomic bond-lengths on the 1st coordination shell (Ni-O) during charge with the the mean-square disorder (σ^2) from the EXAFS Debye-Waller factor. Black arrow indicates the spectral shift at R ~4.9 Å during charge.

The Fourier transforms of Ni EXAFS in the R-space during initial charge is presented in Figure 6.7b. The EXAFS fitting procedure was almost identical to that of Mn and Co, but the coordination

numbers for Ni-O varied upon the state of charge (e.g. CN = 6, 4/2, 3.9/2.1, 1/5…) because of the Ni^{3+} Jahn-Teller effect which leads to the separation into a long and a short Ni-O bond. During charge, the Ni-O bond decreases, and a bond splitting was observed from XAS collection point 7 (~4.2 V). On further charge, the bond length difference between the long Ni-O and short Ni-O tends to gradually increase, and it reached maximum at point 15 (~4.6 V). The bond length difference is projected to drop on further charge above ~4.6 V.

6.4 Conclusion

This chapter has given an investigation on the charge compensation mechanism in the graphene-coated $Li(Li_{0.2}Mn_{0.54}Ni_{0.13}Co_{0.13})O_2$ cathode for a lithium-ion battery. The results obtained from the electrochemical evaluation on the general coin cell revealed the likelihood of the phase transition into the spinel structure. It appears that the graphene coating is able to improve the capacity fading/voltage decay, but it couldn't suppress the phase transition process during charge-discharge.

The *in operando* XANES investigation at Mn K-edge showed a spectral shift of ~1.37 eV during the initial charge. It should be noted that a large fraction of the energy shift (1.16 eV) was already observed before the voltage level of ~4.5 V. The oxidation state of the Mn in the pristine state is believed to be +4 and remain unchanged during charge. Thus, in principle, there should be no spectral shift in the Mn K-edge XANES. However, an obvious energy shift was monitored. There are two possible explanations for this result. One possible reason may be that the spectral shift is due to the structural distortion in the MnO_6 symmetry and/or the effect from the 'Voltage-induced' energy shift. Another reason can be the practical oxidation change of the Mn such as from +3.88 to +4 during charge. It has been found that the Mn in the pristine state can exist in a mixed oxidation state between low-spin Mn^{3+} and Mn^{4+}. This is confirmed by the results obtained

from the SQUID measurements in section 5.3.4 and 5.3.7. The contradiction of the Mn-O length on charge observed by EXAFS is possibly attributed to the oxidation reaction. Also, the location of the Mn K-edge XANES at REF point was found to be lower than that of the $Li(Ni_{1/3}Mn_{1/3}Co_{1/3})O_2$ (NMC: Mn^{4+}) composite. Hence, the oxidation state of Mn in the pristine state appears to be slightly lower than +4. The crucial observation here is the small spectral shift (~0.21 eV) above 4.5 V, implying little contributions to the charge compensation mechanism by the Mn oxidation. However, a large extra capacity was yielded above ~4.5 V as shown in the galvanostatic profile. In this voltage range, oxidation is not the case that can explain the battery capacity. This aspect is also supported by the findings from chapter 7 and chapter 9. The oxidation state change was reversible whether it has a long voltage-plateau as in the initial cycle or not as in the further cycles. One possible explanation of the charge capacity above ~4.5 V is the participation of the O^{2-} both from the surface and the bulk leading to oxygen evolution from the surface of the electrode ($O^{2-} \rightarrow 1/2O_2 + 2e^-$). In the Co K-edge XANES, the spectral shift was measured to be ~2.11 eV. The Co K-edge XANES imply the oxidation change between +3 and +4 during Li^+ deintercalation. The spectral shift in Ni K-edge XANES was found to be the largest among the transition metals as it was calculated to be ~3.31 eV on charge. This large energy shift is attributed to the two stage oxidation changes from Ni^{2+}/Ni^{3+} to Ni^{3+}/Ni^{4+} and thus contributes to the charge compensation mechanism in large extent. It is also interesting to note the bond length separation into the long Ni-O and short Ni-O bonds at ~4.2 V by the Jahn-Teller effect of Ni^{3+} (d^7), as evidenced by the EXAFS analysis. A most notable finding in the Ni local environment is the appearance of the Ni-O-Ni peaks at R ~3.5 Å and the systematic spectral shift at R ~4.9 Å on charge. The peak at R ~3.5 Å is indicative of the Li/Ni exchange. The variations in those peaks suggest the migration of the transition metal ions during the charge compensation mechanism.

Chapter 7 In Operando XAS Study of Atomic Phase Reversibility in the Graphene Coated $Li(Li_{0.2}Mn_{0.54}Ni_{0.13}Co_{0.13})O_2$ Cathode

It is generally known that the oxidation and electronic structure changes are reversible on electrochemical cycle. Also, the interatomic bond-length change of the coordination shells appears to be reversible. In addition, the bond-length splitting from the Jahn-Teller distortion attributed to the Ni^{3+} ion is likely to be reversible on charge-discharge. The reversibility is more pronounced in terms of the crystal structure changes during cycle, as identified from numerous studies. In this chapter, for the first time in the lithium-ion battery study, the Continuous Cauchy Wavelet Transform (CCWT) method is applied to the *in operando* EXAFS signals to further understand the atomic environment. A particular attention is paid to the impact on the 'atomic phase change' from the Li^+ (de)intercalation.

7.1 Introduction

In the present study, *in operando* XAS was conducted on the graphene-coated $Li(Li_{0.2}Mn_{0.54}Ni_{0.13}Co_{0.13})O_2$ cathode battery with the help of the Continuous Cauchy Wavelet Transform (CCWT)[147] analysis to examine in more detail the atomic state of the transition elements during the initial electrochemical cycle. Developing a high capacity cathode with good chemical and structural stability remains the main objective of the lithium-rich Mn-based composites. The capacity/voltage fading and stability issues in this battery system has been already discussed in the previous chapter, but it is worth summarizing that the Lithia (Li_2O) removal followed by the extraction of the oxide ion vacancies involving the transition metals migration is known to be the dominant mechanism of irreversible capacity loss during the first cycle[7,8,122,171]. This is likely to be linked to the nature of structural integration between Li_2MnO_3 (monoclinic,

C2/m) and $LiMO_2$ (trigonal, $R\bar{3}m$), where M indicates a transition metal ion (Mn, Ni or Co), in the lithium-rich Mn-based oxide cathode. The mixed transition metals (M) play the key role in charge compensation mechanism that allows the Li^+ (de)intercalation between electrodes. The charge compensation mechanism during the initial charge and further electrochemical cycles is not yet clearly understood, but its main principle can be described by the redox reaction of the transition metals with the capability to reach their maximum oxidation state (+4) during the charge and reverse to their initial oxidation state (Co^{3+}, Ni^{2+}, and Mn^{4+}) during the following discharge. Numerous attempts have been made[64,66,83,86–92] to examine the charge compensation from the transition metals by using X-ray absorption spectroscopy (XAS). The results from the normalized XANES spectra reported the full oxidation of the Ni^{2+} and Co^{3+} into Ni^{4+} and Co^{4+} during charge up to ~4.5 V and their reverse reduction during discharge[66,83,88,90,92,116]. In particular, the redox reaction of nickel is believed to be a two-stage reaction such as Ni^{2+}/Ni^{3+} and $Ni^{3+/}Ni^{4+}$. Therefore, it results in a large energy shift (approximately 3.0 ~ 4.0 eV) in K-edge XANES compared with that of the Co and Mn[66,88,90,92]. On the other hand, it is believed that the Mn stays at a tetravalent (+4) state during the electrochemical process. The electrostatic repulsion between the transition metals and/or Li^+ is one of the vital factors that must be considered. For example, the activation of the Li_2MnO_3 phase causes the increase in the electrostatic repulsion between the close-packed oxygen layers and thus results in the expansion of the *c*-lattice in the $R\bar{3}m$ crystal structure[122,123,172]. Therefore, many studies[88,90,91,99,118,122,123] linked the crystal structure, local atomic environment and chemical state changes with electrochemical properties in order to elucidate key reactions and mechanisms that determine the battery performance/stability during electrochemical cycle. However, much of the studies up to now has been focused on quantifying the structural differences between the charge and discharge states, based on the phase transition in the crystal lattice or local geometry changes during Li^+ (de)intercalation. Structural changes can be examined and quantified

at the atomic level by X-ray absorption spectroscopy (XAS) method due to its highly element-specific manner[173]. However, the information obtained from the quantification is limited to a one-dimensional function, and this may provide incomplete interpretation of the atomic environment during the electrochemical process.

Here, a new approach is suggested in order to examine in more detail the atomic state of the transition elements with the help of the Continuous Cauchy Wavelet Transform (CCWT)[147] analysis performed on *in operando* XAS data for graphene-coated $Li(Li_{0.2}Mn_{0.54}Ni_{0.13}Co_{0.13})O_2$ cathode. A specially designed cell (refer to section 4.2.1) was prepared for the *in operando* study. The visualization of the CCWT modulus were obtained from the decomposition of the *k*-space and R-space signals from the K-edge EXAFS of Mn, Co, and Ni. With the wavelet transform, precise characterization was performed on the atomic environment of each transition metal in the lithium-ion battery system of the graphene-coated $Li(Li_{0.2}Mn_{0.54}Ni_{0.13}Co_{0.13})O_2$ cathode during the first electrochemical cycle (0.5 C rate). One of the major findings from the visual inspection is the information about the 'atomic phase reversibility' which is difficult to obtain from one-dimensional Fourier transformed EXAFS plots. It is because the one-dimensional plot is likely to emphasize the low values in the *k*-space, omitting important structural information linked with the multi-scattering in the signal at high *k*-value. As such, the current study delivers a new approach to examine the precise phase transition in the atomic environment for the lithium ion battery electrodes during electrochemical cycle.

7.2 Experimental Section

7.2.1 Active material synthesis

The active material $Li(Li_{0.2}Mn_{0.54}Ni_{0.13}Co_{0.13})O_2$ was synthesized by the spray-dryer assisted sol-gel method. The synthesis process is described in section 4.1.1 and 4.1.2.

7.2.2 Magnetic measurement

Magnetic properties of the active material was investigated using a SQUID-VSM Magnetometer (Quantum Design). The weight of the graphene-coated active material was precisely measured by a digital scale (=1.2 mg). The measured sample was put into a small capillary, and placed into a brass stick (holder). The magnetization measurement was conducted under a magnetic field of 1000 Oe in the temperature range of 5 – 300 K. Magnetic field of 60k Oe was applied (at 5 K) to evaluate the magnetic susceptibility.

7.2.3 Assembling of *in operando* coin cell

A specially-designed coin cell (CR-2025-alpha) with X-ray window was prepared to perform the *in operando* investigation. The assembling procedure is presented in section 4.2.1. The diameter and thickness of the coin cells were measured to be 20 mm and 2.5 mm, respectively.

7.2.4 In operando XANES/EXAFS

The synchrotron *in operando* XAS experiment was conducted on B18 Core EXAFS beamline at Diamond Light Source (DLS, UK). XANES/EXAFS spectra were collected in transmission mode at the Mn (6.537 keV), Co (7.712 keV), and Ni (8.339 keV) K-edges using a Si (111) double crystal monochromator at room temperature. The intensity of incident and transmitted X-ray beam was measured by ionization chambers. The monochromatized beam on the cell window was approximately 140 x 140 microns. The beam energy was initially calibrated using the reference foil spectra of Mn, Ni, and Co, and then the energy was tuned to 7.1 keV, 8.225 keV, and 9.3 keV, for Mn, Co, and Ni K-edge analysis respectively. The CR-2025-alpha cell (6.34 mg) was charged at a rate of 0.5 C (0.634 mA) in the voltage window of 4.8-2.0 V vs. Li^0/Li^+ in which the 1C signifies 250 mA/g current density. The electrochemical cycle was conducted on the *in operando* cell by clamping the coin cell to the battery charger with electric wires.

7.2.5 XAS Data interpretation and CCWT analysis

Data interpretation was carried out with a IFEFFIT computation code by using the ATHENA[159] software package. The collected XAS spectra were normalized. The EXAFS spectra were then converted from energy into frequency in *k*-space with multiplication of k^3 in order to amplify the oscillations in high k-space ($k^3\chi(k)$). This was followed by the Fourier transformation of the EXAFS oscillations (k-space) into the *R*-space (uncorrected phase shift), so as to evaluate the distance information between coordination shells. Major EXAFS parameters such as the distance between the neighbouring shells (R), EXAFS Debye–Waller factor ($\exp(-2\sigma^2k^2)$), amplitude reduction factor (S_0^2), energy shift (ΔE_0), and the EXAFS *R*-factor were obtained by fitting within the ARTEMIS application. The fitting was processed using the FEFF 6 algorithm with atomic coordination number (CN) of 6 for Mn and Co transition metals. Multiple atomic coordination numbers, which correspond to long and short Ni-O bonds, were used for the Ni EXAFS fitting. After a preliminary refinement, the amplitude reduction factor (S_0^2) was scaled to 0.7, 0.67, and 0.92 for Mn, Co, and Ni respectively. The EXAFS least square fits were carried out based on two-phase composite system with the fitting range of 1-3.65 Å for Mn, Co, and Ni. The Continuous Cauchy wavelet transform (CCWT) analysis was performed on the k^3-weighted normalized EXAFS data using a matlab code. The values in the k-space for the wavelet transform were 0-11.9 $Å^{-1}$, 0-11.7 $Å^{-1}$, and 0-15.8 $Å^{-1}$ for Mn, Co, and Ni, respectively. The Cauchy wavelet order (n) for Mn, Co, and Ni were set to 500, 150, and 250, respectively. The *R*-space for the wavelet analysis was limited from 0.2 Å to 6.0 Å with the interval number of 400, which corresponds to the pixel numbers.

7.3 Results and Discussion

7.3.1 Oxidation states evaluation and magnetic properties measurements

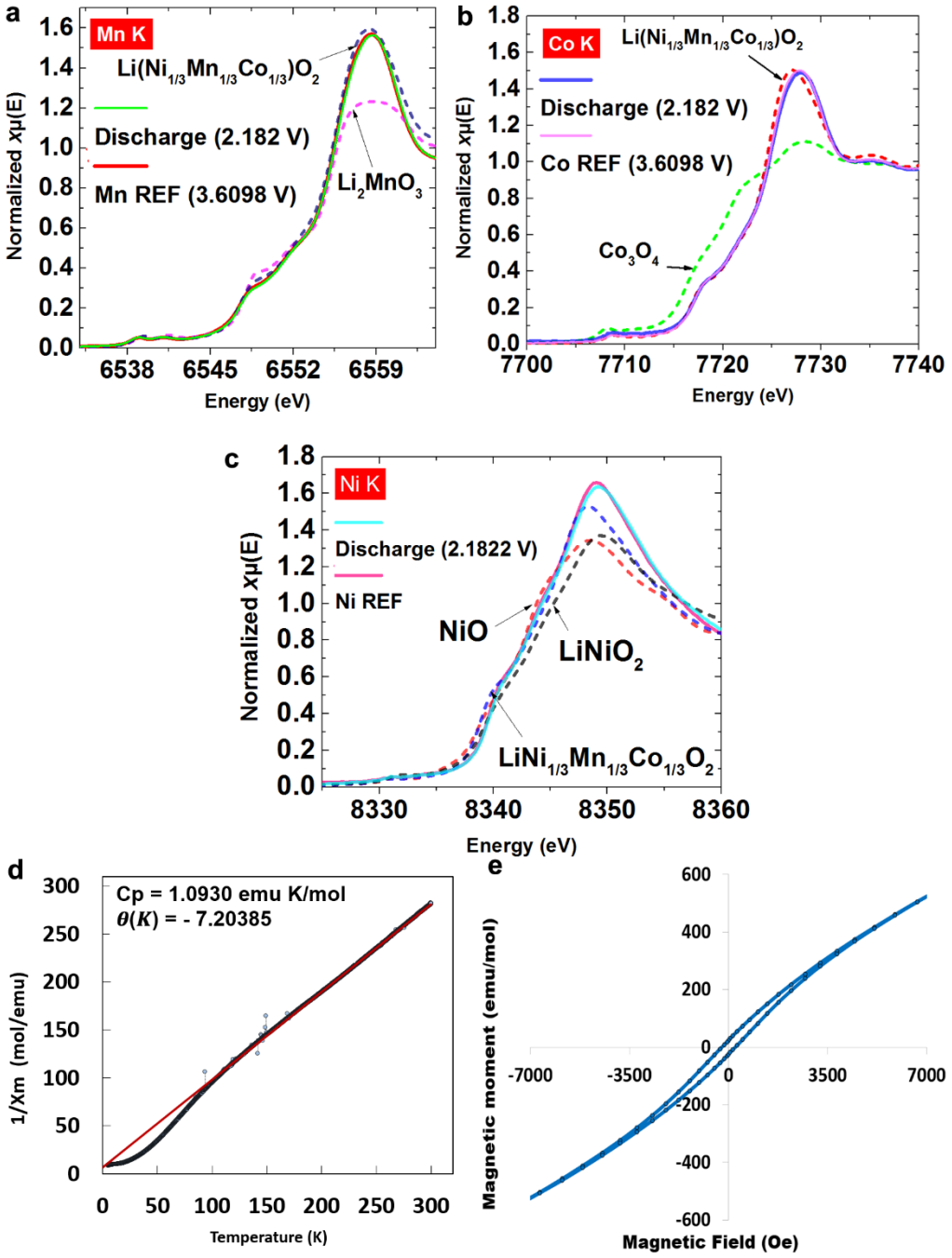


Figure 7.1 Oxidation states and magnetic properties of graphene-coated $Li(Li_{0.2}Mn_{0.54}Ni_{0.13}Co_{0.13})O_2$. Normalised XANES spectra (a) at Mn K-edge in REF (no current applied) and last discharged point (2.182 V), (b) at Co K-edge in REF (no current applied) and last discharged point (2.182 V), and (c) at Ni K-edge in REF (no current applied) and last discharged point (2.182 V). (d) Reciprocal magnetic susceptibility. The straight red-line is the fit to the Curie-Weiss law in the range of 150 – 300 K. Applied magnetic field is 1000 Oe. (e) Magnetization curve at 5 K.

Figure 7.1a,b,c. compares the normalized XANES spectra at Mn, Co, and Ni K-edge of REF (with no current applied) and last discharge point (=2.182 V). The magnetic susceptibility measurements for the graphene-coated $Li(Li_{0.2}Mn_{0.54}Ni_{0.13}Co_{0.13})O_2$ cathode are displayed in Figure 7.1d,e. Precise oxidation states and electronic structure of the cathode material could be evaluated by the results obtained from XANES and SQUID measurements. The highly sensitive nature to the oxidation (valence) state and symmetry of the absorber atom in XANES[110,130] allows us to estimate a target component by the XANES spectra comparison between the sample and the corresponding reference composite. It is apparent from the XANES chart that there has been little difference at Mn K-edge between before charge and after 1st cycle discharge. From the spectra position, the oxidation state of Mn can be evaluated as slightly lower than that of the Li_2MnO_3 (+4).

At the Co K-edge XANES, the spectra of the absorption edge are located higher than the reference composite of Co_3O_4 and it closely corresponds to the reference state of the $Li(Ni_{1/3}Mn_{1/3}Co_{1/3})O_2$ compound (+3), as shown in Figure 7.1. It can be thus suggested that Co is likely to present as an oxidation state at between +2.7 and +3. The location of the Co K-edge spectra before charge and after 1st cycle discharge is almost same (Figure 7.1b). This trend is similar to that of the Mn K-edge and thus suggests the minimal change of the electronic and chemical states of Mn and Co during the electrochemical cycle.

The position of XANES spectra at the Ni K-edge of REF appears to be located between those for NiO (Ni^{2+}) and $LiNiO_2$ (Ni^{3+}) as can be seen in Figure 7.1c. The absorption edge of the Ni K-edge is very close to that of $Li(Ni_{1/3}Mn_{1/3}Co_{1/3})O_2$. As such, the oxidation state of Ni in the graphene-coated $Li(Li_{0.2}Mn_{0.54}Ni_{0.13}Co_{0.13})O_2$ composite can be estimated as +2. After 1st cycle discharge, the Ni K-edge spectrum appears to be shifted marginally higher than the initial state of the cathode.

XANES is a useful method to evaluate the oxidation state in a composite, but it should be considered that the oxidation evaluation from the XANES spectra location may not be accurate because those spectra shifts may also arise from the crystal structure distortion or induced voltage effect during charge. Therefore, a magnetic measurement was conducted by Superconducting Quantum Interference Device (SQUID) analysis to provide the complementary information in determining the precise oxidation state of the transition metals. The magnetization measurement was performed under a magnetic field of 1000 Oe in the temperature range of 5 – 300 K. In addition, magnetic field of 60k Oe was applied (at 5 K) to evaluate the magnetic susceptibility. The results from SQUID analysis offers the correct oxidation state of each transition element in the initial state of the $Li(Li_{0.2}Mn_{0.54}Ni_{0.13}Co_{0.13})O_2$ cathode, as well as the information for the electronic structure of the transition metal oxides. The reciprocal molar magnetic susceptibility $1/\chi_m$ (H/M) of the graphene-coated composite as a function of temperature is shown in Figure 7.1d. The chart indicates that the composite is paramagnetic above approximately 160 K where it follows the Curie-Weiss law $\chi_m = N_a\mu^2/3k_B(T-\theta)$, with k_B the Boltzmann constant and N_a the Avogadro number. The Curie constant ($C_P = N_a\mu^2/3k_B$) and Curie-Weiss temperature were determined to be 1.0930 emu K/mol and -7.20385 K, respectively, according to the fitting at the linear regime in Figure 7.1d. It seems to be that this system is close to the antiferromagnetic. The theoretical value ($\mu_{\text{calculation}}$) of the magnetic moment on the cathode composite was calculated to be 3.02828 μ_B, while the experimental results was $\mu_{\text{experiment}}$ = 2.94823 μ_B. The theoretical calculation of the magnetic moment was performed with the consideration as Mn^{4+} (spin state S=3/2, $\mu_S = 3.87\ \mu_B$), Co^{3+}(LS, $\mu_S = 0\ \mu_B$) and Ni^{2+}(spin state S=1, $\mu_S = 2.83\ \mu_B$). The discrepancy between the theoretical and experimental magnetic moment is possibly attributed to the presence of the low spin Mn^{3+} in the composite [93,94]. When we incorporate the low spin Mn^{3+} in this composite system, a theoretical value of $\mu_{calculation}$ = 2.95767 μ_B is obtained which is close to the experimental

effective magnetic moment. This spin states consideration leads to the precise estimation of the oxidation states as Mn: +3.889, Co: +3, and Ni: +2.

7.3.2 In operando XANES of Mn, Co, and Ni K-edge

Figure 7.2 reveals the normalized K-edge and pre-edge XANES spectra shift for Mn during the initial charge-discharge (0.5 C rate) of the lithium-ion battery. A total of 7 scans were collected during the 1st electrochemical cycle including the REF point at which no current was applied, as shown in Figure 7.2e. The initial cell potential at the reference point was measured to be ~3.6098 V. Four significant absorption features have been identified at the Mn K-edge XANES as presented with the numbers in Figure 7.2a. Absorption **2** is associated with the electric dipole transition from 1s to 4p with a shakedown process from ligand-to-metal charge transfer (LMCT), while absorption 4 corresponds to the dipole transition without the shakedown process. It is therefore that the final states of absorption **2** and **4** can be respectively represented as $1s^1c3d^{n+1}$ $L4p^1$ and $1s^1c3d^n4p^1$, where c is a 1s core hole and L is an oxygen 2p ligand (Mn^{4+}: n=3). On the other hand, absorption **1** indicates the Mn K pre-edge peaks found between 6537 and 6543 eV as shown in Figure 7.2c. Those two peaks correspond to 1*s*-3d_{t2g} and 1*s*-3d_{eg} transitions which are electric dipole forbidden. The presence of those peaks is explained by the 3*d*-4*p* orbital mixing or/and a weak quadrupolar coupling ($\Delta l=0, \pm 2$), with the loss of centrosymmetric environment by the distortion of MnO_6 octahedra. There was a slight spectra shift in Mn K-edge XANES during charge-discharge. This shift may be explained by the actual oxidation change of Mn between +3.889 and +4 although the change is not distinctive. In the Mn K pre-edge, it appears that the Li^+ deintercalation give rise to the peak intensity as displayed in Figure 7.2c. The spectra shift of the normalized XANES can be also observed in the Co and Ni K-edge during the 1st charge as presented in Figure 7.3a,c. There was a similarity in the shape change of XANES spectra between Mn and Co, and this indicates that the atomic environment of Co is somewhat similar to that of the Mn.

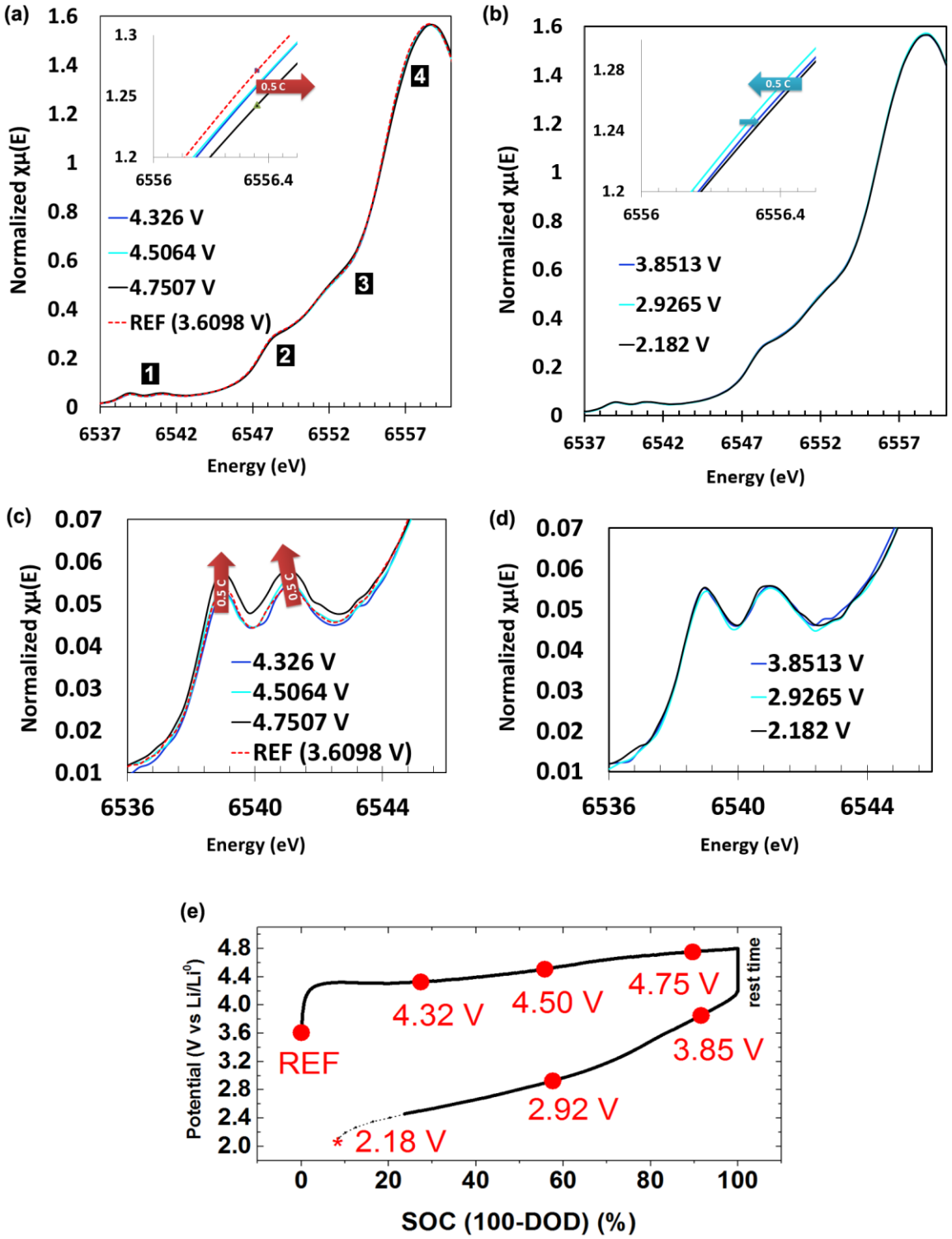


Figure 7.2 Normalised XANES spectra at K-edge of graphene-coated $Li(Li_{0.2}Mn_{0.54}Ni_{0.13}Co_{0.13})O_2$. Spectra shift of Mn K-edge (a) during 1st charge and (b) 1st discharge. Spectra shifts in Mn K pre-edge (c) during 1st charge and (d) 1st discharge. (e) Galvanostatic profile with XAS collection points.(0.5 C-rate).

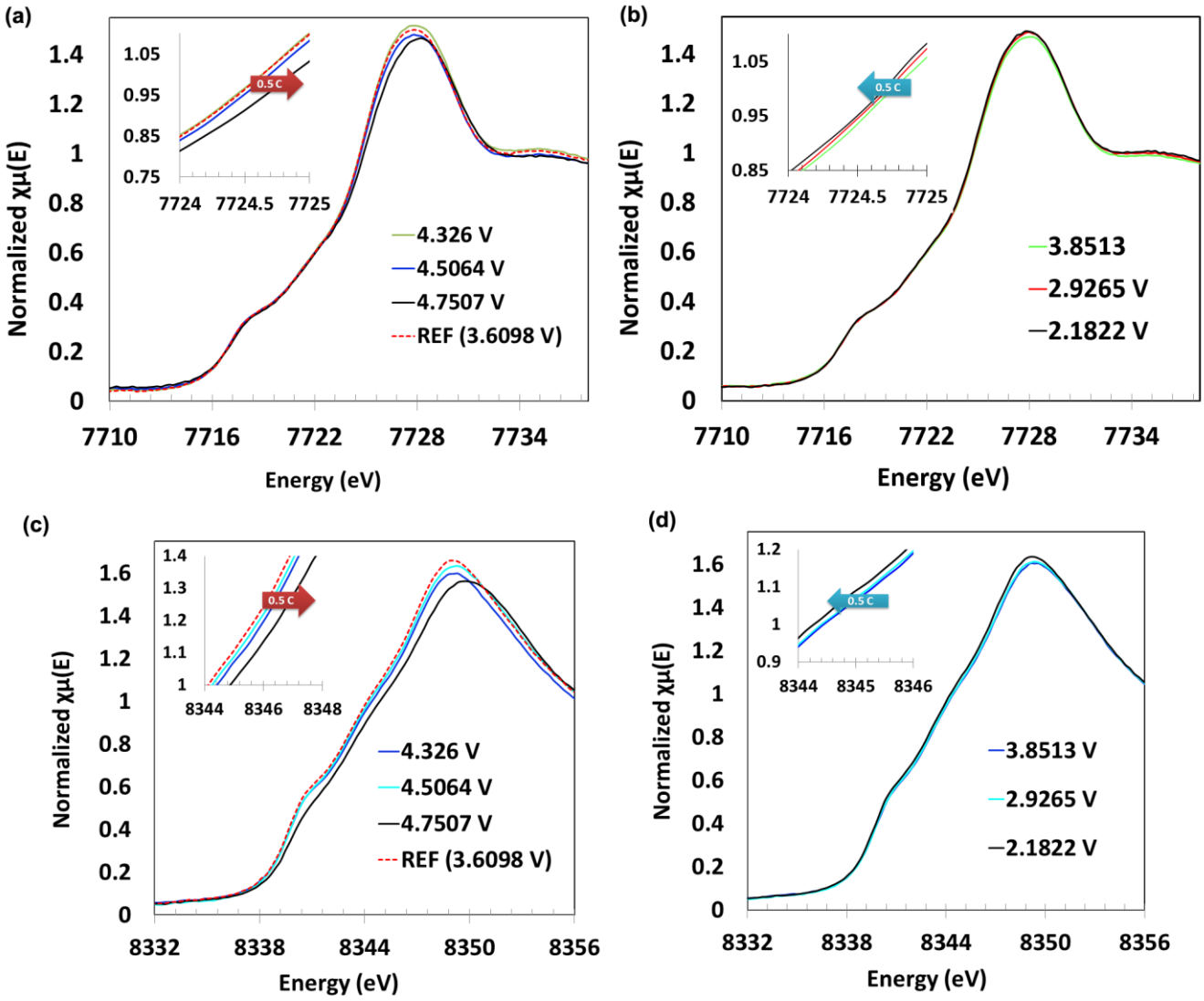


Figure 7.3 Normalised XANES spectra at K-edge of graphene-coated $Li(Li_{0.2}Mn_{0.54}Ni_{0.13}Co_{0.13})O_2$. Spectra shift of Co K-edge (a) during 1st charge and (b) 1st discharge. Spectra shifts of Ni K-edge (c) during 1st charge and (d) 1st discharge.

The spectral shifts of Mn, Co, and Ni K-edge were found to be 0.4 eV, 0.61 eV, and 1.07 eV, respectively. From the XANES data (Figure 7.3), the shifts in the Ni K-edge revealed relatively large change, which is at least double, compared with Mn and Co. The oxidation changes of the transition metals are the key process that contributes to the charge compensation mechanism of the $Li(Li_{0.2}Mn_{0.54}Ni_{0.13}Co_{0.13})O_2$ cathode battery. The distinct spectra shift of the Ni is likely to be attributed to the two-stage redox reaction between Ni^{2+}/Ni^{3+} and Ni^{3+}/Ni^{4+} [99,117,174]. The compensation mechanism that describes the participation of each transition metal to the capacity

contribution during Li^+ (de)intercalation is not yet clearly understood. A number of studies have found the direct contribution of the Ni^{2+} and Co^{3+} to the battery specific capacity during charge[90,92,175]. The XANES results from Ni and Co K-edge exhibit that there has been a gradual increase until 57 % SOC, but a sudden shift in the photon energy (eV) has been observed at ~89% SOC.

7.3.3 In operando EXAFS of Mn, Co, and Ni with Wavelet Transform Analysis

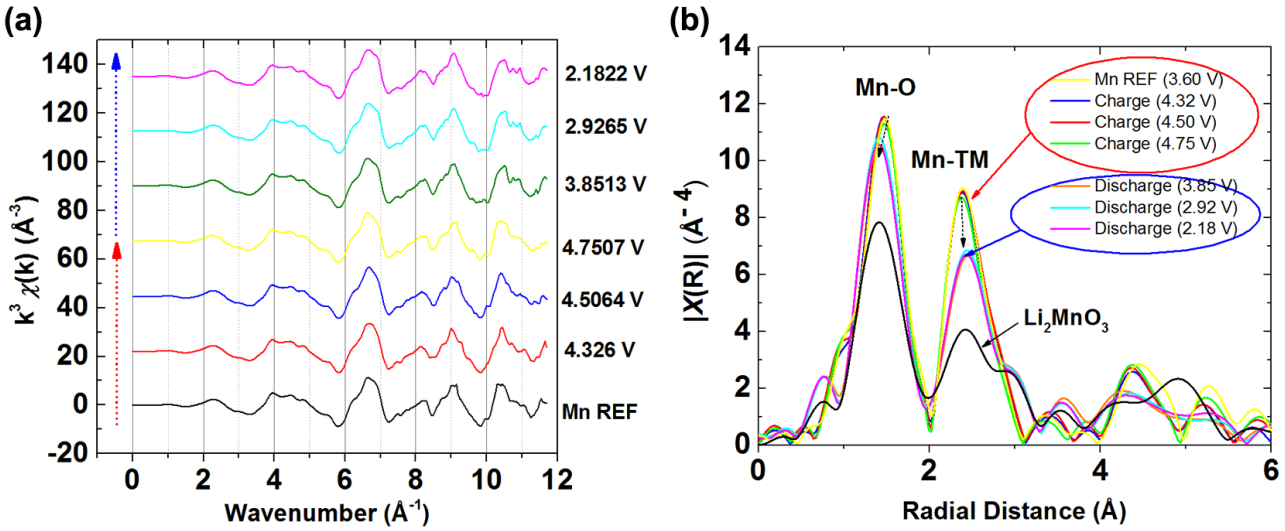


Figure 7.4 In operando EXAFS measurement of Mn in graphene-coated $Li(Li_{0.2}Mn_{0.54}Ni_{0.13}Co_{0.13})O_2$ during the 1st cycle. (a) k^3-weighted EXAFS oscillations $\chi(k)$ above Mn K-edge during charge-discharge. (b) k^3-weighted Fourier transform magnitudes of Mn K-edge during charge-discharge (TM = Mn, Co, and Ni). Red and blue arrows indicate charge and discharge, respectively.

The Mn K-edge EXAFS oscillations during charge and discharge is compared in k-space and R-space as displayed in Figure 7.4. It can be seen from the Fourier transformed EXAFS data in Figure 7.4.b that the amplitude of Mn-O is always higher than the Mn-TM amplitude (TM=Mn, Co, and Ni) throughout the cycle. This might be explained in part of the cation ordering in the $xLi_2MnO_3 \cdot (1-x)LiMO_2 (M = Mn, Ni, Co)$ composite system. The atomic environment around Mn-O in the layered oxide component ($LiMO_2$) can be described with 6 well-coordinated transition metals. On the other hand, the atomic environment around the Mn-TM shell appears to be mainly surrounded by a relatively light scatterer such as oxygen vacancies or lithium ions. As a consequence, the peak

intensity is always higher in the 1st shell because of the neighbouring transition metals during the (de)intercalation process. Both the peak intensity from Mn-O and Mn-TM decreases after the full charge as can be seen in Figure 7.4. Especially, the amplitude of Mn-TM dramatically reduces after the initial charge. This implies the cation ordering of $LiMn_6$ in the transition metal layers[176]. The peak amplitude at ~ 4.4 Å also decreases, and it is interesting to note that the spectra patterns are likely to resemble the Li_2MnO_3 compound (Figure 7.4) while discharging. This might be related to the scattering between Mn ions within the hexagonal $LiMn_6$ units[176]. The radial distance change around the Mn absorber was not significant since the difference of Mn-O between largest (~1.50 Å) and smallest (~1.44 Å) value in R-space (uncorrected for phase shift) was approximately 0.06 Å during the 1st cycle. As shown in Figure 7.4b, the variation in the EXAFS $\chi(k)$ spectra can be divided into two main patterns. One with the higher amplitudes through the charge and another one with the lower amplitudes through discharge. The pattern dividing into two groups can be also confirmed in the k-space of EXAFS oscillations as shown in Figure 7.4a. The migration environment of the transition metals may be slightly modified after the initial charge, as evidenced by the change of the oscillation pattern between charge and discharge (Figure 7.4b). The pattern variations between the different cell potentials within charge (or discharge) are not significant, as their spectra pattern are rather similar at different state of charge (SOC) or different depth of discharge (DOD). It is probable therefore that the atomic environment of Mn in the graphene-coated $Li(Li_{0.2}Mn_{0.54}Ni_{0.13}Co_{0.13})O_2$ cathode is likely to maintain good stability during the Li^+ (de)intercalation.

Continuous Cauchy Wavelet Transform (CCWT) analysis[147] was carried out for each transition metal. The CCWT analysis offers special advantages to further understand the EXAFS signals for the complex composite through a three dimensional visualization of the EXAFS spectra by decomposing the *k*-space and R-space (uncorrected for phase shift) signals[147,177,178]. The major

advantage of using the wavelet transform is the detailed information on the local atomic structure with the visualized signals being afforded. The CCWT to the collected signals of EXAFS measurements of Mn K-edge during the 1st cycle is presented in Figure 7.5. The intensity of the color is proportional to the CCWT modulus which describes the decomposition of the EXAFS amplitude term[147]. A color scale bar is presented on the bottom. At the reference point (REF), the locations of the highest intensity for Mn-O and Mn-TM in k-space were observed at ~7.1 $Å^{-1}$ and ~8.5 $Å^{-1}$, respectively. It should be noted that an element with higher atomic number results in more intense signal at high *k*-space owing to more efficient backscattering. The blurry appearance of the CCWT modulus at high order shells (~ 4.4 Å) observed at ~8.7 $Å^{-1}$ and ~11.0 $Å^{-1}$ indicates the multiple scattering effects from the combined transition metals (Mn, Co, and Ni). Interestingly, the visual inspection revealed that the highest coordination shell at ~11.0 $Å^{-1}$ (R-space: ~5.42 Å) is losing its signal intensity, whereas the second highest coordination shell (~8.7 $Å^{-1}$ and ~4.46 Å in R-space) maintains the intensity during the initial cycle. Better symmetry on the shape could be observed during charge-discharge compared with REF state. This finding may suggest the process of the transition metals rearrangement with preferential ordering. On the other hand, as the wavelet transform displays a closely symmetric shape with high intensity, the transition metals (Mn, Co, and Ni) in the transition metal layer (3a-site) are likely to be highly ordered around Mn-O coordination. Also note that the Mn-O signal showing the highest intensity (dark-red) of the CCWT modulus at 4.5064 V and 4.7507 V disappeared during battery discharge (Figure 7.5). It can thus be suggested that there has been a slight modification in the atomic environment around the Mn absorber after initial charge. Figure 7.6 presents the results obtained from the operando EXAFS measurement of Co K-edge in *k*-space and R-space during charge-discharge. The difference between the largest (~1.41 Å) and smallest (~1.50 Å) bond-length in R-space

(uncorrected for phase shift) was found to be ~0.09 Å during the initial cycle. This value was 33% higher than that of the Mn-O, signifying larger structural change in the Co-O local environment.

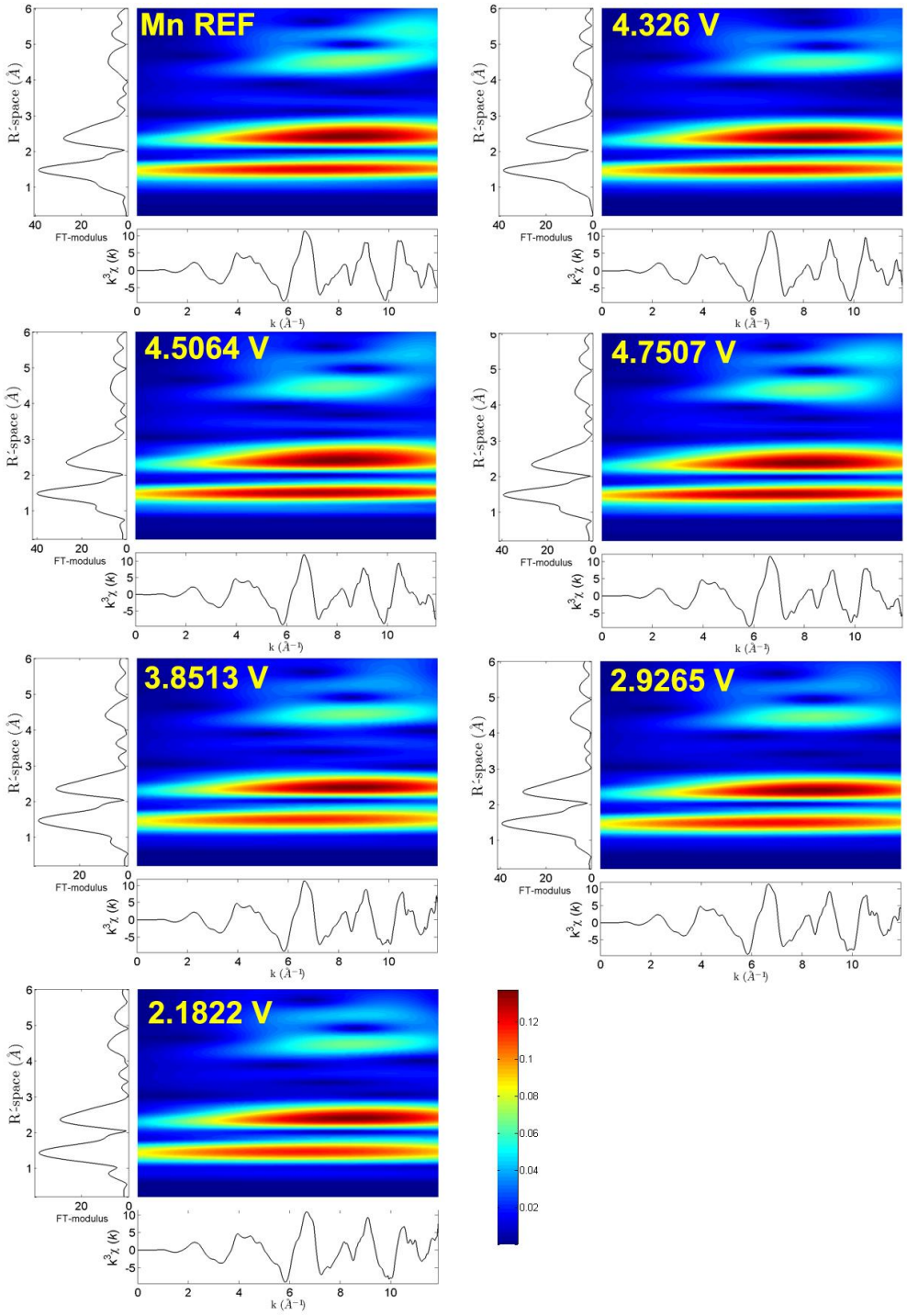


Figure 7.5 In operando EXAFS measurement of Mn in graphene-coated $Li(Li_{0.2}Mn_{0.54}Ni_{0.13}Co_{0.13})O_2$ during the 1st cycle with continuous Cauchy wavelet transform (CCWT) analyses of EXAFS spectra for each voltage point. The color intensity is the magnitude of the CCWT modulus. Dark-red signifies higher intensity, while blue is the lower intensity.

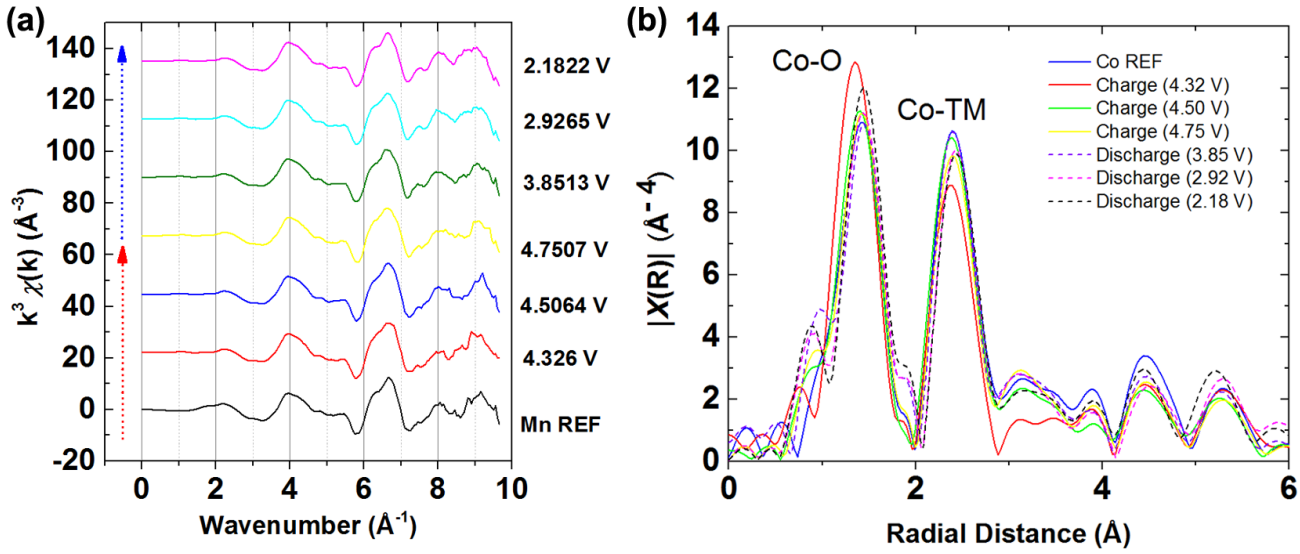


Figure 7.6 In operando EXAFS measurement of Co in graphene-coated $Li(Li_{0.2}Mn_{0.54}Ni_{0.13}Co_{0.13})O_2$ during the 1st cycle. (a) k^3-weighted EXAFS oscillations $\chi(k)$ above Co K-edge during charge-discharge. (b) k^3-weighted Fourier transform magnitudes of Co K-edge during charge-discharge (TM = Mn, Co, and Ni). Red and blue arrows indicate charge and discharge, respectively.

The CCWT analysis to the collected signals of EXAFS measurements of Co K-edge during the 1st cycle is shown in Figure 7.7. From this chart, it could be also identified that the atomic environment of Co-O/Co-TM (~6.5 $Å^{-1}$/~8.4 $Å^{-1}$ in *k*-space) displays a structural disorder from the initial point (REF) as evidenced by the less symmetrical shape of the CCWT modulus than that of the Mn-O/Mn-TM. This may be related to some defects in the synthesis condition of the $Li(Li_{0.2}Mn_{0.54}Ni_{0.13}Co_{0.13})O_2$ active material. The atomic environment between Co and TM is obviously disordered from the initial state (Co REF) as can be seen from the different EXAFS oscillation pattern (red curve) in Figure 7.6b, but it is likely to retain its local symmetry as the highest CCWT intensity (dark-red at ~8.4 $Å^{-1}$ in *k*-space and ~2.46 Å in R-space) displays little changes during charge and discharge (Figure 7.7). This is also consistent to the Co K-edge EXAFS pattern that exhibits relatively less alteration in the 2nd order shell (Co-TM) during charge-discharge. On the other hand, lithium-ions (de)intercalation results in a change in the highest intensity of the CCWT modulus in the Co-O shell (Figure 7.7). This might be associated with the oxygen removal which leads to the modification of the Co-O local environment.

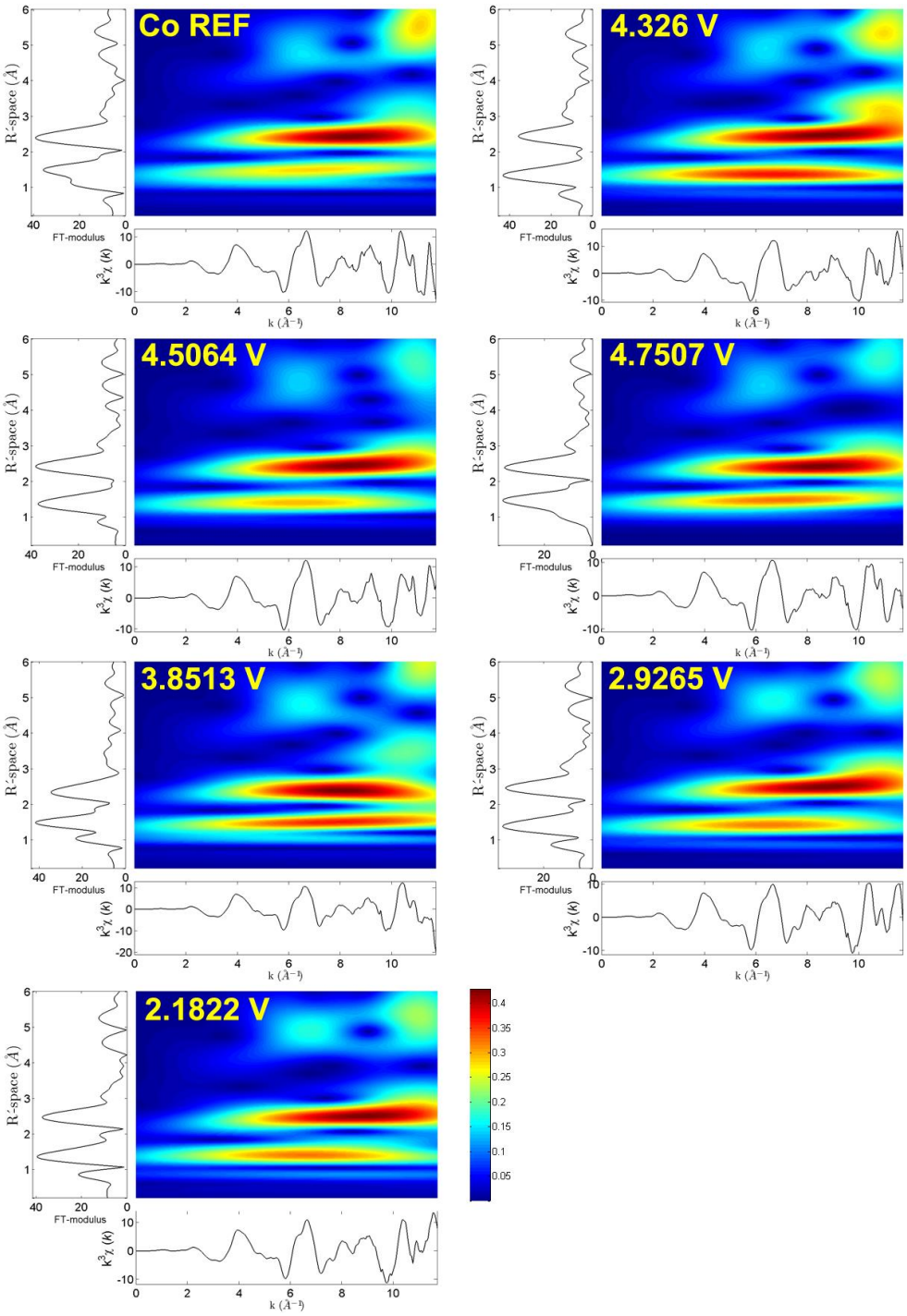


Figure 7.7 In operando EXAFS measurement of Co in graphene-coated $Li(Li_{0.2}Mn_{0.54}Ni_{0.13}Co_{0.13})O_2$ during the 1st cycle with continuous Cauchy wavelet transform (CCWT) analyses of EXAFS spectra for each voltage point. The color intensity is the magnitude of the CCWT modulus. Dark-red signifies higher intensity, while blue is the lower intensity.

It appears that the redox reaction of Co contributes to the battery capacity over the entire voltage range, while Mn is only involved at > ~4.5 V during initial charge. This could be drawn from the

visual information on CCWT from Figure 7.5 and Figure 7.7. A similarity could be observed in the local atomic environment of the highest order shell at k~10.9 $Å^{-1}$ and R~ 5.3 Å between the REF (3.6098 V) and 4.326 V. Single scattering paths mainly constitute the EXAFS signals at these two points although they look rather blurred compared with the 1st or 2nd shells. From the wavelet information, we can see that the tendency of having single scattering disappears from 4.5064 V while the contributions from multiple scattering increase on further charge and the discharge.

The local atomic environments are different between the Co K-edge and Mn K-edge, but the trend of the Co K-edge CCWT is comparable to that analysed in Mn K-edge during the 1st cycle as there is a clear similarity in the phase change relevant to the voltage. A notable change could be observed in the center of the highest intensity from both elements. The 1st shell for Mn K-edge and 3rd shell for Co K-edge displayed the distinct variations of the wavelet modulus at before and behind ~4.5 V. Another interesting observation is that the phase change of those shells with the local atomic environment is likely to be irreversible since the wavelet pattern with intensity change on charge differs from discharge.

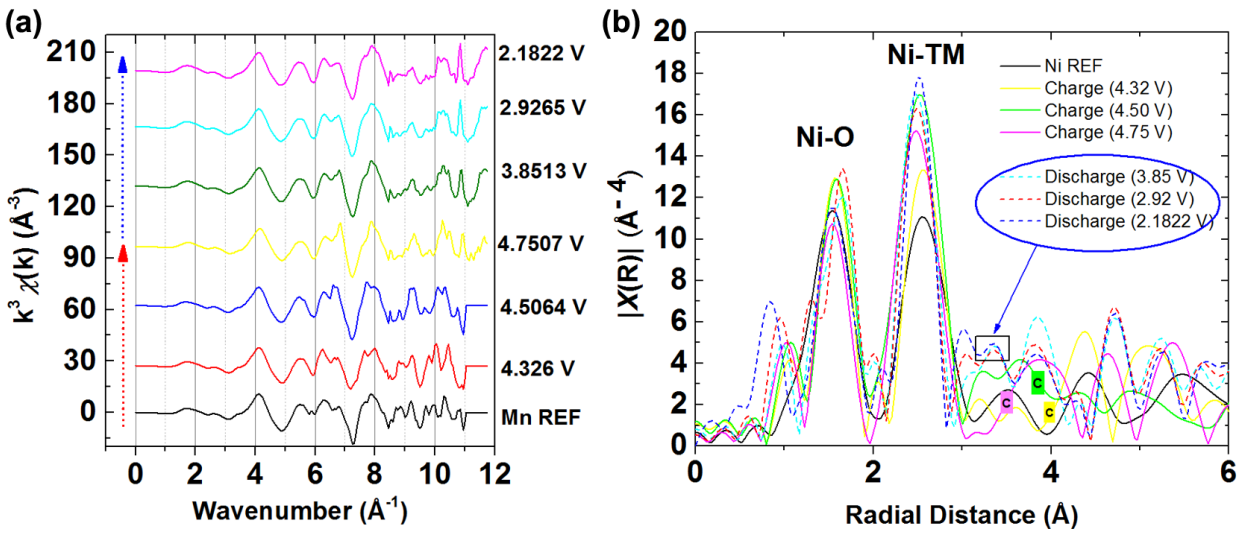


Figure 7.8 In operando EXAFS measurement of Ni in graphene-coated $Li(Li_{0.2}Mn_{0.54}Ni_{0.13}Co_{0.13})O_2$ during the 1st cycle. (a) k^3-weighted EXAFS oscillations $\chi(k)$ above Ni K-edge during charge-discharge. (b) k^3-weighted Fourier transform magnitudes of Ni K-edge during charge-discharge (TM = Mn, Co, and Ni). Red and blue arrows indicate charge and discharge, respectively. 'C' in the color denotes those spectra belong to charge group.

Figure 7.8 compares the results obtained from the in operando EXAFS measurement of Ni K-edge in *k*-space and R-space during the initial cycle. The Fourier transformed EXAFS data at Ni K-edge displays a complicated and dynamic local environment changes in R-space (Figure 7.8b). Both the amplitude and the location of the Ni-O/Ni-TM peaks change significantly on charge and discharge. The maximum deviation from the REF point of Ni-O was found to be 0.13 Å in R-space. This is more than two times higher that of the Mn-O (= 0.06 Å). The larger discrepancy of the R-space shift in Ni is attributed to the two stage oxidation changes from Ni^{2+}/Ni^{3+} to Ni^{3+}/Ni^{4+} which result in higher local structure modification. In addition, the Jahn-Teller effect from Ni^{3+} (d^7) having an electronic configuration of $t_{2g}^6 e_g^1$ also contributes to the dynamic local environment changes in the graphene-coated $Li(Li_{0.2}Mn_{0.54}Ni_{0.13}Co_{0.13})O_2$ composite. The CCWT analysis to the Ni K-edge EXAFS is shown in Figure 7.9. As expected, the wavelet analysis gives complex signals which correspond to the complicated environment change of Ni-O/Ni-TM during the 1st cycle. The correlation between the cell voltage and variation in the wavelet signals in Ni K-edge provide significant information about the local atomic changes and the electrochemical process involved. The highest order shell at 9.8 $Å^{-1}$ in k-space (5.7 Å in R-space) could be clearly observed mostly with single scattering effect at Ni REF state. The effect from multiple scattering arises once the current (0.5 C) was applied, which in turn leads to the blurry appearance of that shell signature. This result might be explained by the multiple scattering impacts from the migration of the transition metals. The peak intensity at ~5.8 $Å^{-1}$ in k-space (1.5 Å in R-space), which corresponds to the 1st shell Ni-O CCWT, tends to decrease and illustrates splits in the shape from the cell voltage of 2.9265 V to 2.1822 V. It can thus be suggested that there has been a significant distortion in the octahedra NiO_6 of the Ni absorber in the 1st shell. The variation trend of the wavelet transform on the 2nd (Ni-TM) shell is similar to that of the 1st shell, but the local atomic

distortion in the 2nd shell reveals relatively lower degree as the center (~7.5 $Å^{-1}$ in k-space and ~2.5 Å in R-space) of the shell retains the high CCWT modulus (dark-red).

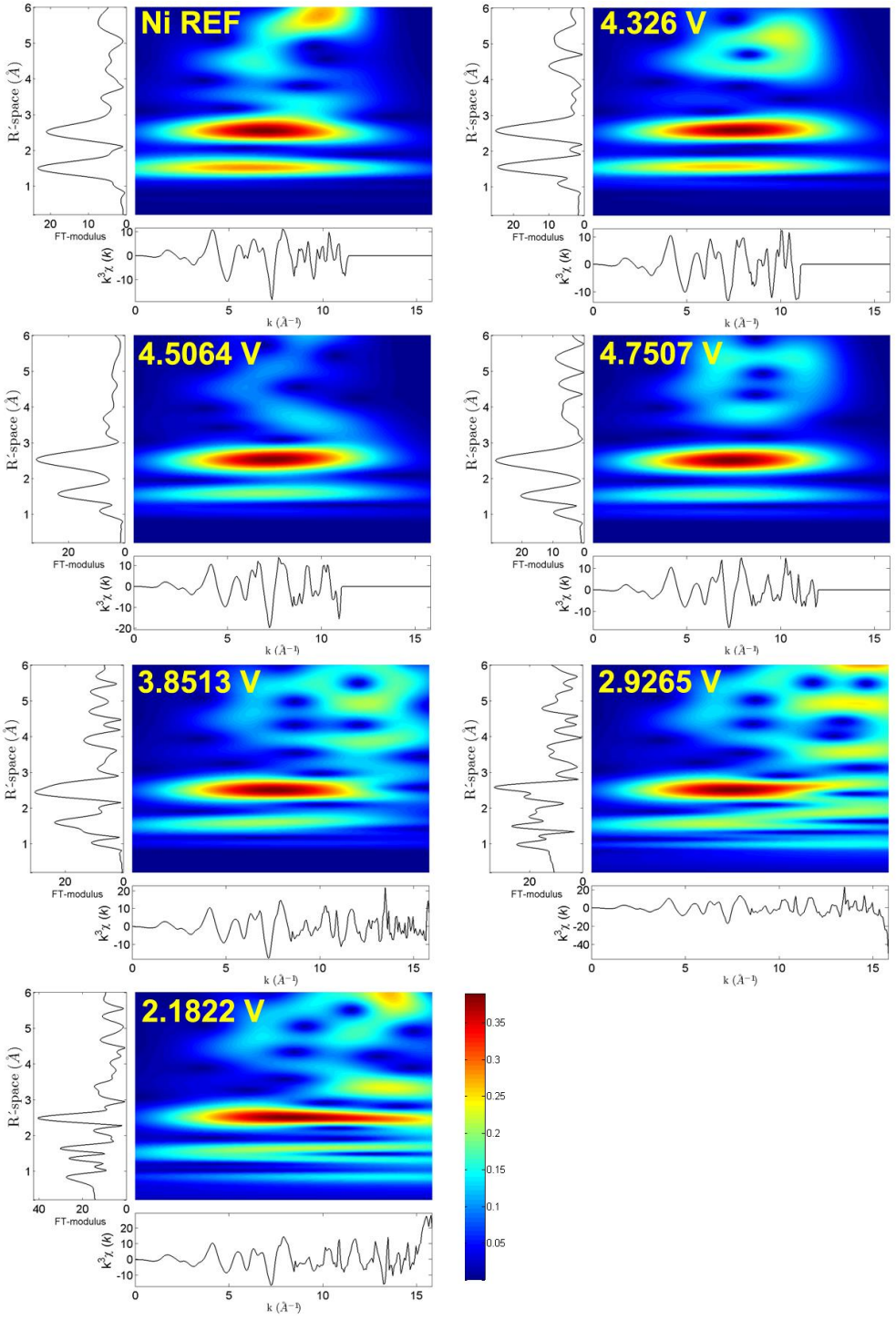


Figure 7.9 In operando EXAFS measurement of Ni in graphene-coated $Li(Li_{0.2}Mn_{0.54}Ni_{0.13}Co_{0.13})O_2$ during the 1st cycle with continuous Cauchy wavelet transform (CCWT) analyses of EXAFS spectra for each voltage point. The color intensity is the magnitude of the CCWT modulus. Dark-red signifies higher intensity, while blue is the lower intensity.

One of the more significant findings to emerge from this analysis is that the atomic environment change is irreversible during Li^+ (de)intercalation as evidenced by the distinctive difference in the shape and scattering effects between charge and discharge, while Mn and Co displays similar visualization patterns. It is apparent from the Ni K-edge XANES that the oxidation change is reversible in Ni-O (Figure 7.1c). However, it should be noted that the NiO_6 symmetry is likely to undergo an irreversible local environment modification as identified by the Ni K-edge wavelet signals, although the redox reaction of Ni appears to be reversible. This structural change is believed to be the consequence of bond-length separation of long Ni-O and short Ni-O by the Jahn-Teller effect from Ni^{3+}. TM-O bond length changes with the mean-square disorder (σ^2) from the EXAFS Debye-Waller factor at different voltage levels is presented in Figure 7.10. EXAFS fitting was performed in order to determine major EXAFS parameters: radial distance to neighbouring atom (R), EXAFS Debye-Waller factor ($e^{-2\sigma k^2}$), amplitude reduction factor (S_0^2), and energy shift (ΔE_0). Here the EXAFS Debye-Waller factor is related to either thermal vibrations or structural disorder on the central absorbing atoms (Mn, Ni, and Co)[126,128]. In this study, this factor would represent the structural disorder as no thermal treatment was applied. The amplitude reduction factors were scaled to constant values such as 0.7, 0.67, and 0.92 for Mn, Co, and Ni, respectively, after the refinement with reference samples.

As shown in Figure 7.10a, the interatomic bond of Mn-O slightly decreases upon charge, but there was a sudden rise at ~4.5 V. This may be attributed to the activation of the Li_2MnO_3 phase with cation ordering/rearrangement leading to a distinct change in the atomic environment. The bond of Mn-O tends to increase upon discharge. The bond length difference in Mn-O was found to be ~0.006 Å, while the largest difference in the Co-O appears to be 0.02 Å. This discrepancy is attributed to the different route of the contribution to the charge compensation mechanism.

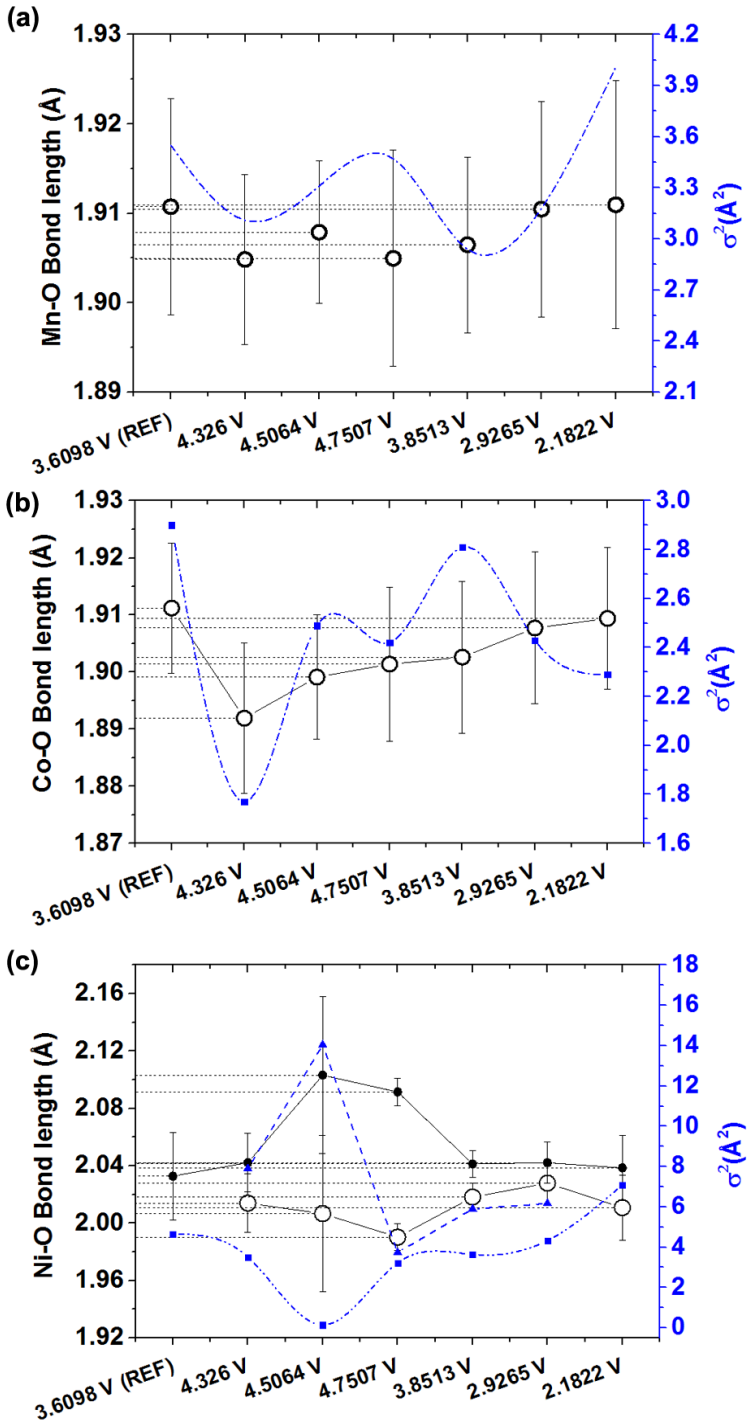


Figure 7.10 Evolution of the bond length and structural disorder ($\boldsymbol{\sigma}$) changes during charge-discharge for graphene-coated $Li(Li_{0.2}Mn_{0.54}Ni_{0.13}Co_{0.13})O_2$ battery. (a) Mn-O with 1st shell disorder. (b) Co-O with 1st shell disorder. (c) Ni-O with 1st shell disorder. Ni-O bond-length is separated because of the Ni^{3+} Jahn-Teller effect.

Co contributes to the battery capacity by the redox reaction of Co^{3+}/Co^{4+}, whereas the contribution from Mn is mainly linked to the oxygen site in the Li_2MnO_3 by the concomitant release of lithia

(Li_2O). The trend of the structural disorder (σ^2) of Mn-O is similar to that of the Co-O during the initial charge. The Ni revealed the highest bond length changes among the 1st shell TM-O as it was evaluated to be 0.11 Å. This can be described as a consequence of two-stage redox reaction between Ni^{2+}/Ni^{3+} and Ni^{3+}/Ni^{4+}.

7.4 Conclusion

For the first time, this study has shown an *in operando* XAS investigation with a wavelet transform [148] analysis to further understand the atomic environment of the transition metals (Mn, Co, and Ni) in the graphene-coated $Li(Li_{0.2}Mn_{0.54}Ni_{0.13}Co_{0.13})O_2$ lithium ion battery during electrochemical cycle. It is of interest to precisely correlate the atomic environment with oxidation and electronics states of the transition metals during the 1st electrochemical cycle. This correlation serves as a basis for designing a high energy density Li-rich oxide cathode with enhanced stability. It was successful to characterize the correct atomic environments of each transition metal during the 1st cycle (0.5 C rate) with the CCWT visualization in three-dimensional signals by decomposing the k-space and R-space signals from the K-edge EXAFS of Mn, Co, and Ni[148]. The results obtained from XANES and SQUID measurement indicate that the oxidation change during Li^+ (de)intercalation is likely to be reversible. The EXAFS modelling for the inter-atomic bond length changes provide some support for the reversible oxidation change as the bond lengths of Mn-O, Co-O, and Ni-O tend to regain their initial values. On the other hand, the local atomic change from the Jahn-Teller Ni^{3+} (d^7) in the graphene-coated $Li(Li_{0.2}Mn_{0.54}Ni_{0.13}Co_{0.13})O_2$ cathode appears to be irreversible as evidenced by the visual inspection from the wavelet transform, although the redox change of Ni was reversible. A significant difference in the intensity and symmetry of the shapes on the wavelet transform modulus was observed between the initial charge and discharge on the Ni atomic environment. In addition, we could identify the splitting of Ni-O into the long and short Ni-O

attributed to the Jahn-Teller effect showing a maximum bond length difference at 4.5064 V (Figure 7.10c).

The use of the mean-square disorder parameter (σ^2) from the EXAFS Debye-Waller factor ($e^{-2\sigma k^2}$) links the relative displacement of absorber-scatterer to the structural disorder in the two-composite cathode system of $xLi_2MnO_3 \cdot (1-x)LiMO_2$. In general, the fluctuation of the structural disorder (σ^2) was found to be higher in the 2nd shell than the 1st shell. Note that the structural disorder in Mn-TM (σ^2 = 0.01 Å^2) and Ni-TM (σ^2 = 0.014 Å^2) were evaluated to be maximum at the voltage level of 4.5064 V. This result is possibly attributed to the electrochemically activated Li_2MnO_3 component with the participation of cation ordering/transition metal migrations. On the other hand, the maximum intensity of the wavelet transform modulus in Co-O and Ni-O slightly reduced at 4.5064 V. This signifies a higher structural disorder because of the oxygen removal as Co and Ni are likely to participate in the charge compensation mechanism during electrochemical cycle. The Co-O tends to regain its symmetry whereas Ni-O shows irreversible modifications on the atomic environment upon further charge and discharge. Overall, based on the CCWT analysis, the Mn-O reveals the minimum changes compared with Co-O and Ni-O. This discrepancy could be explained by the different way of contributions to the charge compensation mechanism.

In the present study a new approach was employed to examine the atomic environment change during electrochemical cycle. We propose a new concept, namely, 'atomic phase reversibility' offers a means of optimizing material design to develop an improved high-energy density electrode with advanced stability for the lithium-ion battery.

Chapter 8 Charge Rate Dynamic in the Graphene Coated Li-rich Mn-based Cathode Studied by In Operando XAS

This chapter deals with the *in operando* XAS study on the graphene-coated $Li(Li_{0.2}Mn_{0.54}Ni_{0.13}Co_{0.13})O_2$ cathode cells with different charge rates (0.125 C vs 0.5 C). Note that the charge process is based on the constant current charge stage, thus a faster charge rate results in a lower capacity than that of the slow charge which is a deep charge that enables the full potential from the charge compensation mechanism. That is to say, the rapid charge doesn't always assure the full charge state although the battery can be reached quicker at the target voltage with a fast charge rate. The main idea of this study lies in the assumption that the Li^+ will show a distinctive diffusion behaviour resulting from the different activation condition in the oxidation of the transition metals.

8.1 Introduction

The Li-rich Mn-based oxide transition metal cathode, represented as $xLi_2MnO_3 \cdot (1-x)LiMO_2$, is considered as a dual layer system. Lithium-ion layer at 3b sites and transition metal layer at 3a sites constitute the two-composite integrated system. As the term 'Li-rich' implies, Li^+ not only occupies the lithium-layer in the trigonal structure ($R\bar{3}m$), it can also partially occupy the transition metal layer in the monoclinic structure (C2/m) as illustrated in Figure 8.1[2,58,122]. It is believed that the lithium-ion surrounded by Mn^{4+} in the transition metal layer of C2/m generates the cation ordering ($LiMn_6$) in the Li_2MnO_3 component[2,4,162]. The electrochemical performance and electrode stability might be directly linked to the Li_2MnO_3 phase in the Li-rich layered oxide system [2,4]. This is due to three main reasons: (1) The Li_2MnO_3 phase can be electrochemically activated above 4.5

vs Li^0/Li^+ providing additional capacity to the battery by the concomitant removal of lithia (Li_2O), (2) the activation process results in the formation of MnO_2 which offers good stability to the host structure ($Li_2MnO_3 \rightarrow Li_2O + MnO_2$), and (3) the component is likely to transform into a spinel phase that deteriorates the battery performance and stability upon further electrochemical cycles[1,2,10,72,82,179,180].

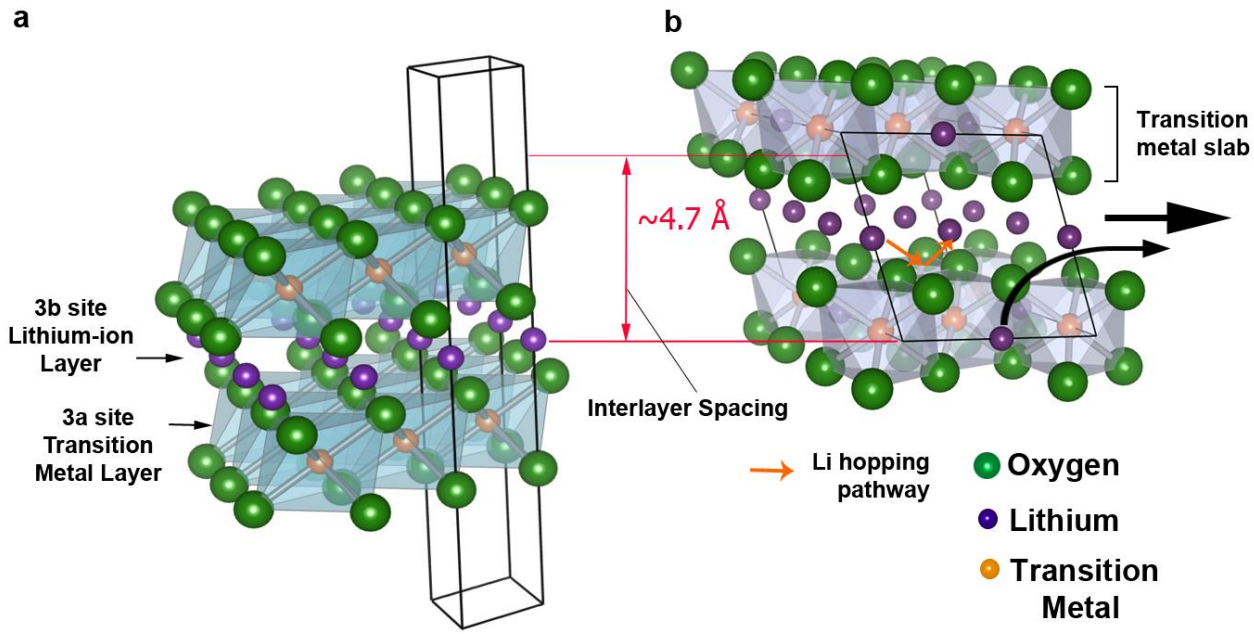


Figure 8.1 Crystal structure of (a) $LiMO_2$ (trigonal, $R\bar{3}m$) and (b) Li_2MnO_3 (monoclinic, C2/m). Due to the presence of the interlayer spacing (~4.7 Å), the crystal structure can be combined in an integrated composite. Black arrows indicates the extraction of the lithium-ions. In principle, Li+ must be deintercalated from lithium layer and TM-layer either continuously or simultaneously during charge.

On the one side, the Li_2MnO_3 contributes to the battery capacity, on the other side, it is also the main factor that leads to the capacity fading and electrode degradation during charge and discharge. By contrast, at low voltage level between 2.0 and 4.4 V vs Li^0/Li^+, the layered $LiMO_2$ phase can be electrochemically activated, but the transition metal layers are only occupied by the transition metal ions (e.g. Mn, Co, Ni)[2,4,85]. In the Li-layered component, the oxidation change of the transition metals is the key factor that contributes to the battery capacity during Li^+ (de)intercalation. Also, the layered $LiMO_2$ component can undergo a phase transition into a spinel

structure during electrochemical cycles[10,53,101,122,124,181,182], especially this is the case when a large amount of Mn occupies the transition metal layers, i.e. Li-rich Mn-based oxide cathode. Interestingly, it has been reported that the phase transition in the layered component mainly appears at a low charge rate (slow charge)[79].

Li^+ ion mobility has become a crucial issue that is related to the battery performance and cathode stability in the lithium layered oxide system which is composed of alternating layers with the transition metals. It is the O3 structure with the alternating layers that provides conduction pathways for the lithium-ions. The conduction mechanism of the Li^+ is usually described by the Li^+ hopping process between octahedral sites *via* an intermediate tetrahedral site[29,30]. The electrostatic repulsion between Li^+ and transition metals (Mn, Co, and Ni) and the Li slab spacing have been proposed as vital factors that affect the Li^+ diffusion and thus the rate capability in the layered oxide cathode, by an *ab initio* modelling performed by Kang and Ceder[29,30]. The calculation with the density functional theory (DFT) shows that the activation barrier for the Li^+ diffusion tends to decline with the Li slab spacing. It has been also revealed that the Li^+ mobility is highly sensitive to the distance between the oxygen layers as the oxygen electron density affects the activation barrier by screening the electrostatic interactions between transition metals[29]. Better screening results in a lower activation barrier.

At the tetrahedral site, the electrostatic repulsion between Li^+ and the cation from MO_6 octahedron which shares the face to that tetrahedral site is another vital factor that should be considered for the Li^+ diffusivity in the lithium-layered structure[29,30].

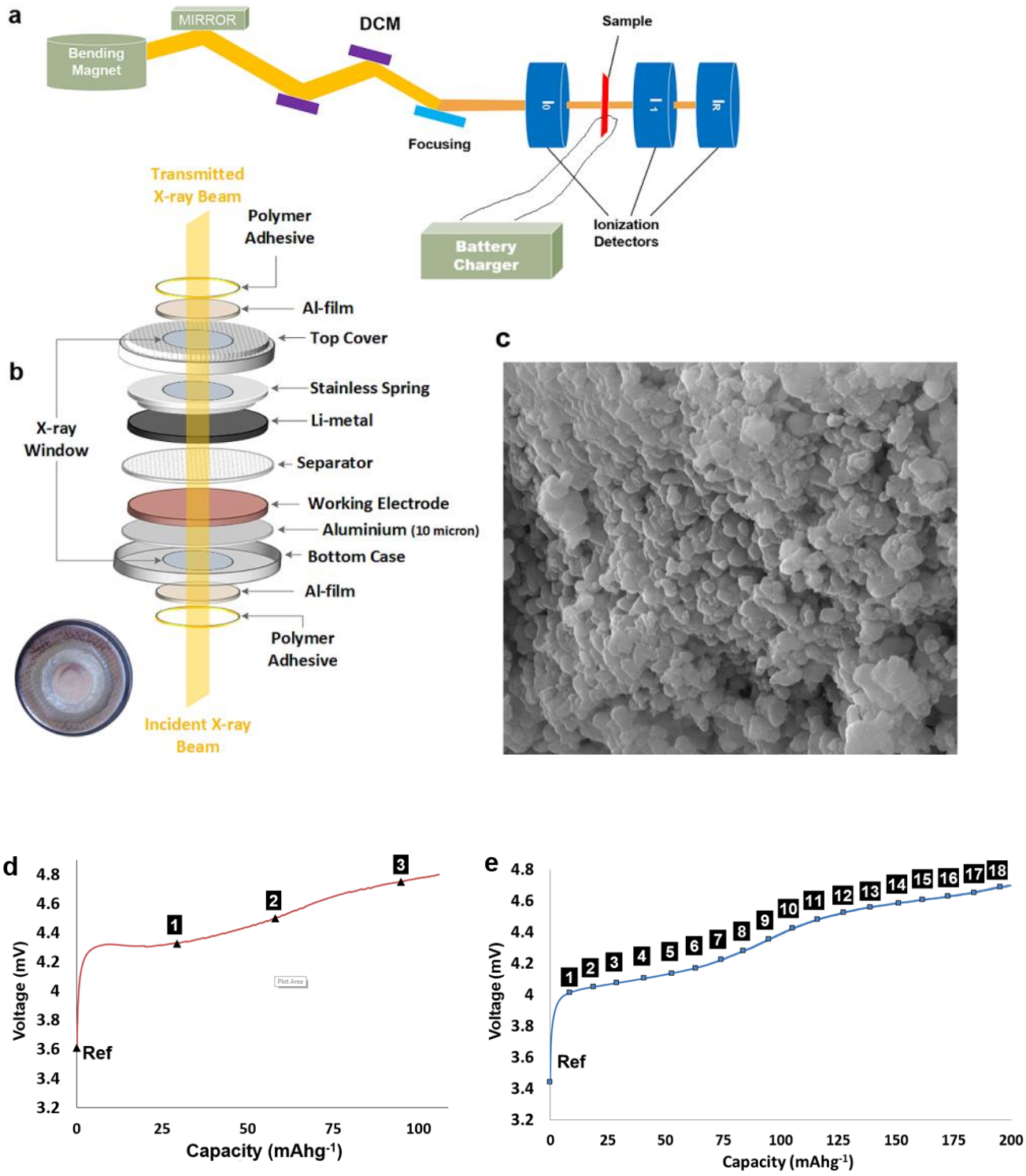


Figure 8.2 In operando synchrotron investigation of lithium-ion batteries. (a) In Operando XAS setup. (b) Illustration of the special modified cell design. (c) Scanning Electron Microscopy of $Li(Li_{0.2}Mn_{0.54}Ni_{0.13}Co_{0.13})O_2$ cathode. (d) Galvanostatic profile of the operando cells at fast charge (0.5 C) and (e) slow charge (0.125 C) rates. Points signify the collection of XAS spectra numbered 1, 2 …18, collected at charge points in the galvanostatic profile. Ref indicates the measurement of coin cell without any current.

The activation barrier not only depends on the cation type, but also its oxidation state. It was reported that lower oxidation states result in a lower activation barrier[29]. It has been also studied that the cation mixing which causes defects in the lithium-layer is strongly connected to the Li^+ mobility. The calculated activation barrier increases with cation mixing. For example, Li/Ni cation mixing in the lithium-layer tends to reduce the Li slab spacing, which in turn leads to a higher activation barrier by changing its equilibrium. It is therefore that the battery performance, i.e. rate capability is highly affected by the local atomic environment that surrounds the Li^+. Reversely, the local atomic environment may vary upon the Li^+ (de)intercalation rate, because the mechanism involved is associated with 'electrostatic interaction' which is a bidirectional process. As a portable energy source for the electric vehicles (EV/HEV), the charge rate is in fact of primary interest to the engineers. It is important to point out here that lithium-ion batteries have a range of optimized charge rate that corresponds to the capacity with full saturation. As a consequence, increasing the charge current does not result in a practical full charge state although the battery can reach it quicker at the target voltage with a fast charge rate. This is due to the multiple charge stages in the lithium-ion battery. Especially, the second stage known as the 'saturation charge' must be taken into account when we consider a full capacity of the battery. On the other hand, the first stage of charge is based on the constant current process. If we apply a slow charge rate, a large amount of the capacity can be achieved during the initial charge stage owing to the deep charge process. By contrast, at a fast charge rate, the cell should obtain the rest of the capacity during the saturation charge stage in order to achieve the full battery capacity.

The present study introduces an *in operando* XAS study on the graphene-coated $Li(Li_{0.2}Mn_{0.54}Ni_{0.13}Co_{0.13})O_2$ cathode coin cells with different charge rates. Note that the charge process is based on the constant current charge stage, thus a faster charge rate results in a lower capacity than that of the slow charge which is a deep charge that enables the full potential from

the charge compensation mechanism. The specially developed X-ray window in the coin cell (Figure 8.2) allows us to precisely investigate the local atomic environment changes of the integrated-composite cathode during initial charge. For the first time, the XAS investigation has found the differences in the local atomic environment change in the lithium-rich layered cathode upon charge rates (0.125 C vs 0.5 C) in the constant current charge stage. The spectra collected in the Extended X-Ray Absorption Fine Structure (EXAFS) enabled the quantification of the structural changes on charge. The Li^+ hopping mechanism appears to be dependent on the charge rates that lead to the different level of charge compensation mechanism from the transition metals (Mn, Co, and Ni). We could also clearly identify the two-phase reaction in the slow charge cell with the separation of the two local environments at ~4.224 V for each transition metal by the EXAFS analyses. It is likely that Li^+ are mostly extracted from the lithium-layer in the fast charge, whereas they are extracted both from the transition metal layer and lithium-layer in the slow charge.

8.2 Experimental Section

8.2.1 Active material synthesis

The active material $Li(Li_{0.2}Mn_{0.54}Ni_{0.13}Co_{0.13})O_2$ was synthesized by the spray-dryer assisted sol-gel method. A detail description of the synthesis method is presented in section 4.1.1 and 4.1.2

8.2.2 Assembling of *in operando* coin cell

A specially-designed coin cell (CR-2025-D) with X-ray window was prepared to perform the *in operando* XAS as illustrated in Figure 8.2. The assembling procedure is well described in section 4.2.1 in detail. The diameter and thickness of the coin cells were 21 mm and 2.6 mm, respectively.

8.2.3 Synchrotron X-ray Absorption Spectroscopy (XAS)

The synchrotron *in operando* XAS experiment was conducted on B18 Core EXAFS beamline at Diamond Light Source (DLS, UK). XANES/EXAFS spectra were collected in transmission mode

at the Mn (6.537 keV), Co (7.712 keV), and Ni (8.339 keV) K-edges using a Si (111) double crystal monochromator at room temperature. The intensity of incident and transmitted X-ray beam were measured by the unit of ionization chambers. The monochromatized beam spotted on the cell window was approximately 140 x 140 microns. The beam energy was initially calibrated using the reference foil spectra of Mn, Ni, and Co, and then the energy was tuned to 7.1 keV, 8.225 keV, and 9.3 keV, for Mn, Co, and Ni K-edge analysis respectively. The G1 (active material: 6.34 mg) cell was charged at a rate of 0.5C (0.634 mA), whereas the G2 cell (active material: 6.58 mg) was charged at a rate of 0.125C (0.164 mA) in the voltage window of 4.8-2.0 V vs. Li^0/Li^+ in which the 1C signifies 250 mA/g current density. The prepared coin cells were directly clamped to the galvanostatic charger with wires in order to perform the *in operando* XAS investigation.

8.2.4 XAS data interpretation

Data interpretation was performed with a IFEFFIT computation code by using the ATHENA [159] software package. The XAS data were normalized with a spline function, and the normalized EXAFS spectra were converted from energy (eV) to k-space and weighted by k^3 in order to amplify the EXAFS signals in high k-space ($k^3\chi(k)$). This was followed by the Fourier transformation of the EXAFS oscillations (k-space) into the *R*-space (uncorrected phase shift), so as to evaluate the distance information between coordination shells. Major EXAFS parameters such as the distance between the neighbouring shells (R), EXAFS Debye–Waller factor ($\exp(-2\sigma^2k^2)$), amplitude reduction factor (S_0^2), energy shift (ΔE_0), and the EXAFS R-factor were obtained by fitting within the ARTEMIS application. The fitting was processed using the FEFF 6 algorithm with atomic coordination number (CN) of 6 for Mn and Co transition metals. Multiple numbers of atomic coordination (e.g. CN=6, CN=5.1/0.9, CN=2/4) were used for the Ni EXAFS fitting during the initial charge. The EXAFS least square fits were carried out based on two-phase composite system with the fitting range of 1-3.65 Å for Mn, Co, and Ni.

8.3 Results and Discussion

8.3.1 In operando XANES at Mn K-edge

The results obtained from the *in operando* XAS at the Mn K-edge from cell G1 and cell G2 are presented in Figure 8.3. The G1 cell was charged at a rate of 0.5 C (fast charge), whereas the G2 cell was charged at a rate of 0.125 C (slow charge). Their corresponding galvanostatic profile can be seen in Figure 8.2. During initial charge, a total of four points of XAS were collected for the fast charge cell (G1) while 19 data points were taken for the slow charge cell. The 'REF' point indicates the collecting point where no current was applied. Four significant absorption features (A1 - A4) were identified at the Mn K-edge XANES (Figure 8.3). The red arrows in the XANES figures indicate the direction of spectral changes during the initial charge. Absorption feature **A1** represents the Mn K pre-edge peaks located between 6536 and 6542 eV. The double pre-edge peaks increased upon charge, and the pattern of energy shifts appears to be similar at both charge rates (Figure 8.3a,b). These weak peaks are assigned to 1s-3d_{t2g} and 1s-3d_{eg} transitions. The transitions from 1s to unoccupied 3d states are formally dipole-electric forbidden in a centrosymmetric system, but the double peaks appear due to a pure quadrupole coupling or/and 3*d*-4*p* orbital hybridization from the non-centrosymmetric environment by the distortion of the octahedral MnO_6 3a site in the layered structure (space group: $R\bar{3}m$). It is thus that the information about local symmetry around the absorber (Mn) can be deduced from the peak intensity. Lower intensity signifies higher centrosymmetric environment in the octahedral structure. As shown in Figure 8.4, the slow charge cell (G2) displayed significantly higher structural distortion than the fast charge cell (G1) during Li^+ deintercalation, as evidenced by the peak intensity. Another interesting observation is that the energy difference between 1*s*-3d_{t2g} and 1*s*-3d_{eg} transitions decreases during the initial charge, and this trend was apparent in the slow charge cell.

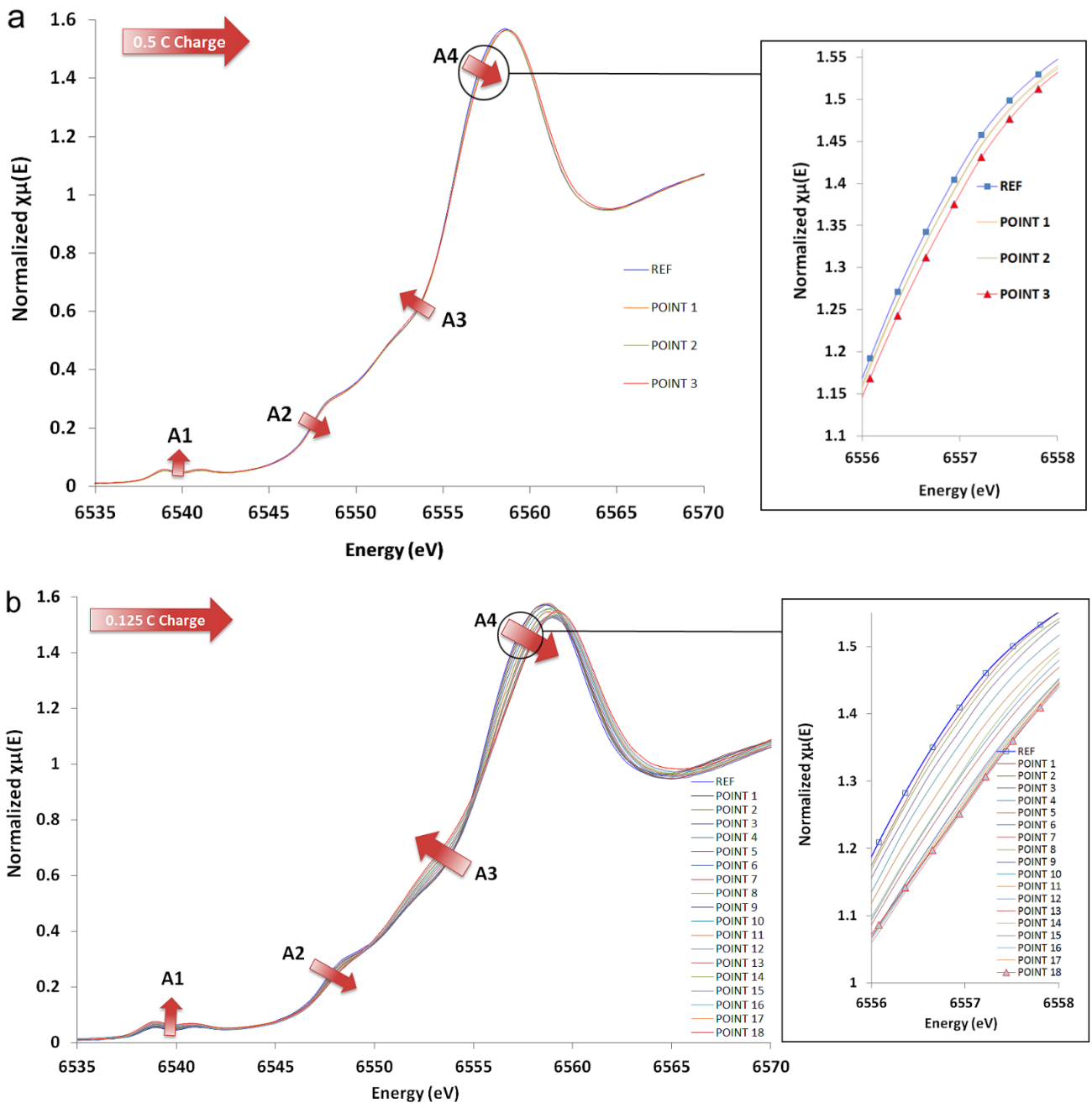


Figure 8.3 Normalised XANES spectra at Mn K-edge of $Li(Li_{0.2}Mn_{0.54}Ni_{0.13}Co_{0.13})O_2$ during the initial charge (a) Distinctive absorptions and the trend of the spectra shift in the fast charge (0.5 C) cell (G1). (b) Distinctive absorptions and the trend of the spectra shift in the slow charge (0.125 C) cell (G2). POINT signifies the collection point of XAS spectra and it is numbered as 1, 2 …18, which corresponds to the charge points in the galvanostatic profile. REF indicates the measurement point of the coin cell without any current.

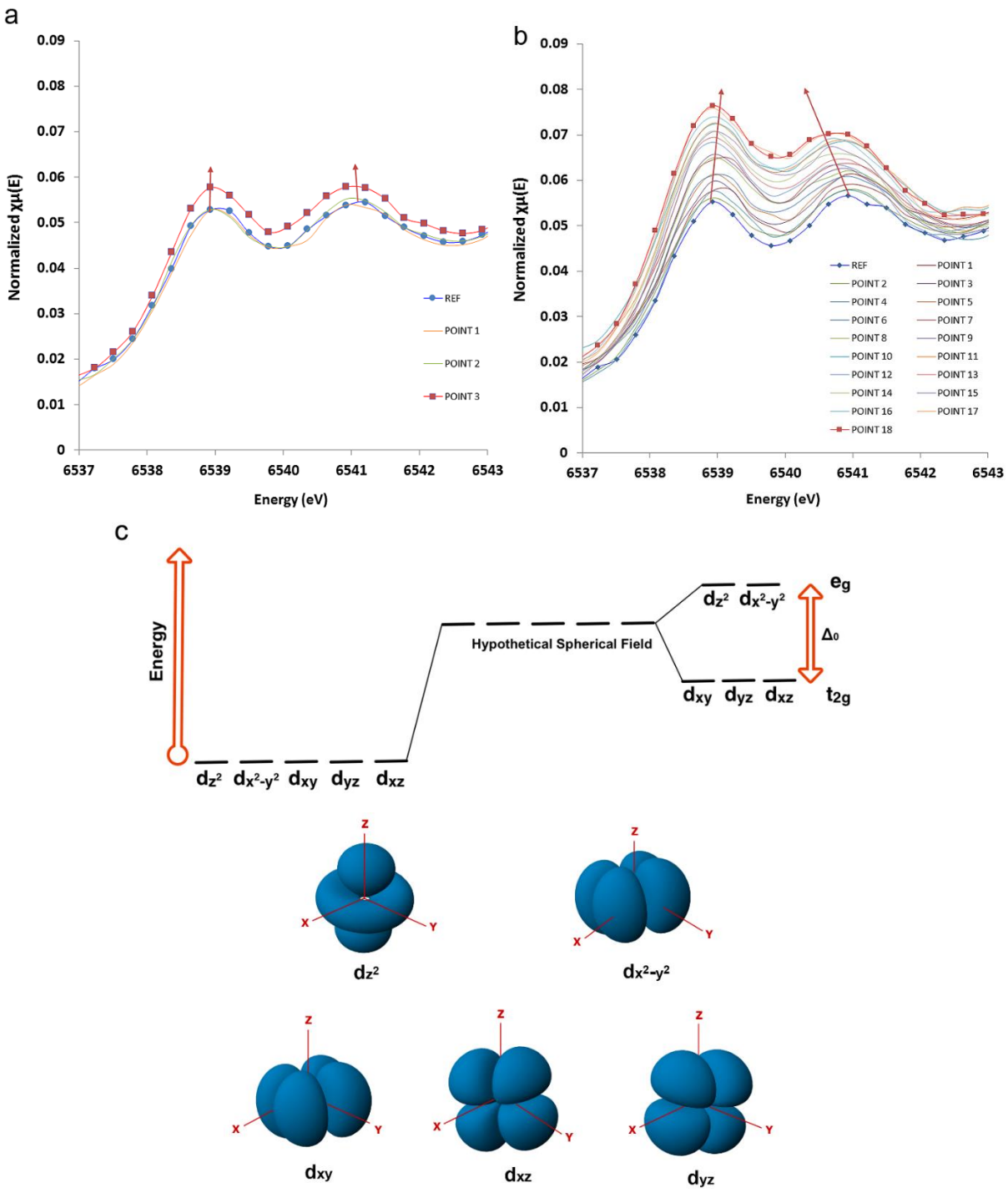


Figure 8.4 Normalised XANES spectra at Mn K pre-edge of $Li(Li_{0.2}Mn_{0.54}Ni_{0.13}Co_{0.13})O_2$ during the initial charge at (a) fast charge (0.5 C) and (b) slow charge (0.125 C) cells. (c) Illustration of the crystal field splitting diagram of d-orbitals in Mn octahedral environment. Δ_o denotes crystal field splitting energy.

This result would be explained by the crystal field theory for the octahedral geometry in transition metals. It is known that a free transition metal ion remains degenerate with the identical energy level of five 3*d* orbitals (d_z^2,d_x^2-$_y^2$, d_{xy}, d_{xz}, and d_{yz}). If the Mn atom is encircled by a spherically

symmetrical field of negative charges, then the energy of the *d* orbitals will increase, but still the five *d* orbitals remain degenerate. However, when a negatively charged ligand atoms (O^{2-}) approach the transition metal, the degeneracy of the *d* orbitals is removed due to the Coulomb repulsion between the negative charges and the electrons in *d* orbitals. The elimination of the degeneracy results in the energy splitting of the two *d* orbital groups into a doubly degenerate orbital set of e_g and a triply degenerate orbital set of t_{2g} as illustrated in Figure 8.4c. The energy difference between e_g and t_{2g} sets is called **crystal field splitting energy** (Δ_o). The Mn pre-edge XANES result shows that there has been a gradual decrease in the crystal field splitting energy (Δ_o) on both charge rates. The energy decrease in the slow charge rate was measured to be 0.58 eV as it shifts from 2 eV to 1.42 eV on charge. Absorption feature **A2** (Figure 8.3) recorded between 6545 eV and 6550 eV represents the electric dipole transition from 1s to 4p with a shakedown process resulting from the ligand-to-metal charge transfer (LMCT), while feature **A4** is assigned to the electric dipole transition from 1s to 4p without the shakedown process. As such, the final states of absorption feature **A2** and **A4** in the REF state correspond to $1s^1c3d^{n+1}$ $L4p^1$ and $1s^1c3d^n4p^1$, respectively, where c denotes a 1s core hole and L indicates an oxygen 2p ligand (Mn^{4+}: n=3). The gradual decline in the peak intensity of absorption feature **A2** on charge possibly implies the suppression of the tetragonal distortion in the MnO_6 octahedron[183]. The spectral shift of Mn was found to be only 0.4 eV in the fast charge cell (G1). This value is more than three times lower than that of the slow charge cell (G2) as it was measured to be 1.3 eV. The notable larger amount of the spectral shift in the slow charge cell can be considered as the consequence of actual oxidation change in the Mn and/or the effect from the structural modification resulting from Li^+ removal. It is generally believed that the oxidation state of Mn is +4 in the pristine material and it will not change upon charge. However, previous studies[91,93,94] have reported the Mn in the pristine material may present in a mixed oxidation state between low-spin Mn^{3+} and Mn^{4+}, i.e. +3.75 on average.

8.3.2 In operando XANES at Co K-edge

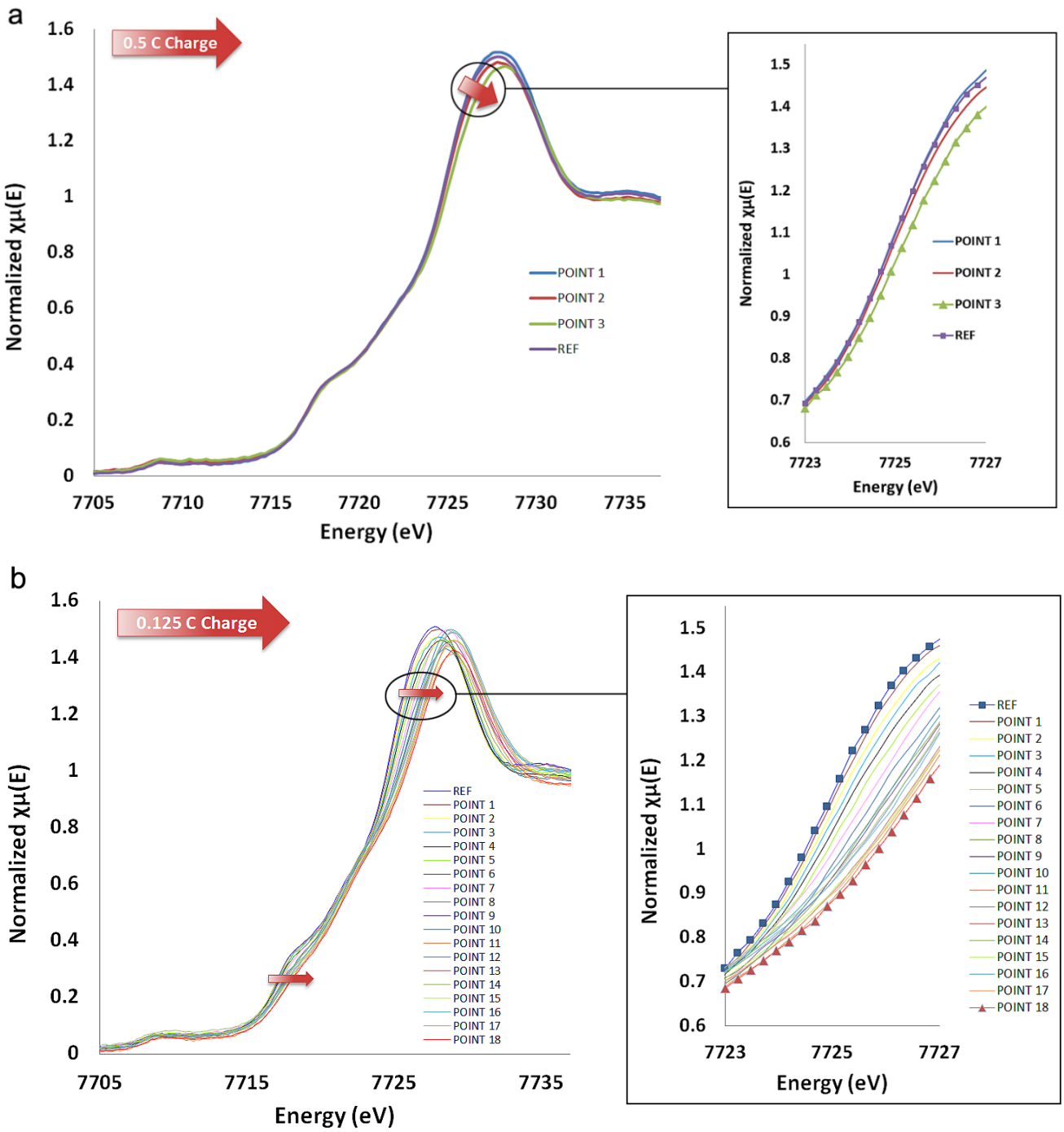


Figure 8.5 Normalised XANES spectra at Co K-edge of $Li(Li_{0.2}Mn_{0.54}Ni_{0.13}Co_{0.13})O_2$ during the initial charge of (a) fast charge (0.5 C) and (b) slow charge (0.125 C) cells.

XANES spectra collected at the Co K-edge on initial charge are compared in Figure 8.5. The overall trend of the spectra shift in G1 cell was similar to that of G2 cell. Both cells moved towards

higher energy upon charge. However, the magnitude of the spectral shift between the fast and slow charge rates was found to be significantly different as the spectral shift of the Co K-edge in G1 cell was 0.61 eV, whereas the spectral shift in the G2 cell was measured to be 1.41 eV which is more than two times larger than the fast charge rate. It can thus be suggested that the contribution to the charge compensation mechanism by the oxidation change of Co ions was distinctively higher in the slow charge rate during the Li^+ deintercalation.

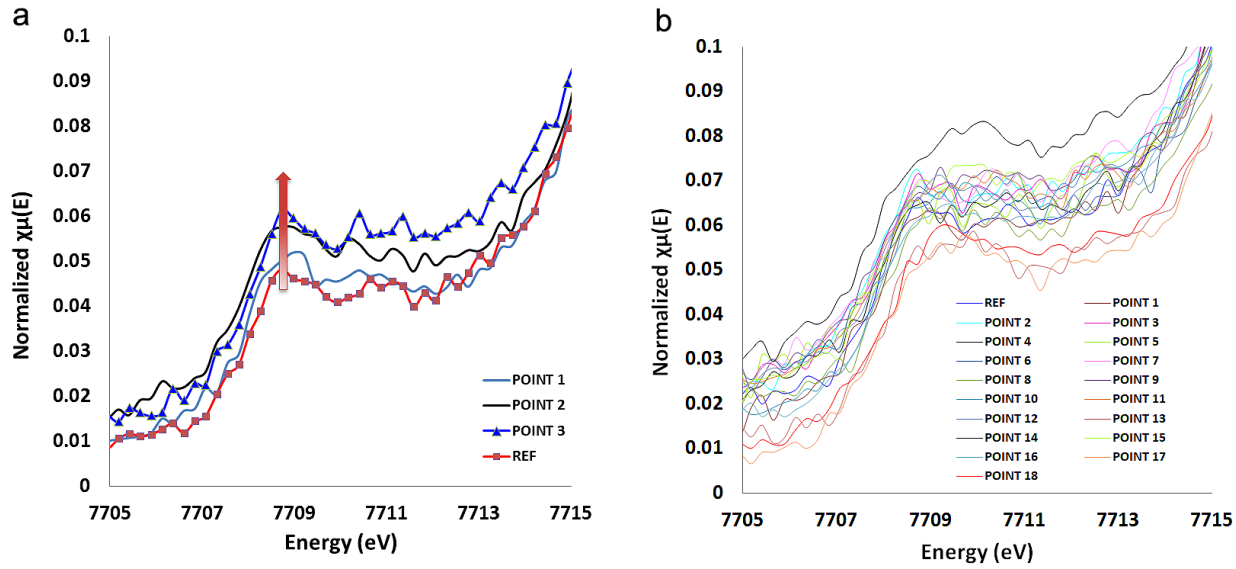


Figure 8.6 Normalised XANES spectra at Co K pre-edge of $Li(Li_{0.2}Mn_{0.54}Ni_{0.13}Co_{0.13})O_2$ during the initial charge of (a) fast charge (0.5 C) and (b) slow charge (0.125 C) cells.

On the other hand, a similarity could be observed in the trend of the XANES spectral shift between Co and Mn. The similarity of the overall shape of the XANES implies the similar local environment on charge. The XANES spectra collected at the Co K pre-edge for G1 and G2 cells were presented in Figure 8.6. A weak peak was found at around 7708.8 eV at the Co K-edge in XANES on both charge rates. The appearance of this single peak is due to the 1s to 3d transition. Interestingly, the peak in the G1 cell exhibits continuous increment in the normalized intensity on charge, whereas no systematic change was observed in the slow charge cell (G2).

8.3.3 In operando XANES at Ni K-edge

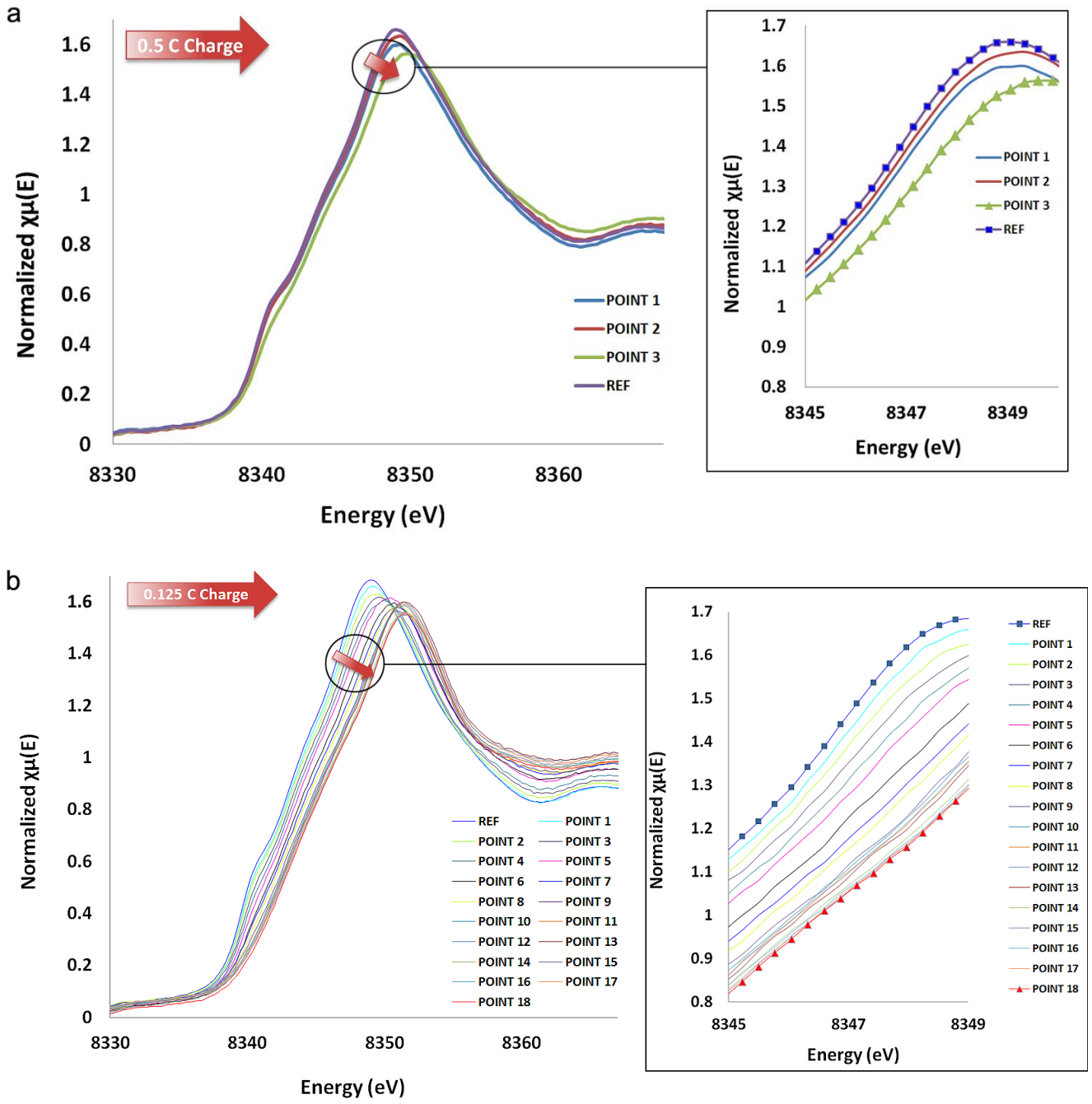


Figure 8.7 Normalised XANES spectra at Ni K-edge of $Li(Li_{0.2}Mn_{0.54}Ni_{0.13}Co_{0.13})O_2$ during the initial charge of (a) fast charge (0.5 C) and (b) slow charge (0.125 C) cells.

The results obtained from the normalised XANES spectra at Ni K edge on initial charge of G1 and G2 cells were respectively compared in Figure 8.7a and Figure 8.7b. Similarly as Mn and Co K-edge XANES, the Ni XANES spectra shift towards higher energy upon charge. However, no pre-

edge peak was observed in the Ni XANES, especially in the range of 8330-8338 eV. This is indicative of a symmetric local environment around the Ni absorber. The observed spectral shift of Ni K-edge with parallel patterns implies a different local environment compared with that of Mn and Co. The spectral shift of the fast charge cell (G1) was 1.07 eV, whereas the spectral shift of the slow charge cell (G2) was found to be 2.6 eV. The smaller energy shift in the G1 cell indicates smaller oxidation changes during Li^+ deintercalation from the composite. It should be noted that the Ni displayed the largest energy shifts of XANES spectra at K-edge among the transition metals. This finding is attributed to the two-stage redox reaction of the Ni between Ni^{2+}/Ni^{3+} and Ni^{3+}/Ni^{4+} [99,117,174]. In the slow charge cell, more than double of the XANES energy shift was recorded compared with the fast charge cell. Therefore, we may explain that this large discrepancy is attributed to the different amount of the oxidation change on charge rates. Strictly, the Jahn-Teller effect from the low spin Ni^{3+}:$d^7(t_{2g}^6 e_g^1)$ must be also taken into account as the main factor that contributes to the larger spectral shift. It seems that fewer Ni^{3+} Jahn-Teller ions appeared in the G1 cell and thus results in a minimum impact on the structural modification in the composite.

8.3.4 In operando EXAFS at Mn K-edge

Figure 8.8 reveals the Fourier transform magnitudes on Mn K-edge EXAFS $\chi(k)$ of the graphene-coated $Li(Li_{0.2}Mn_{0.54}Ni_{0.13}Co_{0.13})O_2$ cathode during charge. The EXAFS data is presented in R-space. EXAFS fitting was performed with FEFF 6 algorithm in order to evaluate the bond length changes of Mn-O and Mn-TM (TM: Mn, Co, and Ni) on charge. Coordination number of 6 was used for the Mn fitting.

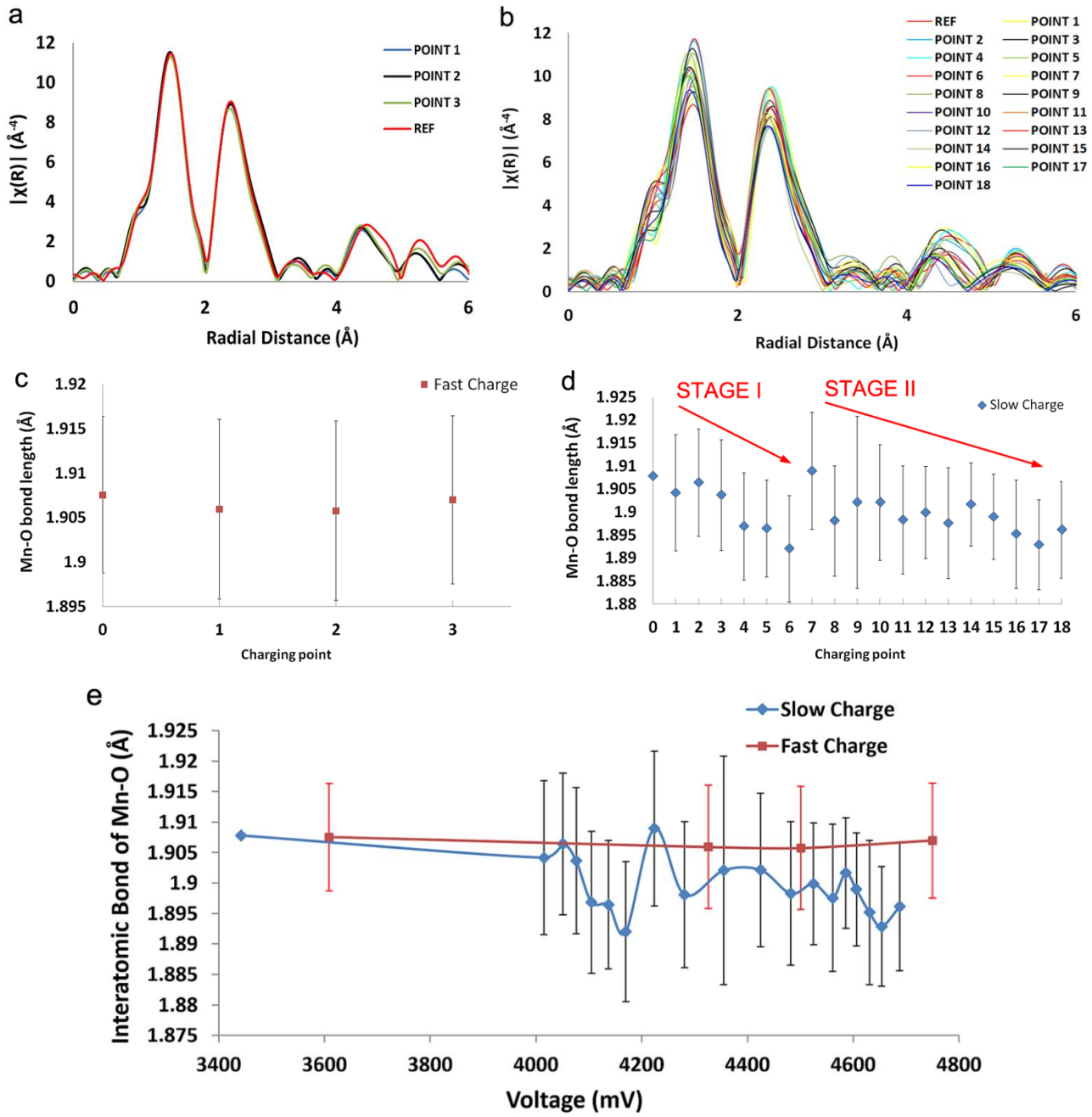


Figure 8.8 Fourier transform magnitudes (k^3-weighted) at Mn K-edge of the graphene-coated $Li(Li_{0.2}Mn_{0.54}Ni_{0.13}Co_{0.13})O_2$ during charge of (a) fast charged (0.5 C) G1 and (b) slow charged (0.125 C) G2 cells. Evaluation of the atomic bond-lengths of (c) G1 1st shell (Mn-O) and (d) G2 1st shell (Mn-O). (e) Comparison of Mn-O changes vs voltage during charge. POINT signifies the collection point of XAS spectra and it is numbered as 1, 2 …18, which corresponds to the charge points in the galvanostatic profile. REF (point 0) indicates the measurement point of the coin cell without any current.

Major EXAFS parameters such as radial distance (Å), mean square disorder (σ^2), amplitude reduction factor (S_0^2), energy shift (ΔE_0), and R-factors were refined by the calculation. There has been a gradual decline in the level of the intensity from the first coordination shell (Mn-O) on

charge. This change was distinctive in the slow charge cell (G2) as the amplitude of the 1st coordination shell (Mn-O) at ~1.53 Å of the slow charge cell (G2) dropped by 27%, while it only dropped by 1.1% at fast charge cell (G1), as shown Figure 8.8a,b. This discrepancy on charge rates could be also confirmed by the bond length changes of Mn-O during the initial charge as can be seen in Figure 8.8e. The maximum bond length difference in the slow charge cell was found to be 0.016 Å, which is significantly higher than that of the fast charge cell (R~ 0.001 Å). This combination of findings offers some insights into the phase transition issue originated from the local atomic change of the Mn. It is likely that the fast charge may undergo less phase transformation, which is the major problem linked to the capacity fading/voltage decay, in the constant current charge state (stage 1 charge) relative to the slow charge rate. Another important finding is the presence of the two-stage reaction in the $xLi_2MnO_3 \cdot (1-x)LiMO_2$ cathode system as presented in Figure 8.8d. The evidence of the two-stage reaction can be clearly seen in the slow charge cell, but it was not apparent in the fast charge rate data. It appears that the second stage begins from approximately ~4.224 V (charge point 7) in the G2 cell, as shown in Figure 8.8d,e. The appearance of the second-stage reaction might be related to the process involved for the activation of the Li_2MnO_3 component in the graphene-coated $Li(Li_{0.2}Mn_{0.54}Ni_{0.13}Co_{0.13})O_2$ cathode on charge. This result implies that the Mn was not electrochemically activated, even above ~4.5 V in terms of the fast charge rate as evidenced by the Mn-O bond length change in the fast charge cell (Figure 8.8c). In principle, at > ~4.5 V, the removal of lithia (Li_2O) from the Li_2MnO_3 component produces an electrochemically activated MnO_2 compound, which is the key reaction that provides the extra charge capacity. As a result, a notable bond length change between Mn and O would be observed during charge.

8.3.5 In operando EXAFS at Co K-edge

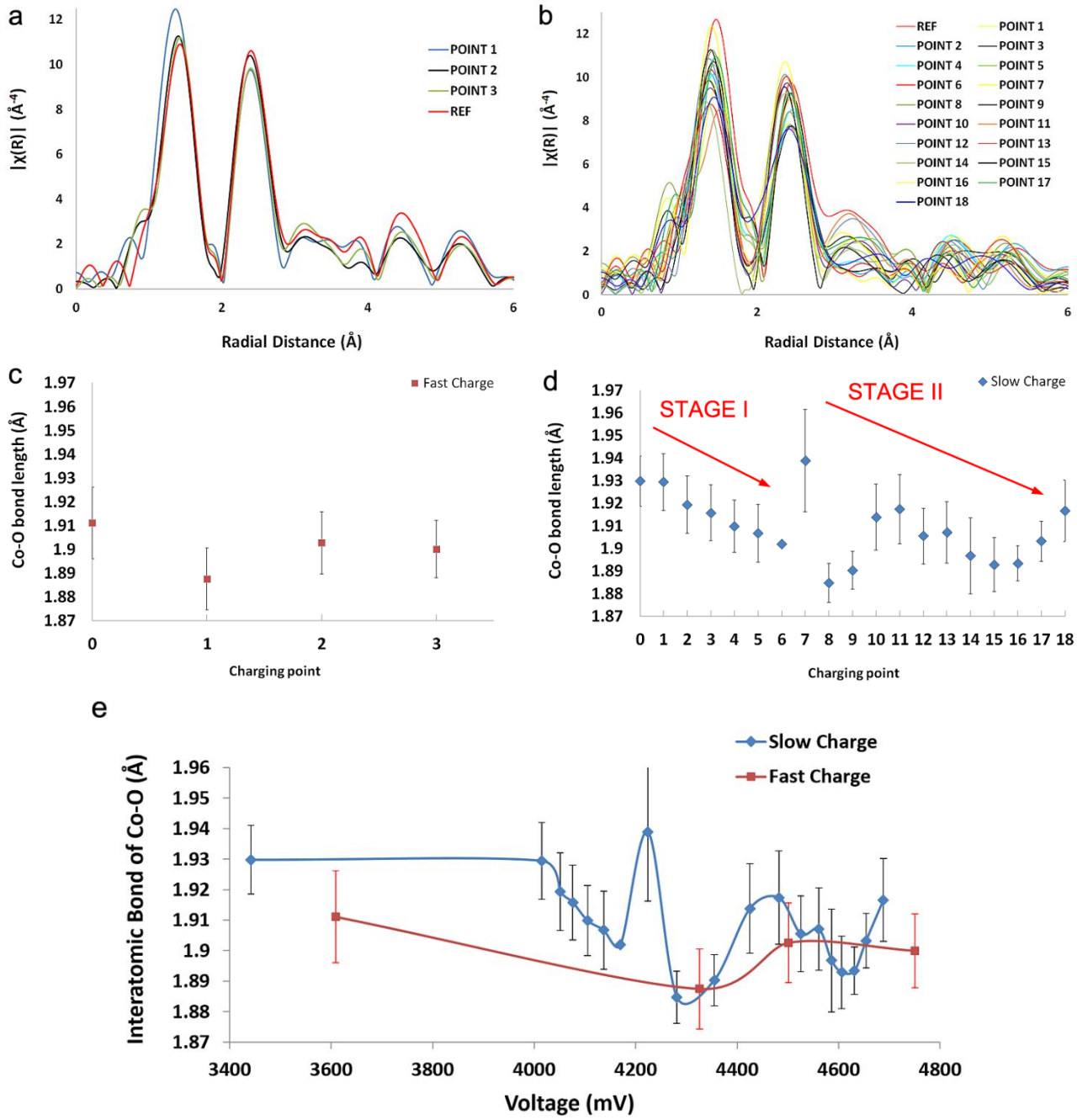


Figure 8.9 Fourier transform magnitudes (k^3-weighted) at Co K-edge of the graphene-coated $Li(Li_{0.2}Mn_{0.54}Ni_{0.13}Co_{0.13})O_2$ during charge of (a) fast charged G1 (0.5 C) and (b) slow charged G2 (0.125 C) cells. Evaluation of the atomic bond-lengths of (c) G1 1st shell (Co-O) and (d) G2 1st shell (Co-O). (e) Comparison of Co-O changes vs voltage during charge. POINT signifies the collection point of XAS spectra and it is numbered as 1, 2 …18, which corresponds to the charge points in the galvanostatic profile. REF (point 0) indicates the measurement point of the coin cell without any current.

The results obtained from the Fourier transform magnitudes on the Co K-edge EXAFS $\chi(k)$ in the R-space on charge are shown in Figure 8.9. The coordination number was constrained to be 6 for the fitting of the Co-O/Co-TM pairs. Other structural and statistical parameters of Co EXAFS were refined by the fitting calculation. A similar pattern emerges in terms of the impacts from different charge rates on the host structure compared with those for Mn. As can be seen from Figure 8.9a, the slow charge cell (G2) exhibits larger deviations from the reference EXAFS signal (red spectra) on charge. The modifications in the Co local atomic environment was indeed significant in the slow charge rate. Not only the amplitude of 1st shell (Co-O) and 2nd shell (Co-TM) significantly changes, but also the higher coordination shell varies remarkably in peak amplitudes upon charge. Similarly as for Mn, a two-stage reaction relevant to the Co local environment was also clearly identified as presented in Figure 8.9d. The chart reveals that the second stage seems to begin from the voltage level between 4.2 V and 4.3 V, where it corresponds to the collection point 7 in G2 cell. This range is identical to that of Mn in terms of the two-stage local environment. From the Co EXAFS fitting, the maximum bond length change in the slow charge cell was measured to be 0.054 Å, whereas the fast charge cell revealed smaller changes with the maximum difference of 0.024 Å. It can therefore be assumed that the slow charge cell contributes to the charge compensation mechanism by larger oxidation change during Li^+ deintercalation.

8.3.6 In operando EXAFS at Ni K-edge

Figure 8.10 compares the Fourier transform magnitudes on Ni K-edge EXAFS $\chi(k)$ in the R-space during initial charge. Remarkable variations could be observed in the oscillation pattern of Ni K-edge EXAFS on both charge rates. It appears that the local atomic environment of Ni varies more dynamically during Li^+ deintercalation compared with Mn and Co.

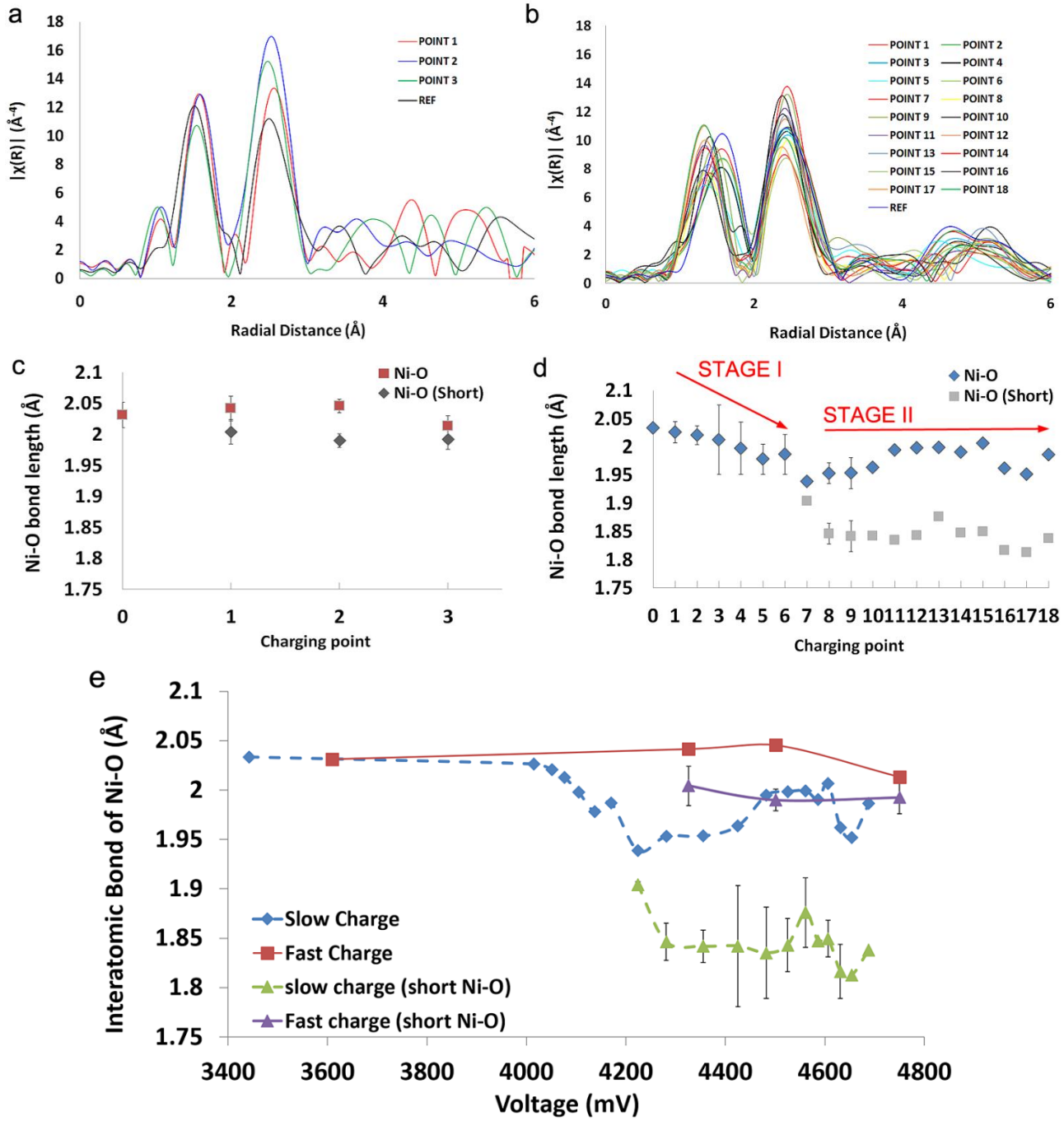


Figure 8.10 Fourier transform magnitudes (k^3-weighted) at Ni K-edge of the graphene-coated $Li(Li_{0.2}Mn_{0.54}Ni_{0.13}Co_{0.13})O_2$ during charge of (a) fast charged G1 and (b) slow charged G2 cells. Evaluation of the atomic bond-lengths of (c) G1 1st shell (Ni-O) and (d) G2 1st shell (Ni-O). (e) Comparison of Ni-O changes vs voltage during charge. POINT signifies the collection point of XAS spectra and it is numbered as 1, 2 …18, which corresponds to the charge points in the galvanostatic profile. REF (point 0) indicates the measurement point of the coin cell without any current.

This observation can be explained by three major reasons: (1) contribution to the charge compensation mechanism by two-step oxidation ($Ni^{2+} \rightarrow Ni^{3+} \rightarrow Ni^{4+}$) of Ni, (2) Li/Ni cation

mixing[58,68,175], and (3) the Jahn-Teller effect from the low-spin Ni^{3+} (d^7). Especially, the bond-length splitting into long Ni-O and short Ni-O that begins from ~4.224 V (Figure 8.10e) is attributed to the Jahn-Teller distortion from Ni^{3+}. In addition, the local environment changes with two-stage was also identified in the Ni K-edge EXAFS. Although the pattern of Ni-O changes is different, the range of those stages are consistent with those for Mn and Co. The appearance of the Jahn-Teller distortion is likely to begin from ~4.2-4.3 V on both charge rates. Apparently, the bond-length difference between the long Ni-O and short Ni-O was more considerable in the slow charge cell as can be seen from Figure 8.10e. This finding is also supported by the EXAFS oscillations in R-space since the slow charge reveals notable location shifts in the 1st coordination shell (Ni-O) peak between 1.31 Å and 1.56 Å upon charge, as presented in Figure 8.10b. The location shift of the Ni-O peak in the fast charge rate was very small as the range of the peak shift was between 1.53 Å and1.56 Å (Figure 8.10a). The Ni EXAFS fitting was conducted with the coordination number of 6 at REF point. Major EXAFS parameters were refined during the fitting computation. The coordination number of 4 and 2 were used at charge point 7 in the G2 cell, and the coordination numbers of Ni-O varies upon the voltage levels. The bond-length difference was found to be 0.0373 Å at 4.224 V in the fast charge cell, but it only increases up to 0.0556 Å (charge point 2). This value is three times smaller than that of the slow charge rate as it reached up to 0.157 Å. The Jahn-Teller distortion from Ni is believed to be reversible with the oxidation change of the Ni ion. For the fast charge cell, the reversible trend is well reflected as the separated bond-length of Ni-O tends to return in a single length as can be seen from Figure 8.10e, at around ~4.78 V. On the other side, for the slow charge cell, it seems to be the distortion effect remains as the bond-length difference is notable at ~4.7 V. There are two possible explanations for this discrepancy. Firstly, it may be the case that the bond splitting in slow charge cell eventually disappears on

further charge. Secondly, although the Jahn-Teller effect gradually diminish according to the oxidation change of Ni, the structural modifications may be irreversible in the slow charge cell.

8.3.7 Two-stage reaction and general implications

The challenge for the next generation lithium-ion battery is to develop a battery system that enables portable electric device or electric vehicles (EV/HEV) to charge at a remarkable speed, i.e. 100 times faster than the current lithium-ion batteries. However, the concept of 'fast charge rate' sometimes become confusing when multiple charge stages have not taken into account for the lithium-ion battery. Especially, the second stage known as the 'saturation charge' should be also considered when the battery was not able to achieve its full capacity during the constant current stage. The galvanostatic profile presented in the study is based on the constant current method. The increase of the charge rate in the galvanostatic tester can reach the high cell potential in a relatively short time, but it extends the time of the saturation charge accordingly, in order to achieve the original full capacity. As such, the current study reports the different impacts on the structural modifications of the cathode composite as a function of charge rate in the constant current stage.

It is believed that the Li^+ extraction from the host composite appears either sequentially or concurrently both from the lithium layers and the transition metal layers[58,174]. However, the amount of those lithium-ions with full chemical potential attributed to the charge compensation mechanism possibly vary upon the charge rates (0.125 C vs 0.5 C). It is speculated that the Li^+ in the slow charge rate tend to be deintercalated from the transition metal layers more deeply, which in turn exerts a strong influence on the underlying structure. On the other hand, in fast charge rate, the charge capacity was notably reduced not only because of the smaller oxidation change of the transition metals, but also less activation in the Li_2MnO_3 implying less lithia (Li_2O) extraction ($Li_2MnO_3 \rightarrow Li_2O + MnO_2$) even above ~4.5 V. The discrepancy in the influences can be deduced

on the basis of EXAFS interpretation. It is interesting to note that the maximum bond length difference for Mn-O was 16 times higher (ΔR~ 0.016 Å) in the slow charge cell than that of the fast charge cell (ΔR~ 0.001 Å), whereas the maximum difference in the Co-O bond length was calculated to be 0.054 Å for the slow charge cell that is only approximately two times higher than the fast charge cell (ΔR~ 0.024 Å). This finding indicates that there has been little activation during fast charge in the Li_2MnO_3 component which is responsible for the larger initial charge capacity, as well as the possible phase transition from the layered structure into the spinel. This explains the slight dimensional change in terms of the Mn-O bond length on fast charge, and due to this little modification in the Mn local environment, the phase transition into the spinel may be hindered in this case. Another interesting observation is the appearance of the two-stage local atomic environment which is separated at the voltage level of ~4.224 V. This result would be explained by the crystal lattice change in the trigonal system ($R\bar{3}m$) on charge. A number of studies using *in situ* XRD[4,8,58,65,76,122] have reported the gradual rise of the c-lattice parameter and a decrease in the a-lattice parameter upon the battery charge. The c-lattice expansions can be described by the electrostatic repulsion between the oxygen ions after the deintercalation of the Li^+ from the lithium layers.

The largest difference of Ni-O bond length in slow charge rate was evaluated to be 0.220 Å, while it was only 0.055 Å at the fast charge rate. Also, this result indicates the active oxidation in the slow charge cell because of the charge compensation mechanism. When the Jahn-Teller distortion from Ni^{3+} is considered, the process interpretation becomes more complicated in terms of the EXAFS modelling. It is likely that the Jahn-Teller distortion leads to the Ni-O bond splitting at charge point 7 (~4.224 V) where a sudden rise in the bond length was observed in the Mn-O and Co-O EXAFS computation. The largest discrepancy between the short Ni-O and long Ni-O

bonds at slow charge rate was measured to be 0.159 Å at 4.482 V, and this is around three times larger than that of the fast charge cell as it was ΔR ~0.055 Å at 4.501 V.

The K-edge XANES spectral shifts for each transition metal were quantified during the initial charge. The spectral shifts of Mn, Co, and Ni K-edge were found to be 0.4 eV, 0.61 eV, and 1.07 eV in the fast charge rate, respectively. In contrast, larger spectral shifts could be examined in the slow charge rate such as 1.3 eV, 1.41 eV, and 2.6 eV for Mn, Co, and Ni K-edge, respectively. As previously mentioned, the largest spectral shift at the Ni K-edge is due to the two-stage oxidation change ($Ni^{2+} \rightarrow Ni^{3+} \rightarrow Ni^{4+}$). It is likely that the underlying structure in the fast charge cell had less distortion from the Jahn-Teller ion (Ni^{3+}). On the other hand, the pattern of the parallel energy shift in Ni XANES implies a different local environment compared to that of Mn and Co.

The crystal field splitting at the Mn K pre-edge from the double peaks was also identified. Note that the crystal field splitting energy (Δ_o) declines as lithium ions deintercalate from the cathode composite. This can be explained by the increased number of unpaired electrons of Mn on charge. In the slow charge cell (G2), it was possible to monitor a clear trend of the energy splitting, whereas it was relatively not obvious in the fast charge cell (G1). It can thus be suggested that a large number of electrons could be provided from Mn for Li^+ deintercalation at slow charge rate. This finding implies the activation of the Li_2MnO_3 component in the $xLi_2MnO_3 \cdot (1-x)LiMO_2$ cathode system at slow charge rate (0.125 C), and thus contributes to the charge compensation mechanism, significantly. The distinctive local environment change around the Mn absorber can be considered as one of the precursors that leads to the phase transition from the layered structure into the spinel structure.

8.4 Conclusion

The *in operando* XAS results implies that the nature of the local atomic environment changes in the $xLi_2MnO_3 \cdot (1-x)LiMO_2$ cathode is likely to be different depending on the charge rate. In the constant current stage of the charge process, the slow charge rate (0.125 C-rate) appears to fully activate the reactions involved for the charge compensation mechanism, so as to obtain the high specific capacity such as 200 $mAgh^{-1}$ for the graphene-coated $Li(Li_{0.2}Mn_{0.54}Ni_{0.13}Co_{0.13})O_2$ cathode. On the other side, the rapid diffusion of the Li^+ in the fast charge rate (0.5 C-rate) may be explained by the lower activation barrier of the transition metals attributed to the lower oxidation (valence) state [29] on charge. While the change at fast charge rate appears to be reversible, the local environment modification in the cathode composite at slow charge rate seems to be irreversible as evidenced by the inter-atomic bond length changes, as well as the appearance of the two-stage reaction with Ni-O bond splitting.

The present study has shown the distinguishing difference in the structural impact on the local environments of the transition metals upon different charge rates (0.125 C vs 0.5 C). The major finding of the current investigation is the identification of the two local-atomic environments separated at the voltage level of 4.224 V in the galvanostatic profile. This is associated with the activation of Li_2MnO_3 composite in the voltage range above 4.5 V with cation ordering/migration for each transition metal (Mn, Co, and Ni). As the two-stage reaction in the local environment was clearly reported only in the slow charge rate, it is suggested that the Li^+ deintercalation mechanism slightly changes depending on the charge rate, i.e. the activation barrier determined from particular oxidation levels may affect the Li^+ diffusion pattern. Owing to the novel design of the *in operando* coin cells, the XAS investigation delivers new insight into adjusting the optimal charge rates for the Li-layered Mn-based oxide cathode in order to minimize irreversible phase transitions that lead to capacity fading and voltage decay.

Chapter 9 Evidence of the Precursor that Triggers Spinel Phase Transition in the Li-rich layered Mn-based Oxide Cathode System

Previous studies have revealed the phase transition phenomena from layered structure into the spinel structure upon subsequent electrochemical cycles in the Li-layered transition metal oxide cathode, by the *in situ* neutron or synchrotron XRD investigations. The early parts of this chapter focused on the structural, chemical, and electronic state changes between the 1st cycle with the large voltage-plateau and 2nd cycle without the plateau. *In operando* EXAFS provides the information about the local atomic environment changes coupled with the implication of the cation ordering during two electrochemical cycles. The later parts of this chapter focused on the wavelet transform analysis. Unlike the chapter 7, semi-quantitative analyses was introduced on the back-scatterings from the constituent elements. This approach offers a particular advantage in evaluating the activity of the transition metals during charge and discharge.

9.1 Introduction

Previous studies have reported a phase transition phenomenon from layered structure into the spinel structure upon subsequent electrochemical cycles in the Li-layered transition metal oxide cathode[82,121–124,181,184]. The underlying principle of the phase transition from the layered $LiMnO_2$ into the spinel phase has been investigated by an *ab initio* computation by Reed et al.[121]. According to first-principle calculation, it turns out that the Li_xMnO_2 transforms into the spinel (or spinel-like) phase by a two-stage process[121]. The key factor for the phase transition is believed to be associated with the Mn ions in the layered structure (trigonal, $R\bar{3}m$)[53,113,121]. In fact, the layered structure is reduced to the monoclinic (C2/m) because of the Jahn-Teller distortion resulting from

$Mn^{3+}(d^4)$. The presence of the Mn^{3+} ions assists the phase transition towards spinel-like structure in the cathode composite. It has been computed that the Mn ions tend to move to the adjacent tetrahedral sites into the lithium-layer on charge. This plane will correspond to the 16d site of the spinel, later. On the other hand, a number of lithium ions intercalate to the tetrahedral sites on the opposite part where the octahedral vacancies formed. This position corresponds to the 8a-site of the spinel, later. It should be highlighted that the Mn^{3+} ion tends to disproportionate into the tetrahedral Mn^{2+} ions and octahedral Mn^{4+} ions during charge. As such, in the final stage, the transition process is completed by the rearrangement between the Mn ions in the tetrahedral site and the remaining Li^+ in the octahedral site forming a spinel phase. In order to avoid the phase transition from Mn^{3+} ions, composite with mixed transition metals (Mn, Co, and Ni) are generally pursued for the battery cathode. The coexistence of the Ni^{2+} and Co^{3+} ions prevent the Mn evolving into the Jahn-Teller Mn^{3+} ion by retaining the oxidation state of Mn in the tetravalent (+4) state. Moreover, the presence of Co-ion itself is likely to suppress the local distortion[113]. Ironically, however, the presence of the mixed transition metals appears to be the main factor that leads to the phase transition into the spinel by the cation migration into the lithium layers during Li^+ (de)intercalation[10,185]. On the other side, a correlation between the spinel phase evolution and cation ordering in the Li-Mn-rich cathode system has been reported by Mohanty et al[77]. It has been observed that the disappearance of the cation ordering is involved with the phase transition from the layered structure into the spinel (spinel-like) during electrochemical cycles. The transformation mechanism involved with cation migration and cation ordering still remains unclear.

In the current study, Continuous Cauchy Wavelet Transform (CCWT) method was chosen in order to precisely understand the local atomic environment changes in a highly complicated cathode system that involves diverse electrochemical and physical processes. The active material was also examined by X-ray diffraction (XRD), Raman spectroscopy, and SQUID to confirm the

formation of the integrated composite of $xLi_2MnO_3 \cdot (1-x)LiMO_2$. Also, a structural description of cation arrangement in the pristine material could be obtained from the SQUID measurement. The wavelet transform analysis on the graphene-coated $Li(Li_{0.2}Mn_{0.54}Ni_{0.13}Co_{0.13})O_2$ cathode enables the visualization of the Mn, Co, and Ni K-edge EXAFS in three dimensions by decomposing the *k*-space and R-space (uncorrected for phase shift) signals, during subsequent electrochemical cycles. The *in operando* XAS study suggests that a precursor that triggers the spinel phase transition mechanism possibly exists in the initial cycle.

9.2 Experimental Section

9.2.1 Active material synthesis

The spray-dryer assisted sol-gel method is one of the more practical ways of synthesizing the electrode composite. The synthesis process is described in section 4.1.1 and 4.1.2, in detail.

9.2.2 Electrochemical analysis and active material characterization

The standard coin cell was electrochemically cycled up to 22 times using the galvanostatic tester in the voltage range between 2.0 V and 4.8 V vs. Li^0/Li^+ at room temperature. The weight of the active material was 9.74 mg. The applied charge rate was 0.2 C-rate. The dQ/dV plot was obtained based on galvanostatic profile of the graphene-coated $Li(Li_{0.2}Mn_{0.54}Ni_{0.13}Co_{0.13})O_2$ coin cell. Scanning Electron Microscopy (SEM) analysis was conducted in order to observe the morphology of the active material by JEOL JSM-6610 LV SEM. Raman spectra of the cathode composites were collected using a HORIBA LabRAM HR 800 Dual Microscope at a wavelength of 532 nm with green laser. Raman spectra were measured from 4~5 different points using a 50x lens. X-ray powder diffraction was performed on the graphene-coated $Li(Li_{0.2}Mn_{0.54}Ni_{0.13}Co_{0.13})O_2$ material (labelled as G-type) with the X-ray energy of 11.0 keV (λ=1.127 Å). Magnetic measurement was conducted in order to examine the magnetic susceptibility (H/M) using a SQUID-VSM

Magnetometer (Quantum Design). The magnetic susceptibility (H/M) was measured in the temperature range of 5 – 300 K with a magnetic field of 1000 Oe. The magnetization curve was obtained at 5 K in the magnetic field of 60k Oe.

9.2.3 In operando XAS Study

The In Operando XAS Study was conducted at beam-line B18 Core EXAFS of Diamond Light Source (DLS, UK). XAS spectra were collected in transmission mode at the Mn (6.537 keV), Co (7.712 keV), and Ni (8.339 keV) K-edges with a Si (111) double crystal monochromator at room temperature. The size of the beam-spot on the X-ray window was recorded as ~140 x 140 microns. The intensity of incident and transmitted X-ray beam was measured by the ionization chambers. For Mn, Co, and Ni K-edge analysis, the photon energy was tuned to 7.1 keV, 8.225 keV, and 9.3 keV, respectively. The *in operando* cell, labelled as G-type (active material: 6.34 mg), was charged at a rate of 0.5C (0.634 mA) with the voltage range of 4.8-2.0 V vs. Li^0/Li^+. The coin cell with X-ray window was directly clamped to the galvanostatic charger using electric wires to collect the XANES/EXAFS data on subsequent electrochemical cycles.

9.2.4 Data interpretation for XAS and CCWT

Data interpretation for XAS was carried out with a IFEFFIT computation code incorporated in the ATHENA[159] software package. The collected XAS spectra were normalized and converted from energy into frequency in *k*-space with the multiplication of k^3 in order to emphasize the oscillations in the high k-value ($k^3\chi(k)$). The EXAFS oscillations (k-space) were Fourier transformed into the R-space, so as to evaluate the inter-atomic bond length between neighbouring atoms. EXAFS modelling was conducted to compute fitting parameters: the distance between the neighbouring shells (R), EXAFS Debye–Waller factor ($\exp(-2\sigma^2k^2)$), amplitude reduction factor (S_0^2), and the EXAFS R-factor with the ARTEMIS application. FEFF 6 algorithm was utilized for the

EXAFS fitting with atomic coordination number (CN) of 6 for Mn and Co transition metals. On the other side, multiple atomic coordination numbers (e.g. CN= 5.9/0.1, 5/1, 0.1/5.9, …, and 6) were used for the Ni K-edge EXAFS fitting in order to match the Ni-O bond splitting into long and short Ni-O bonds on charge-discharge. The amplitude reduction factor (S_0^2) was scaled to 0.65, 0.67, and 0.88 for Mn, Co, and Ni, respectively, after a preliminary refinement with reference compounds. The EXAFS least square fits were carried out in accordance with the integrated two-phase composite system. The fitting range of the R-space was 1-3.65 Å for Mn, Co, and Ni. The Continuous Cauchy wavelet transform (CCWT)[147] method was chosen to precisely characterize the local atomic change during electrochemical cycles in the cathode composite. The wavelet transform analysis was conducted on the k^3-weighted normalized EXAFS data using a matlab code. The applied oscillation range for the wavelet transform were 0-11.9 $Å^{-1}$, 0-11.7 $Å^{-1}$, and 0-15.8 $Å^{-1}$ for Mn, Co, and Ni, respectively, in *k*-space. Cauchy wavelet order (n) of 500, 150, and 250 was used for Mn, Co, and Ni, respectively. The range of the R-space was limited between 0.2 Å and 6.0 Å during the CCWT analysis with the interval number of 400 that corresponds to the pixel numbers in the R-space.

9.3 Result and Discussion

9.3.1 Electrochemical characterization of the graphene-coated cathode

Figure 9.1 reveals the electrochemical properties of the graphene incorporated (coated) $Li(Li_{0.2}Mn_{0.54}Ni_{0.13}Co_{0.13})O_2$ cathode up to 22nd cycles. The normal type coin cell was electrochemically cycled in the voltage range of 2.0 – 4.8 V vs. Li^0/Li^+ at the charge rate of 0.2 C (room temperature). The galvanostatic profile on different electrochemical cycles of the cell was compared in Figure 9.1a. The lithium-rich layered Mn-based oxide cathode displays both the

voltage decay and capacity fading upon further cycles. The large voltage-plateau was observed at ~4.5 V only during the initial charge.

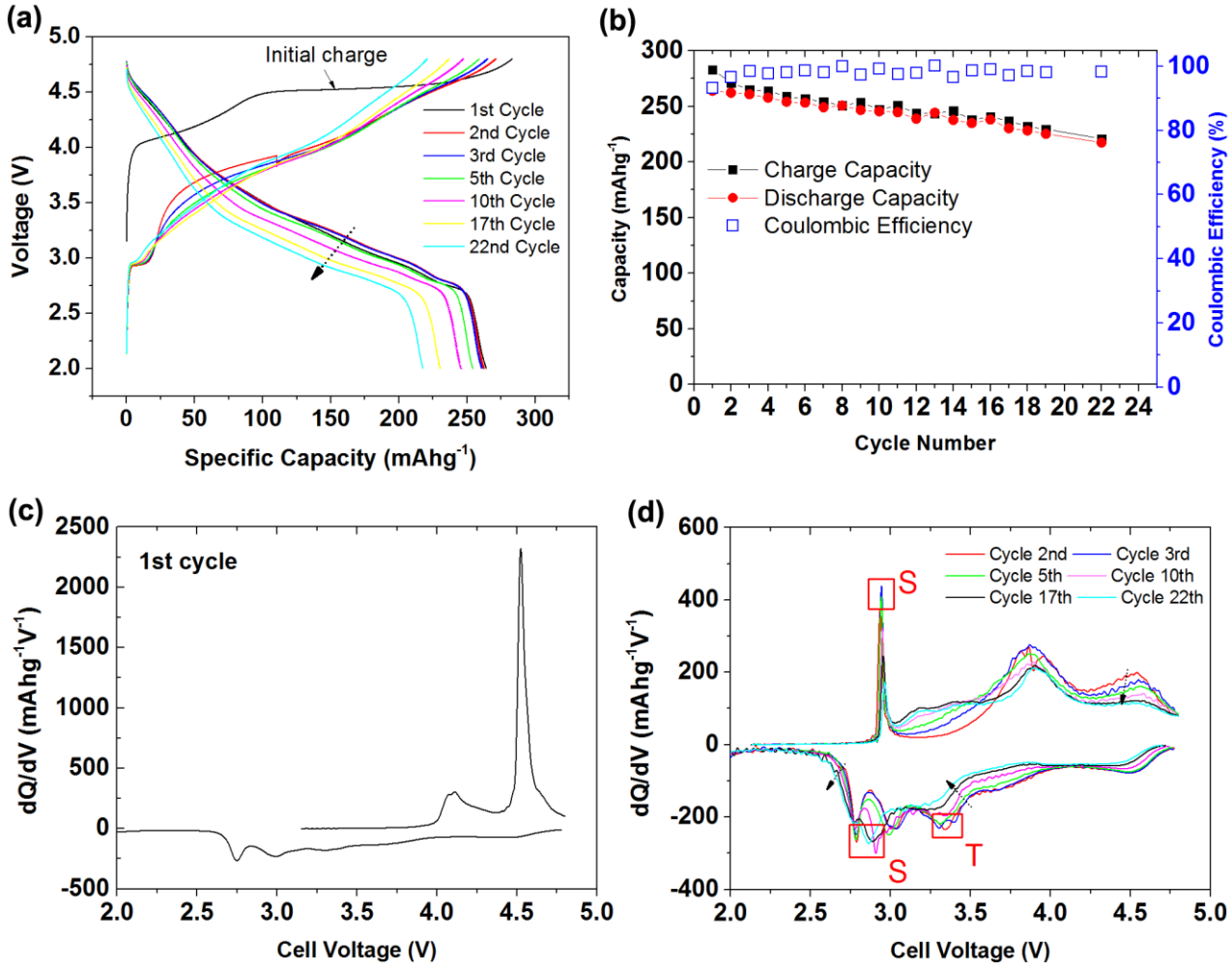


Figure 9.1 Electrochemical properties of the graphene incorporated $Li(Li_{0.2}Mn_{0.54}Ni_{0.13}Co_{0.13})O_2$ lithium-ion battery. (a) Galvanostatic profile until 22nd cycle (cycled with 0.2 C-rate). (b) Charge and discharge capacity with columbic efficiency. The dQ/dV plots during (c) initial cycle and (d) further cycles.

Also, the differential capacity analysis (dQ/dV) was carried out on the galvanostatic profile (Figure 9.1d), as it was considered as the appropriate method to monitor the phase transition in terms of electrochemical process. There appeared a large and sharp peak approximately at 4.5 V in the dQ/dV plot during the 1st cycle, as presented in Figure 9.1c. This peak is attributed to the irreversible lithia (Li_2O) extraction from the Li_2MnO_3 component[8,82,83]. The deintercalation process leads to the formation of a layered MnO_2 component ($Li_2MnO_3 \rightarrow Li_2O + MnO_2$) in the

lattice structure. The other peak at ~ 4.1 V is likely to be associated with the oxidation process of Ni^{2+}/Ni^{4+} and Co^{3+}/Co^{4+} in the layered $LiMO_2$ (M=Mn, Co, and Ni) during charge[2,79–81]. Figure 9.1d reveals the dQ/dV plot from cycle 2 to cycle 22. Apart from the oxidation peaks, some special peaks denoted as 'S' and 'T' were observed during the electrochemical cycles. The peak T at ~3.3 V is attributed to redox reaction from Mn^{4+} into $Mn^{(4-x)+}$, where $0 < x < 1$, in the layered $Li_{1-x}MnO_2$ composite[84,160]. This is likely to be linked to the phase transition into the spinel phase upon subsequent cycles[84,121]. A direct indicative of the phase transition from layered structure into the spinel (or cubic spinel-like) phase can be identified by the peaks denoted as S in the dQ/dV plot[84,160].

9.3.2 Active material characterization.

The graphene incorporated active material was characterized by XRD, RAMAN spectroscopy, SQUID, and SEM in order to complement the structural information obtained from XAS (Figure 9.2). The combined results support the evidence of the two-composite integrated system on the graphene-coated $Li(Li_{0.2}Mn_{0.54}Ni_{0.13}Co_{0.13})O_2$ cathode. XRD data displays the presence of the two phase of Li_2MnO_3 (monoclinic, C2/m) and $LiMO_2$ (trigonal, $R\bar{3}m$) as presented in Figure 9.2a. Mainly, the crystallography peaks could be indexed by the trigonal structure that describes the layered $LiMO_2$ component. On the other hand, the weak peaks at ~ 2θ = 15-18° could be indexed to the monoclinic (C2/m) crystal lattice. These peaks are attributed to the cation ordering of Li^+-ions in the transition metal layers of Li_2MnO_3 component[74,79]. The spectra obtained from the Raman scattering on active materials can be compared in Figure 9.2b. Two distinct Raman active modes were observed between 500 and 650 cm^{-1}. These activities are assigned to O-M-O bending (E_g) and M-O stretching (A_{1g}), and they explain the local atomic environment of octahedra MnO_6 in the layered $LiMO_2$ component[114,146,163,164].

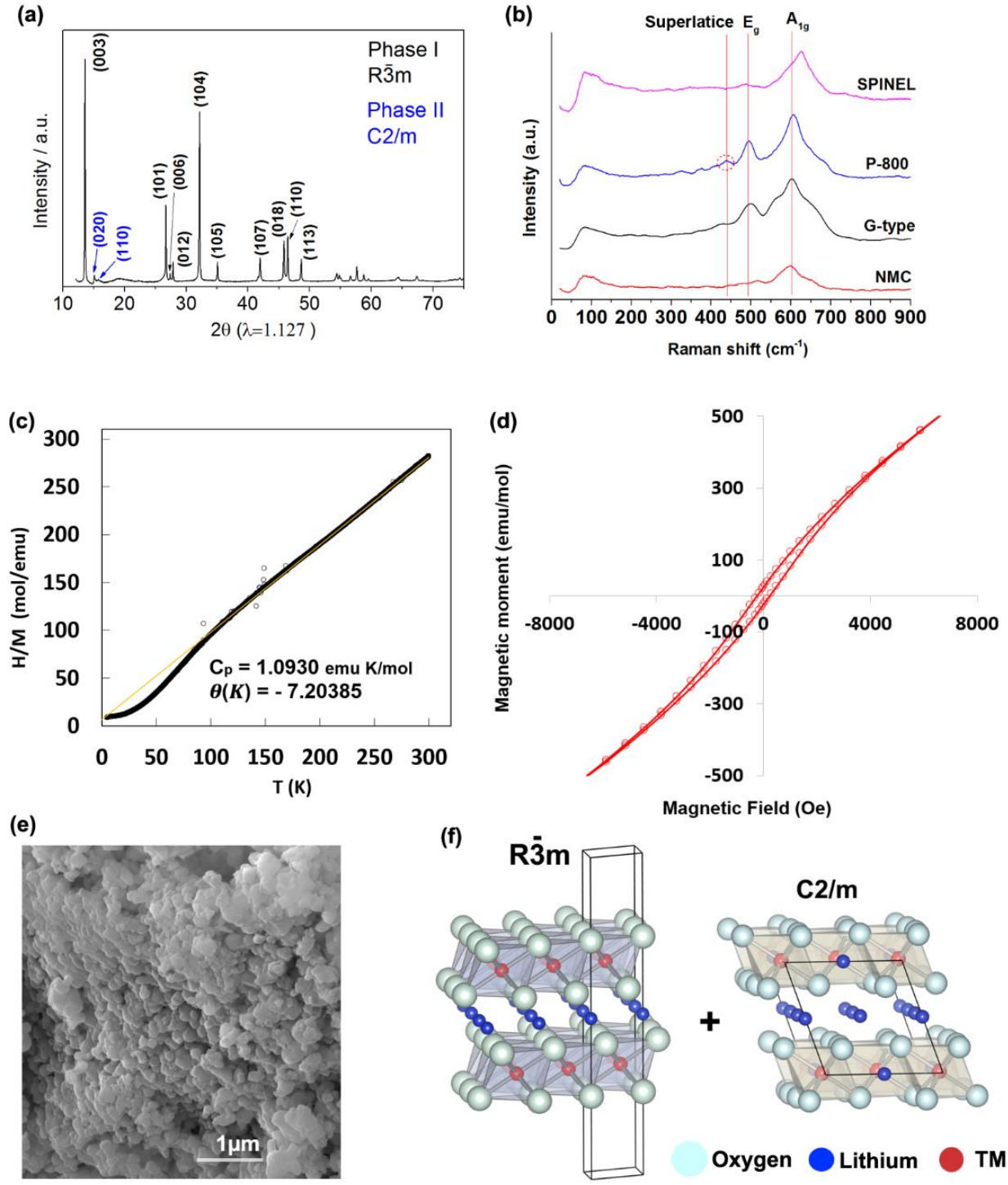


Figure 9.2 Characterization of graphene incorporated $Li(Li_{0.2}Mn_{0.54}Ni_{0.13}Co_{0.13})O_2$ electrode. (a) XRD pattern with two-phase indexing. (b) Raman spectroscopy (Superlattice: superlattice ordering, NMC: $Li(Ni_{1/3}Mn_{1/3}Co_{1/3})O_2$ compound, and P-800: pristine material without graphene) (c) Plot of reciprocal magnetic susceptibility. Fitting according to Curie-Weiss law (yellow line). (d) Magnetization curve obtained at 5 K with 60k Oe applied. (e) SEM images on electrode particles. (f) Presentation of two-phase composite system.

Those Raman activities were found both in the pristine electrode without the graphene coating (denoted as P-800) and with graphene coating (denoted as G-type) samples. A small peak denoted as 'Superlattice' in Figure 9.2b was only identified in the pristine material. This peak is an indicative of the cation ordering (superlattice reflections) in the transition metal layer of the Li_2MnO_3 component. Raman spectroscopy offers the information about the surface chemistry, whereas the XRD mainly provides the long-range structural information on the bulk of the material. Therefore, the analyses from XRD and Raman spectroscopy suggest that the layered component ($LiMO_2$ / M: transition metals) is able to appear both the surface and the bulk, while the Li_2MnO_3 (monoclinic, C2/m) can form only in the bulk of the G-type sample. This may be concerned with the impact from the graphene coating formed on the surface of the electrode particles.

Both the Raman profile of P-800 and G-type samples are closer to that of the $Li(Ni_{1/3}Mn_{1/3}Co_{1/3})O_2$ (NMC) cathode than the spinel compound (SPINEL). This suggests the formation of layered structure on the surface of the electrode particles. The reciprocal molar magnetic susceptibility (H/M) for the graphene incorporated cathode is shown in Figure 9.2c. The composite appears to obey the Curie-Weiss law at above ~150 K and thus the effective magnetic moment (μ) and Curie-Weiss temperature (θ) could be evaluated from the fit to the Curie-Weiss law, $X_m = C/(T - \theta)$ where C_p is the Curie constant (C_p=N$\frac{\mu}{3k_b}$, N: Avogadro number and k_b: Boltzmann constant) and θ is the Weiss constant. Complementary to XANES investigation, SQUID measurement was conducted to examine the precise oxidation states, electronic structure, and magnetic properties that might provide some insight into the location of a particular transition metal in the host structure. The theoretical effective magnetic moment (μ_{theory}) and the experimental effective magnetic moment (μ_{exp}) were evaluated to be 2.95767 (BM) and 2.94824 (BM), respectively. In principal, the graphene incorporated composite should be consisted of Mn^{4+} (spin S=3/2, $\mu_S = 3.87\ \mu_B$), low-spin (LS) Co^{3+} (spin S=0, $\mu_S = 0\ \mu_B$), and Ni^{2+} (spin S=1, $\mu_S =$

2.83 μ_B) transition metal. However, in this case, a discrepancy arises between the theoretical and experimental values as the μ_{theory} was calculated to be 3.02828 (BM). As such, it should be taken into account that the Mn would present as a mixed state between Mn^{4+} and low-spin (LS) Mn^{3+} in the active material. This consideration leads to the correct evaluation of the Mn oxidation state as +3.89. The magnetization (M) vs applied magnetic field (H) at 5 K is plotted in Figure 9.2d. A slight hysteresis loop was recorded and the observed remanent magnetization was measured to be Mr ~ 23.3 emu · mol^{-1}. There was no magnetization saturation as can be seen from the magnetization curve. From the absence of the saturation and the negative value of Curie-Weiss temperature ($\theta = -7.20385\ K$), it can be thus concluded that the type of the magnetic interaction of the G-type cathode is antiferromagnetic exchange.

9.3.3 In operando XANES on Mn, Co and Ni K-edge.

Figure 9.3 compares the in operando XANES measurements of Mn, Co, and Ni K-edge during 1st and 2nd electrochemical cycles. As shown in Figure 9.3a, there were two plateau-like regions in the galvanostatic profile during the initial charge. It could be observed that the plateau-like region above ~4.5 V disappeared after the initial electrochemical cycle. This is a general phenomenon in the lithium-rich layered transition metal oxide electrode. The formation of the plateau in the initial charge is attributed to the Li^+ deintercalation from the Li_2MnO_3 component[2,7,8,78]. High quality of XANES spectra could be collected at the K-edge in transmission mode owing to a specially designed *in operando* cell. Four significant features (A1- A4) are shown in the absorption at the Mn K-edge with numbers (Figure 9.3b). Absorption **A1** indicates the double pre-edge peaks found between 6538 and 6543 eV at the Mn K-edge, and the trend of their spectra changes upon charge-discharge is presented in Figure 9.3c. The amplitude of the pre-edge peak increases upon charge and decreases upon discharge.

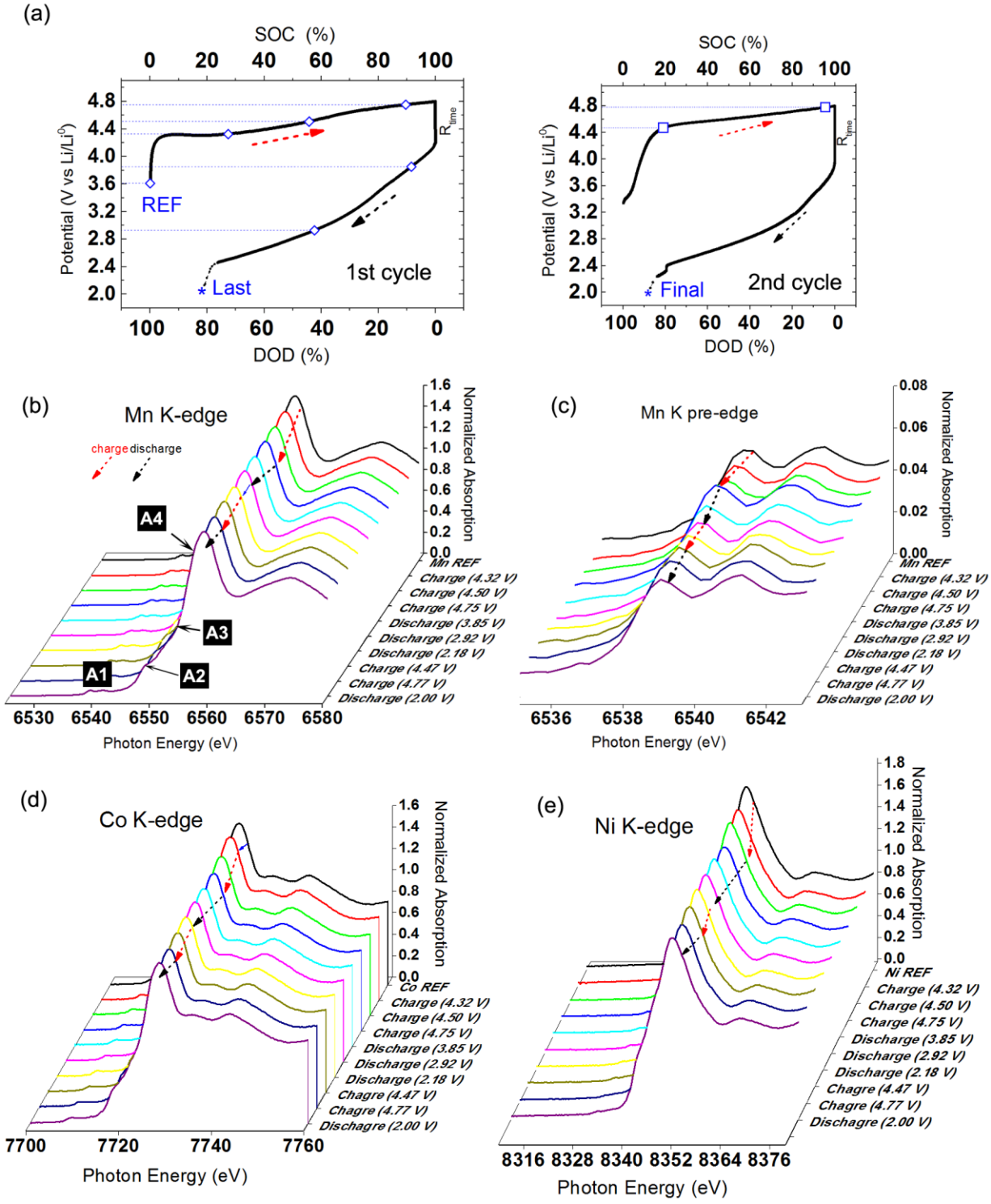


Figure 9.3 In Operando XANES measurements. (a) Galvanostatic profiles (0.5 C-rate) on 1st and 2nd electrochemical cycles. Normalised XANES spectra at (b) Mn K-edge, (c) Mn K pre-edge, (d) Co K-edge, and (e) Ni K-edge of graphene-coated $Li(Li_{0.2}Mn_{0.54}Ni_{0.13}Co_{0.13})O_2$ battery during initial and second cycles. Red arrow indicates the direction of charge, whereas black arrow represents the discharge trend.

These peaks can be assigned to 1s-3d_{t2g} (lower energy) and 1*s*-3d_{eg} (higher energy) transitions. In a centrosymmetric system, the double pre-edge peaks are formally dipole-electric forbidden, but they can appear from a weak quadrupole transition or/and 3*d*-4*p* orbital hybridization with the loss of centrosymmetric environment, which in turn leads to the distortion of the octahedral 3a site in the lithium-layered component ($R\bar{3}m$ space group). Therefore, the pre-edge peak intensity can be used as an indicator to estimate the geometrical distortion. Higher intensity signifies larger structural distortion in the octahedra MnO_6 from the centrosymmetric environment. The absorption feature **A2** is related to the dipole transition from 1s to 4p with a shakedown process stemming from the ligand-to-metal charge transfer (LMCT), which in turn results in a in final state of a $1s^1c3d^4L4p^1$ (Mn^{4+}), where c and L denote a core hole (1*s*) and a ligand hole (2*p*), respectively. On the other side, absorption feature **A4** represents the dipole transition from 1s to 4p without the shakedown process and thus the final state corresponds to $1s^1c3d^34p^1$ (Mn^{4+}). The main absorption edge of the Mn K-edge can be located approximately at absorption **A3**. Although there was a reverse shift between 2.92 and 2.18 V, overall, the XANES spectra shift tends to be reversible during the consecutive charge-discharge at the Mn K-edge and pre-edge. It should be noted here that the energy shifts appeared in the initial cycle is larger than that of the 2nd cycle, indicating dynamic atomic environment changes during the initial cycle. This would be explained by the Li_2O removal followed by the transition metals migration from the transition metal layers into the lithium layers[76]. An irreversible cation rearrangement is expected during this process at the voltage plateau over ~4.5 V. Figure 9.3d exhibits the normalized XANES spectra of the Co K-edge up to two cycles. The trend of the spectra shift in the 1st cycle was similar to that of second cycle, as they shifted towards higher energy during the charge and lower energy while discharge. Also, a small reverse shift was observed from the first charge point. The spectral shifts of Co K-edge was 0.61 eV, which is higher than that of the Mn K-edge (0.4 eV). It is therefore likely that Co

contributes more than Mn in terms of the charge compensation mechanism. In general, the shape of the Co K-edge XANES spectra is similar to that of the Mn throughout the electrochemical cycles. This suggests a similar atomic environment between those two elements in the cathode composite. The normalized XANES spectra at the Ni K edge are shown in Figure 9.3e. The spectra shift of the Ni K-edge XANES can be described as a parallel style energy shift. This somewhat different shift pattern implies a different local environment compared with that of Mn and Co. Moreover, Ni revealed the largest XANES energy shifts at the K-edge as ~1.07 eV among the transition metals. This discrepancy is attributed to the two-stage oxidation change of Ni ($Ni^{2+} \rightarrow Ni^{3+} \rightarrow Ni^{4+}$) which in turn results in a larger shift compared with the single step oxidation change of Co[83,90]. Similarly as Mn and Co K-edge, the energy shifts appeared in the initial cycle was larger than that of the 2nd cycle.

9.3.4 In operando EXAFS on Mn, Co and Ni K-edge

Fourier transformed Mn, Co, and Ni K-edge data in R-space (real space) and EXAFS oscillations in k-space (k^3-weighted $\chi(k)$) are compared in Figure 9.4. What is interesting in this result is the systematic change of the spectra pattern upon the cycle stages. In Mn K-edge EXAFS, the local atomic environment between REF and 4.75 V is similar although there is a slight drop of the Mn-O and Mn-TM peaks intensity upon charge. This can be confirmed by their EXAFS spectra pattern, especially in R-space (Figure 9.4a). Also, three peaks could be observed between 4-6 Å during the initial charge from REF to 4.75 V with a consistent oscillation pattern. However, after the initial charge, it is likely to appear a distinctive structural modification in the local atomic environment of Mn as there has been a significant intensity drop in Mn-O/Mn-TM peaks. This tendency could be also found at high coordination shells located between 4-6 Å in R-space as evidenced by the damping and disappearance of the peak intensity from 3.85 V (red curve in Figure 9.4a), which corresponds to the commencement point of the 1st discharge.

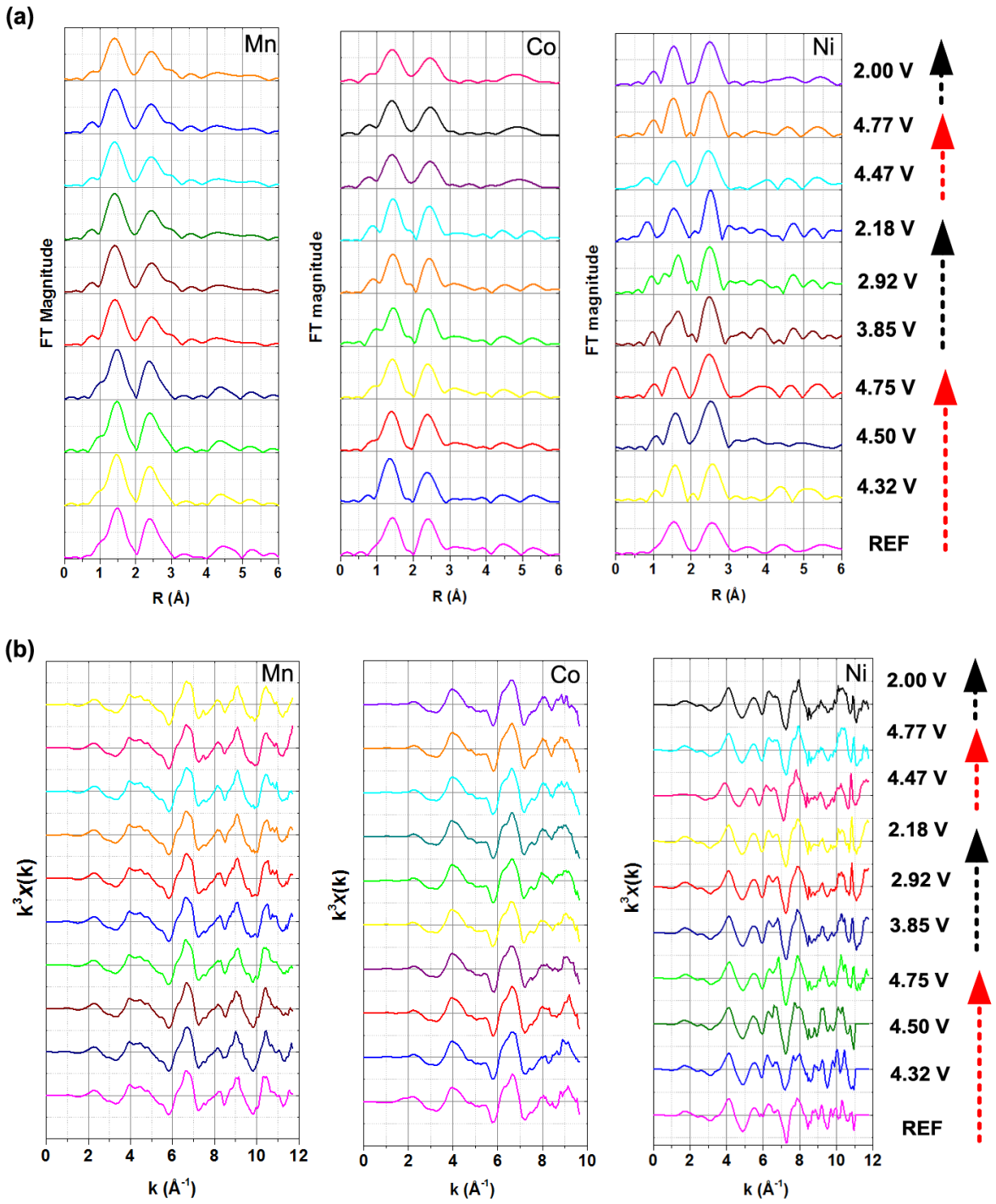


Figure 9.4 Fourier transform magnitudes (k^3-weighted) at (a) Mn, Co, and Ni K-edge of the graphene-coated $Li(Li_{0.2}Mn_{0.54}Ni_{0.13}Co_{0.13})O_2$ during two electrochemical cycles. (b) The corresponded k^3-weighted EXAFS oscillations $\chi(k)$ above Mn, Co, and Ni K-edge. REF is the reference point without any current applied. Red arrow indicates charge process, while black arrow represents discharge process.

A closer inspection reveals that the atomic environment during the 2nd cycle differs from the initial charge, but it was similar to that of the initial discharge. The reduced amplitude of the Mn-O is

possibly attributed to the oxygen loss with a cation ordering during the Li^+ deintercalation. The cation ordering of $LiMn_6$ in the transition metal layers may affect the peak amplitude of Mn-O, as well as Mn-TM at ~2.38 Å (uncorrected phase shift) by lowering the coordination number around Mn. These finding suggests an irreversible atomic-environment change associated with the cation ordering during the initial charge.

The variation pattern of the EXAFS spectra at the Co K-edge is comparable to that of the Mn. Similarly as for Mn, there was a consistency in the oscillations pattern throughout the 2nd cycle in the Co K-edge. However, we could also identify a different tendency of the spectra changes between Co and Mn K-edge EXAFS. Whereas there were two notable type of oscillation patterns in the Mn K-edge EXAFS during initial charge, it was relatively intricate to classify the oscillation patterns of the Co K-edge EXAFS into a particular group in accordance with the spectra similarity. This discrepancy between Mn and Co may originate from the different process involved in the charge compensation mechanism at the voltage plateau (~4.5 V). It is believed that the Li_2MnO_3 can be electrochemically activated at > ~4.5 V by the reaction at oxygen sites with the lithia (Li_2O) extraction, whereas Co contributes to the battery capacity by its redox reaction over wide voltage range. After the initial cycle, those two peaks located between 4-6 Å in Co K-edge EXAFS became a single peak from 4.47 V (Figure 9.4a). It seems to be that the local atomic environment of Co was also changed, irreversibly, as the EXAFS oscillations pattern was different between the 1st cycle and 2nd cycle. The collected EXAFS spectra of Fourier transformed Ni K-edge in R-space (real space) and the oscillations in k-space (k^3-weighted $\chi(k)$) during two cycles is also presented. During charge-discharge, it is obvious that the local environment of Ni undergoes severe modifications compared with Mn and Co. However, it was very difficult to group the EXAFS spectra (R-space) together systematically, because of their concomitant modifications in the peak shape, shell location, and amplitude upon voltage levels. This complexity is attributed to

the combined impacts from the inherent property of the Ni in the cathode composite such as: (1) two-stage redox reaction ($Ni^{2+}/Ni^{3+} \leftrightarrow Ni^{3+}/Ni^{4+}$); (2) Jahn-Teller effect from the low-spin Ni^{3+} (d^7); and (3) Li/Ni cation mixing[58,68,175]. The trend of the spectra patterns may be tentatively divided into two groups according to the k-space pattern as shown in Figure 9.4b at the Ni K-edge. The oscillation pattern was similar from REF to 4.5 V, but it lost its similarity from 4.75 V as evidenced by the scattering patterns in the high *k*-value between 10-12 $Å^{-1}$. Another notable trend is the radial distance change of the 1st coordination shell of Ni-O. It tends to decrease upon the initial charge. For instance, the radial distance of Ni-O was ~1.58 Å (phase shift uncorrected) at 4.32 V. It decreased to ~1.53 Å (phase shift uncorrected) when it reached 4.75 V. This variation is due to the redox reaction of the Ni which contributes to the charge compensation mechanism of the battery system. The impact from the Jahn-Teller distortion generally results in a reduced peak intensity of Ni-O. However, it should be also considered that the cation arrangement around the Ni-O could affect the peak amplitude. Overall, the local atomic environment change of Ni was found to be relatively dynamic in the 1st cycle than the 2nd cycle.

9.3.5 In operando CCWT at Mn, Co and Ni K-edge

The in operando EXAFS measurements of Mn K-edge with the Continuous Cauchy Wavelet Transform (CCWT) during initial and 2nd cycle in the graphene-coated $Li(Li_{0.2}Mn_{0.54}Ni_{0.13}Co_{0.13})O_2$ cathode is displayed in Figure 9.5. The specially designed *in operando* cell allows us to collect high quality XAS signals for the wavelet transform analysis to further understand the atomic environment of the transition metals in the two-composite cathode system. By decomposing the *k*-space and R-space (uncorrected for phase shift) signals, the wavelet transform analysis enables the visualization of the EXAFS spectra in three dimensions [147,177,178]. At the reference point (REF), the locations of the maximum intensity for Mn-O and Mn-TM were k ~7.11 $Å^{-1}$ (R ~1.5 Å) and ~8.4 $Å^{-1}$ (R ~2.41 Å), respectively.

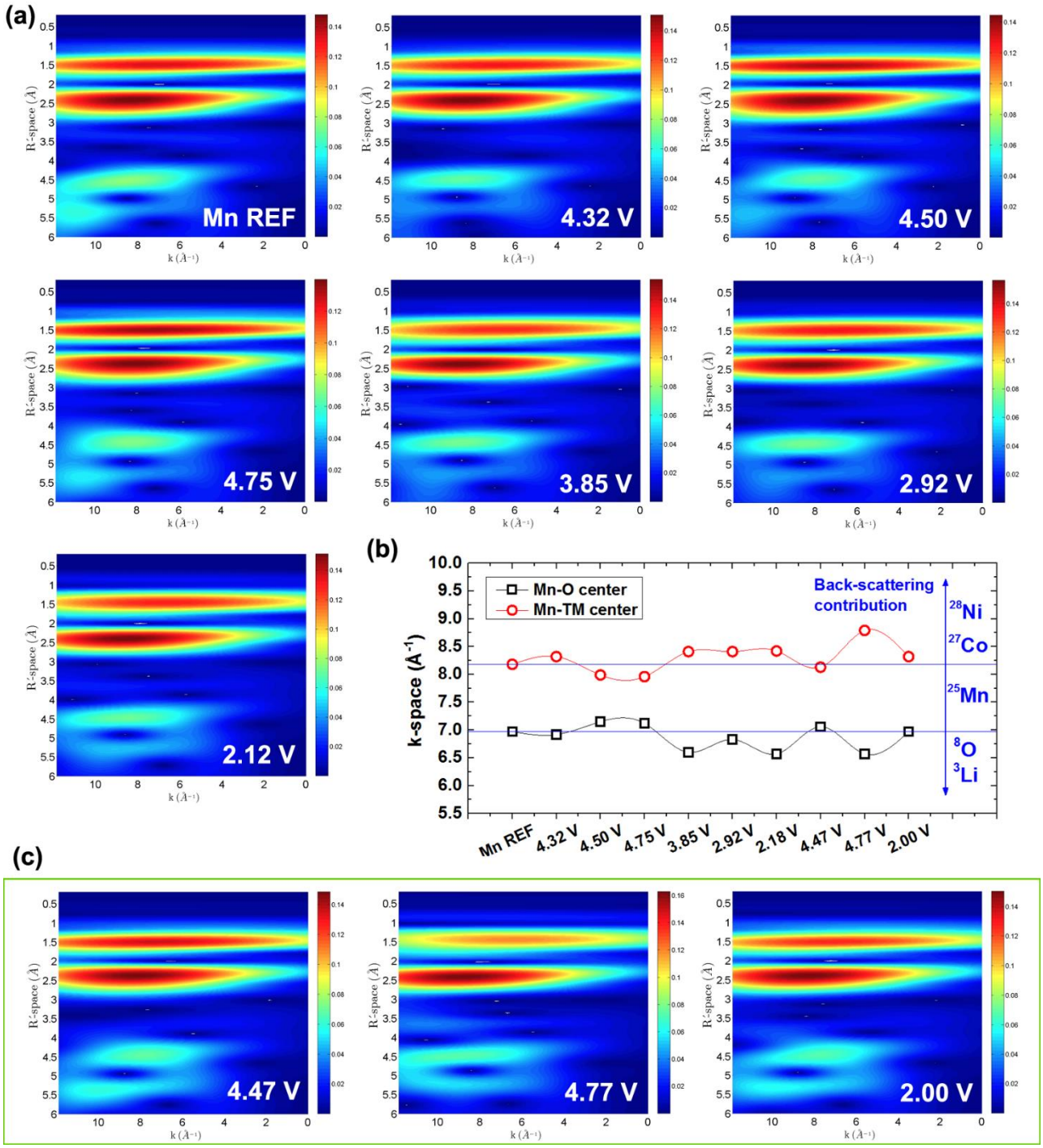


Figure 9.5 Continuous Cauchy Wavelet Transform (CCWT) analyses on Mn K-edge EXAFS spectra at different voltage levels in graphene-coated $Li(Li_{0.2}Mn_{0.54}Ni_{0.13}Co_{0.13})O_2$. Cathode. (a) 1st cycle CCWT (b) Back-scattering contribution (maxima variations in the 1st and 2nd shells) (c) 2nd cycle CCWT. The 1st coordination shell (Mn-O) is presented from top.

The blurry appearance of the CCWT modulus at R ~4.5 Å and ~5.3 Å indicates the multiple scattering effects from the combined transition metals (Mn, Co, and Ni). We could see the wavelet

signal variations in the highest coordination shell (~5.3 Å) upon charge and discharge during initial cycle. By contrast, the variation of the wavelet modulus at this shell was minimum during the 2nd cycle as exhibited in Figure 9.5. Regardless of the cycle stage and voltage level, the coordination shell at ~4.5 Å maintains its intensity during the electrochemical cycles. It became rather dense and symmetric relative to the REF state upon charge. The variations in the multiple scattering at the high coordination shell may be due to the rearrangement of the transition metals, while the static wavelet signals at high coordination shell possibly corresponds to the $LiMn_6$ cation ordering during the Li^+ (de)intercalation. The CCWT signal change was distinctive between 4.5 V and 4.75 V in the 1st cycle. However, their signal changes were less notable during the 2nd cycle. Figure 9.5b reveals the Mn-O/Mn-TM maxima shift of the CCWT modulus during 2 cycles in *k*-space. It should be noted that atoms with higher atomic numbers (heavy element) efficiently backscattered in the high *k*-values whereas the light atoms efficiently backscattered in the low k-values, relatively. The quantification on the CCWT maxima shift is quite revealing as it provides some insights into the back scattering contributions of the transition metals around the absorbing atom. As shown in Figure 9.5b, the backscattering effect from Mn dominates at 4.50 V and 4.75 V, indicating its activation at those voltage levels. This could be explained by the electrochemical activation of Li_2MnO_3 component at high voltage in the lithium-rich layered oxide system. Since this notable oscillation pattern relevant to the Mn activation has not been found elsewhere through the electrochemical cycles, it probably indicates the irreversible local environment change after the initial charge. Also, the irreversible phase change could be visually identified between the initial charge and discharge by the intensity of the CCWT maxima (dark-red). By contrast, during 2nd charge and discharge, it was possible to observe a reversible pattern shift. It can thus be suggested that an irreversible phase transition occurs during the initial charge in the graphene-coated $Li(Li_{0.2}Mn_{0.54}Ni_{0.13}Co_{0.13})O_2$ cathode.

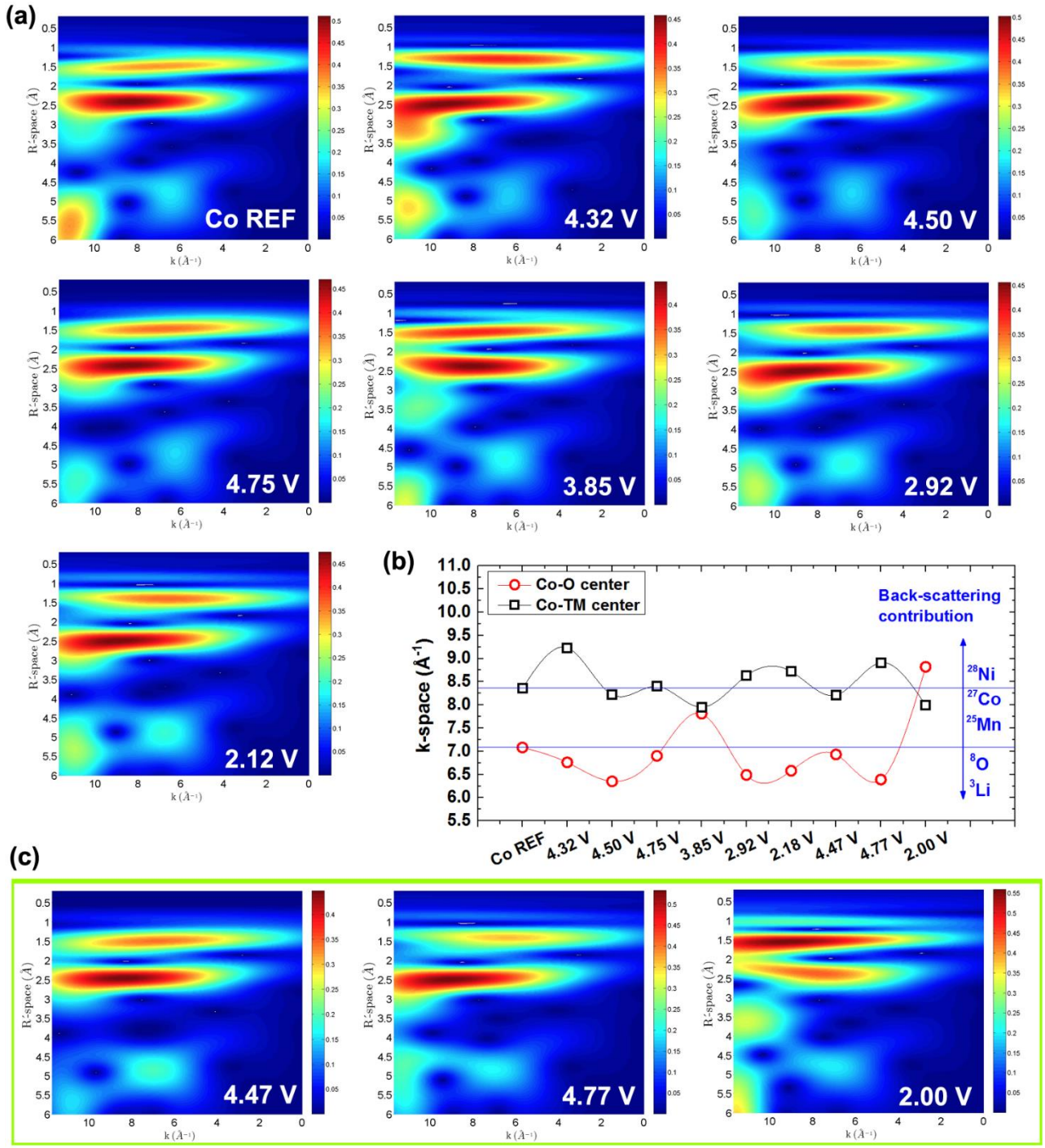


Figure 9.6 Continuous Cauchy Wavelet Transform (CCWT) analyses on Co K-edge EXAFS spectra at different voltage levels in graphene-coated $Li(Li_{0.2}Mn_{0.54}Ni_{0.13}Co_{0.13})O_2$ cathode. (a) 1st cycle CCWT (b) Back-scattering contribution (maxima variations in the 1st and 2nd shells) (c) 2nd cycle CCWT. The 1st coordination shell (Co-O) is presented from top.

Another interesting observation is the appearance of the interconnecting wavelet transform signals between R ~4.5 Å and R ~5.5 Å during further cycles. Especially, they could be well identified

during the second charge and discharge as presented in Figure 9.5c. Note that this pattern of the signal differs from that of Mn REF. The wavelet transform signals found between R ~4.5 Å and R ~5.5 Å possibly implies the tendency of having more activated Li_2MnO_3 phase in the integrated composite[176].

Figure 9.6 reveals the CCWT analysis on the *in operando* EXAFS measurement of the Co K-edge during two electrochemical cycles. The atomic environment of Co-O at k ~6.94 $Å^{-1}$ (R ~1.49 Å) and Co-TM at k ~8.40 $Å^{-1}$ (R ~2.39 Å) shows structural variations during entire cycles. It was difficult to identify this trend in the Fourier transformed R-space. Thus, the inter-atomic bond length change of the Co-O/Co-TM resulting from the charge compensation mechanism seems to be **not** the major factor that contributes to the structural variations in the Co environment during Li^+ (de)intercalation. In addition, the Co-TM is likely to maintain its local symmetry since the maximum intensity of the wavelet transform signals don't change, displaying dark-red at k ~8.40 $Å^{-1}$ and R ~2.39 Å except at the last discharge point in the 2nd cycle. This is consistent with the trend of the EXAFS pattern in R-space of the Co K-edge since there was less modification in Co-TM during charge-discharge. Therefore, the notable variations in the Co atomic phases is may be related to its counter reaction against Mn cation ordering and/or Jahn-Teller distortion of Ni^{3+}. It is believed that the distortion by the Ni oxidation change can be reduced due to the presence of the Co^{3+} ion in the cathode composite[98,129]. On the other side, the centered intensity change on the Co-O CCWT modulus during the electrochemical cycles would be explained by the compensation mechanism from the Co with the oxygen removal. The visualized wavelet signals implies that the redox reaction of Co involves the charge compensation over larger voltage range, whereas Mn only contributes at > ~4.5 V. As can be seen in Figure 9.6b, at the voltage level of 4.5 V or 4.77 V in the 2nd cycle, the back-scattering contribution to Co is mainly attributed to light scatterer such as Li^+ and O^{2-} indicating the charge compensation from the oxidation and/or Li_2O extraction.

The 3rd coordination shell from the Co K-edge is located at R ~5.6 Å and k ~11.2 $Å^{-1}$. A contribution from the single scattering could be observed at REF and 4.326 V as evidenced by the maximum intensity in the center, although the signals looks rather blurred than that of the Co-O or Co-TM shells. However, a further charge and cycles lead to the diminishment of the single scattering from 4.5064 V and thus the tendency of having multiple scattering increases. It should be noted that the trend of the wavelet transform signals in the Co K-edge is comparable to that analyzed in Mn K-edge during the initial cycle. It is apparent that the local atomic environment of Co K-edge differs from that of the Mn K-edge, but a similarity could be observed since a notable change was identified at before and behind ~4.5 V on both local atomic environments. This would be observed from a distinctive change in the center of the maximum intensity from the 1st shell for Mn K-edge and 3rd shell for Co K-edge.

Figure 9.7a compares the CCWT analysis on the EXAFS measurements of the Ni K-edge at different cycle stages. As expected, it displays a dynamic and complicated change in the Ni atomic environment during electrochemical cycles. During the initial charge, the signal variations were not that complicated, and it revealed somewhat a good symmetry in the wavelet signals up to voltage level of 4.75 V. The notable CCWT intensity change in the centre of the Ni-O (R ~1.53 Å and k ~5.98 $Å^{-1}$) is due to the two-stage redox reaction of the Ni transition metal during the charge compensation mechanism. Eventually, the 1st shell signal splits in the shape from 2.9265 V to 2.0 V (second cycle). As can be seen from Figure 9.7b, during 1st cycle, the back-scattering impact was mainly originated from transition metals with low atomic numbers. This may be explained by the cation arrangement of $NiMn_6$ in the $LiMO_2$ component. Interestingly, during further charge and electrochemical cycle, the 2nd coordination shell losses its symmetrical shape and become slightly disrupted.

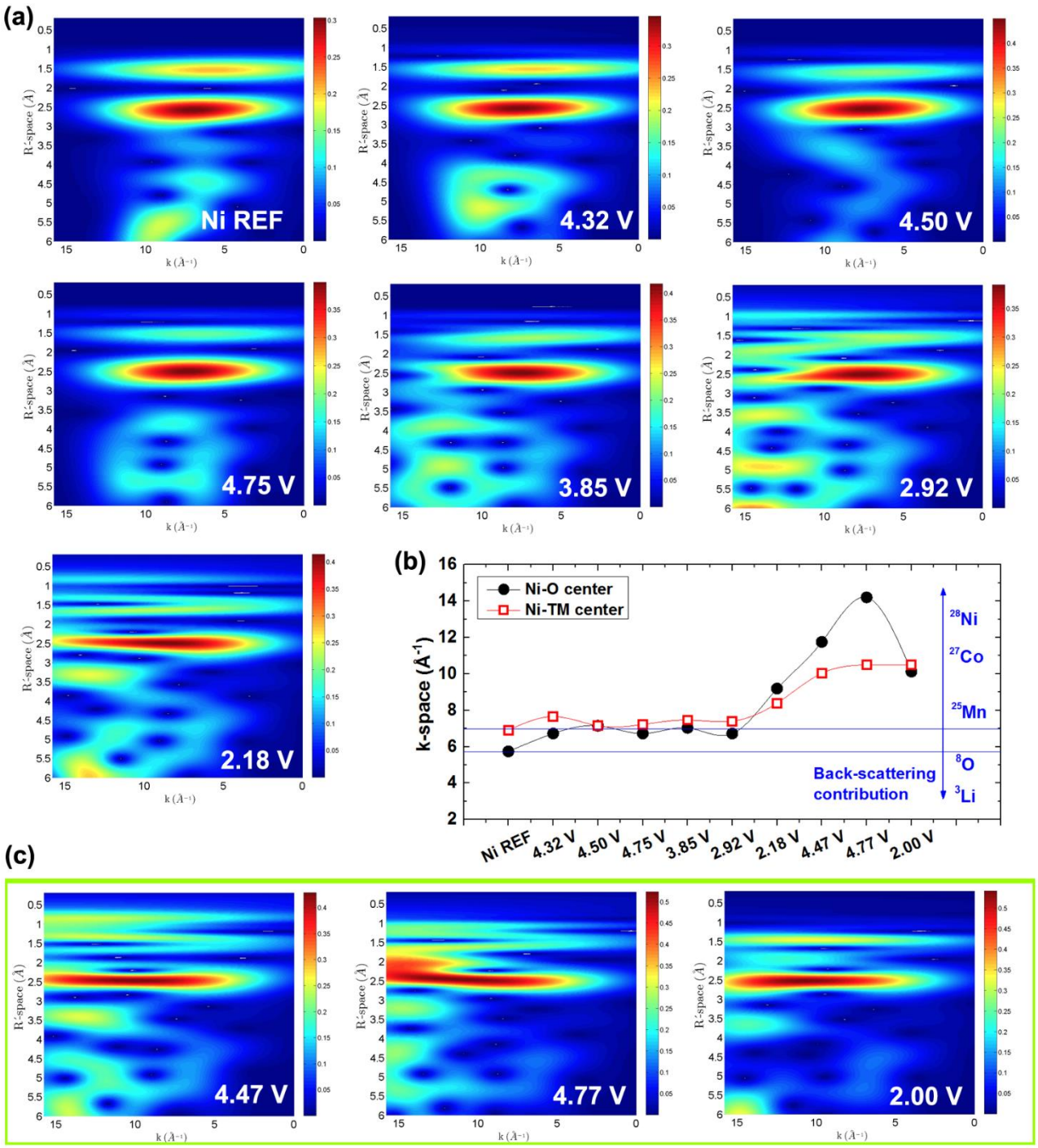


Figure 9.7 Continuous Cauchy Wavelet Transform (CCWT) analyses on Ni K-edge EXAFS spectra at different voltage levels in graphene-coated $Li(Li_{0.2}Mn_{0.54}Ni_{0.13}Co_{0.13})O_2$. cathode. (a) 1st cycle CCWT (b) Back-scattering contribution (maxima variations in the 1st and 2nd shells) (c) 2nd cycle CCWT. The 1st coordination shell (Ni-O) is presented from top.

With this wavelet transform pattern, the back-scattering effect from transition metals with higher atomic numbers increases during further charge-discharge, as presented in Figure 9.7b. In contrast

to Mn and Co, the peak amplitude at the 2nd coordination shell (Ni-TM) was always higher than that of the 1st shell as shown in R-space (Figure 9.7). This implies that there were a number of transition metals around the Ni-O local environment. Another important visual inspection is the CCWT at R ~3.5 Å which is believed to be linked to the Ni-O-Ni environment. Those signals were not possible to monitor during the initial charge, but they could be observed during the initial discharge and further cycle. They are located at high *k*-value between ~10 $Å^{-1}$ and ~15 $Å^{-1}$ indicating the presence of the heavy scatterer. It can thus be suggested that a fraction of the Ni ions migrate from the transition metal layers into the lithium layers on charge-discharge. It is apparent from the Ni K-edge CCWT analysis that the octahedral NiO_6 symmetry undergoes an irreversible atomic environment change, although the XANES reveals a reversible redox change of Ni. This structural modification appears to be the consequence of cation migration and/or bond-length separation of Ni-O resulting from the Jahn-Teller effect from Ni^{3+} during electrochemical cycles.

Figure 9.8 shows the evolution of the Mn-O and Co-O bond length changes with the mean-square disorder (σ^2) from the EXAFS Debye-Waller factor at different cell voltages during the 1st and 2nd cycle. The CCWT analyses presented are the wavelet transform signals that correspond to the high values of σ^2 for Mn and Co local environment. EXAFS fitting was performed to determine the EXAFS structural parameters such as radial distribution to neighbouring atom (*R*), energy shift (ΔE_0), EXAFS Debye-Waller factor ($e^{-2\sigma k^2}$), and amplitude reduction factor (S_0^2) of the reference material. It is known that the EXAFS Debye-Waller factor can represent either thermal disorder or structural disorder of the absorbing atoms (Mn, Co, and Ni)[126,128]. In this current study, the disorder parameter is an indicative of the structural disorder as there were no thermal variations in the experiment condition. In the preliminary EXAFS refinement, the amplitude reduction factors (S_0^2) were evaluated to be 0.65, 0.67, and 0.88 for Mn, Co, and Ni, respectively.

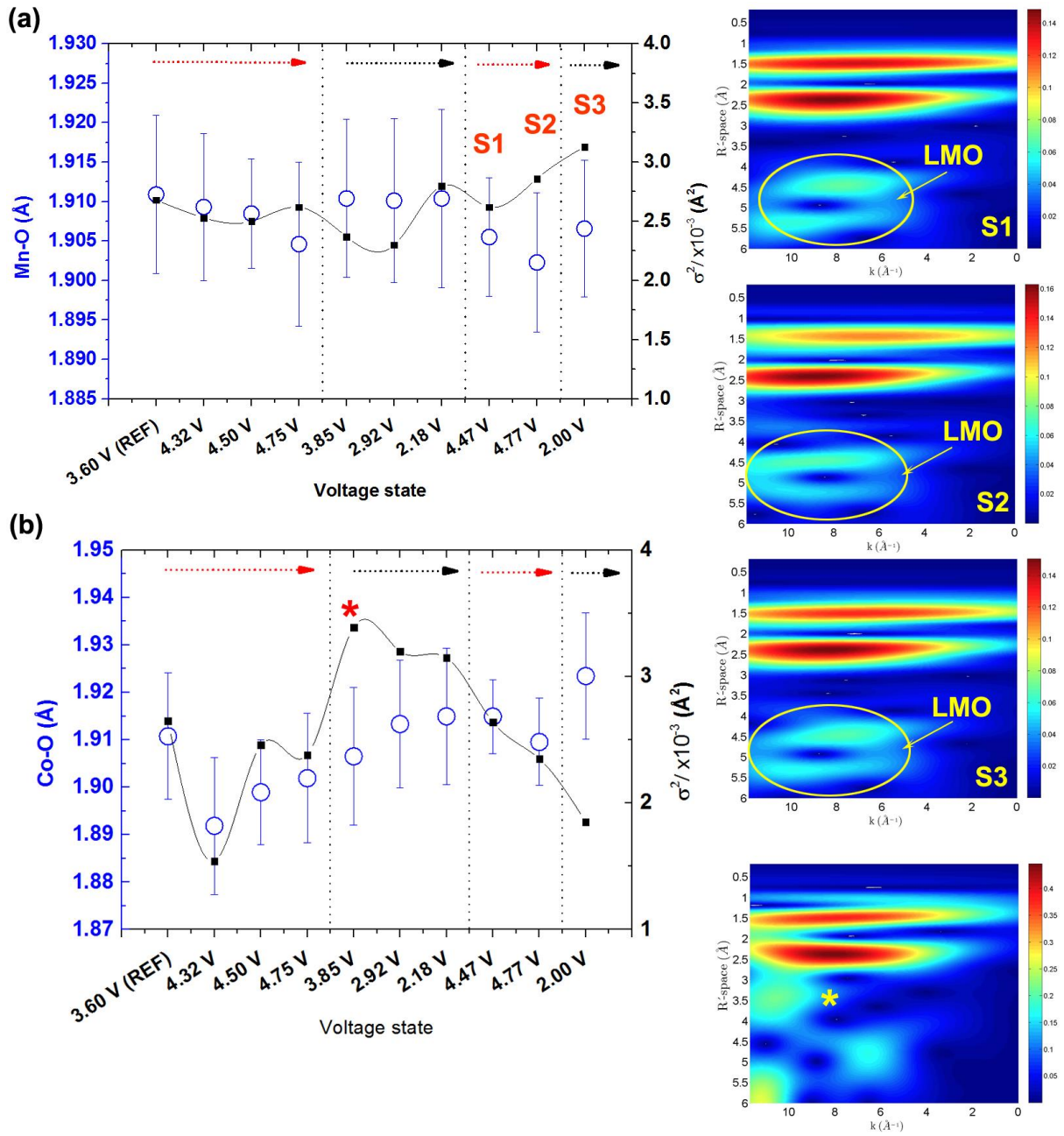


Figure 9.8 Evolution of the bond length and structural disorder (σ) changes during electrochemical cycles (2 cycle) for graphene-coated $Li(Li_{0.2}Mn_{0.54}Ni_{0.13}Co_{0.13})O_2$ battery. (a) Mn-O bond length change with structural disorder (b) Co-O bond length change with structural disorder. CCWT images correspond to the structural disorders with high value. Red arrow indicates charge process, while the black arrow represents the discharge process. 'LMO' signifies a part of the Li_2MnO_3 phase.

As shown in Figure 9.8a, the interatomic bond of Mn-O slightly decreases upon charge and increases upon discharge. A sudden drop of the bond length could be observed at 4.75 V, and this is followed by a sudden increase during the initial discharge. This is possibly explained by the

process involved in the activation of the Li_2MnO_3 component. The maximum difference in the bond length of Mn-O was found to be ~0.008 Å, whereas it was 0.031 Å in the Co-O. This distinctive difference in the Co-O bond length is due to the oxidation change of the Co^{3+}/Co^{4+} during charge compensation mechanism. Also, the trend of the structural disorder (σ^2) of Mn-O is comparable to that of the Co-O during 1st and 2nd cycles. It is of interest to point out that the σ^2 factor of Mn-O shows a similar tendency to that of the Co-O until the voltage level of 4.5 V, and then it reveals a notable reverse pattern during the rest of the charge-discharge as presented in Figure 9.8a,b. Again, this observation seems to be the impact from the counter reaction of the Co against to the cation ordering of Mn ions as mentioned in the Co K-edge CCWT analysis. The major significant correlation could be identified between the σ^2 factor of Mn-O/Co-O and the corresponding CCWT visualizations. The higher in the value of σ^2 factor, the larger modifications in the wavelet signal (shape of the modulus). For the Mn K-edge EXAFS, the activated Li_2MnO_3 character in the integrated composite tends to increase after the initial cycle as presented in Figure 9.5 and Figure 9.8 (denoted as 'LMO'). It seems to be that the tendency being activated LMO results in the higher value of σ^2 factor.

The bond length change of the Ni-O on charge-discharge is shown in Figure 9.9. The largest difference in the Ni-O changes was evaluated to be 0.059 Å from the data with major coordination numbers (Figure 9.9b). Otherwise, it could be estimated by the maximum bond length difference between the long Ni-O and short Ni-O, which is 0.115 Å. This difference is obviously the highest changes among the 1st shell (TM-O). It is therefore that the two-stage redox reaction between Ni^{2+}/Ni^{3+} and Ni^{3+}/Ni^{4+} causes active bond-length changes compared with Mn and Co. The largest amount of the oxidation change in Ni can be also confirmed by the spectra shift of Ni K-edge XANES.

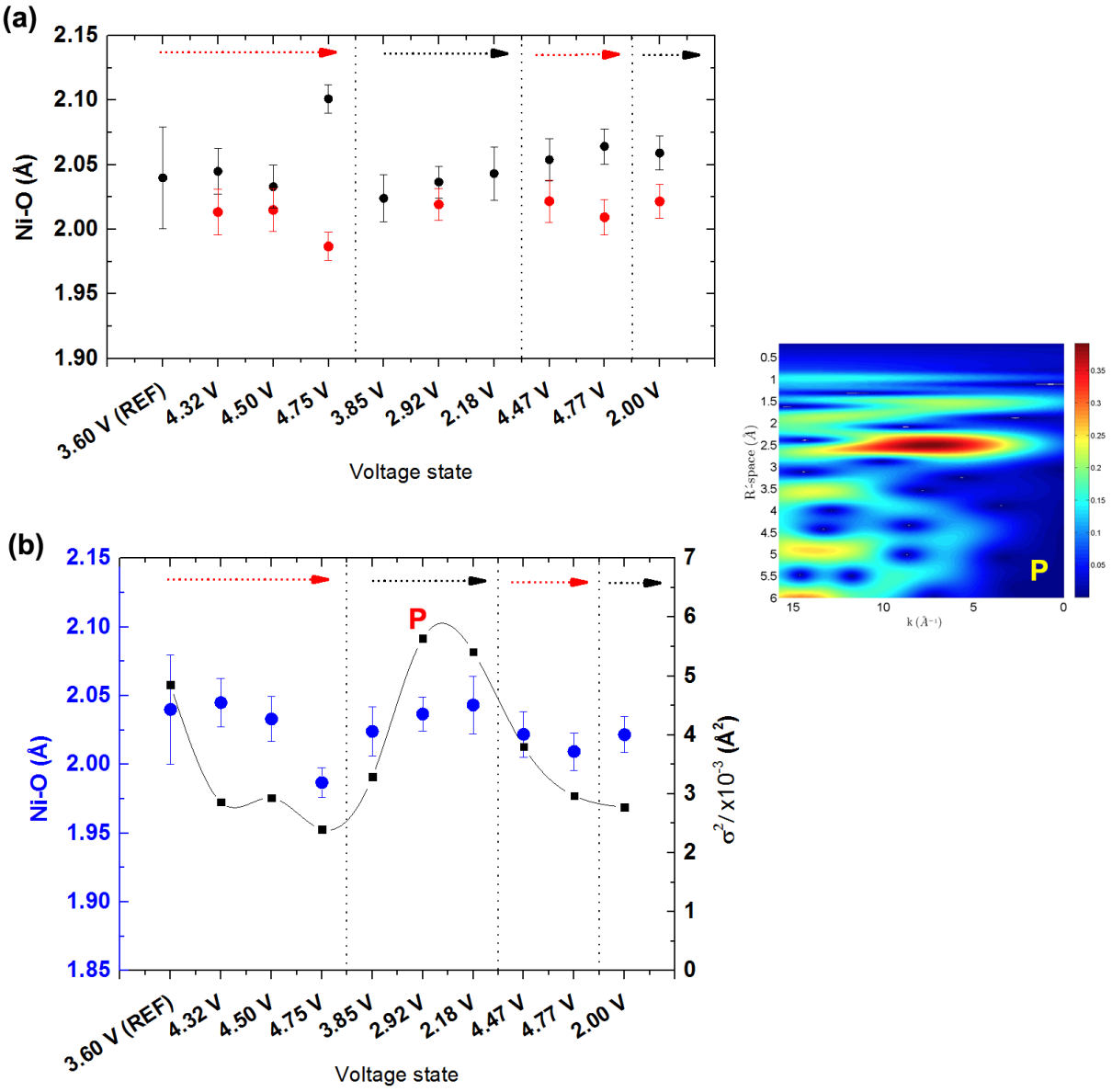


Figure 9.9 Evolution of the Ni-O bond length and structural disorder (σ) changes during electrochemical cycles (2 cycle) for graphene-coated $Li(Li_{0.2}Mn_{0.54}Ni_{0.13}Co_{0.13})O_2$ battery. (a) Ni-O bond length change with long (black) and short (red) Ni-O bonds. (b) Ni-O bond length change for those with major coordination number. The CCWT image corresponds to the structural disorders with a high value. Red arrow indicates charge process, while the black arrow represents the discharge process.

Bond splitting into long and short Ni-O resulting from Jahn-Teller distortion of Ni^{3+} (d^7) was observed during charge and discharge by the EXAFS fitting. It seems that the splitting initially appears between 3.60 V and 4.32 V, and disappeared at some point from 4.75 and 3.85 V after the initial charge as can be seen in Figure 9.9a. One unexpected outcome is the result at the final

discharge point (2.00 V) as it shows the splitting of the Ni-O bond length. One possible explanation for this is that the geometrical symmetry in the octahedral NiO_6 appears to be modified from the severe changes during Li^+ (de)intercalation. This is also consistent with the wavelet transform analysis on Ni K-edge. Note that there are now three observable signals between 1.4 Å and 2.6 Å at the voltage level of 2.0 V (last discharge point) whereas there exist only two wavelet signals between 1.4 Å and 2.6 Å at the Ni REF state. Overall, similarly as Mn-O and Co-O, the interatomic bond of Ni-O decreases upon charge and increases upon discharge, and the higher in the value of σ^2 factor, the larger modifications in the wavelet signal on Ni K-edge EXAFS as displayed in Figure 9.9.

9.4 Conclusion

This chapter presents a new approach to examine the local atomic phase modifications of the transition metals in the $xLi_2MnO_3 \cdot (1-x)LiMO_2$ (M = Mn, Co, Ni) cathode system during Li^+ (de)intercalation. The CCWT analysis on the *in operando* EXAFS signal allows one to precisely characterize the atomic phase change of Mn, Co, and Ni in the graphene-coated $Li(Li_{0.2}Mn_{0.54}Ni_{0.13}Co_{0.13})O_2$ cathode during two electrochemical cycles. One major problem of this graphene-coated cathode is the phase transition from the layered structure into the spinel phase which is known as the main factor that leads to the capacity fading and voltage decay of the lithium-ion battery, during electrochemical cycles. The growth of the spinel phase could be identified by the dQ/dV plot as presented in Figure 9.1c,d. It is likely that the phase transition appears after the initial cycle as evidenced by the redox reaction peaks, those denoted as 'S' and 'T', in the dQ/dV plot. The formation of the two-phase composite of $xLi_2MnO_3 \cdot (1-x)LiMO_2$ was confirmed by the results from the active material characterizations (Figure 9.2). The magnetic measurement reveals a slight tendency of antiferromagnetic exchange in the cathode as the Curie-

Weiss temperature (θ) was evaluated to be $-7.20385\ K$ with no magnetization saturation. This result indicates that most of the Ni ions were well located in the transition metal layers while a tiny amount of Ni^{2+} ions may be also localized in the lithium layers. This finding is consistent to the result obtained from the Ni K-edge EXAFS in R-space since there was no distinctive peak at ~3.8 Å, which is associated with the linear Ni^{2+}-O-Ni^{2+} interaction, in the Ni REF state. It could be therefore deduced that the phase transition observed in the dQ/dV plot was the consequence by electrochemical process, not from the chemical synthesis condition in the graphene-coated $Li(Li_{0.2}Mn_{0.54}Ni_{0.13}Co_{0.13})O_2$ cathode.

Strong evidence of the initial atomic phase transition in the lithium-ion battery cathode was found by the EXAFS evaluation and CCWT analysis. Especially, with the help of wavelet transform method, the semi-quantitative analyses (Figure 9.5b, Figure 9.6b, and Figure 9.7b) on the back-scattering effect from the constituent elements offers insights into the phase change with the connection of cation ordering/migration on charge-discharge. A notable activation of Mn was identified from 4.50 V to 4.75 V as can be deduced from Figure 9.5b. This would be explained by the activation of Li_2MnO_3 component with the concomitant lithia (Li_2O) removal when the battery is charged above 4.5 V. In addition, it appears that the activated Li_2MnO_3 phase slightly increases in the graphene-coated $Li(Li_{0.2}Mn_{0.54}Ni_{0.13}Co_{0.13})O_2$ cathode upon further cycles. This phase growth is identified by: (1) those peaks found damping between R ~4.5 Å and R ~5.5 Å in the R-space of Mn K-edge EXAFS implying a tendency of having more activated Li_2MnO_3 phase after initial charge; (2) the amplitude changes of Mn-TM resulting from $LiMn_6$ ordering in the transition metal layers; (3) the appearance of the interconnecting CCWT signals between R ~4.5 Å and R ~5.5 Å during further cycles (Figure 9.8a); and (4) the corresponded structural disorders ($\boldsymbol{\sigma}$) evaluated from EXAFS fitting on charge-discharge. We believe that this finding is an indicative of the precursor that leads to the phase transition from lithium-layered structure into the spinel

phase which is responsible for the capacity fading and voltage decay in this battery system. Another interesting finding is the trend of the atomic phase change in the Co as it reveals somewhat a counter reaction against to the Mn cation ordering and/or Jahn-Teller distortion of Ni^{3+}. This trend could be deduced from the evaluation of the back-scattering effect (Figure 9.6b), the visual inspection with the CCWT on Co K-edge EXAFS, and the pattern of structural disorders ($\boldsymbol{\sigma}$) on Co K-edge EXAFS (Figure 9.8b). On the other hand, as expected, the local environment around the Ni absorber has shown a complicated and dynamic variations in the peak amplitudes, as well as the location of the coordination shells. The structural disorder ($\boldsymbol{\sigma}$) of Ni reached maximum as 5.6 $\sigma^2/\times 10^{-3}(\text{Å}^2)$ at 2.92 V and very high as 5.4 $\sigma^2/\times 10^{-3}(\text{Å}^2)$ at 2.18 V, and this could be also confirmed by the wavelet transform analysis as it displayed the most entangled CCWT signals (Figure 9.7, Figure 9.9). We believe that this result is the consequence of the Jahn-Teller distortion and Ni cation ordering/migration during the electrochemical cycles. Although the redox reaction of Ni is reversible, the structural modifications appear to be irreversible on charge-discharge. Ni occupation in the lithium layers may affect the Li^+ diffusion environment and thus leads to the poor rate capability.

This study demonstrates completely a new approach to investigate the phase transition in the lithium-ion battery electrode during electrochemical cycles. The investigation on the atomic phase change for the transition metal oxides suggests a possible precursor that triggers the phase conversion mechanism from the layered structure into the spinel on the Li-rich layered Mn-based oxide cathode. The finding from the current study sheds some light on tailoring the composite structure for the lithium-ion battery cathode with improved stability.

Chapter 10 Conclusions and Future Research

10.1 Conclusions

The aim of the current thesis was to enhance the understanding of the local atomic environments linked to the phase transition on charge-discharge of the high-capacity lithium-ion battery. Attention has been devoted to the precise characterization of the atomic phase changes during Li^+ (de)intercalation and its relation to the spinel phase formation. *In operando* X-ray Absorption Spectroscopy (XAS) was chosen as the principal method owing to its highly element-specific sensitivity that allows studying processes even in a complex cathode such as the graphene-coated $Li_{1.2}Mn_{0.54}Ni_{0.13}Co_{0.13}O_2$ composite. In addition, Continuous Cauchy Wavelet Transform (CCWT) analysis was applied on the k^3-weighted normalized EXAFS data as it provides special advantages to further understand the EXAFS signals through a three dimensional visualization of the EXAFS spectra by decomposing the *k*-space and R-space (uncorrected for phase shift) signals. The wavelet transform analysis for the *in operando* XAS investigations on the lithium-ion battery electrode was reported for the first time. Based on the research works of the present thesis, principal conclusions have been drawn as following:

10.1.1 Integrated-composite system in the Li-rich layered transition metal oxide cathode

A full structural description of the $Li(Li_{0.2}Mn_{0.54}Ni_{0.13}Co_{0.13})O_2$ cathode could be obtained by the combined interpretation of the data from XRD, Rietveld refinement, Raman spectroscopy, ATR-FTIR, SQUID measurement, and synchrotron XAS. The structure of the Li-rich layered transition metal oxide is still under debate: whether it is a solid-solution or an integrated-composite between Li_2MnO_3 (monoclinic, C2/m) and $LiMO_2$ (trigonal, $R\bar{3}m$) components. The in-depth investigations on the active material presented in Chapter 5 indicate that the cathode presents a composite arising

from the integration of those two components rather than a solid-solution. This can be also confirmed by the fact that the assumption (atomic model for the FEFF 6 calculation) of the integrated components leads to better EXAFS fitting results. In section 5.2, it was also shown that the calcination temperature plays an important role in the formation of the Li_2MnO_3 and $LiMO_2$ components in the cathode material. The calcination temperature of 800 °C resulted in a balanced condition which is likely to maximize the battery performance.

10.1.2 Charge compensation mechanism in the graphene-coated $Li(Li_{0.2}Mn_{0.54}Ni_{0.13}Co_{0.13})O_2$ lithium-ion battery

Chapter 6 presents the charge compensation mechanism in the graphene-coated $Li(Li_{0.2}Mn_{0.54}Ni_{0.13}Co_{0.13})O_2$ cathode for the lithium-ion battery. The charge compensation in a full electrochemical cycle can be described with the results obtained from Chapter 7. The *in operando* XANES investigations suggest that Ni undergoes two-stage oxidation changes between Ni^{2+}/Ni^{3+} and Ni^{3+}/Ni^{4+}, while Co reveals a single stage oxidation change between Co^{3+} and Co^{4+}. In general, the oxidation state of Mn in the pristine state is known as +4 and remain unchanged during charge. However, an obvious energy shift was monitored at the Mn K-edge XANES during charge. It has been found that the Mn in the pristine state can exist in a mixed oxidation state between low-spin Mn^{3+} and Mn^{4+}. The findings deduced from the SQUID measurements (in section 5.3.4 and 5.3.7.) support the presence of Mn in a mixed oxidation state, i.e., +3.88 in the pristine. Hence, a part of the spectral shift at Mn K-edge XANES on charge can be attributed to the practical oxidation change. It should be noted that almost 85% of spectral shift was shown to occur before the voltage level of ~4.5 V. On the other hand, the spectral shift observed from ~4.5 V to 4.8 V was very small, implying little contribution to the charge compensation mechanism by the Mn. On the contrary, large extra capacity was yielded above ~4.5 V as shown in the galvanostatic profile. Furthermore, the XANES spectra shifts for each transition metal (Mn, Co, and Ni) were reversible on charge-

discharge (Chapter 7). This indicates that the oxidation change was reversible during the Li^+ (de)intercalation in the graphene-coated $Li(Li_{0.2}Mn_{0.54}Ni_{0.13}Co_{0.13})O_2$ cathode. Taken together, it appears that the electrochemical activation of the Li_2MnO_3 component above ~4.5 V is **not** related to the charge compensation mechanism from the oxidation change. The lithia (Li_2O) extraction followed by the migration of the transition metals from the surface into the vacated lithium sites is the key that provides the extra capacity above ~4.5 V in this battery system. During the reaction, the participation of the O^{2-} both from the surface and the bulk is likely to cause the oxygen evolution from the surface of the electrode ($O^{2-} \rightarrow 1/2O_2 + 2e^-$), and this process is linked to the charge compensation mechanism at the large voltage-plateau in the galvanostatic profile.

10.1.3 Charge rate dynamic in the Li-rich layered oxide cathode

Chapter 6 applies the *in operando* XAS study on different charge rates (0.125 C vs 0.5 C) in the graphene-coated $Li(Li_{0.2}Mn_{0.54}Ni_{0.13}Co_{0.13})O_2$ cathode. The main idea lies in the assumption that the Li^+ will show a different diffusion behaviour because of the different activation condition in the oxidation state for each transition metal. The conduction mechanism of the Li^+ is usually described by the Li^+ hopping process between octahedral sites *via* an intermediate tetrahedral site. The electrostatic repulsion between Li^+ and transition metals (Mn, Co, and Ni) is the driving force for the Li^+ mobility. Thus, the activation barrier correlated to the oxidation state for each transition metal is the crucial factor that determines the diffusion rate of the Li^+ in the layered channel. Lithium-ion batteries have their unique range for the optimized charge rate that corresponds to the capacity with full saturation. It was found that the rapid charge doesn't always assure the full charge state although the battery can be reached quicker at the target voltage with a fast charge rate. The second charge stage known as the 'saturation charge' must be taken into account when to assess the full battery capacity. The amount of charge compensation from the oxidation state change could be evaluated by the spectra shifts of K-edge XANES. Although the fast charge cell

reached quicker at the target voltage, the charge compensation both from the oxidation state change and the activation of the Li_2MnO_3 was relatively smaller than that of the slow charge cell, as evidenced by the structural quantification of EXAFS and the XANES spectra shifts. It is likely that Li^+ are mostly extracted from the lithium-layer in the fast charge, whereas they are extracted both from the transition metal layer and lithium-layer in the slow charge. The extraction of the Li^+ based on the latter can significantly contribute to the charge compensation.

10.1.4 Local atomic environment changes and phase transition into spinel

Chapter 9 demonstrates the practical use of the Continuous Cauchy Wavelet Transform (CCWT) analysis with the *in operando* XAS study on the lithium-ion battery cathode having a complex material system. The wavelet transform was applied on the k^3-weighted normalized EXAFS data obtained from the *in operando* XAS investigations on the graphene-coated $Li(Li_{0.2}Mn_{0.54}Ni_{0.13}Co_{0.13})O_2$ cathode during two electrochemical cycles. A dQ/dV plot was used on the galvanostatic data of the battery cathode (section 9.3.1) to monitor the phase transition process with the redox reactions. In $x\mathrm{Li_2MnO_3} \cdot (1-x)\mathrm{LiMO_2}(\mathrm{M} = \mathrm{Mn, Ni, Co})$ cathode system, it appears that the phase transition from the layered structure into the spinel-(like) is unavoidable even if special treatments were applied, i.e., graphene coating or Cr-doping (Chapter 5). The formation of the integrated two components between Li_2MnO_3 (monoclinic, C2/m) and $LiMO_2$ (trigonal, $R\bar{3}m$) were confirmed by the active material characterization (in section 9.3.2). Magnetic measurements was performed in order to evaluate not only the oxidation state of the transition metal, but also the magnetic behaviour of the cathode composite and thus provide information about the Ni^{2+} ions arrangement. The measurement suggested that most of the Ni ions were well located in the transition metal layers, but a tiny amount of Ni^{2+} ions may be also localized in the lithium layers. This finding is consistent with the result obtained from the Ni K-edge EXAFS in

R-space. Hence, it could be deduced that the phase transition observed in the dQ/dV plot was the consequence of electrochemical process, not by the side effect from chemical synthesis. *In operando* XANES/EXAFS/CCWT with semi-quantitative analysis (section 9.3.3, 9.3.4, and section 9.3.5) were employed to trace the initial trigger reaction for the phase transition into the spinel. A notable activation of Mn was identified from 4.50 V to 4.75 V. The phase growth of the activated Li_2MnO_3 component was identified by: (1) the peaks found damping between R ~4.5 Å and R ~5.5 Å in the R-space of Mn K-edge EXAFS implying a tendency of having more Li_2MnO_3 phase after initial charge; (2) the amplitude change of Mn-TM resulting from $LiMn_6$ ordering in the transition metal layers; (3) the appearance of the interconnecting CCWT signals between R ~4.5 Å and R ~5.5 Å during further cycles (Figure 9.8a); and (4) the corresponding structural disorders ($\boldsymbol{\sigma}$) evaluated from EXAFS fitting on charge-discharge. We believe that this finding is indicative of the precursor that leads to the phase transition from lithium-layered structure into the spinel phase which is responsible for the capacity fading and voltage decay in this battery system.

10.2 Recommendations for future research

The notable findings reported in the present thesis will shed some light on tailoring the electrode material for the next generation lithium-ion battery. It is therefore recommended that further research be undertaken in the following areas:

(I) *In operando* study of the oxygen evolution during the initial electrochemical cycle:

The charge compensation mechanism during the initial charge and discharge is not yet clearly understood. In order to explain the large battery capacity, both the oxygen ions from the surface and bulk are considered to evolve into oxygen gas. This is followed by the Li^+ migration from the transition metal layers into the lithium layers forming vacancies in the transition metal layers. A simultaneous migration of the transition metal ions into the lithium layers is expected through the

vacancies formed. Several studies so far have indirectly observed the evolution of the oxygen gas using differential electrochemical mass spectroscopy (DEMS). A further recommendation is to build a special experimental set-up that combines the DEMS with *in operando* synchrotron X-ray radiography. The main advantage of this set-up is the direct observation of oxygen evolution (bubbles) during the electrochemical cycle.

(II) 2D or 3D *in operando* XANES-imaging study on the lithium-ion battery electrode

The XANES can be turned into a 2D elemental mapping or a 3D functional imaging technique when it is combined with tomographic data collection and interpretation routines. The imaging process with XANES is based on the K-edge subtraction. In order to maximize the differences in the absorption of a target component (e.g. NiO in the electrode), two images are taken. One image from right above the K-edge, and another image from right below the K-edge. Therefore, the target component can increase its contrast while those other composition become dim. The *in operando* XANES-imaging study is a novel technique for examining the chemical phase transitions in relation to the electrode morphology of lithium-ion batteries.

(III) Improvement of the wavelet transform method in the phase transition study

In the current study, the wavelet transform on the K-edge EXAFS signals provide detailed information about the local atomic environment around the absorber atom. The interpretation is mostly based on the visual inspection, i.e., the modulus intensity (colour) or spectral shape and symmetry. In chapter 9, a semi-quantitative analysis is introduced to assess the scattering contributions from the individual transition metals. However, further improvements to the interpretation method of the wavelet transform are required. Especially, establishing a mathematical model will maximize the potential of this method in terms of *in situ* or *in operando* studies on the lithium-ion battery electrodes.

REFERENCES

1. Rossouw, M. & Thackeray, M. Lithium manganese oxides from Li_2MnO_3 for rechargeable lithium battery applications. *Mater. Res. Bull.* **26,** 463–473 (1991).
2. Thackeray, M. M. *et al.* Li_2MnO_3-stabilized $LiMO_2$ (M = Mn, Ni, Co) electrodes for lithium-ion batteries. *J. Mater. Chem.* **17,** 3112 (2007).
3. Johnson, C. S. *et al.* The significance of the Li_2MnO_3 component in 'composite' $xLi_2MnO_3 \cdot (1-x)LiMn_{0.5}Ni_{0.5}O_2$ electrodes. *Electrochem. commun.* **6,** 1085–1091 (2004).
4. Thackeray, M. M., Kang, S.-H., Johnson, C. S., Vaughey, J. T. & Hackney, S. a. Comments on the structural complexity of lithium-rich $Li_{1+x}M_{1-x}O_2$ electrodes (M=Mn, Ni, Co) for lithium batteries. *Electrochem. commun.* **8,** 1531–1538 (2006).
5. Kim, J., Johnson, C. S. & Thackeray, M. M. Layered $xLiMO_2 \cdot (1\text{-}x)Li_2M'O_3$ electrodes for lithium batteries : a study of $0.95LiMn0.5Ni_{0.5}O_2 \cdot 0.05Li_2TiO_3$ *Electrochem. commun.* **4,** 205–209 (2002).
6. Brodd, R. J. *Batteries for Sustainability: Selected Entries from the Encyclopedia of Sustainability Science and Technology*. (Springer Science & Business Media, 2012).
7. Armstrong, R. *et al.* Demonstrating oxygen loss and associated structural reorganization in the lithium battery cathode $Li[Ni_{0.2}Li_{0.2}Mn_{0.6}]O_2$. *J. Am. Chem. Soc.* **128,** 8694–8 (2006).
8. Lu, Z. & Dahn, J. R. Understanding the Anomalous Capacity of $Li/Li[Ni_xLi_{(1/3-2x/3)}]Mn_{(2/3-x/3)}]O_2$ Cells Using In Situ X-Ray Diffraction and Electrochemical Studies. *J. Electrochem. Soc.* **149,** A815 (2002).
9. Column: The Future of the Electric car is dim. at <http://www.bmwblog.com/2012/11/22/column-the-future-of-the-electric-car-is-dim/>
10. Gu, M. *et al.* Formation of the spinel phase in the layered composite cathode used in Li-ion batteries. *ACS Nano* **7,** 760–7 (2013).
11. Ceder, G. & Van der Ven, A. Phase diagrams of lithium transition metal oxides: investigations from first principles. *Electrochim. Acta* **45,** 131–150 (1999).
12. Molenda, J. Modification in the electronic structure of cobalt bronze Li_xCoO_2 and the resulting electrochemical properties. *Solid State Ionics* **36,** 53–58 (1989).
13. G. Bruce, P. Solid-state chemistry of lithium power sources†. *Chem. Commun.* 1817 (1997).
14. Bruce, P. G. *Solid State Electrochemistry*. (Cambridge University Press, 1997).
15. Oxtoby, D. W. *Principles of Modern Chemistry*. (Cengage Learning, 2011).
16. Goodenough, J. Design considerations. *Solid State Ionics* **69,** 184–198 (1994).
17. Goodenough, J. B. & Kim, Y. Challenges for Rechargeable Li Batteries †. *Chem. Mater.* **22,** 587–603 (2010).
18. Bruce, P. G. Energy storage beyond the horizon: Rechargeable lithium batteries. *Solid State Ionics* **179,** 752–760 (2008).
19. Fong, R. Studies of Lithium Intercalation into Carbons Using Nonaqueous Electrochemical Cells. *J. Electrochem. Soc.* **137,** 2009 (1990).
20. Whittingham, M. S. Lithium batteries and cathode materials. *Chem. Rev.* **104,** 4271–301 (2004).
21. Wakihara, M. Recent developments in lithium ion batteries. **33,** (2001).
22. Thackeray, M. M., David, W. I. F., Bruce, P. G. & Goodenough, J. B. Lithium insertion into manganese spinels. *Mater. Res. Bull.* **18,** 461–472 (1983).
23. Padhi, A. K. Phospho-olivines as Positive-Electrode Materials for Rechargeable Lithium Batteries. *J. Electrochem. Soc.* **144,** 1188 (1997).
24. Yamada, A. *et al.* Olivine-type cathodes. *J. Power Sources* **119-121,** 232–238 (2003).
25. Yamada, a., Chung, S. C. & Hinokuma, K. Optimized $LiFePO_4$ for Lithium Battery Cathodes. *J. Electrochem. Soc.* **148,** A224 (2001).
26. Yuan, L.-X. *et al.* Development and challenges of LiFePO4 cathode material for lithium-ion batteries. *Energy Environ. Sci.* **4,** 269 (2011).
27. Park, M., Zhang, X., Chung, M., Less, G. B. & Sastry, A. M. A review of conduction phenomena in Li-ion batteries. *J. Power Sources* **195,** 7904–7929 (2010).

28. Mendiboure, A., Delmas, C. & Hagenmuller, P. New layered structure obtained by electrochemical deintercalation of the metastable $LiCoO_2$ (O2) variety. *Mater. Res. Bull.* **19,** 1383–1392 (1984).
29. Kang, K. & Ceder, G. Factors that affect Li mobility in layered lithium transition metal oxides. *Phys. Rev. B* **74,** (2006).
30. Kang, K., Meng, Y. S., Bréger, J., Grey, C. P. & Gerbrand Ceder. Electrodes with High Power and High Capacity for Rechargeable Lithium Batteries. *Science (80-.).* **311,** 977–980 (2006).
31. Julien, C. M., Pereira-Ramos, J.-P. & Momchilov. *New Trends in Intercalation Compounds for Energy Storage*. (Springer, 2002).
32. Chebiam, R. V., Prado, F. & Manthiram, A. Soft Chemistry Synthesis and Characterization of Layered $Li_{1-x}Ni_{1-y}Co_yO_{2-\delta}$ ($0 \leq x \leq 1$ and $0 \leq y \leq 1$). *Chem. Mater.* **13,** 2951–2957 (2001).
33. April, R. & Goodenough, C. J. B. A NEW CATHODE MATERIAL FOR BATTERIES OF HIGH ENERGY DENSITY. **15,** 783–789 (1980).
34. Chebiam, R. V, Kannan, A. M., Prado, F. & Manthiram, A. Comparison of the chemical stability of the high energy density cathodes of lithium-ion batteries. **3,** 624–627 (2001).
35. Chebiam, R. V., Prado, F. & Manthiram, a. Comparison of the Chemical Stability of $Li_{1-x}CoO_2$ and $Li_{1-x}Ni_{0.85}Co_{0.15}O_2$ Cathodes. *J. Solid State Chem.* **163,** 5–9 (2002).
36. Ohzuku, T. & Ueda, A. Solid-State Redox Reactions of LiCoO (R3m) for 4 Volt Secondary Lithium Cells. **141,** 2972–2977 (1994).
37. Myung, S., Kumagai, N., Komaba, S. & Chung, H. Effects of Al doping on the microstructure of $LiCoO_2$ cathode materials. **139,** 47–56 (2001).
38. Jung, Y. S. *et al.* Enhanced Stability of $LiCoO_2$ Cathodes in Lithium-Ion Batteries Using Surface Modification by Atomic Layer Deposition. *J. Electrochem. Soc.* **157,** A75 (2010).
39. Yoon, W., Lee, K. & Kim, K. Structural and Electrochemical Properties of $LiAlyCo_{1-y}O_2$ Cathode for Li Rechargeable Batteries. **147,** 2023–2028 (2000).
40. Fang, T., Duh, J.-G. & Sheen, S.-R. Improving the Electrochemical Performance of $LiCoO_2$ Cathode by Nanocrystalline ZnO Coating. *J. Electrochem. Soc.* **152,** A1701 (2005).
41. Kim, J., Noh, M., Cho, J., Kim, H. & Kim, K.-B. Controlled Nanoparticle Metal Phosphates (Metal=Al, Fe, Ce, and Sr) Coatings on LiCoO[sub 2] Cathode Materials. *J. Electrochem. Soc.* **152,** A1142 (2005).
42. A. Rougier, P. Gravereau and C. Delmas. Optimization of the Composition of the $Li_{1-Z}Ni_{1+z}O_2$ Electrode Materials - Structural, Magnetic, and Electrochemical Studies. *J. Electrochem. Soc.* **143,** 1168–1175 (1996).
43. Nakai, I. *et al.* X-ray absorption fine structure and neutron diffraction analyses of de-intercalation behavior in the $LiCoO_2$ and $LiNiO_2$ systems. *J. Power Sources* **68,** 536–539 (1997).
44. Delmas, C. *et al.* On the behavior of the Li_xNiO_2 system: an electrochemical and structural overview. *J. Power Sources* **68,** 120–125 (1997).
45. Guilmard, M., Croguennec, L., Denux, D. & Delmas, C. Thermal Stability of Lithium Nickel Oxide Derivatives. Part I: LixNi1.02O2 and LixNi0.89Al 0.16O2 (x = 0.50 and 0.30). *Chem. Mater.* **15,** 4476–4483 (2003).
46. Ohzuku, T., Ueda, A. & Nagayama, M. Electrochemistry and Structural Chemistry of LiNi02 (R3m) for 4 Volt Secondary Lithium Cells. *J. Electrochem. Soc.* **140,** 1862–1870 (1993).
47. Bruce, P. G., Armstrong, A. R. & Gitzendanner, R. L. New intercalation compounds for lithium batteries: layered LiMnO † 2. *J. Mater. Chem.* **9,** 193–198 (1999).
48. Armstrong, A. R. & Bruce, P. G. Synthesis of layered LiMnO2 as an electrode for rechargeable lithium batteries. *Nature* **381,** 499–500 (1996).
49. Shao-Horn, Y. Structural Characterization of Layered LiMnO2 Electrodes by Electron Diffraction and Lattice Imaging. *J. Electrochem. Soc.* **146,** 2404 (1999).
50. Wang, M. & Navrotsky, A. LiMO2 (M=Mn, Fe, and Co): Energetics, polymorphism and phase transformation. *J. Solid State Chem.* **178,** 1230–1240 (2005).
51. He, P., Yu, H., Li, D. & Zhou, H. Layered lithium transition metal oxide cathodes towards high energy lithium-ion batteries. *J. Mater. Chem.* **22,** 3680 (2012).

52. Armstrong, A. R., Dupre, N., Paterson, A. J., Grey, C. P. & Bruce, P. G. Combined Neutron Diffraction, NMR, and Electrochemical Investigation of the Layered-to-Spinel Transformation in $LiMnO_2$. *Chem. Mater.* **16,** 3106–3118 (2004).
53. Armstrong, A. R., Paterson, A. J., Dupre, N., Grey, C. P. & Bruce, P. G. Structural Evolution of Layered Li x Mn y O 2 : Combined Neutron , NMR , and Electrochemical Study. *Chem. Mater.* **19,** 1016–1023 (2007).
54. Ohzuku, T. & Makimura, Y. Layered Lithium Insertion Material of $LiNi_{1/2}Mn_{1/2}O_2$: A Possible Alternative to $LiCoO_2$ for Advanced Lithium-Ion Batteries. *Chem. Lett.* **2,** 744–745 (2001).
55. Makimura, Y. & Ohzuku, T. Lithium insertion material of $LiNi_{1/2}Mn_{1/2}O_2$ for advanced lithium-ion batteries. *J. Power Sources* **119-121,** 156–160 (2003).
56. Koyama, Y., Makimura, Y., Tanaka, I., Adachi, H. & Ohzuku, T. Systematic Research on Insertion Materials Based on Superlattice Models in a Phase Triangle of $LiCoO_2$-$LiNiO_2$-$LiMnO_2$. *J. Electrochem. Soc.* **151,** A1499 (2004).
57. Lu, Z., MacNeil, D. D. & Dahn, J. R. Layered Cathode Materials $Li[Ni_xLi_{(1/3-2x/3)}Mn_{(2/3-x/3)}]O_2$ for Lithium-Ion Batteries. *Electrochem. Solid-State Lett.* **4,** A191 (2001).
58. Li, H. H. *et al.* Changes in the Cation Ordering of Layered O3 $Li_xNi_{0.5}Mn_{0.5}O_2$ during Electrochemical Cycling to High Voltages: An Electron Diffraction Study. *Chem. Mater.* **19,** 2551–2565 (2007).
59. Yabuuchi, N. & Ohzuku, T. Novel lithium insertion material of $LiCo_{1/3}Ni_{1/3}Mn_{1/3}O_2$ for advanced lithium-ion batteries. *J. Power Sources* **119-121,** 171–174 (2003).
60. Choi, J. & Manthiram, a. Role of Chemical and Structural Stabilities on the Electrochemical Properties of Layered LiNi[1⁄3]Mn[1⁄3]Co[1⁄3]O[2] Cathodes. *J. Electrochem. Soc.* **152,** A1714 (2005).
61. Ohzuku, T. & Makimura, Y. Layered Lithium Insertion Material of $LiCo_{1/3}Ni_{1/3}Mn_{1/3}O_2$ for Lithium-Ion Batteries. *Chem. Lett.* 642–643 (2001).
62. Akántara, R., Lavela, P. & Tirado, J. Changes in Structure and Cathode Performance with Composition and Preparation Temperature of Lithium Cobalt Nickel Oxide. *J. Electrochem. Soc.* **145,** 730–736 (1998).
63. Zhecheva, E., Stoyanova, R., Alcántara, R., Lavela, P. & Tirado, J.-L. Cation order/disorder in lithium transition-metal oxides as insertion electrodes for lithium-ion batteries. *Pure Appl. Chem.* **74,** (2002).
64. Kim, J.-M. & Chung, H.-T. Role of transition metals in layered $Li[Ni,Co,Mn]O_2$ under electrochemical operation. *Electrochim. Acta* **49,** 3573–3580 (2004).
65. Kim, J.-M. & Chung, H.-T. The first cycle characteristics of $Li[Ni_{1/3}Co_{1/3}Mn_{1/3}]O_2$ charged up to 4.7 V. *Electrochim. Acta* **49,** 937–944 (2004).
66. Deb, A., Bergmann, U., Cramer, S. P. & Cairns, E. J. In situ x-ray absorption spectroscopic study of the Li[Ni[1⁄3]Co[1⁄3]Mn[1⁄3]]O[2] cathode material. *J. Appl. Phys.* **97,** 113523 (2005).
67. Hwang, B. J., Tsai, Y. W., Carlier, D. & Ceder, G. A Combined Computational/Experimental Study on $LiNi_{1/3}Co_{1/3}Mn_{1/3}O_2$. *Chem. Mater.* **15,** 3676–3682 (2003).
68. Lu, Z., Beaulieu, L. Y., Donaberger, R. a., Thomas, C. L. & Dahn, J. R. Synthesis, Structure, and Electrochemical Behavior of $Li[Ni_xLi_{1/3-2x/3}Mn_{2/3-x/3}]O_2$. *J. Electrochem. Soc.* **149,** A778 (2002).
69. Jarvis, K. A., Deng, Z., Allard, L. F., Manthiram, A. & Ferreira, P. J. Atomic Structure of a Lithium-Rich Layered Oxide Material for Lithium-Ion Batteries: Evidence of a Solid Solution. *Chem. Mater.* **23,** 3614–3621 (2011).
70. Koga, H. *et al.* $Li_{1.20}Mn_{0.54}Co_{0.13}Ni_{0.13}O_2$ with Different Particle Sizes as Attractive Positive Electrode Materials for Lithium-Ion Batteries: Insights into Their Structure. *J. Phys. Chem. C* **116,** 13497–13506 (2012).
71. Long, B. R. *et al.* Effect of cooling rates on phase separation in $0.5Li_2MnO_3{\cdot}0.5LiCoO_2$ *Chem. Mater.* 3565−3572 (2014).
72. Amalraj, F. *et al.* Integrated Materials $xLi_2MnO_3{\cdot}(1-x)LiMn_{1/3}Ni_{1/3}Co_{1/3}O_2$ (x=0.3, 0.5, 0.7) Synthesized. *J. Electrochem. Soc.* **157,** A1121 (2010).

73. Kang, S.-H. *et al.* Interpreting the structural and electrochemical complexity of $0.5Li_2MnO_3 \cdot 0.5LiMO_2$ electrodes for lithium batteries ($M = Mn_{0.5-x}Ni_{0.5-x}Co_{2x}$, $0 \leq x \leq 0.5$). *J. Mater. Chem.* **17,** 2069 (2007).
74. Weill, F., Tran, N., Croguennec, L. & Delmas, C. Cation ordering in the layered $Li_{1+x}(Ni_{0.425}Mn_{0.425}Co_{0.15})_{1-x}O_2$ materials (x=0 and 0.12). *J. Power Sources* **172,** 893–900 (2007).
75. Meng, Y. S. *et al.* Cation Ordering in Layered O3 $Li[Ni_xLi_{1/3-2x/3}Mn_{2/3-x/3}]O_2$ ($0 \leq x \leq 1$). *Chem. Mater.* **17,** 2386–2394 (2005).
76. Tran, N. *et al.* Mechanisms Associated with the 'Plateau' Observed at High Voltage for the Overlithiated $Li_{1.12}(Ni_{0.425}Mn_{0.425}Co_{0.15})_{0.88}O_2$ System. *Chem. Mater.* **20,** 4815–4825 (2008).
77. Mohanty, D. *et al.* Correlating cation ordering and voltage fade in a lithium-manganese-rich lithium-ion battery cathode oxide: a joint magnetic susceptibility and TEM study. *Phys. Chem. Chem. Phys.* **15,** 19496–509 (2013).
78. Thackeray, M. M., Johnson, C. S., Vaughey, J. T., LiCurrent address: eVionyx Inc., Ha, N. & Hackney, S. A. Advances in manganese-oxide 'composite' electrodes for lithium-ion batteries. *J. Mater. Chem.* **15,** 2257 (2005).
79. Johnson, C. S., Li, N., Lefief, C., Vaughey, J. T. & Thackeray, M. M. Synthesis , Characterization and Electrochemistry of Lithium. *Chem. Mater.* **2,** 6095–6106 (2008).
80. Lu, Z. & Dahn, J. R. Structure and Electrochemistry of Layered Li[Cr[x]Li[(1/3−x/3)]Mn[(2/3−2x/3)]]O[2]. *J. Electrochem. Soc.* **149,** A1454 (2002).
81. Zhang, X. *et al.* Novel composites $Li[Li_xNi_{0.34-x}Mn_{0.47}Co_{0.19}]O_2$ ($0.18 \leq x \leq 0.21$): Synthesis and application as high-voltage cathode with improved electrochemical performance for lithium ion batteries. *Electrochim. Acta* **81,** 233–238 (2012).
82. Yu, H. *et al.* High-energy 'composite' layered manganese-rich cathode materials via controlling Li2MnO3 phase activation for lithium-ion batteries. *Phys. Chem. Chem. Phys.* **14,** 6584–95 (2012).
83. Yabuuchi, N., Yoshii, K., Myung, S.-T., Nakai, I. & Komaba, S. Detailed studies of a high-capacity electrode material for rechargeable batteries, Li_2MnO_3-$LiCo_{1/3}Ni_{1/3}Mn_{1/3}O_2$. *J. Am. Chem. Soc.* **133,** 4404–19 (2011).
84. Rajarathinam, S., Mitra, S. & Petla, R. K. Li_2MnO_3 rich-$LiMn_{0.33}Co_{0.33}Ni_{0.33}O_2$ integrated nano-composites as high energy density lithium-ion battery cathode materials. *Electrochim. Acta* **108,** 135–144 (2013).
85. Johnson, C. S., Li, N., Lefief, C. & Thackeray, M. M. Anomalous capacity and cycling stability of $xLi_2MnO_3 \cdot (1-x)LiMO_2$ electrodes (M=Mn, Ni, Co) in lithium batteries at 50°C. *Electrochem. commun.* **9,** 787–795 (2007).
86. Yoon, W., Grey, C. P., Balasubramanian, M., Yang, X. & Mcbreen, J. In Situ X-ray Absorption Spectroscopic Study on $LiNi_{0.5}Mn_{0.5}O_2$ Cathode Material during Electrochemical Cycling. 3161–3169 (2003).
87. Yoon, W.-S. *et al.* Investigation of the charge compensation mechanism on the electrochemically Li-ion deintercalated $Li_{1-x}Co_{1/3}Ni_{1/3}Mn_{1/3}O_2$ electrode system by combination of soft and hard X-ray absorption spectroscopy. *J. Am. Chem. Soc.* **127,** 17479–87 (2005).
88. Ito, A. *et al.* In situ X-ray absorption spectroscopic study of Li-rich layered cathode material $Li[Ni_{0.17}Li_{0.2}Co_{0.07}Mn_{0.56}]O_2$. *J. Power Sources* **196,** 6828–6834 (2011).
89. Petersburg, C. F., Li, Z., Chernova, N. A., Whittingham, M. S. & Alamgir, F. M. Oxygen and transition metal involvement in the charge compensation mechanism of $LiNi_{1/3}Mn_{1/3}Co_{1/3}O_2$ cathodes. *J. Mater. Chem.* **22,** 19993 (2012).
90. Oishi, M. *et al.* Charge compensation mechanisms in $Li_{1.16}Ni_{0.15}Co_{0.19}Mn_{0.50}O_2$ positive electrode material for Li-ion batteries analyzed by a combination of hard and soft X-ray absorption near edge structure. *J. Power Sources* **222,** 45–51 (2013).
91. Simonin, L. *et al.* In situ investigations of a Li-rich Mn–Ni layered oxide for Li-ion batteries. *J. Mater. Chem.* **22,** 11316 (2012).
92. Yu, X. *et al.* Understanding the Rate Capability of High-Energy-Density Li-Rich Layered $Li_{1.2}Ni_{0.15}Co_{0.1}Mn_{0.55}O_2$ Cathode Materials. *Adv. Energy Mater.* **4,** (2014).

93. Huang, Z.-F., Du, F., Wang, C.-Z., Wang, D.-P. & Chen, G. Low-spin Mn^{3+} ion in rhombohedral LiMnO2 predicted by first-principles calculations. *Phys. Rev. B* **75,** 054411 (2007).
94. Prasad, R. *et al.* Divalent-dopant criterion for the suppression of Jahn-Teller distortion in Mn oxides - First-principles calculations and x-ray absorption spectroscopy measurements for Co in LiMnO2. *Phys. Rev. B* **68,** 012101 (2003).
95. Ni, L. *et al.* Demonstrating Oxygen Loss and Associated Structural Reorganization in the Lithium Battery Cathode. *Electrochem. commun.* **128,** 8694–8698 (2006).
96. Croy, J. R., Kang, S.-H., Balasubramanian, M. & Thackeray, M. M. Li2MnO3-based composite cathodes for lithium batteries: A novel synthesis approach and new structures. *Electrochem. commun.* **13,** 1063–1066 (2011).
97. Yabuuchi, N. *et al.* Structural and Electrochemical Characterizations on Li_2MnO_3-$LiCoO_2$-$LiCrO_2$ System as Positive Electrode Materials for Rechargeable Lithium Batteries. *J. Electrochem. Soc.* **160,** A39–A45 (2012).
98. Mansour, A. N., Croguennec, L. & Delmas, C. A Unique Structure of Ni(III) in $LiNi_{0.3}Co_{0.7}O_2$ Without Jahn-Teller Distortion. *Electrochem. Solid-State Lett.* **8,** A544 (2005).
99. Croy, J. R., Balasubramanian, M., Kim, D., Kang, S.-H. & Thackeray, M. M. Designing High-Capacity, Lithium-Ion Cathodes Using X-ray Absorption Spectroscopy. *Chem. Mater.* **23,** 5415–5424 (2011).
100. Jiang, J. & Dahn, J. R. Insignificant impact of designed oxygen release from high capacity electrodes during the cycling of Li-ion cells. *Electrochim. Acta* **51,** 3413–3416 (2006).
101. Ates, M. N., Mukerjee, S. & Abraham, K. M. A Li-Rich Layered Cathode Material with Enhanced Structural Stability and Rate Capability for Li-on Batteries. *J. Electrochem. Soc.* **161,** A355–A363 (2014).
102. Wang, C.-C., Jarvis, K. A., Ferreira, P. J. & Manthiram, A. Effect of Synthesis Conditions on the First Charge and Reversible Capacities of Lithium-Rich Layered Oxide Cathodes. *Chem. Mater.* **25,** 3267–3275 (2013).
103. Wang, J. *et al.* The structure, morphology, and electrochemical properties of $Li_{1+x}Ni_{1/6}Co_{1/6}Mn_{4/6}O_{2.25+x/2}$ ($0.1 \leq x \leq 0.7$) cathode materials. *Electrochim. Acta* **66,** 61–66 (2012).
104. Arunkumar, T. A., Wu, Y. & Manthiram, A. Factors Influencing the Irreversible Oxygen Loss and Reversible Capacity in Layered $Li[Li_{1/3}Mn_{2/3}]O_2$−$Li[M]O_2$ (M = $Mn_{0.5-y}Ni_{0.5-y}$ Solid Solutions. *Chem. Mater.* **19,** 3067–3073 (2007).
105. Ceder, G., Ven, A. Van der, Marianetti, C. & Morgan, D. First-principles alloy theory in oxides. *Model. Simul. Mater. Sci. Eng.* **8,** 311–321 (2000).
106. Aydinol, M. K. First-Principles Prediction of Insertion Potentials in Li-Mn Oxides for Secondary Li Batteries. *J. Electrochem. Soc.* **144,** 3832 (1997).
107. Huang, Z.-F., Meng, X., Wang, C.-Z., Sun, Y. & Chen, G. First-principles calculations on the Jahn–Teller distortion in layered LiMnO2. *J. Power Sources* **158,** 1394–1400 (2006).
108. Hahn, J. E. *et al.* Observation of an electric quadrupole transition in the X-ray absorption spectrum of a Cu(II) complex. *Chem. Phys. Lett.* **88,** 595–598 (1982).
109. Belli, M. *et al.* X-ray absorption near edge structures (XANES) in simple and complex Mn compounds. *Solid State Commun.* **35,** 355–361 (1980).
110. Yano, J. & Yachandra, V. K. X-ray absorption spectroscopy. *Photosynth. Res.* **102,** 241–54 (2009).
111. Thackeray, M. M. Manganese oxides for lithium batteries. *Prog. Solid State Chem.* **25,** 1–71 (1997).
112. Rougier, A., Delmas, C. & Chadwick, A. V. Non-cooperative Jahn-Teller effect in LiNiO2: An EXAFS study. *Solid State Commun.* **94,** 123–127 (1995).
113. Armstrong, A. R., Robertson, A. D., Gitzendanner, R. & Bruce, P. G. The Layered Intercalation Compounds $Li(Mn_{1-y}Co_y)O_2$: Positive Electrode Materials for Lithium–Ion Batteries. *J. Solid State Chem.* **145,** 549–556 (1999).
114. Baddour-Hadjean, R. & Pereira-Ramos, J.-P. Raman Microspectrometry Applied to the Study of Electrode Materials for Lithium Batteries. *Chem. Rev.* **110,** 1278–1319 (2010).

115. Deb, A., Bergmann, U., Cramer, S. P. & Cairns, E. J. Local structure of $LiNi_{0.5}Mn_{0.5}O_2$ cathode material probed by in situ x-ray absorption spectroscopy. *J. Appl. Phys.* **99,** 063701 (2006).
116. Deb, A., Bergmann, U., Cramer, S. P. & Cairns, E. J. In Situ X-Ray Absorption Spectroscopic Study of $Li_{1.05}Ni_{0.35}Co_{0.25}Mn_{0.4}O_2$ Cathode Material Coated with $LiCoO_2$. *J. Electrochem. Soc.* **154,** A534 (2007).
117. Rumble, C. *et al.* Structural and Electrochemical Investigation of $Li(Ni_{0.4}Co_{0.15}Al_{0.05}Mn_{0.4})O_2$ Cathode Material. *J. Electrochem. Soc.* **157,** A1317 (2010).
118. Croy, J. R. *et al.* Examining Hysteresis in Composite $xLi_2MnO_3 \cdot(1-x)LiMO_2$ Cathode Structures. *J. Phys. Chem. C* **117,** 6525–6536 (2013).
119. Vetter, J. *et al.* Ageing mechanisms in lithium-ion batteries. *J. Power Sources* **147,** 269–281 (2005).
120. Wohlfahrt-Mehrens, M., Vogler, C. & Garche, J. Aging mechanisms of lithium cathode materials. *J. Power Sources* **127,** 58–64 (2004).
121. Reed, J., Ceder, G. & Van Der Ven, a. Layered-to-Spinel Phase Transition in Li_xMnO_2. *Electrochem. Solid-State Lett.* **4,** A78 (2001).
122. Mohanty, D. *et al.* Structural transformation of a lithium-rich $Li_{1.2}Co_{0.1}Mn_{0.55}Ni_{0.15}O_2$ cathode during high voltage cycling resolved by in situ X-ray diffraction. *J. Power Sources* **229,** 239–248 (2013).
123. Mohanty, D. *et al.* Investigating phase transformation in the $Li_{1.2}Co_{0.1}Mn_{0.55}Ni_{0.15}O_2$ lithium-ion battery cathode during high-voltage hold (4.5 V) via magnetic, X-ray diffraction and electron microscopy studies. *J. Mater. Chem. A* **1,** 6249 (2013).
124. Nayak, P. K., Grinblat, J., Levi, M., Markovsky, B. & Aurbach, D. Structural and Electrochemical Evidence of Layered to Spinel Phase Transformation of Li and Mn Rich Layered Cathode Materials of the Formulae $xLi[Li_{1/3}Mn_{2/3}]O_2 \cdot (1-x)LiMn_{1/3}Ni_{1/3}Co_{1/3}O_2$ (x = 0.2, 0.4, 0.6) upon Cycling. *J. Electrochem. Soc.* **161,** A1534–A1547 (2014).
125. Lytle, F. W. The EXAFS family tree: a personal history of the development of extended X-ray absorption fine structure. *J. Synchrotron Radiat.* **6,** 123–134 (1999).
126. Sayers, D. E., Stern, E. a. & Lytle, F. W. New technique for investigating noncrystalline structures: Fourier analysis of the extended x-ray-absorption fine structure. *Phys. Rev. Lett.* **27,** 1204–1207 (1971).
127. Vlaica, G. & Olivi, L. EXAFS Spectroscopy: a Brief Introduction. *Croat. Chem. Acta* **77,** 427–433 (2004).
128. Rehr, J. J. Theoretical approaches to x-ray absorption fine structure. *Rev. Mod. Phys.* **72,** 621–654 (2000).
129. Nakai, I.K. Takahashi, y. Shiraishi, T. Nakagome, F. Izumy, Nishikawa d, T. K. X-ray absorption fine structure and neutron diffraction analyses of de-intercalation behavior in the LiCoO2and LiNiO2systems. *J. Power Sources* **68,** 536–539 (1997).
130. Bunker, G. *Introduction to XAFS: A Practical Guide to X-ray Absorption Fine Structure Spectroscopy*. (Cambridge University Press, 2010).
131. Koningsberger, D. C., Mojet, B. L., Dorssen, G. E. van & Ramaker, D. E. XAFS spectroscopy; fundamental principles and data analysis. *Top. Catal.* **10,** 143–155 (2000).
132. Rehr, J. J. & Ankudinov, A. L. Progress in the theory and interpretation of XANES. *Coord. Chem. Rev.* **249,** 131–140 (2005).
133. Shulman, G. R., Yafet, Y., Eisenberger, P. & Blumberg, W. E. Observations and interpretation of x-ray absorption edges in iron compounds and proteins. *Proc. Natl. Acad. Sci. U. S. A.* **73,** 1384–8 (1976).
134. Han, Y.-F., Ramesh, K., Chen, L. W., Chen, F. X. & Borgna, A. X-Ray Absorption Spectroscopy Study Of Mn 2 O 3 And Mn 3 O 4 Nanoparticles Supported On Mesoporous Silica Sba-15. *Adv. Synchrotron Radiat.* **01,** 67–78 (2008).
135. Stern, E. Number of relevant independent points in x-ray-absorption fine-structure spectra. *Phys. Rev. B. Condens. Matter* **48,** 9825–9827 (1993).

136. Newville, M. IFEFFIT: interactive XAFS analysis and FEFF fitting. *J. Synchrotron Radiat.* **8,** 322–4 (2001).
137. Song, B., Lai, M. O., Liu, Z., Liu, H. & Lu, L. Graphene-based surface modification on layered Li-rich cathode for high-performance Li-ion batteries. *J. Mater. Chem. A* **1,** 9954 (2013).
138. Hummers, W. S. & Offeman, R. E. Preparation of Graphitic Oxide. *J. Am. Chem. Soc.* **80,** 1339–1339 (1958).
139. Deng, H. *et al.* Nanostructured Lithium Nickel Manganese Oxides for Lithium-Ion Batteries. *J. Electrochem. Soc.* **157,** A447 (2010).
140. Deng, H., Belharouak, I., Sun, Y.-K. & Amine, K. LixNi0.25Mn0.75Oy ($0.5 \leq x \leq 2$, $2 \leq y \leq 2.75$) compounds for high-energy lithium-ion batteries. *J. Mater. Chem.* **19,** 4510 (2009).
141. Bloom, I. *et al.* Differential voltage analyses of high-power, lithium-ion cells 1. Technique and application. *J. Power Sources* **139,** 295–303 (2005).
142. Bloom, I., Christophersen, J., Abraham, D. & Gering, K. Differential voltage analyses of high-power lithium-ion cells - 2. Applications. *J. Power Sources* **139,** 304–313 (2005).
143. Bragg's_law @ en.wikipedia.org. at <http://en.wikipedia.org/wiki/Bragg's_law>
144. Rietveld, H. M. A profile refinement method for nuclear and magnetic structures. *J. Appl. Crystallogr.* **2,** 65–71 (1969).
145. Julien, C. M. Vibrational Spectroscopy Of Electrode Materials For Rechargeable Lithium Batteries I. Basic Considerations. in *Proceedings of the International Workshop 'Advanced Techniques for Energy Sources Investigation and Testing'* 1–14 (2004).
146. Julien, C. M. & Massot, M. Lattice vibrations of materials for lithium rechargeable batteries I. Lithium manganese oxide spinel. *Mater. Sci. Eng. B* **97,** 217–230 (2003).
147. Uñoz, M. A. M., Rgoul, P. I. A. & Arges, F. R. F. Continuous Cauchy wavelet transform analyses of EXAFS spectra : A qualitative approach. *Am. Mineral.* **88,** 694–700 (2003).
148. Muoz, M., Farges, F. & Argoul, P. Continuous Cauchy Wavelet Transform of XAFS Spectra. *Phys. Scr.* **2005,** 221 (2005).
149. Croy, J. R. *et al.* Countering the Voltage Decay in High Capacity $xLi_2MnO_3 \cdot (1-x)LiMO_2$ Electrodes (M=Mn, Ni, Co) for Li+-Ion Batteries. *J. Electrochem. Soc.* **159,** A781 (2012).
150. Su, F.-Y. *et al.* Could graphene construct an effective conducting network in a high-power lithium ion battery? *Nano Energy* **1,** 429–439 (2012).
151. Kim, H., Seo, D.-H., Kim, S.-W., Kim, J. & Kang, K. Highly reversible Co3O4/graphene hybrid anode for lithium rechargeable batteries. *Carbon N. Y.* **49,** 326–332 (2011).
152. He, Z. *et al.* A simple method of preparing graphene-coated $Li[Li_{0.2}Mn_{0.54}Ni_{0.13}Co_{0.13}]O_2$ for lithium-ion batteries. *Mater. Lett.* **91,** 261–264 (2013).
153. Song, B., Lai, M. O., Liu, Z., Liu, H. & Lu, L. Graphene-based surface modification on layered Li-rich cathode for high-performance Li-ion batteries. *J. Mater. Chem. A* **1,** 9954–9965 (2013).
154. Mai, Y. J. *et al.* MnO/reduced graphene oxide sheet hybrid as an anode for Li-ion batteries with enhanced lithium storage performance. *J. Power Sources* **216,** 201–207 (2012).
155. Chen, L., Zhang, M. & Wei, W. Graphene-based composites as cathode materials for lithium ion batteries. *J. Nanomater.* **2013,** 1–8 (2013).
156. Persson, K. *et al.* Lithium Diffusion in Graphitic Carbon. *J. Phys. Chem. Lett.* **1,** 1176–1180 (2010).
157. Mangani, I. R., Park, C. W., Yoon, Y. K., Beom, J. H. & Kim, J. Synthesis and Characterization of Li[Li[0.27]Cr[0.15]Al[0.05]Mn[0.53]]O[2] Cathode for Lithium-Ion Batteries. *J. Electrochem. Soc.* **154,** A359 (2007).
158. Song, B. *et al.* Advances in Sustain Stable Voltage of Cr-Doped Li-Rich Layered Cathodes for Lithium Ion Batteries. *J. Electrochem. Soc.* **161,** A1723–A1730 (2014).
159. Ravel, B. & Newville, M. ATHENA, ARTEMIS, HEPHAESTUS: Data analysis for X-ray absorption spectroscopy using IFEFFIT. *J. Synchrotron Radiat.* **12,** 537–541 (2005).
160. Song, B., Lai, M. O., Liu, Z., Liu, H. & Lu, L. Graphene-based surface modification on layered Li-rich cathode for high-performance Li-ion batteries. *J. Mater. Chem. A* **1,** 9954 (2013).

161. Kim, J. *et al.* Electrochemical and Structural Properties of $xLi_2M'O_3\cdot(1-x)LiMn_{0.5}Ni_{0.5}O_2$ Electrodes for Lithium Batteries (M' = Ti, Mn, Zr; $0 \leq x \leqslant 0.3$). *Chem. Mater.* **16**, 1996–2006 (2006).
162. Yoon, W. *et al.* Local Structure and Cation Ordering in O3 Lithium Nickel Manganese Oxides with Stoichiometry. 167–171 (2004). doi:10.1149/1.1737711
163. Jeong, S. K., Song, C.-H., Nahm, K. S. & Stephan, a. M. Synthesis and electrochemical properties of $Li[Li_{0.07}Ni_{0.1}Co_{0.6}Mn_{0.23}]O_2$ as a possible cathode material for lithium-ion batteries. *Electrochim. Acta* **52,** 885–891 (2006).
164. Julien, C. Local structure of lithiated manganese oxides. *Solid State Ionics* **177,** 11–19 (2006).
165. Raki, V., Dondur, V. & Hercigonja, R. FTIR study of carbon monoxide adsorption on ion-exchanged X , Y and mordenite type zeolites *. *J. Serbian Chem. Soc.* **68,** 409–416 (2003).
166. Bhargava, S. K. & Akolekar, D. B. Adsorption of NO and CO over transition-metal-incorporated mesoporous catalytic materials. *J. Colloid Interface Sci.* **281,** 171–8 (2005).
167. Manceau, A., Marcus, M. A. & Grangeon, S. Determination of Mn valence states in mixed-valent manganates by XANES spectroscopy. *Am. Mineral.* **97,** 816–827 (2012).
168. S, Stoll. *et al.* Copper K-Edge X-ray Absorption Studies of $La_{2-x}K_xCuO_4$ Superconductors. *Inorg. Chem.* **4,** 1838–1841 (1997).
169. Bareño, J. *et al.* Long-Range and Local Structure in the Layered Oxide $Li_{1.2}Co_{0.4}Mn_{0.4}O_2$. *Chem. Mater.* **23,** 2039–2050 (2011).
170. Wang, Q., Hanson, J. C. & Frenkel, A. I. Solving the structure of reaction intermediates by time-resolved synchrotron x-ray absorption spectroscopy. *J. Chem. Phys.* **129,** 234502 (2008).
171. Armstrong, a. R., Robertson, a. D. & Bruce, P. G. Overcharging manganese oxides: Extracting lithium beyond Mn^{4+}. *J. Power Sources* **146,** 275–280 (2005).
172. Ma, M., Chernova, N. A., Toby, B. H., Zavalij, P. Y. & Whittingham, M. S. Structural and electrochemical behavior of LiMn0.4Ni0.4Co0.2O2. *J. Power Sources* **165,** 517–534 (2007).
173. McBreen, J. The application of synchrotron techniques to the study of lithium-ion batteries. *J. Solid State Electrochem.* **13,** 1051–1061 (2008).
174. Yabuuchi, N., Yoshii, K., Myung, S.-T., Nakai, I. & Komaba, S. Detailed Studies of a High-Capacity Electrode Material for Rechargeable Batteries, Li_2MnO_3−$LiCo_{1/3}Ni_{1/3}Mn_{1/3}O_2$. *J. Am. Chem. Soc.* **133,** 4404–4419 (2011).
175. Li, Z. *et al.* Comparative Study of the Capacity and Rate Capability of $LiNi_yMnyCo_{1-2y}O_2$ ($y = 0.5$, 0.45, 0.4, 0.33). *J. Electrochem. Soc.* **158,** A516 (2011).
176. Croy, J. R., Gallagher, K. G., Balasubramanian, M., Long, B. R. & Thackeray, M. M. Quantifying Hysteresis and Voltage Fade in $xLi_2MnO_3\cdot(1-x)LiMn_{0.5}Ni_{0.5}O_2$ Electrodes as a Function of Li2MnO3 Content. *J. Electrochem. Soc.* **161,** A318–A325 (2013).
177. Jing, C., Liu, S., Patel, M. & Meng, X. Arsenic Leachability in Water Treatment Adsorbents. *Environ. Sci. Technol.* **39,** 5481–5487 (2005).
178. Harfouche, M. *et al.* Assessment of Zn bioavailability: XAFS study on speciation of zinc-particulate organic matter associations in polluted soils. *J. Phys. Conf. Ser.* **190,** 012189 (2009).
179. Mishra, S. & Ceder, G. Structural stability of lithium manganese oxides. *Phys. Rev. B* **59,** 6120–6130 (1999).
180. Yu, D. Y. W. & Yanagida, K. Structural Analysis of Li_2MnO_3 and Related Li-Mn-O Materials. *J. Electrochem. Soc.* **158,** A1015 (2011).
181. Shen, C.-H. *et al.* Facile synthesis of the Li-rich layered oxide $Li_{1.23}Ni_{0.09}Co_{0.12}Mn_{0.56}O_2$ with superior lithium storage performance and new insights into structural transformation of the layered oxide material during charge-discharge cycle: in situ XRD characterization. *ACS Appl. Mater. Interfaces* **6,** 5516–24 (2014).
182. Armstrong, A., Robertson, A. & Bruce, P. Structural transformation on cycling layered $Li(Mn_{1-y}Co_y)O_2$ cathode materials. *Electrochim. Acta* **45,** 285–294 (1999).
183. WEI, Y., NAM, K., KIM, K. & CHEN, G. Spectroscopic studies of the structural properties of Ni substituted spinel LiMn2O4. *Solid State Ionics* **177,** 29–35 (2006).

184. Boulineau, A. *et al.* Evolutions of $Li_{1.2}Mn_{0.61}Ni_{0.18}Mg_{0.01}O_2$ during the Initial Charge/Discharge Cycle Studied by Advanced Electron Microscopy. *Chem. Mater.* **24,** 3558–3566 (2012).
185. Xu, B., Fell, C. R., Chi, M. & Meng, Y. S. Identifying surface structural changes in layered Li-excess nickel manganese oxides in high voltage lithium ion batteries: A joint experimental and theoretical study. *Energy Environ. Sci.* **4,** 2223 (2011).